

APPLIED COMPUTATIONAL ELECTROMAGNETICS SOCIETY JOURNAL

July 2016
Vol. 31 No. 7
ISSN 1054-4887

The ACES Journal is abstracted in INSPEC, in Engineering Index, DTIC, Science Citation Index Expanded, the Research Alert, and to Current Contents/Engineering, Computing & Technology.

The illustrations on the front cover have been obtained from the research groups at the Department of Electrical Engineering, The University of Mississippi.

THE APPLIED COMPUTATIONAL ELECTROMAGNETICS SOCIETY

<http://aces-society.org>

EDITOR-IN-CHIEF

Atef Elsherbeni

Colorado School of Mines, EECS Dept.
Golden, CO 80401, USA

ASSOCIATE EDITORS-IN-CHIEF

Sami Barmada

University of Pisa. ESE Dept.
Pisa, Italy, 56122

Mohamed Bakr

McMaster University, ECE Dept.
Hamilton, ON, L8S 4K1, Canada

Antonio Musolino

University of Pisa
56126 Pisa, Italy

Mohammed Hadi

Kuwait University, EE Dept.
Safat, Kuwait

Abdul Arkadan

Marquette University, ECE Dept.
Milwaukee, WI 53201, USA

Marco Arjona López

La Laguna Institute of Technology
Torreon, Coahuila 27266, Mexico

Alistair Duffy

De Montfort University
Leicester, UK

Paolo Mezzanotte

University of Perugia
I-06125 Perugia, Italy

EDITORIAL ASSISTANTS

Matthew J. Inman

University of Mississippi, EE Dept.
University, MS 38677, USA

Shanell Lopez

Colorado School of Mines, EECS Dept.
Golden, CO 80401, USA

EMERITUS EDITORS-IN-CHIEF

Duncan C. Baker

EE Dept. U. of Pretoria
0002 Pretoria, South Africa

Ahmed Kishk

Concordia University, ECS Dept.
Montreal, QC H3G 1M8, Canada

Allen Glisson

University of Mississippi, EE Dept.
University, MS 38677, USA

Robert M. Bevensee

Box 812
Alamo, CA 94507-0516, USA

David E. Stein

USAF Scientific Advisory Board
Washington, DC 20330, USA

EMERITUS ASSOCIATE EDITORS-IN-CHIEF

Yasushi Kanai

Niigata Inst. of Technology
Kashiwazaki, Japan

Alexander Yakovlev

University of Mississippi, EE Dept.
University, MS 38677, USA

Levent Gurel

Bilkent University
Ankara, Turkey

Ozlem Kilic

Catholic University of America
Washington, DC 20064, USA

Erdem Topsakal

Mississippi State University, EE Dept.
Mississippi State, MS 39762, USA

Fan Yang

Tsinghua University, EE Dept.
Beijing 100084, China

EMERITUS EDITORIAL ASSISTANTS

Khaled ElMaghoub
Trimble Navigation/MIT
Boston, MA 02125, USA

Christina Bonnington
University of Mississippi, EE Dept.
University, MS 38677, USA

Anne Graham
University of Mississippi, EE Dept.
University, MS 38677, USA

Mohamed Al Sharkawy
Arab Academy for Science and Technology, ECE Dept.
Alexandria, Egypt

JULY 2016 REVIEWERS

Ramin Aghajafari
Shahid Ahmed
Md Rezwanul Ahsan
Mohamed Al-Sharkaway
Mohammad Alibakhshi Kenari
Gulam Alsath
Ru-shan Chen
Fangyuan Chen
Michael Chryssomallis
Ali Foudazi
Yongxin Guo
Yan-Jie Guo
Anders Hook
Yasushi Kanai
Mahmood Karami
Sanghoek Kim
Toshiro Kodera
Yingsong Li
Stanislav Maslovski
Ladislau Matekovits
Zicong Mei

Zahéra Mekkioui
Donglin Meng
Fan-Yi Meng
Biswajeet Mukherjee
Mohammad Naser-Moghadasi
Erika Pittella
Anastasis Polycarpou
Hamid Rajabalipanah
Shivraj Rathod
Blaise Ravelo
Abhishek Rawat
Luca Rienzo
Vince Rodriguez
Daniel Rodríguez Prado
Kapil Sharma
Katherine Siakavara
Daniel Sievenpiper
Lauri Sydanheimo
Zhengqing Yun
Xueying Zhang

THE APPLIED COMPUTATIONAL ELECTROMAGNETICS SOCIETY
JOURNAL

Vol. 31 No. 7

July 2016

TABLE OF CONTENTS

Direction Finding System Using Planar Luneburg Lens Hao Yu, Xumin Ding, Kuang Zhang, Yuming Wu, and Qun Wu.....	731
Mutual Coupling Reduction in MIMO Patch Antenna Array Using Complementary Split Ring Resonators Defected Ground Structure Hany A. Atallah, Adel B. Abdel-Rahman, Kuniaki Yoshitomi, and Ramesh K. Pokharel.....	737
Experimental Study of Coupling Compensation of Low Profile Spiral Antenna Arrays Response for Direction-finding Applications Taherah S. Ghazaany, Shron Zhu, Raed A. Alhameed, James M. Noras, Steven M. R. Jones, Tyler V. Buren, Tim Suggett, and Simon Marker	744
Mutual Coupling Reduction in CBS Antenna Arrays by Utilizing Tuned EM-EBG and Non-planar Ground Plane Saeed Manshari, Farokh Hodjat Kashani, and Gholamreza Moradi	750
Artificial Neural Network based Design of RF MEMS Capacitive Shunt Switches Zlatica Marinković, Taeyoung Kim, Vera Marković, Marija Milijić, Olivera Pronić-Rančić, Tomislav Ćirić, and Larissa Vietzorreck	756
Vector Hysteresis Modeling in Arbitrarily Shaped Objects Using an Energy Minimization Approach Amr A. Adly and Salwa K. Abd-El-Hafiz.....	765
Generalized Spectral Decomposition Approach to a Stochastic Finite Integration Technique Electrokinetic Formulation Lorenzo Codecasa and Luca Di Rienzo.....	771
Efficient Representation of Multilevel QR Algorithm for Analysis of Microstrip Structures Zhaoneng Jiang and Ting Wan	777
Analytical Solution for Line Source Excitation of a PEMC Cylinder Coated with Multilayer Anisotropic Media Ali Shahi, Mahmoud Fallah, and Ali Abdolali	782

A Compact Design of Planar Array Antenna with Fractal Elements for Future Generation Applications Naser Ojaroudiparchin, Ming Shen, and Gert Frølund Pedersen	789
A Compact Design and New Structure of Monopole Antenna with Dual Band Notch Characteristic for UWB Applications Saeed Hoseyni, Javad Nourinia, Changiz Ghobadi, Sayed V. Masuminia, and Bahman Mohammadi.....	797
A Compact and Miniaturized Broadband Phase Shifter Using Coupled-lines Yongle Wu, Siyue Zhou, Xiaochuan Shen, and Yuanan Liu	806
Mode Matching in Microstrip Antenna with both Electric and Magnetic Surface Current on Sidewall in Cavity Model Fazel Rangriz Rostami, Gholamreza Moradi, and Reza Sarraf Shirazi.....	812
Design of Lowpass Filter and Lowpass-Highpass Diplexer with LTCC Technology Chunxia Zhou, Yongxin Guo, and Wen Wu.....	817
Ferrite-Loaded Substrate Integrated Waveguide Frequency-Agile Bandpass Filter Qiu Dong Huang and Yu Jian Cheng	823
Simulating CW Light Propagation Through Macroscopic Scattering Media Via Optical Phase Conjugation Yi-An Huang, Cheng-Hao Tsai, and Snow H. Tseng.....	829
Analysis of Highly Sensitive Photonic Crystal Biosensor for Glucose Monitoring Mohamed S. Mohamed, Mohamed Farhat O. Hameed, Nihal F. F. Areed, Mohamed M. El-Okri, and Salah S. A. Obayya	836
Ultra-Wideband Polarization Conversion Metasurface Based on Topology Optimal Design and Geometry Tailor Sai Sui, Jibao Yu, Hua Ma, Jieqiu Zhang, Jiafu Wang, Zhuo Xu, and Shaobo Qu.....	843
A Circuit Human Body Model for an Indirect Lightning Strike Analyzed by means of an FDTD Method Viviane A. Alrim, Stamatios A. Amanatiadis, Antonios X. Lalas, and Christos S. Antonopoulos	847
Numerical Analysis of Thermal Gradient & Magnetic Field using Ferrofluid Cooling Harry Garg, Sahib Singh, Vipender Singh Negi, Ashish Singh Kharola, and Arun K. Lall.....	853

Direction Finding System Using Planar Luneburg Lens

Hao Yu¹, Xumin Ding¹, Kuang Zhang¹, Yuming Wu², and Qun Wu¹

¹Dept. of Electronic & Communications Engineering
Harbin Institute of Technology, Harbin, 150001, China
yuhao4746@163.com, g0302dxm@163.com, zhangkuang@126.com, qwu@hit.edu.cn

²School of Information and Electronics
Beijing Institute of Technology, Beijing, 100081, China
ymwu@ntu.edu.sg

Abstract — In this paper, a novel two-dimensional Luneburg lens, composed of artificial impedance surfaces (AIS), is proposed for direction of arrival (DOA) estimation. Several detectors are mounted around the Luneburg lens to estimate the DOA of a microwave signal, owing to the surface wave can be focused perfectly on the diametrically opposite side of the lens. The desired refractive index profile of the Luneburg lens is controlled by the variable surface impedance of the unit cells, which is obtained by using an array of complementary unipolar compact photonic band gap (UC-PBG) structure inside a parallel plate waveguide. The proposed Luneburg lens with several probes, which operate in X-band region, are fabricated and measured to demonstrate the direction finding system. Both simulation and measured results show that the system has an excellent focusing ability, and the measured resolution of the system agrees very well with the theoretical value.

Index Terms — Artificial impedance surfaces, direction of arrival estimation, Luneburg lens, surface wave.

I. INTRODUCTION

Direction of arrival (DOA) estimation has attracted lots of attentions because it has a great potential in wireless communications and electronic warfare. But the typical direction finding system always need a large number of elements and complex algorithms, which have hindered the development of the DOA estimation.

In the last few years, artificial impedance surfaces (AISs), such as high impedance surfaces (HISs) [1-3], electromagnetic band gap (EBG) surfaces [4], and simply “metasurfaces” [5], drew a lot of attentions because of the great potential values in new antenna applications and technological solutions. Their unique electromagnetic responses, which are difficult to be realized with conventional materials, bring a lot of novel applications. For example, the mushroom surface, which

has a high impedance property for plane wave reflection in the EBG frequency bandwidth, can be used in fabrication of low-profile antennas and TEM waveguide.

AISs are usually composed of a grounded dielectric layer covered with a pattern of sub-wavelength conductive patches. According to effective medium theory [6,7], the scattering parameters of the AISs can be artificially tailored with different unit geometries and dimensions, rather than the intrinsically chemical components. By varying the size of the patches, we can control the surface impedance of the unit cells at different position. These features make an attractive approach for designing gradient index lens antennas [8-10].

The Luneburg lens, proposed by R. K. Luneburg in 1944 [11], is a well-known gradient index lens which shows the advantages of broadband, multi-beam and low loss. The refractive index of Luneburg lens varies along the radius, which can be expressed by Eq. (1):

$$n = \sqrt{2 - (r/R)^2} \quad (r \leq R). \quad (1)$$

Here, R is the radius of the lens and r is the distance from any point to the center of the lens. Because of the varying refractive index, the path of incident wave can be bended while travelling within the lens. It can be demonstrated that the incident collimated beam would be focused perfectly on the diametrically opposite side on the lens [12]. This characteristic makes Luneburg lens widely used in the fields such as navigation and satellite communications.

Traditional Luneburg lenses are fabricated with concentric shells with stepped approximation, and each shell made of different dielectric material, has the desired refractive index. It is complex and expensive to be fabricated, and the high radio frequency loss limit its practical application. Another newly developed method proposed by Xue [13] shows that Luneburg lenses can be realized by using a planar structure, whose permittivity distribution can be modified in two ways. In the central

region, the permittivity is changed by controlling the density of the holes. While on the edge, it is achieved by controlling the dielectric thickness. All these previous designs are bulky and difficult to be integrated in low profile equipment. Developments in the field of AISs, which overcome the difficulties in traditional way of fabrication, provide an alternative way to realize a planar Luneburg lens structure.

In this paper, a planar Luneburg lens used in direction finding system is proposed and investigated. The diameter of the lens is 120 mm, which is about 4λ (λ is the free-space wavelength). A simplified unipolar compact photonic band gap (UC-PBG) structure is chosen as the unit cell. A focusing wave-front is achieved by changing the size of UC-PBG, which is equivalent to changing the local dispersion and the local phase velocity. The Luneburg lens is applied to calculate the DOA and the experiment results shows the resolution of the proposed estimation method is about 5° .

II. SURFACE IMPEDENCE ANALYSIS

Differing from the traditional Luneburg lens, the two-dimensional Luneburg lens is usually placed inside a parallel-plate waveguide (PPW), as shown in Fig. 1. In order to control the propagation of the surface wave, the boundary conditions of one wall of the parallel-plate waveguide must be modified. The effect of changing the boundary conditions is equivalent to change the local dispersion and the local phase velocity. Generally it can be done by changing the geometrical parameters, such as modulating the height of periodic tiny metal posts, changing the loading of transmission lines, varying the size of metallic patches, etc. In this paper, we will focus on a complementary unipolar compact photonic band gap (UC-PBG) structure.

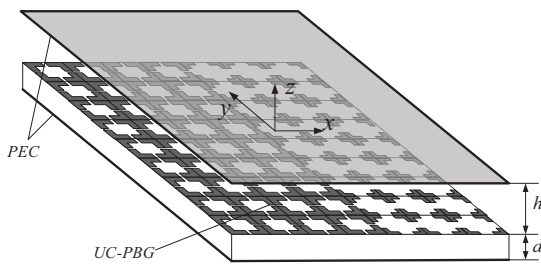


Fig. 1. The variable printed structures is placed inside a parallel-plate waveguide.

The equivalent refractive index n_{eq} can be interpreted as the ratio of the free-space wavenumber k and wavenumber along the propagation (parallel to the plate) k_ρ :

$$n_{eq} = k_\rho / k = \sqrt{1 - (k_z^2 / k^2)}, \quad (2)$$

where k_z is the wavenumber along the z axis. In order to have a refractive index $n_{eq} > 1$, k_z should be imaginary. In

Fig. 2, the transverse resonance equivalent circuit for TM mode of the surface is presented. Using the transmission-line theory, the surface impedance, which depends on the size of the local patch, is derived as:

$$Z_s^{TM}(k_\rho) = -jZ_0^{TM}(k_z) \tan(k_z h) = j\eta_0 \frac{\beta_z}{k} \tanh(\beta_z h), \quad (3)$$

where $Z_0^{TM} = \eta_0 k_z / k$, $k_z = -j\beta_z$ (β_z is positive), η_0 is free space impedance. By combining (1), (2) and (3), we obtain:

$$Z_s^{TM}(k_\rho) = j\eta_0 \sqrt{1 - (r/R)^2} \tanh(kh \sqrt{1 - (r/R)^2}). \quad (4)$$

Equation (4) provides a surface impedance profile corresponding to the Luneburg lens. The diameter of the lens is set to be 120 mm (4λ). A practical height for the top wall h is about $\lambda/2$ because this concept is based on single TM mode propagation inside the parallel-plate waveguide. The surface impedance profile is shown in Fig. 3.

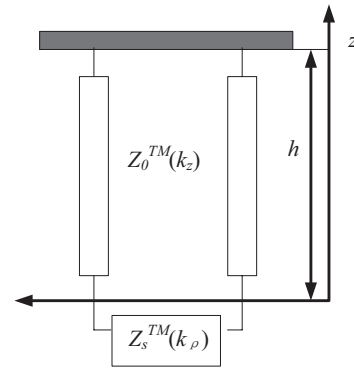


Fig. 2. Transverse resonance equivalent circuit for TM mode.

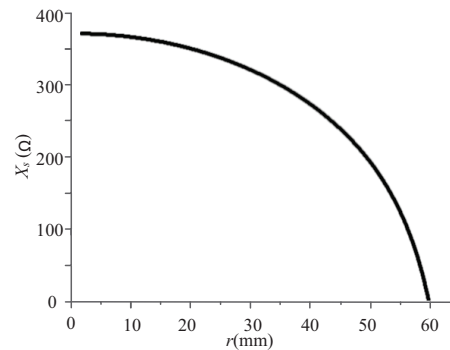


Fig. 3. The surface impedance profile of the Luneburg lens.

The complementary UC-PBG structure is chosen as the unit cell of the Luneburg lens. As shown in Fig. 4, metal patterns are placed on the dielectric substrate. The permittivity of the substrate is 3.5, and the thickness is 3 mm. The loss tangent of the substrate is smaller than 0.001 at 10 GHz. According to the effective medium

theory, the dimension of the unit cell square is set to be 3 mm (0.1λ). The surface impedance of the unit cell can be obtained by using CST Microwave Studio. The eigenmode solver is adopted to calculate the properties of surface waves and extract the effective surface impedance.

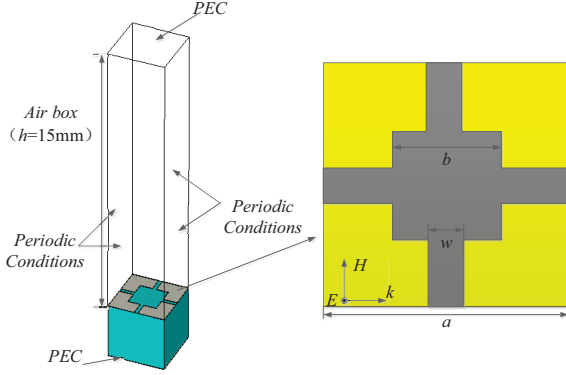


Fig. 4. The boundary conditions settings of the complementary UC-PBG structure.

As shown in Fig. 4, the periodic conditions are applied to the four vertical walls of the simulation volume. The top and bottom walls are both perfect electrical conductors. An eigenfrequency ω , which traverses a unit cell for a given phase difference φ , can be simulated by using the eigenmode solver. The phase difference φ is related to the wavenumber along the propagation k_p :

$$\varphi = k_p a; \quad k_p = \sqrt{k^2 - k_z^2}. \quad (5)$$

Then the surface impedance, which determined by the geometrical dimensions of the unit cell, can be calculated. By simulating and calculating different unit cells, it shows that the surface impedance decreases when the variable parameters b and w increase, as shown in Fig. 5. Therefore, the unit cell can achieve the corresponding surface impedance of the Luneburg lens.

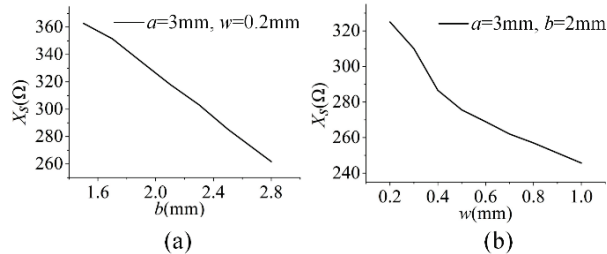


Fig. 5. The relationship between the surface impedance and the dimensions of the complementary UC-PBG structure. (a) $a=3$ mm, $w=0.2$ mm, and b is variable parameter. (b) $a=3$ mm, $b=2$ mm, and w is variable parameter.

III. LUNEBURG LENS SIMULATION AND EXPERIMENTS

As shown in Fig. 6, a planar Luneburg lens is proposed and designed, which is placed in a parallel-plate waveguide with the height $h=15$ mm. There are 20 units arranged along the radius. The variation of the surface impedance from the center to the edge of the lens is realized by varying the variable parameters b and w , as shown in Table 1. The Luneburg lens was discretized into seven concentric regions, where the surface impedance is required to be equal at each circle with the same radius. This design consideration makes sure that the structure is more close to the perfect lens.

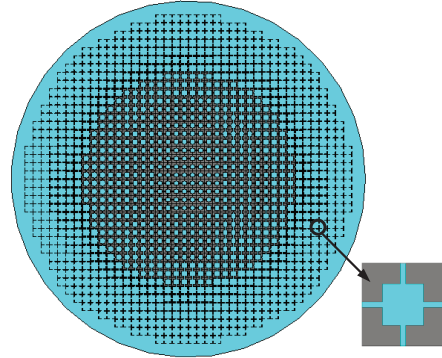


Fig. 6. An array of complementary UC-PBG structure with the surface impedance profile corresponding to the Luneburg lens.

Table 1: Dimensions and surface impedences of the unit cell in the different concentric regions of the lens

Region	b (mm)	w (mm)	$X_s^{TM}(\Omega)$
1	1.5	0.2	362.7
2	1.7	0.2	351.5
3	1.8	0.3	322.4
4	2.0	0.4	291.3
5	2.5	0.5	242.9
6	2.7	0.6	194.0
7	2.8	1.0	43.4

CST Microwave Studio is used to simulate the electric field distribution of the Luneburg lens. The plane waves incident from the right side of the lens. It is obvious that the wave front is changed gradually when it passes through the lens, and finally focused at the opposite side of the lens. From Figs. 7 (a) to 7 (d), we can find that the focusing point keeps the same at different operational frequency.

The proposed planer Luneburg lens shows excellent focusing ability from 9 GHz to 12 GHz, which means it can operate very well in a broad bandwidth. In order to evaluate the isotropy of Luneburg lens, the incident angle α is changed, as shown in Fig. 8. Since the unit cell has a

symmetric structure, the focusing performance keeps very well at 10 GHz with different incident angle. It is important to note that, the polarization of the incident waves must be perpendicular to the Luneburg lens, because only in this case, a virtual current circuit can be constructed by the complementary UC-PBG structure and the upper ground plane. The transverse resonance dispersion equation is obtained by solving the equivalent circuit in Fig. 2. So the proposed planar Luneburg lens in this paper is designed for the TM incident wave.

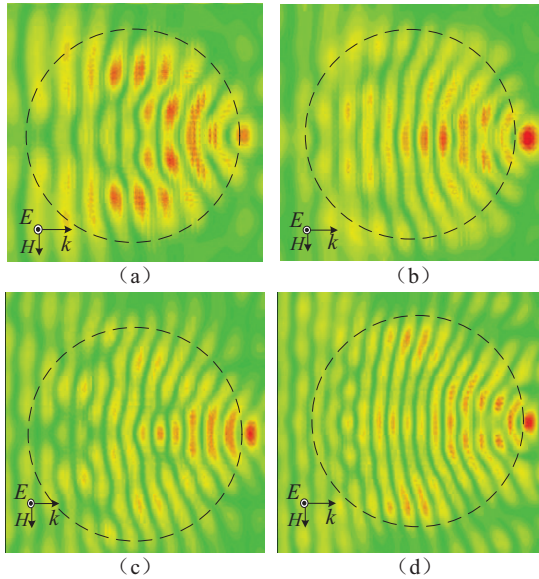


Fig. 7. Distribution of the electric field inside the Luneburg lens: (a) $f=9$ GHz, (b) $f=10$ GHz, (c) $f=11$ GHz, and (d) $f=12$ GHz.

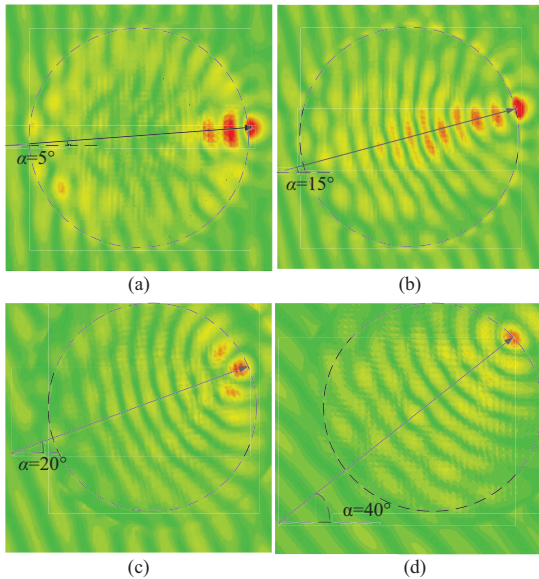


Fig. 8. Distribution of the electric field with different incident angles at 10 GHz.

To verify the design, a planar Luneburg lens placed inside a PPW is fabricated. As shown in Fig. 9, three nylon hexagonal standoffs of 15 mm height are used to support the top plate of PPW. It can be seen that 11 probes with a separation of 5 degrees are mounted on the surface of the lens. The source and probes are connected to a vector network analyzer (VNA) to measure the magnitude of the electric field at different position. In this case, all the values from the 11 probes are normalized to the probe which directly facing the source, so that the attenuation between transmitter and receiver could be ignored. The normalized electric field magnitudes are shown in Fig. 10. The probe which placed in the direction of the incident wave, has the maximum value. This characteristic can be used in direction of arrival (DOA) estimation. The resolution is determined by the separation of the probes. In the proposed design, the resolution is limited to be 5° due to the space around the lens couldn't allow us to mount more probes.

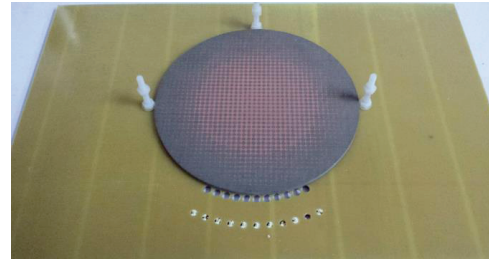


Fig. 9. Top view of the fabricated Luneburg lens.

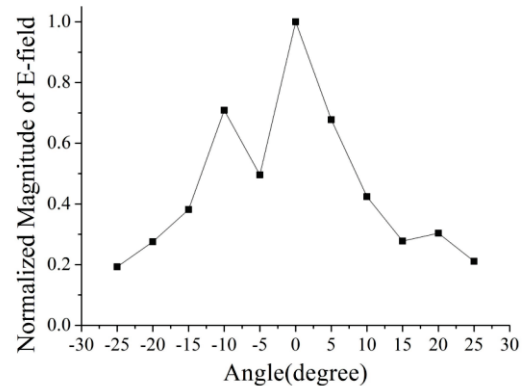


Fig. 10. Normalized E-field magnitude.

IV. CONCLUSION

In this paper, a novel direction finding system using planar Luneburg lens is proposed. The Luneburg lens is composed of multilayer arrays of complementary UC-PBG structure which printed on a dielectric substrate inside a parallel-plate waveguide. By changing the boundary conditions of the plate, the converging wave can be obtained. The relationship between the surface impedance and dimensions of the unit cell has been

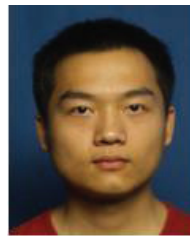
studied through numerical simulations. The distribution of the electric field inside the lens has been simulated. The proposed Luneburg lens shows a good focusing ability in X-band region. When the incident angle is rotated, the focusing performance of the proposed Luneburg lens keeps very well. The proposed Luneburg lens can be used in direction of arrival estimation. Using the proposed system, the DOA estimation can be achieved accurately and effectively, which makes our design a good option for practical applications.

ACKNOWLEDGMENT

This work is supported by National Natural Science Foundation of China (No. 61571155, No. 61371044, No. 61401025). This work is also supported by Beijing Natural Science Foundation (4154085) Shanghai Academy of Spaceflight Technology (SAST 201439), and the Basic Research Foundation of Beijing Institute of Technology, China (Grant No. 20140542002).

REFERENCES

- [1] D. Sievenpiper, L. Zhang, R. F. J. Broas, N. G. Alexopoulos, and E. Yablanovitch, "High-impedance electromagnetic surfaces with a forbidden frequency band," *IEEE Trans. Microw. Theory Tech.*, vol. 47, no. 11, pp. 2059-2074, Nov. 1999.
- [2] B. H. Fong, J. S. Colburn, J. J. Ottusch, J. L. Visher, and D. F. Sievenpiper, "Scalar and tensor holographic artificial impedance surfaces," *IEEE Trans. Antennas Propag.*, vol. 58, no. 10, pp. 3212-3221, Oct. 2010.
- [3] R. Quarfoth and D. Sievenpiper, "Artificial tensor impedance surface waveguide," *IEEE Trans. Antennas Propag.*, vol. 61, no. 7, pp. 3597-3606, Jul. 2013.
- [4] J. D. Shumpert, W. J. Chappell, and L. P. B. Katehi, "Parallel-plate mode reduction in conductor-backed slots using electromagnetic bandgap substrates," *IEEE Trans. Microwave Theory Tech.*, vol. 47, pp. 2099-2104, Nov. 1999.
- [5] S. Maci and P.-S. Kildal, "Hard and soft surfaces realized by FSS printed on a grounded dielectric slab," in *Proc. URSI-IEEE AP-S Symp.*, Monterrey, CA, USA, pp. 285-288, Jun. 2004.
- [6] T. Koschny, M. Kafesaki, and E. N. Economou, "Effective medium theory of left-handed materials," *Physical Review Letters*, vol. 93, no. 10, pp. 107402, 2004.
- [7] M. C. K. Wiltshire, J. B. Pendry, and W. Williams, "An effective medium description of 'Swiss Rolls', a magnetic metamaterial," *Journal of Physics: Condensed Matter*, vol. 19, no. 45, pp. 456216, 2007.
- [8] Y. J. Park, A. Herschlein, and W. Wiesbeck, "A photonic bandgap (PBG) structure for guiding and suppressing surface waves in millimeter-wave antennas," *IEEE Trans. Microw. Theory Tech.*, vol. 49, no. 10, pp. 1854-1859, Oct. 2001.
- [9] C. Pfeiffer and A. Grbic, "A printed, broadband Luneburg lens antenna," *IEEE Trans. Antennas Propag.*, vol. 58, no. 9, pp. 3055-3059, Sep. 2010.
- [10] M. Bosiljevac, M. Casaletti, F. Caminita, Z. Sipus, and S. Maci, "Non-uniform metasurface Luneburg lens antenna design," *IEEE Trans. Antennas Propag.*, vol. 60, no. 9, pp. 4065-4073, Sep. 2012.
- [11] R. K. Luneburg, *Mathematical Theory of Optics*. Providence, RI: Brown Univ. Press, 1944.
- [12] G. D. M. Peeler and H. P. Coleman, "Microwave stepped-index Luneburg lenses," *IEEE Trans. Antennas Propag.*, vol. 6, no. 2, pp. 202-207, Apr. 1958.
- [13] L. Xue and V. F. Fusco, "Printed holey plate Luneburg lens," *Microw. Opt. Technol. Lett.*, vol. 50, pp. 378-380, Dec. 2007.



Hao Yu received the B.S. and M.S. degrees in Electromagnetic Field and Microwave Technology from Harbin Institute of Technology Harbin, China, in 2010 and 2014, respectively. He is currently working toward the Ph.D. degree in the Department of Electronic and Communications Engineering, Harbin Institute of Technology. His research interests include antenna design and electromagnetic compatibility.



Xumin Ding received the B.S., M.S. and Ph.D. degrees in Information and Communication Engineering from Harbin Institute of Technology, Harbin, China in 2010, 2012 and 2015, respectively. He is currently an Assistant Professor of Department of Microwave Engineering, Harbin Institute of Technology. His research interests are in the areas of metamaterials, metasurfaces and antennas.



Kuang Zhang received the B.S., M.S. and Ph.D. degrees in Information and Communication Engineering from Harbin Institute of Technology, Harbin, China in 2005, 2007 and 2011, respectively. He is currently an Associate Professor of Department of Microwave Engineering, Harbin Institute of Technology since Dec. 2014. His current research interests are in the areas of metamaterials & metasurfaces, transform optics, microwave lenses and optical force.



Yuming Wu received the B.S. degree in Communication Engineering from Harbin Institute of Technology, China in 2006 and Ph.D. degree in Microwave and RF in National University of Singapore, Singapore in 2011. From 2011 to 2013, she worked at Nanyang Technological University, Singapore as a Postdoctoral Research Fellow. Since 2013, she joined the Beijing Key Laboratory of Millimeter Wave and Terahertz Technology, School of Information and Electronics, Beijing Institute of Technology as an Assistant Professor. Her current research interest includes characterization, analysis and design of nanoantennas for their conformal/flexible/wearable applications, meta-material based/Terahertz antenna and advanced functional devices.



Qun Wu received the B.S. degree in Radio Engineering, M.S. degree in Electromagnetic Fields and Microwaves, and Ph.D. degree in Communication and Information Systems, all from Harbin Institute of Technology, Harbin, China in 1977, 1988 and 1999, respectively. He worked as a Visiting Professor at Seoul National University (SNU) in Korea, from 1998 to 1999, and Pohang University of Science and Technology, from 1999 to 2000, respectively. Since 1990, he has been with School of Electronics and Information Engineering at HIT, China, where he is currently a Professor. His recent research interests are mainly in metamaterials, microwave passive circuits, and millimeter wave MEMS devices.

Mutual Coupling Reduction in MIMO Patch Antenna Array Using Complementary Split Ring Resonators Defected Ground Structure

Hany A. Atallah^{1,2}, Adel B. Abdel-Rahman^{1,2}, Kuniaki Yoshitomi³,
and Ramesh K. Pokharel³

¹ Electronics and Communications Engineering Department
School of Electronics, Communications and Computer Engineering
Egypt-Japan University of Science and Technology (E-JUST), Alexandria 21934, Egypt

² Faculty of Engineering, South Valley University, Qena 83523, Egypt
hany.mohamed@ejust.edu.eg, h.atallah@eng.svu.edu.eg, adel_b15@eng.svu.edu.eg

³ School of Information Science and Electrical Engineering
Kyushu University, Nishi-ku, Fukuoka 819-0395, Japan
yoshitomi@ejust.kyushu-u.ac.jp, pokharel@ejust.kyushu-u.ac.jp

Abstract — In this paper, complementary split ring resonators (CSRRs) defected ground structure (DGS) is introduced to suppress surface waves and to reduce the mutual coupling between E-plane coupled two elements of a microstrip patch MIMO antenna array. The CSRRs-DGS is easily etched on the ground plane between the array elements. The CSRRs-based DGS acts as a bandstop filter between the array elements and operates in the same desired frequency band of the array at 9.2 GHz. Significant reduction of the electromagnetic (EM) mutual coupling is achieved between array elements with a reduced edge-to-edge spacing of 7.5 mm ($0.22 \lambda_0$). Experimental results show that more than 30 dB isolation between the array elements is obtained using an array of CSRR-based DGS. Moreover, the antenna array parameters are successfully optimized with a numerical experimentation technique using a 3D full-wave EM simulator. The design of the proposed array is fabricated and measured for verification purposes. The proposed design has been simulated and validated experimentally. Good agreement is found between the simulated and the measured data.

Index Terms — Bandstop filter, CSRRs (complementary split ring resonators), DGS (defected ground structure), mutual coupling, surface waves.

I. INTRODUCTION

In recent years, isolation enhancement in antenna array applications poses a strong challenge in the antenna community [1,2]. The mutual coupling or isolation between closely placed antenna elements is important in a number of applications. These include systems depending on array antennas and more recently multiple-

input-multiple-output (MIMO) wireless communication systems [3,4]. Surface waves cause many disadvantages for microstrip antennas such as a mutual coupling effect between elements on an antenna array, which exists whenever the substrate has a dielectric permittivity greater than one ($\epsilon_r > 1$). In an antenna array, the mutual coupling effect will deteriorate the radiation properties of the array. To achieve low mutual coupling between closely spaced antenna elements and to suppress surface waves, several studies have been conducted including defected ground structure (DGS) [5-10]. This idea can be extended to a specific application like reducing scan blindness in microstrip arrays. Many shapes and configurations of DGS have been studied such as rectangular slots [5,6], circle [7], dumbbells [8], polygonal [9], and inter-digital capacitor [10]. Each DGS shape can be represented as an equivalent circuit model consisting of an inductance and a capacitance, which leads to a certain frequency band gap determined by the shape, dimension and position of the defect [7]. DGS gives an extra degree of freedom in microwave circuit design and can be used for a wide range of applications.

Recently, a pioneer research of the complementary split ring resonator (CSRR) has been proposed [11]. It can be derived from the split ring resonator (SRR) structure in a straightforward way by using the concepts of duality and complementarity. This CSRR structure provides a negative effective permittivity [12]. Because of their small size, CSRRs are called sub-lambda structures. Due to this fact, a super-compact reject band structure can be implemented using CSRRs. The CSRRs are etched in the ground plane or the conductor line of planar transmission structures, such as a microstrip line or a coplanar waveguide (CPW), and provide a negative

effective permittivity to the dielectric media [13]. The electromagnetic (EM) behaviors of the CSRRs are similar to those of the electromagnetic bandgap (EBG) structures [14,15]. However, it is difficult to design the dimension and to find the equivalent circuits of EBG. Although EBG structures, DGS and CSRR can provide the similar stop-band characteristics, it may be worth pointing out the attenuation property of the CSRR which is better than EBG structures and other DGS shapes. It seems to be good in cognitive radio (CR) systems to reduce the mutual coupling between the sensing antenna and communication antenna in cognitive radio MIMO applications using a simple technique [16].

In this paper, simple designs of bandstop filter using CSRRs-based DGS are proposed to suppress surface waves and to reduce the mutual coupling effect between E-plane coupled antenna array elements [17,18]. The designed microstrip antenna arrays operate at the X-band (9.2 GHz). Usually, the array elements are susceptible to strong mutual coupling due to the surface wave, space wave and near field overlapping. The coupling is stronger in E-plane coupled antennas than in H-plane coupled antennas. Thus, the mutual coupling effect in the E-plane direction is mainly investigated in this work. The CSRRs are etched in the ground plane and occupy a small area allowing for small antenna separation in their use with compact ground planes. Moreover, the radiation properties of the proposed antenna array are also observed and discussed. Simulations results based on a 3D full-wave EM simulator and measurements are presented. In Section II, the structure of the bandstop filter is discussed. Section III presents and illustrates the proposed array design. Section IV is devoted to the comparison of the simulated and measured results.

II. CSRR-DGS BANDSTOP FILTER DESIGN

Figure 1 shows the top and bottom 2-D views of the single CSRR-DGS geometry. The CSRR structure is designed to operate at stopband of 9.2 GHz in the same desired band of the antenna array. The dimensions of the CSRR structure are $r_{in} = 0.75$ mm, and $c = g = d = 0.4$ mm. The ground plane dimensions are 20×20 mm². The substrate is Rogers Ro 3003 with a thickness of $t = 1.524$ mm, dielectric constant of 3 and loss tangent of 0.0013. The CSRR structure is etched in the ground plane below the center of the microstrip line, which has a width of 3.4 mm. The width of the microstrip line is designed to match the characteristic impedance of 50 Ω . Figure 1 (c) shows the simulated $|S|$ -parameters of the single CSRR. The presented bandstop filter was optimized through simulations using a commercial 3D full-wave analysis software package computer simulation technology (CST) [19].

The simulation results show a reject band characteristic at the transmission zero frequency of 9.24 GHz as shown in Fig. 1 (c). Using only a single

CSRR structure in the ground plane, we can obtain a wide stop band response with a high rejection level which is difficult to achieve with conventional microstrip resonators.

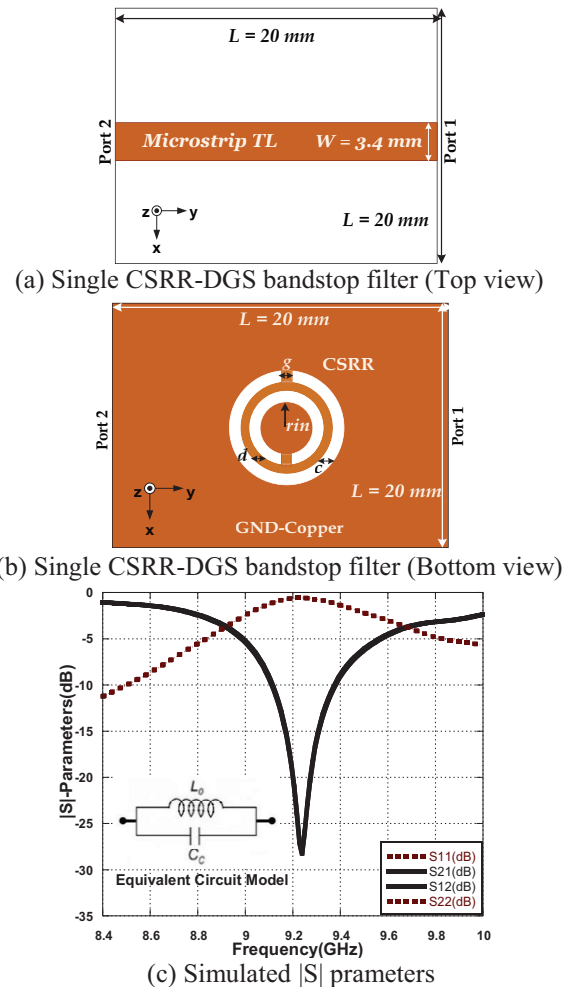


Fig. 1. Schematic of the optimized CSRR-DGS bandstop filter and $|S|$ -parameters results.

III. PROPOSED MICROSTRIP PATCH ANTENNA ARRAY WITH CSRRs-DGS

The proposed geometry of the antenna array with CSRRs-based DGS and $|S|$ -parameters are shown in Fig. 2. The rectangular patch has dimensions $W = 11$ mm, and $L = 8.7$ mm, whereas the feeding microstrip has length $L_{il} = 17.5$ mm and width $W_{il} = 3.4$ mm which ensure a 50 Ω characteristic impedance. The inset length is $L_{inset} = 3.8$ mm which in essence provides the necessary impedance matching. The substrate used for this array is the same as that used for the bandstop filter design in Section II. The spacing between the elements is chosen to be 7.5 mm ($0.22 \lambda_0$). The CSRR structures are designed to operate at the transmission zero frequency in the same band of the antenna array. The chosen dimensions of the

CSRR structures for this frequency of operation are $r_{in} = 0.65$ mm, $r_{inl} = 0.8$ mm, and $c = g = d = 0.4$ mm, respectively after intensive optimization and co-design for the array with the CSRRs-DGS. The bandstop filter affects significantly the array mutual coupling and the isolation between the two elements [17]. However, the proposed design with CSRRs has a very small deviation in the resonant frequency about 0.3% (29 MHz) compared to the conventional array due to the presence of the CSRRs DGS in the ground plane. The proposed configuration produces a mutual coupling about -61 dB better than the conventional array with the same dimensions through simulations as shown in Fig. 2 (c). The total dimensions of the array are $a = 40$ mm and $b = 60$ mm.

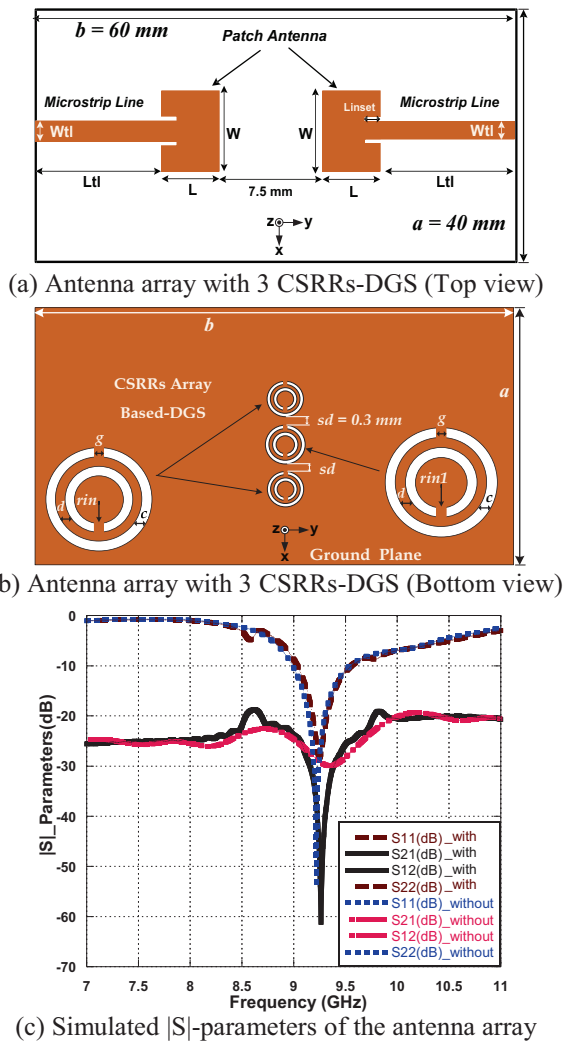


Fig. 2. Antenna array configurations and simulated $|S|$ -parameters with and without CSRRs-DGS.

Figure 3 contains the radiation pattern results of the proposed antenna array with and without 3-CSRRs. It is

obvious that the radiation patterns in the E (yz -plane) and H (xz -plane) planes are stable over the operating frequency band. In addition the radiation pattern results show that there is a slight decrease in the main lobe due to the presence of the CSRRs-based DGS, which is acceptable compared to the obtained significant isolation and mutual coupling reduction.

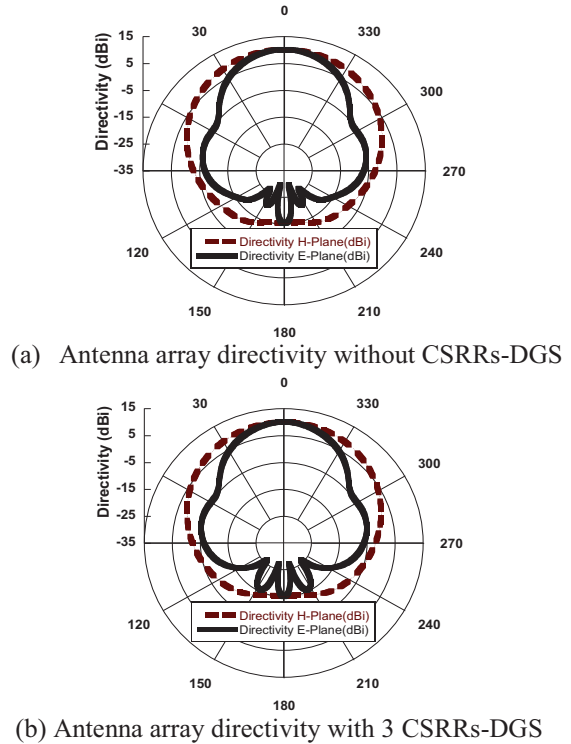


Fig. 3. Optimized antenna array radiation pattern results with and without 3 CSRRs-DGS at 9.22 GHz.

Table 1 contains summary of the simulation results of the proposed array with single, two, and three CSRRs-DGS and compared with the conventional array. The coupling reduction has been achieved by optimally positioning the array of two and three CSRRs-DGS between the antenna array elements. It is obvious from Table 1 that the proposed arrays have a significant and a good isolation than the array without CSRRs-DGS where about 33 dB reduction is achieved using an array of three CSRRs-DGS with a less edge-to-edge spacing [20], thus leading to the design of compact MIMO antenna arrays. In addition to this, using more than three CSRRs will not provide better isolation due to the internally mutual coupling between the CSRRs that will change the resonant frequency of the bandstop filter.

Table 2 shows a comparison for different approaches and configurations that were reported and implemented to reduce the mutual coupling. The proposed array exhibits a better isolation and compact size compared to Ref. [10] and Ref. [20] in terms of nearly the same edge-

to-edge separation. Compared to other techniques, the proposed array has a significant improvement in the isolation.

Table 1: Performance comparison of the proposed antenna arrays with the conventional

Antenna Structure	Results			
	Mutual Coupling (dB)	Improvement (dB)	Directivity (dBi)	Realized Gain (dB)
Conventional	-28	-	10.23	10.2
Proposed array with CSRR-DGS	-38	10	9.67	9.37
Proposed array with 2 CSRRs-DGS	-42	14	9.7	9.4
Proposed array with 3 CSRRs-DGS	-61	33	10	9.87

Table 2: Performance comparison of the proposed antenna array with other approaches in the literature

Ref. No.	Approach	Size of the Array in mm ²	Improvement (dB)	Edge-to-Edge Spacing
[4]	Meta-material	300×300	20	0.125 λ_0 (30 mm)
[5]	High order DGS filter	75×50	20	0.2 λ_0 (10.4 mm)
[8]	Dumbbell DGS	140×100	6.19	0.5 λ_0 (18.8 mm)
[10]	Inter-digital DGS capacitor	60×50	17	0.25 λ_0 (9.5 mm)
[14]	Uniplanar-EBG	78.3×78.3	10	0.5 λ_0 (26 mm)
[20]	Slotted CSRR	78×60	10	0.25 λ_0 (15 mm)
Proposed	CSRR DGS	60×40	33	0.22 λ_0 (7.5 mm)

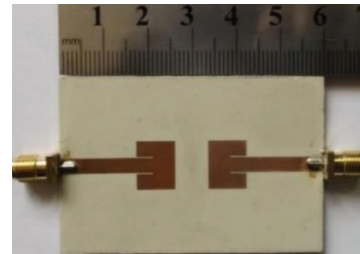
IV. EXPERIMENTAL RESULTS AND DISCUSSION

The proposed antenna array has been fabricated and measured to validate experimentally the approach to achieve a significant isolation and mutual coupling reduction. The photographs of the top and bottom layers of fabricated antenna array with CSRRs-based DGS are shown in Fig. 4. The $|S|$ parameters measurements were carried out using the Agilent N5227A PNA vector network analyzer and the calibration was done with the Agilent N4691B-Ecal module in the RF and microwave laboratory at E-JUST. While the pattern measurements were done at Kyushu University. The Experimental

results show a significant reduction in the mutual coupling of 30 dB between the array elements.

The fabricated antenna array provides a measured mutual coupling of -24 dB and -54 dB at the center frequency of 9.22 GHz for the array with and without CSRRs as shown in Figs. 4 (c), and (d), respectively. In addition, there is a very slight and tolerable shift between the simulated and measured resonant frequencies is found due to the fabrication tolerance. Furthermore, a good agreement between the resonant frequency and the bandstop frequency is observed for the array with and without the CSRRs-DGS.

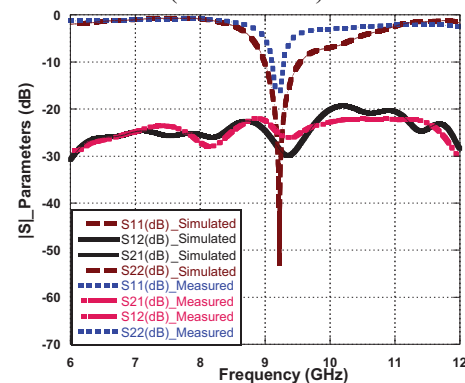
The measured and simulated normalized radiation patterns of one side element of the proposed antenna array with and without CSRRs-DGS at 9.22 GHz in the E and H-planes are presented in Fig. 5. While the other array element is terminated with a 50 Ω load. Obviously, these results do not show any significant difference between the main lobes patterns. As shown in the plots, the applied technique using CSRRs-DGS has a minor effect on the radiation pattern. Moreover, an excellent agreement is observed.



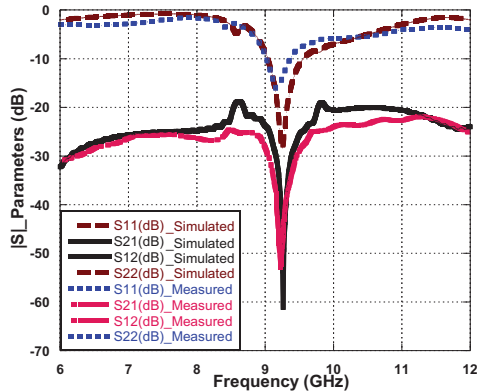
(a) Photograph of the fabricated antenna array (Top view)



(b) Photograph of the fabricated antenna array (Bottom view)

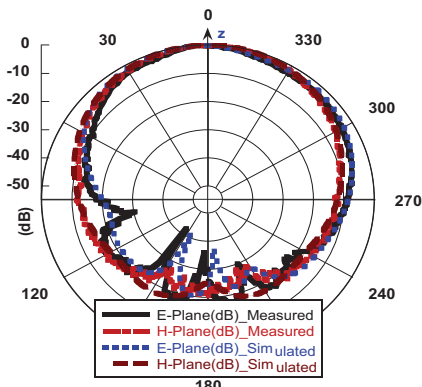


(c) Measured and simulated $|S|$ parameters of the conventional array without CSRRs-DGS

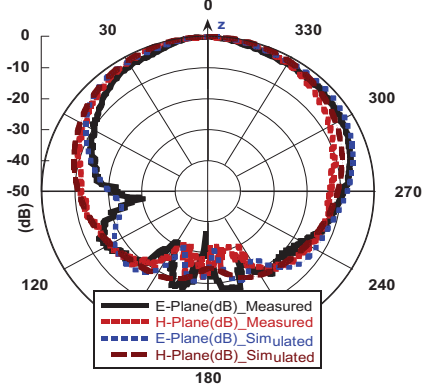


(d) Measured and simulated $|S|$ parameters of the proposed array with 3 CSRRs-DGS

Fig. 4. Photograph of the fabricated array, simulated and measured $|S|$ parameters without and with CSRRs-DGS.



(a) Single element normalized pattern without CSRRs



(b) Single element normalized pattern with 3 CSRRs

Fig. 5. Measured and simulated E and H-planes radiation patterns for single element of the proposed array with and without CSRRs-DGS at 9.22 GHz.

V. CONCLUSION

In this paper, a design of compact antenna array with low mutual coupling has been presented, fabricated and measured for the validation purposes. The approach for isolation improvement is proposed by inserting a

bandstop filter composed of an array of three CSRRs-based DGS between the two elements antenna array. In this simple design, the isolation has been significantly improved and the experimental results show that the proposed antenna array can improve the isolation between array elements by 30 dB. Furthermore, the measured radiation patterns are stable over the operating frequency band with and without the CSRRs. The measured and simulation results are in a good agreement. Thus, the proposed antenna array with this better isolation is suitable for MIMO communications.

ACKNOWLEDGMENT

This work is supported by the mission department of the Egyptian Ministry of Higher Education (MOHE) and E-JUST. The authors would like to thank the ERI, Egypt, for the help during CST simulation process and Kyushu University for supporting the facilities for the measurements of this research.

REFERENCES

- [1] H. Arun, A. Sarma, M. Kanagasabai, S. Velan, C. Raviteja, and M. Alsath, "Deployment of modified serpentine structure for mutual coupling reduction in MIMO antennas," *IEEE Antennas and Wireless Propagation Letters*, vol. 13, pp. 277-280, 2014.
- [2] Q. Li, A. P. Feresidis, M. Mavridou, and P. S. Hall, "Miniaturized double-layer EBG structures for broadband mutual coupling reduction between UWB monopoles," *IEEE Trans. on Antennas and Propag.*, vol. 63, no. 3, pp. 1168-1171, 2015.
- [3] L. Liu, S. W. Cheung, and T. I. Yuk, "Compact MIMO antenna for portable UWB applications with band-notched characteristic," *IEEE Transactions on Antennas and Propagation*, vol. 63, no. 5, pp. 1917-1924, May 2015.
- [4] M. Bait-Suwailam, M. S. Boybay, and O. Ramahi, "Electromagnetic coupling reduction in high-profile monopole antennas using single-negative magnetic metamaterials for MIMO applications," *IEEE Transactions on Antennas and Propagation*, vol. 58, no. 9, pp. 2894-2902, September 2010.
- [5] M. A. Abdallah and I. S. Mohamed, "Mutual coupling reduction in integrated transmit-receive array antennas using high order DGS filter," *IEEE AP-S Symposium on Antennas and Propagation and URSI CNC/USNC*, pp. 432-433, 2015.
- [6] A. Habashi, J. Naurinia, and C. Ghbadi, "A rectangular defected ground structure for reduction of mutual coupling between closely spaced microstrip antennas," *IEEE 20th Iranian Conf. Elect. Eng. (ICEE)*, pp. 1347-1350, 2012.
- [7] D.-J. Woo, T.-K. Lee, and J. W. Lee, "Equivalent circuit model for a simple slot-shaped DGS microstrip line," *IEEE Microwave and Wireless Components Letters*, vol. 23, no. 9, pp. 447-449,

September 2013.

- [8] F. Y. Zulkifli, E. T. Rahardjo, and D. Hartanto, "Mutual coupling reduction using dumbbell defected ground structure for multiband microstrip antenna array," *Progress In Electromagnetics Research Letters*, vol. 13, pp. 29-40, 2010.
- [9] A. Farahbakhsh, G. Moradi, and S. Mohanna, "Reduction of mutual coupling in microstrip array antenna using polygonal defected ground structure," *Applied Computational Electromagnetics Society Journal*, vol. 26, pp. 334-339, 2011.
- [10] A. Abdel-Rahman, "Coupling reduction of antenna array elements using small interdigital capacitor loaded slots," *PIER C*, vol. 27, pp. 15-26, 2012.
- [11] R. S. Kshetrimayum and S. S. Karthikeyan, "A parametric study on the stop band characteristics of CSRRs," *International Journal of Recent Trends in Engineering*, vol. 1, no. 3, May 2009.
- [12] Hany A. Atallah and Ehab K. I. Hamad, "Radiation pattern improvement of RDRA using LHM flat lens composed of CSRR," *IEEE-APS Middle East Conference on Antennas and Propagation*, 2010.
- [13] F. Martin, J. Bonache, F. Falcone, M. Sorolla, and R. Marques, "Split ring resonator-based left-handed coplanar waveguide," *Physics Letters*, vol. 83, no. 22, 2003.
- [14] H. Farahani, M. Veysi, M. Kaymyab, and A. Tadjalli, "Mutual coupling reduction in patch arrays using a UC-EBG superstrate," *IEEE Antennas and Wireless Propag. Letters*, vol. 9, pp. 57-59, 2010.
- [15] M. J. Al-Hasan, T. A. Denidni, and A. R. Sebak, "Millimeter-wave compact EBG structure for mutual coupling reduction applications," *IEEE Transactions on Antennas and Propagation*, vol. 63, no. 2, pp. 823-828, February 2015.
- [16] W.-J. Lu, Z.-Y. Zhang, and H.-B. Zhu, "Integrated wideband and narrowband antenna with low mutual coupling for cognitive radio applications," *International Conf. on Microwave and Millimeter Wave Technology*, vol. 3, pp. 1-4, May 2012.
- [17] J. S. Hong and M. J. Lancaster, *Microstrip Filters for RF/Microwave Applications*. 1st ed., ch. 6, John Wiley, New York, 2001.
- [18] I. Sassi, L. Talbi, and K. Hettak, "Compact multi-band filter based on multi-ring complementary split ring resonators," *PIER C*, vol. 57, pp. 127-135, 2015.
- [19] CST Microwave Studio, ver. 2011, Computer Simulation Technology, Framingham, MA, 2011.
- [20] M. M. Bait-Suwailam, O. Siddiqui, and O. Ramahi, "Mutual coupling reduction between microstrip patch antennas using slotted-complementary split-ring resonator," *IEEE Antennas and Wireless*

Propagation Letters, vol. 9, pp. 876-878, 2010.



Hany A. Atallah was born in Qena, Egypt in 1984. He received his B.Sc. and M.Sc. in Electrical Engineering, Electronics and Communications from South Valley University, Egypt, in 2007 and 2012, respectively. From 2008 to 2013, He worked as Teaching/Research Assistant in Faculty of Engineering, South Valley University. Currently, Hany is a full time Ph.D. graduate student, Electronics and Communications Engineering Department, E-JUST and preparing for the Ph.D. degree. His research interests include antenna design, dielectric resonators, metamaterials, and microwave filters. His recent research has been on cognitive radio (CR) antennas, reconfigurable antennas, tunable filters, and FDTD.



Adel B. Abdel-Rahman was born in Aswan, Egypt, in 1968. He received the B.Sc. and M.Sc. degrees in Electrical Engineering, Communication and Electronics, Assuit University, Egypt, in 1991 and 1998, respectively. The Ph.D. degree in Microwave Engineering from the University of Magdeburg, Magdeburg, Germany. He is currently working as Assoc. Prof. at Faculty of Engineering - South Valley University, Qena, Egypt and also at E-JUST, Alexandria, Egypt. His research interests include the design and analysis of microstrip antennas, filters, and its application in WLAN and mobile communication. His recent research has been on cognitive radios, wireless power transfer, and on chip antennas.



Kuniaki Yoshitomi received the B.S. and M.S. degrees in Electronics, in 1979 and 1981, respectively, and the D.E. degree in Communication Engineering, in 1986, all from Kyushu University, Fukuoka, Japan. He joined the Faculty of Engineering, Kyushu University in 1981, and is currently a Professor of Center for Japan-Egypt Cooperation in Science and Technology, Kyushu University. His current research interests include antenna theory and technology, electromagnetic compatibility. Yoshitomi received the Shinohara

Memorial Young Scientist Award from the Institute of Electronics, Information and Communication Engineers (IEICE) of Japan in 1989.



Ramesh K. Pokharel received the M.E. and Doctorate degrees from the University of Tokyo, Japan in 2000 and 2003, respectively in Electrical Engineering. He had been a Post-doctoral Research-fellow with the Electrical Engineering and Electronics, Aoyama Gakuin University, Japan. In April 2005, he joined the Graduate

School of Information Science and Electrical Engineering, Kyushu University. His current interests include the employment of passive components such as CPW in RF CMOS system, LSI, EMC and signal integrity of low-noise and high linear RF front-end architectures. Pokharel was an excellent COE research presentation award from Tokyo University in 2003. He is the Director of the Center for Egypt-Japan Cooperation in Science and Technology of Kyushu University from April 2014. He has been serving as the Vice-chair of Education Committee of IEEE-MTT-S Japan Society since Jan. 2014.

Experimental Study of Coupling Compensation of Low Profile Spiral Antenna Arrays Response for Direction-finding Applications

Taherah S. Ghazaany¹, Shron Zhu¹, Raed A. Alhameed², James M. Noras²,
Steven M. R. Jones², Tyler V. Buren¹, Tim Suggett¹, and Simon Marker¹

¹ Research and Development Office
Seven Technologies Group, Leeds, UK, LS18 4EG
Tahereh.Ghazaany@7techgroup.com, Sharon.zhu@7techgroup.com, Tyler.vanburen@7techgroup.com,
Tim.suggett@7techgroup.com, simon.marker@gmail.com

² School of Engineering and Informatics
University of Bradford, Bradford, UK, BD7 1DP
r.a.a.abd@Bradford.ac.uk, s.m.r.jones@Bradford.ac.uk, jmnoras@Bradford.ac.uk

Abstract — An experimental study of coupling compensation for AOA estimation using compact low profile antenna arrays with element separations of a quarter wavelength has been conducted. Two circular arrays of low profile miniaturised logarithmic spiral antennas deployed on a circular metal plate were used for data acquisition. Using the MUSIC direction-finding algorithm, the AOA estimation errors in receiving mode were observed before and after compensation: the errors were significantly decreased by coupling compensation.

Index Terms — Covariance, direction-finding, interferometry, mutual coupling.

I. INTRODUCTION

In RF covert tracking systems based on Angle-of-Arrival (AOA) estimation, compact antenna arrays with omni-directional radiation patterns are desirable [1]. However, in antenna arrays with a relatively short separation between elements, mutual coupling between the elements affects the performance of array signal processing algorithms in most cases. Mutual coupling effects are normally analysed in terms of the mutual impedances between the radiators: these have complex values, and are related to the geometrical positions of the array elements. Moreover, the mutual coupling behaviour of an antenna array in transmitting mode is demonstrably different from that in receiving mode [2, 3]. In the receiver array, when antennas receive simultaneously, the total field on each element will be the sum of the radiated and re-scattered fields from antenna elements. In radio direction-finding systems, where the directional information is obtained from the characteristic structure of the received signal matrix, mutual coupling changes the corresponding vectors of the antenna array, perturbing this correlation matrix.

This results in degradation of the AOA estimation accuracy [4, 5].

To ensure accurate direction-finding, we need to address mutual coupling explicitly, and to compensate for it using a suitable decoupling method. Recently, the present authors investigated the performance of the AOA error of a 4-element uniform circular array using simple monopoles on a square metal plate in which they improved the AOA accuracy by 50% [6]. In this paper, we report an experimental study of receiving mode coupling compensation for a direction-finding application based on the Multiple Signal Classification (MUSIC) algorithm using four and six-element uniform circular arrays of spiral antennas.

II. LOW PROFILE SPIRAL ANTENNA ARRAY

To examine the performance of arrays in receiving mode using compensation, two networks, with either four or six-elements, using low profile miniaturised logarithmic spiral antennas were designed. Each antenna provides a monopole-like radiation pattern and supports platform installations at TETRA/UHF frequencies [7].

The antenna prototype with its measured radiation pattern is shown in Fig. 1. It should be noted that the radiation pattern for the designed prototype antenna was considered at its resonant frequency and it is assumed that the radiation performance will be in agreement for all the elements at their resonances frequencies over all working frequency bands. Prototypes were fabricated and installed on circular ground planes of diameter one meter, as shown in Fig. 2. The inter-element spacing is set to a quarter wavelength and the radii of the four and six-element circular arrays are 0.1325 and 0.1595 meters respectively. The measured return losses of all the prototypes over the desired frequency band (420 MHz to

425 MHz) are shown in Fig. 3. The minor dissimilarity in the frequency responses is due to the mismatches in hardware designs of the elements. The measured array response acquired in the array calibration process and used in the MUSIC algorithm includes these mismatches, but the final estimated AOA results are not significantly affected.

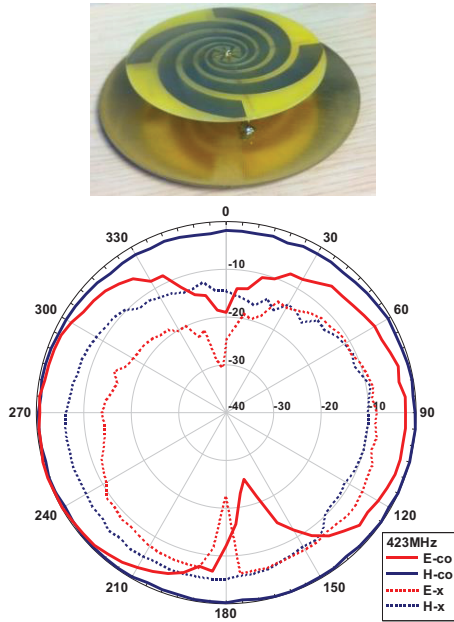


Fig. 1. Multi-element low profile spiral antenna prototype and its measured radiation pattern in principal E-plane and H-plane co-polarization and cross-polarization.

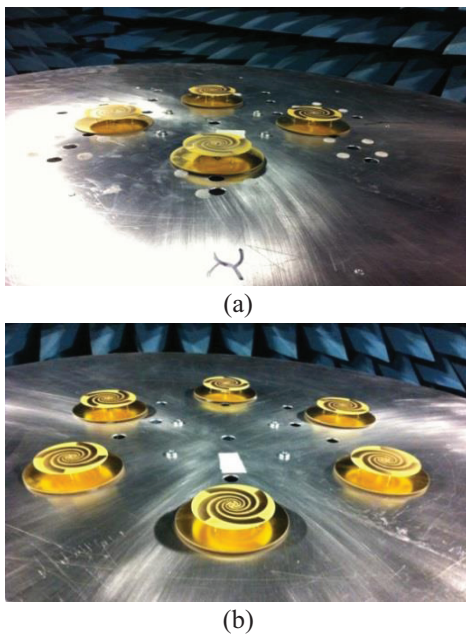


Fig. 2. Antenna array geometries used for data acquisition.

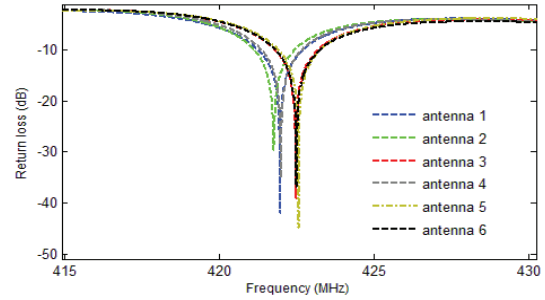


Fig. 3. Measured return losses of low profile spiral antennas

III. RECEIVING MUTUAL IMPEDANCES USING S-PARAMETER MEASUREMENT

The mutual impedance is calculated under the conditions that the antenna elements are terminated with known impedance, Z_L and that they are in receiving mode under an external plane-wave excitation [2, 3, and 8]. Consider an antenna array with N antenna elements, each of which is terminated with an identical load impedance, Z_L . When the array is excited by an external source, the voltage at antenna terminal V_k can be written as:

$$V_k = Z_L I_k = U_k + W_k, \quad (1)$$

where U_k is the terminal voltage due solely to the direct incoming signal and W_k is the voltage due to the mutual coupling with other antenna elements. W_k can be written as:

$$W_k = I_1 Z_t^{k,1} + I_2 Z_t^{k,2} + \dots + I_{k-1} Z_t^{k,k-1} + I_{k+1} Z_t^{k,k+1} + \dots + I_N Z_t^{k,N}, \quad (2)$$

where $Z_t^{k,i}$ is the receiving mutual impedance between antenna elements k and i , and I_i is the current induced at the terminal of antenna element i . The subscript t denotes that the receiving mutual impedance is defined at the antenna's terminals. The relationship between U_k and V_k can be written as:

$$\begin{bmatrix} 1 & -\frac{Z_t^{12}}{Z_L} & \dots & -\frac{Z_t^{1N}}{Z_L} \\ -\frac{Z_t^{21}}{Z_L} & 1 & \dots & -\frac{Z_t^{2N}}{Z_L} \\ \vdots & \vdots & \ddots & \vdots \\ -\frac{Z_t^{N1}}{Z_L} & -\frac{Z_t^{N2}}{Z_L} & \dots & 1 \end{bmatrix} \begin{bmatrix} V_1 \\ V_2 \\ \vdots \\ V_N \end{bmatrix} = \begin{bmatrix} U_1 \\ U_2 \\ \vdots \\ U_N \end{bmatrix}. \quad (3)$$

Using Equations (1) and (2), determination of the receiving mutual impedances is based on terminal currents or voltages. Since the miniaturised logarithmic spiral antenna has an omni-directional radiation pattern, it is assumed that the current distribution remains unchanged irrespective of the azimuth angle of the incoming signal when the signal is coming from the plane perpendicular to the axis of the antenna ($\theta=90^\circ$). As a result, the receiving mutual impedance should remain constant with respect to the

azimuth angle of the incoming signal, and thus is suitable for direction-of-arrival estimation applications [2].

In order to obtain mutual impedances, two elements of the array at a time should be considered, with the remaining elements loaded. The following steps are repeated to retrieve the corresponding S_{12} parameters:

- (1) Measure S_{12} at element 1's terminal with element 2's terminal connected to a load. Denote this as $S_{12,1}$;
- (2) Measure S_{12} at element 2's terminal with element 1's terminal connected to a load. Denote this as $S_{12,2}$;
- (3) Measure S_{12} at element 1's terminal with element 2 removed from the array. Denote this as $S'_{12,1}$;
- (4) Measure S_{12} at element 2's terminal with element 1 removed from the array. Denote this as $S'_{12,2}$.

Accordingly the receiving mutual impedances can be obtained as follows:

$$Z_t^{12} = \frac{S_{12,1} - S'_{12,1}}{S_{12,2}} Z_0, \quad (4)$$

$$Z_t^{21} = \frac{S_{12,2} - S'_{12,2}}{S_{12,1}} Z_0. \quad (5)$$

The above procedure needs to be repeated for all pairs of elements in an array. Figure 4 shows calculated mutual impedances between the first antenna and the rest of the radiators, both (a) real and (b) imaginary parts, using the measured S-parameters for a 4-element array. In this example, signals are arriving from 150 and 320 degrees. These two angles are chosen to illustrate cases where the measured array responses in the azimuth plane without coupling compensation give rise to considerable angular errors.

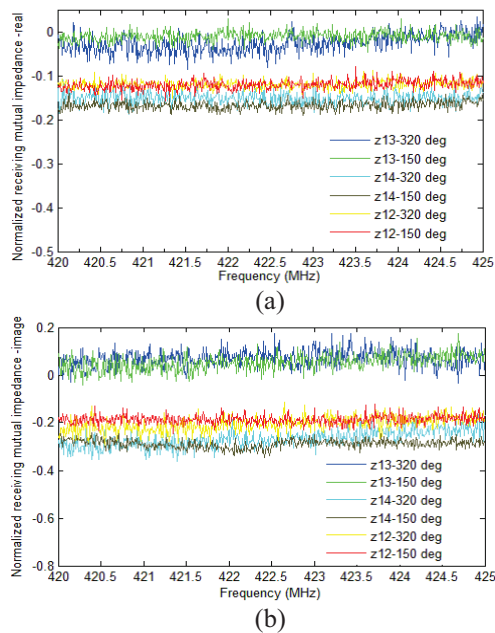


Fig. 4. Normalized mutual impedance for AOA = 150 and 320 degrees over the frequency band: (a) real part and (b) imaginary part.

In order to obtain the compensation matrix in Equation (3), mutual impedances for pairs of antennas are determined for many directions which show considerable angular errors in the measured array response in the azimuth plane. It is clear from the graphs in Fig. 4, that the variation of the mutual impedances over the 5 MHz of bandwidth is negligible, and thus narrowband compensation would be sufficient. Thus, the mutual impedances are averaged from 420 MHz to 425 MHz and over different angles. The mutual coupling values for both array geometries are listed in Tables 1 and 2.

IV. AOA ESTIMATION RESULTS

Deriving mutual coupling compensation entails developing an estimate for the actual array response for the specified geometries via the results from Tables 1 and 2. The resultant vectors must subsequently be applied to the MUSIC algorithm for direction-finding. In this study, in order to capture the array response to signals coming from different azimuth angles, the data acquisition setup shown in Fig. 5 was used. Log-periodic antennas have been used as transmitters to create the plane wave source in an anechoic chamber. To send data from each terminal in turn to the network analyser, a microwave switch has been deployed under the turntable while the dc controller of the switch was located outside the chamber. The amplitude and phase responses from each antenna have been captured for rays from the azimuth plane and post-processed using the compensation matrices and AOA estimation algorithm. Figures 6 and 7 show the spatial spectra generated using uncompensated and compensated array responses for measurement data due to pairs of signal sources to the four and six-element spiral arrays, respectively.

When the measured voltages are used without any compensation for mutual coupling for the four-element array, Fig. 6 shows that although the MUSIC spatial spectrum function shows two peaks, the peaks are not adequately sharp and also are misplaced by about 20 and 40 degrees for the signals coming from 30 and 150 degree azimuth angles, respectively.

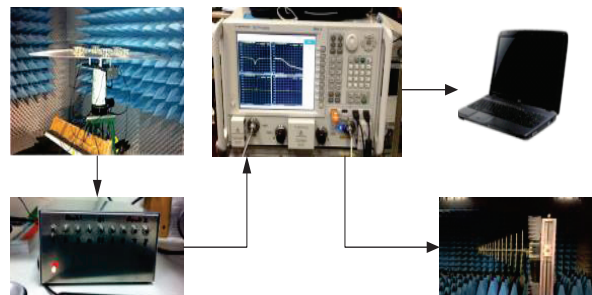


Fig. 5. Data acquisition setup for the AOA estimation experiment.

Table 1: Normalized receiving mutual impedances for a 4-element spiral array

Var.	Value	Var.	Value
Z_t^{12}	-0.126 - 0.213i	Z_t^{31}	0.098 + 0.171i
Z_t^{13}	-0.019 + 0.089i	Z_t^{32}	0.139 - 0.307i
Z_t^{14}	-0.184 - 0.234i	Z_t^{34}	0.288 - 0.085i
Z_t^{21}	0.054 + 0.192i	Z_t^{41}	-0.114 + 0.079i
Z_t^{23}	0.164 - 0.170i	Z_t^{42}	0.203 - 0.006i
Z_t^{24}	0.169 + 0.334i	Z_t^{43}	0.176 - 0.113i

Table 2: Normalized receiving mutual impedances for a 6-element spiral array

Var.	Value	Var.	Value
Z_t^{12}	-0.540 + 0.089i	Z_t^{41}	-0.135 - 0.236i
Z_t^{13}	0.054 - 0.651i	Z_t^{42}	0.220 - 0.335i
Z_t^{14}	0.025 - 1.067i	Z_t^{43}	0.461 + 0.143i
Z_t^{15}	-0.488 - 0.028i	Z_t^{45}	0.336 - 0.229i
Z_t^{16}	0.173 + 0.444i	Z_t^{46}	-0.182 - 0.100i
Z_t^{21}	0.220 + 0.044i	Z_t^{51}	0.066 + 0.100i
Z_t^{23}	-0.290 - 0.364i	Z_t^{52}	-0.085 + 0.171i
Z_t^{24}	0.092 - 0.227i	Z_t^{53}	-0.333 - 0.246i
Z_t^{25}	0.048 + 0.150i	Z_t^{54}	0.456 - 0.470i
Z_t^{26}	0.210 + 0.103i	Z_t^{56}	0.342 + 0.108i
Z_t^{31}	0.164 - 0.142i	Z_t^{61}	0.225 + 0.221i
Z_t^{32}	0.307 + 0.090i	Z_t^{62}	-0.326 + 0.108i
Z_t^{34}	0.014 + 0.385i	Z_t^{63}	0.163 - 0.334i
Z_t^{35}	0.269 + 0.024i	Z_t^{64}	-0.136 - 0.610i
Z_t^{36}	0.058 - 0.313i	Z_t^{65}	-0.158 + 0.001i

However, applying the receiving mode compensation matrix from Table 1 to these results provides sharper peaks and reduces the AOA estimation error to less than ± 2 degrees. In the second experiment, two incident waves irradiate the six-element spiral array from 40 and 110 degree azimuth angles. As shown in Fig. 7, applying the receiving mode compensation matrix using data from Table 2 results in an AOA estimation accuracy of about ± 1 degree for the two directions.

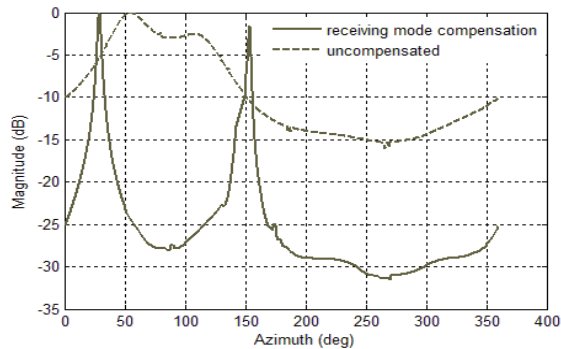


Fig. 6. MUSIC spatial spectrum for two incident signals with azimuth angles of 30 and 150 degrees, four-element low profile spiral array.

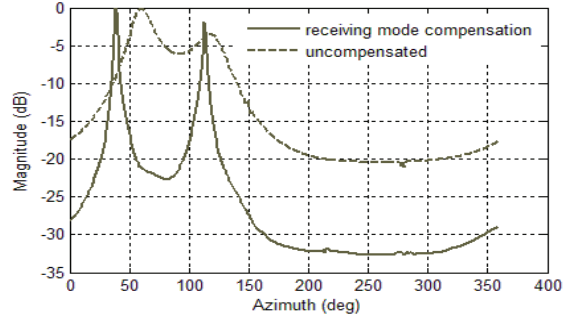


Fig. 7. MUSIC spatial spectrum for two incident signals with azimuth angles of 40 and 110 degrees, six-element low profile spiral array.

V. CONCLUSION

In this experimental study, the benefit of mutual coupling compensation during AOA estimation process using low profile spiral antenna arrays has been examined. The receiving mode compensation matrices were derived by numerical calculations using measured data from four and six-element arrays. It was shown that over the 5 MHz bandwidth the mutual impedances do not vary significantly, and thus narrowband compensation would be sufficient. Moreover, since the low profile spiral antenna has an omni-directional radiation pattern, the compensation matrix is independent of angle. The marked performance improvement in terms of AOA estimation, due to the compensated array responses, allows for easier and more accurate determination of multiple signal sources.

ACKNOWLEDGMENT

The authors would like to acknowledge support from the TSB-KTP project Grant No. 008734 with the Seven Technologies Group, Leeds, United Kingdom.

REFERENCES

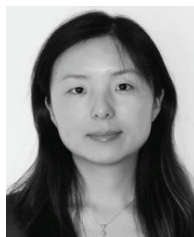
- [1] K. Bobier, J. Wells, and M. Dapper, "Enhanced unattended ground sensor system communications," *MILCOM Proc.*, vol. 1, pp. 282-289, Oct. 7-10, 2002.
- [2] H. T. Hui, H. P. Low, T. T. Zhang, and Y. L. Lu, "Receiving mutual impedance between two normal-mode helical antennas," *IEEE Antenna and Propagation Magazine*, vol. 48, no. 4, pp. 92-96, 2006.
- [3] K. R. Dandekar, H. Ling, and G. Xu, "Experimental study of mutual coupling compensation in smart antenna applications," *IEEE Transactions on Wireless Communications*, vol. 1, no. 3, pp. 480-486, 2002.
- [4] H. S. Lui and H. T. Hui, "Mutual coupling compensation for direction-of-arrival estimations using the receiving-mutual-impedance method," *International Journal of Antennas and Propagation*, Article ID 373061, 2010.
- [5] I. J. Gupta and A. A. Ksienski, "Effect of mutual

coupling on the performance of adaptive arrays,” *IEEE Transactions on Antennas and Propagation*, vol. 31, no. 5, pp. 785-791, 1983.

- [6] T. S. Ghazaany, S. Zhu, R. A. Alhameed, S. M. R. Jones, J. M. Noras, T. Van Buren, T. Suggett, and S. Marker, “Coupling compensation of the antenna array response for direction finding applications,” *9th IET International Conference on Computational and Electromagnetics (CEM 2014)*, Imperial College, pp. 1-2, Apr. 2014.
- [7] S. Zhu, T. S. Ghazaany, R. A. Abd-Alhameed, S. M. R. Jones, J. M. Noras, T. Suggett, T. Van Buren, and S. Marker, “Reconfigurable wideband low profile multi element miniaturized logarithmic spiral antenna,” *The 8th European Conference on Antennas and Propagation (EuCAP)*, pp. 2276-2278, Apr. 2014.
- [8] H. T. Hui, “A new definition of mutual impedance for application in dipole receiving antenna arrays,” *IEEE Antennas and Wireless Propagation Letters*, vol. 3, no. 1, pp. 364-367, 2004.

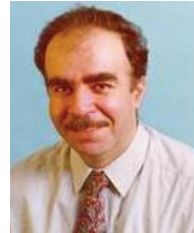


Tahereh S. Ghazaany received the B.Sc. degree in Electronic and Telecommunication Engineering from Iran University of Science and Technology in 2003, and the Ph.D. degrees from University of Bradford, West Yorkshire, U.K., in 2012. Her research interests include characterization and modelling of active RF circuits, linearization of microwave nonlinear components, DSP for wireless communication, antenna array processing and energy efficient reconfigurable transceivers. From March 2012 to February 2014, she was a Knowledge Transfer Partnership (KTP) Associate with DATONG of Seven Technologies Group in Leeds, U.K. Her work focused on combining new and modern RF direction-finding methods for covert tracking using advanced signal processing techniques: the project was recognized by the British Technology Strategy Board (TSB) as outstanding. Since March 2014 she has been in the R&D Department of Seven Technologies Group in Leeds, U.K.



Shaozhen Zhu received the M.S. degree in Electronics Engineering from University of Kent, Canterbury, U.K., in 2004 and Ph.D. degree from University of Sheffield, U.K., in 2008. From 2008 to 2012, she worked as a Postdoctoral Research Associate within the Comms. Research Group, Department of Electronics and Electrical Engineering,

University of Sheffield. From March 2012 to February 2014 she was a KTP Associate between University of Bradford and DATONG of Seven Technologies Group, Leeds, U.K. Since March 2014 she has been in the R&D Department of Seven Technologies Group in Leeds, U.K. The completed project with DATONG was recognized by the TSB as outstanding. Her research interests include RF and antenna design for direction-finding applications and medical implanted wireless communications.



Raed A. Abd-Alhameed is Professor of Electromagnetic and Radio Frequency Engineering at the University of Bradford. Currently, he is the Leader of the Communication Research Group and Head of RF, Antenna Design and Electromagnetic Research in the School of Engineering and Informatics, Bradford University. He is Principal Investigator for several funded projects from EPSRC, EU, TSB, RDP and has led several successful knowledge transfer programmes for Pace PLC, YW PLC, DATONG of Seven Technologies Group, WiMAC and ITEG Ltd. He has published over 400 academic journal and conference papers and is co-author of three books and several book chapters. Abd-Alhameed is a Fellow of the Institution of Engineering and Technology, Fellow of Higher Education Academy, and a Chartered Engineer in the U.K.



James Noras is a Senior Lecturer in the School of Engineering and Informatics at the University of Bradford, UK, and has published 59 journal and 93 conference papers, in fundamental semiconductor physics, analogue and digital circuit design, digital signal processing and RF system design and evaluation. He is the Director of three internationally franchised B.Eng. courses in Electrical and Electronic Engineering. His main research interests are now in digital system design and implementation, DSP and coding for communication systems, and localization algorithms for mobile systems. Noras is a Member of the Institute of Physics and a Chartered Physicist.



Steve Jones, a Senior Lecturer in Telecommunications, is Director of Studies for Electronics and Telecommunications in the School of Engineering and Informatics at the University of Bradford. Since joining the University in 1987, he has worked on a wide variety of

projects in the area of satellite slant-path propagation and mobile radio propagation (notably Mobile VCE and TEAMS projects). He served as an Associate Editor for the IEEE Transactions on Antennas and Propagation 2004-8. Recently, he has worked on multiple-antenna technologies, signal processing, localization and propagation modelling for broadband wireless access systems.



Tyler Van Buren earned a B.A. in Physics from Lawrence University, a B.Sc. in Electrical and Computer Engineering from the University of Wisconsin at Madison and a M.Sc. in Communications and Signal Processing from the University of Leeds. He has held various PCB-

level and chip-level (RTL) design engineering and team leader positions at Plexus, Spirent Communications, and Pace, and is currently the Electronics Team Leader at Seven Technologies Group having been the DSP & FPGA Team Leader at DATONG before the merger. His professional responsibilities include development and modeling of end-to-end communications, tracking and locating, position estimation and direction finding systems and algorithms and their subsequent implementation optimized for performance, power consumption, size and cost and often employing FPGA technology for signal processing.



Tim Suggett holds a B.Eng. Hons. in Electronic Communication Systems from Leeds Metropolitan University. He is the RF Team Leader at Seven Technologies group and has been responsible for the design of Frequency Agile Antenna systems, low power RF systems and Analogue circuit design. From March 2012 to February 2014 he was a Company Supervisor during the KTP between the University of Bradford and Seven Technologies.



Simon Marker graduated from Bradford University with an M.Eng. degree in Electronic Engineering in 1991. Joining DATONG (now known as Seven Technology Group) in 1992, Marker has contributed to the development of three generations of DF system and many associated tracking beacons. Marker initially worked as a Development Engineer becoming Head of Research and Development in 2000 and Head of the Engineering System for Seven Technologies Group Ltd. from October 2013 – October 2014. Then from November 2014 he was appointed as the Interim Engineering Manager for Denchi Power and now Director for Misas Technology from January 2015 to present.

Mutual Coupling Reduction in CBS Antenna Arrays by Utilizing Tuned EM-EBG and Non-planar Ground Plane

S. Manshari¹, F. Hodjat Kashani¹, and Gh. Moradi²

¹ Department of Electrical Engineering
Iran University of Science and Technology, Tehran, Iran
manshari@elec.iust.ac.ir, kashani@iust.ac.ir

² Department of Electrical Engineering
Amirkabir University of Technology, Tehran, Iran
ghmoradi@aut.ac.ir

Abstract — Radiation surface wave (surface current) on ground plane has a destructive effect on the characteristics of antennas which benefits from a common ground plane, especially Cavity Backed Slot (CBS) antennas. Surface current increases mutual coupling in an antenna array. This in turn causes unwanted characteristics in array applications. The main goal of this work is to design a new modified antenna array achieving less mutual coupling by reshaping ground plane and using tuned Elongated Mushroom Electromagnetic Band Gap (EM-EBG). Moreover, in this study, we focus on the influence of changing depth of EM-EBG holes. In this regard, four different designs for CBS antenna arrays are investigated. The results reveals that by using two new methods, namely stepped ground plane and tuned EM-EBG, mutual coupling will be decreased by more than 9 dB. Decrement of mutual coupling improve radiation characteristic of array such as Front to Back Ratio (FBR) by 8 dB. The effectiveness of our design is confirmed by experimental results.

Index Terms — CBS antennas array, EM-EBG, High Impedance Surface (HIS), mutual coupling, phase center of antennas.

I. INTRODUCTION

Cavity backed slot antennas, because of their structures, are the most popular antennas for satellite application, aerospace and aircraft structures. In the two recent decades, extensive research on CBS arrays regarding influence of surface currents on this antenna has been performed [1]-[2]. Surface currents have destructive effects on antennas which have common ground plane specially cavity backed slot antennas. Surface currents increase mutual coupling of these antennas which in-turn causes unwanted characteristics in array applications such as grazing SLL [1]-[2].

To minimize the effects of surface currents, several

methods have been introduced which mostly include the application of absorbers and lossy materials having the negative effects of being bulky and costly [1]-[4]. Using slits and utilizing High Impedance Surface (HIS) such as EBG structures have been proposed recently [2]-[7]. Recent investigations about HIS have showed that these methods are capable of confining mutual coupling [5], [6], [8] and [11]. EBG structures in specific frequency band suppress travelling surface waves [3]. Recently several types of EBGs have been introduced and investigated [8].

This study focuses on the S21 parameter and mutual coupling in a CBS antenna array, [5] and [12]. Two new methods for reduction in mutual coupling using non-planar ground plane, and tuning EM-EBG are suggested.

In the following sections, four designs are introduced which are dedicated to work at Ku band. Influence of ground plane shape on distribution and mutual coupling are fully investigated. First three designs are described in Section II and the last one is described in Section III and IV.

In Section II, planar (common) ground plane and non-planar (stepped) ground plane are compared. In Section III, EM-EBG having a band gap frequency similar to resonance-frequency CBS antennas is introduced.

In Section IV, effect of HIS is investigated for the proposed designs. Effect of the EM-EBG hole depth on mutual coupling is also studied; whereas, effect of non-equal depth of the holes has not been considered in previous works [8]-[9]. Depths of EM-EBG holes are tuned to achieve the highest isolation between antennas. All simulations are conducted for full wave condition by Ansoft HFSS 14 software [13]. In Section V, experimental results for confirmation of our simulation are written.

II. ANTENNA DESIGN

As mentioned in the previous section, one of the

destructive effects of surface waves on CBS antennas is increasing mutual coupling [8]. In this section, at first, CBS array antenna similar to antenna which was introduced by Georgakopoulos [2], [11] is designed for working at 15 GHz.

The CBS antenna comprises of three parts: excitation probe, waveguide, and ground plane with slot. In Fig. 1 (a), three designs of CBS antenna array are presented. Main dimensions of the ground plane, aperture size and feed waveguide as well as aperture spacing in all three designs are the same. The only different aspect of these designs is the shape of ground plane. Slot size and excitation probe length inside the waveguide are depicted in Fig. 1 (b).

TE₁₀ mode is excited in the feed waveguide, whose characteristic impedance for dominant mode is as below [14]:

$$Z_0 = \frac{\eta_0}{\sqrt{1 - \left(\frac{f_c}{f}\right)^2}} \times \frac{b}{a}, \quad (1)$$

where its value at 15 GHz, is 328 Ω, which could provide good impedance matching to free space.

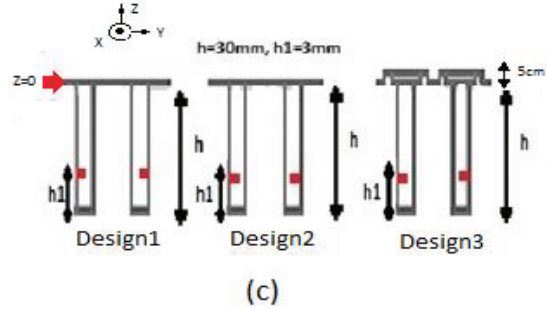
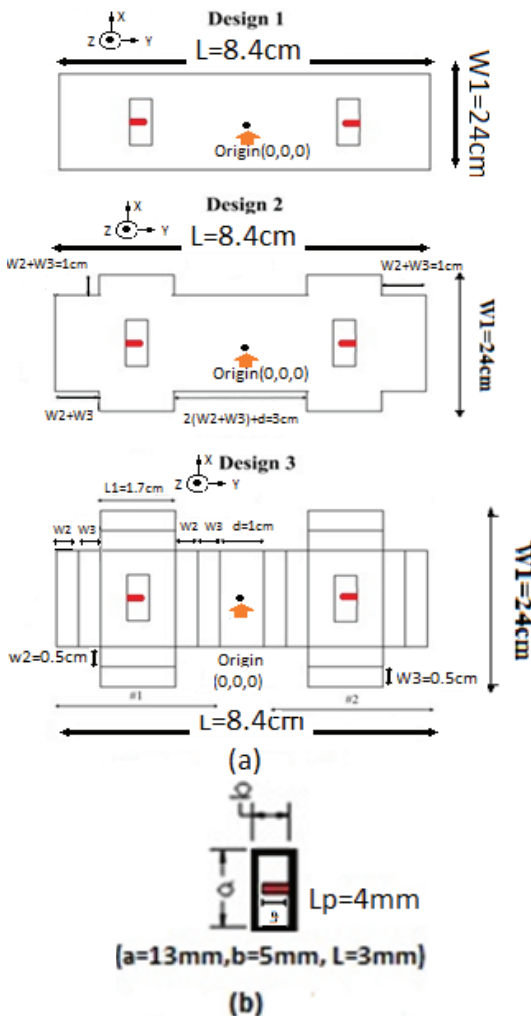


Fig. 1. The employed designs: (a) top view, (b) slot dimension and excitation probe length, and (c) side view (L_p is length of excitation probe, h is height of backed cavity and h₁ is place of probe from the back of structure).

The CBS antenna with rectangular planar ground plane is named design 1. Next, the corner notched ground plane is introduced as design 2. The third design composes of two non-planar CBS antenna which has a distance of 0.5λ₀ from each other. These three structures are designed to work at 15 GHz [9]-[10]. In Fig. 2, current distribution of all the three designs at 15 GHz are shown. The current surface distributed on the ground plane reaches together and thus causing mutual coupling.

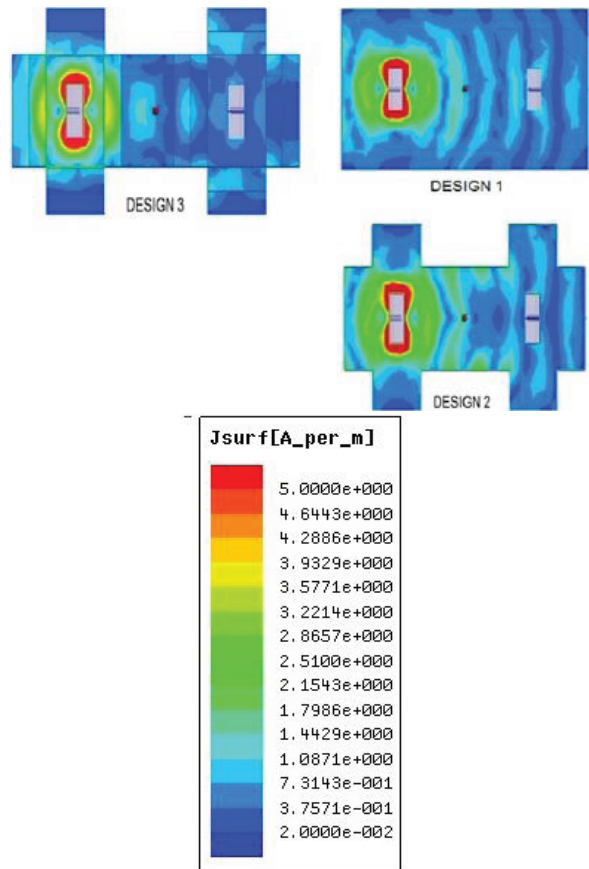


Fig. 2. Current distribution on the three designs.

Results of simulation for scattering parameters of the designs reveal that design 3 has the minimum reflection (Fig. 3), and the best mutual (Fig. 4). One can see that for non-planar structure, mutual coupling is improved by 2.5 dB. It is evident that non-planar structure suppresses current distribution more than the others and has the best isolation.

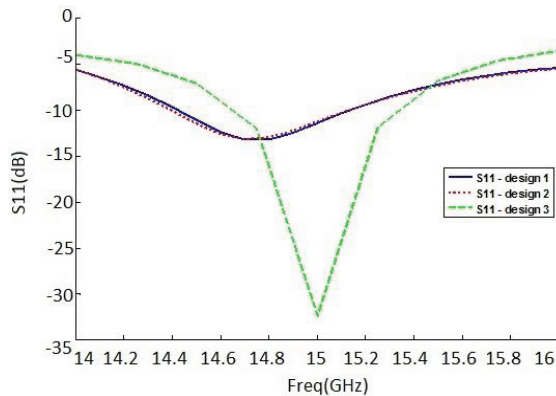


Fig. 3. Reflection coefficient, S_{11} for designs 1, 2 and 3.

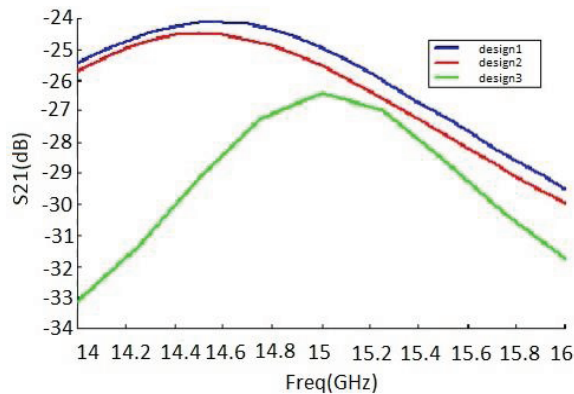


Fig. 4. Mutual coupling extracted by HFSS simulator for the three designs.

III. UTILIZING EBG STRUCTURE

One important feature of high impedance surface is its ability to compensate surface current in band gap [3]. A new type of this structure has been recently introduced as an EM-EBG [8]-[9], which confines the surface current more than the common mushroom EBG. Compactness of EM-EBG is its advantage in comparison to common EBG. Fabrication of EM-EBG is straightforward. To fabricate EM-EBG in order to work at 15 GHz, lumped circuit model as mentioned in [8] is utilized. Side view of EM-EBG is illustrated in Fig. 5. It consists of two parts, top part has more capacitive effect. As a result, it is named capacitance part while the bottom part, named inductive part, has inductive effect. In a normal EM-EBG cell, the depth of two parts are the same.

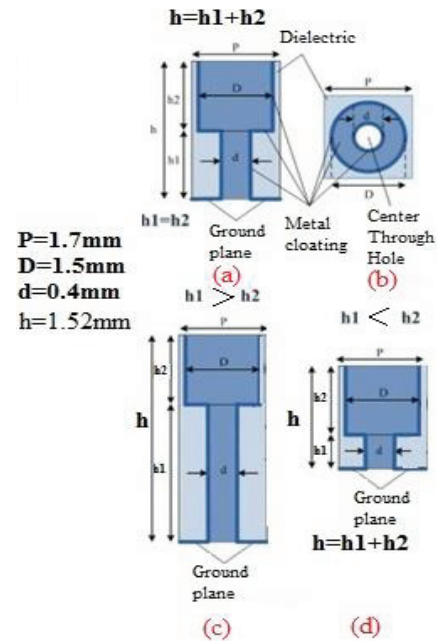


Fig. 5. An EM-EBG cell is composed by two metalized holes (vias) with two different diameters. Diameter of the top hole is (D) and the other hole is (d). (a) Side view of normal EM-EBG ($h_1=h_2=h/2$), (b) top view, and (c) tuned EM-EBG, the first case ($h_1 < h_2$) tuned EM-EBG, the second case ($h_1 > h_2$).

IV. TUNING EM-EBG HOLES DEPTH

As mentioned in a normal EM-EBG cell, the depth of the two parts is similar. For more suppression of the current distribution on ground plane, tuned EM-EBG which is designed on Taconic RF35 (60 mil) is applied on the ground plane of design 3, this new design is named design 4. Width, length and height of tuned EM-EBG structure are selected as 10 mm, 24 mm and 1.52 mm, respectively, which fills the distance between the two slots on non-planar ground plane. This EM-EBG structure has 14 rows and 6 columns.

Depth of holes (h_1, h_2) as mentioned above, referring to capacitive part and inductive parts of EM-EBG, are changed to achieve the best isolation. Depth of the holes influences the bandwidth and parameters of EBG. For achieving more isolation, EM-EBG holes depth is tuned. Top holes depth (h_1) and that of bottom holes (h_2) influence the capacitive and inductive parts, respectively [8]. The result of mutual coupling simulation between two antennas are extracted by numerical methods using Ansoft HFSS Designer.

In Fig 6, mutual coupling for different depths are presented. The best mutual couplings at 14.6-15.5 GHz bandwidth is obtained for $h_1=0.9h, h_2=0.1h$.

By tuning h_1, h_2 , i.e., by changing capacitive and inductive parts of EM-EBGs, mutual coupling is decreased by 9 dB in comparison to design 3.

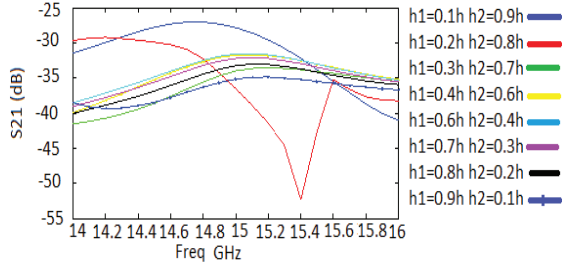


Fig. 6. Simulation result of mutual coupling for different capacitive and inductive parts.

Using numerical methods, the dispersion diagram can be extracted. In Fig. 7, the dispersion diagram of the tuned EM-EBG in periodic condition for the first three modes (TM_0 , TE_1 , and TE_2) are illustrated. The band gap of 15-17 GHz between the two first modes is seen. Also, between TM_0 and TE_1 modes, a band gap is observed where none of surface modes are supported.

Result of current distribution on design 4 is depicted in Fig. 8. By comparing Figs. 2 and 8, it is obvious that by inserting EM-EBG, the surface current on second antenna has been decreased. Phase center is one of most important characteristics of aperture antennas such as cavity backed slot antennas for interferometer applications. Result of calculation of place of phase center of two antennas for design 3 and design 4 are presented in Tables 1 and 2. For design 3 and 4, place of phase centers in Y direction are symmetric and in Z direction are similar. By inserting EM-EBGs (reduction of mutual coupling) phase center of antennas of design 4 move forward in Z direction. These results are calculated by CST Microwave Studio Software.

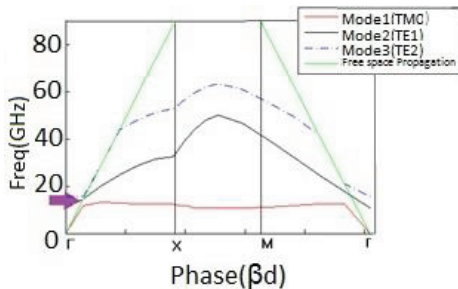


Fig. 7. Dispersion diagram of the tuned EM-EBG cell.

Table 1: Place of phase centers of antennas design 3

Frequency (GHz)	Left Antenna (X,Y,Z) mm	Right Antenna (X,Y,Z) mm
14.6	(0,-23.8,-1.77)	(0,23.8,-1.65)
14.8	(0,-24,0.38)	(0,24.04,0.56)
15	(0,-23.89,0.56)	(0,23.95,1.65)
15.2	(0,-23.82,1.3)	(0,23.86,0.89)
15.4	(0,-23.97,-1.47)	(0,24,-1.13)
15.6	(0,-24.44,-2.6)	(0,24.45,-2.53)

Table 2: Place of phase centers of antennas design 4

Frequency (GHz)	Left Antenna (X,Y,Z) mm	Right Antenna (X,Y,Z) mm
14.6	(0,-23.59,8.7)	(0,23.61,8.83)
14.8	(0,-23.52,9.45)	(0,23.57,9.56)
15	(0,-23.33,9.28)	(0,23.42,9.4)
15.2	(0,-23.17,7.98)	(0,23.26,8.09)
15.4	(0,-23.14,5.7)	(0,23.24,5.77)
15.6	(0,-23.3,3.78)	(0,23.4,3.58)

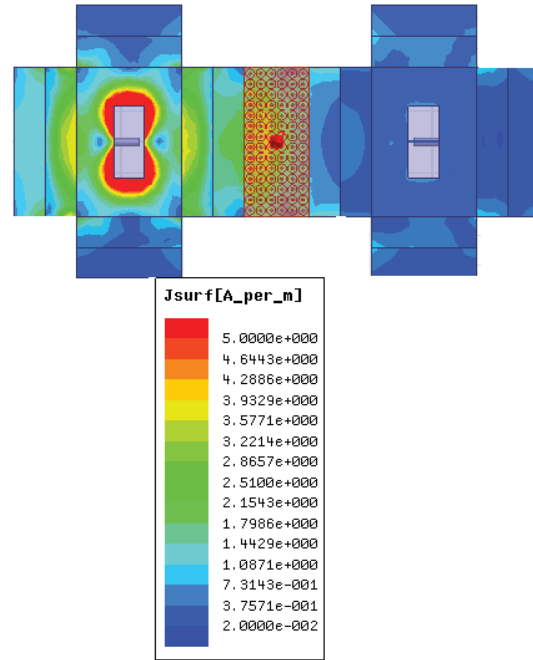


Fig. 8. EM-EBG effect on current distribution for design 4.

V. MEASUREMENT RESULTS

To validate the results of simulation for different designs of isolation antennas in array, especially effect of applying a tuned EM-EBG structure, based on designs 3 and 4, two non-planar CBS antenna arrays (2×1) were fabricated. In one array, between the two antennas a tuned EM-EBG is inserted as shown in Fig. 9. The results of measurement of S parameters for designs 3 and 4 are extracted by Agilent 8720ES network analyzer. And also result of pattern and gain measurements have been extracted in Antenna Chamber of KN Toosi Technical University. The fabricated antennas have 5% return loss bandwidth and 26 dB isolation for design 3 comparing to 33 dB for design 4 as shown in Figs. 10 to 13. The measurement results reveal that by inserting tuned EM-EBG mutual coupling is decreased by 7 dB, FBR is decreased by 7.5 dB and total gain is improved by 0.5 dB. On the whole, from both simulation and measurement, it could be understood that design 4 has a better performance compared with design 3.

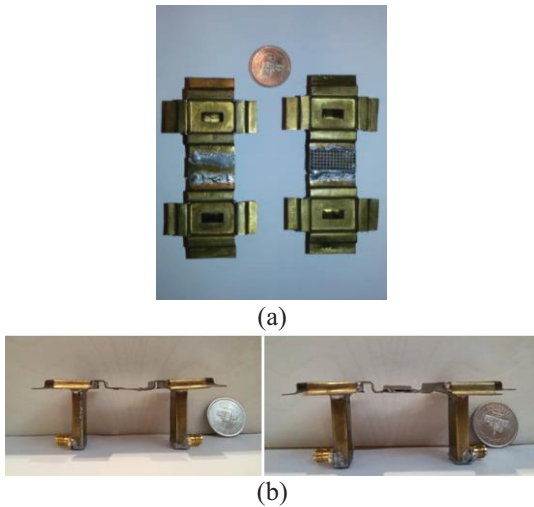


Fig. 9. Fabricated cavity backed slot antenna non-planar array: (a) top view and (b) side view (left) design 3, (right) design 4.

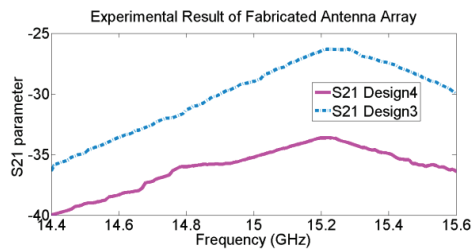


Fig. 10. Mutual coupling improvement by applying tuned EM-EBG.

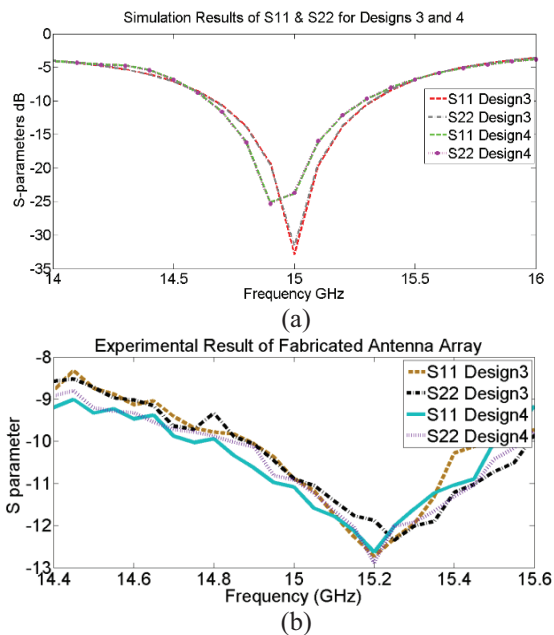


Fig. 11. (a) Simulated and (b) measured S_{11} and S_{22} for design 3 and 4.

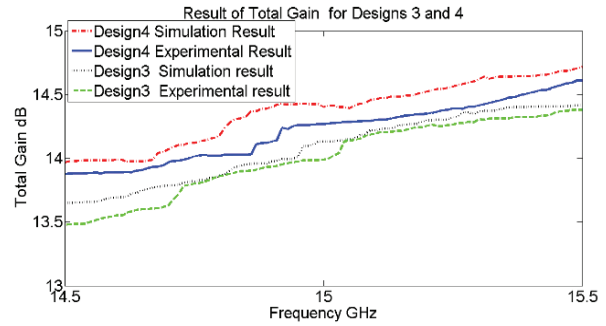


Fig. 12. Gain of designs 3 and 4.

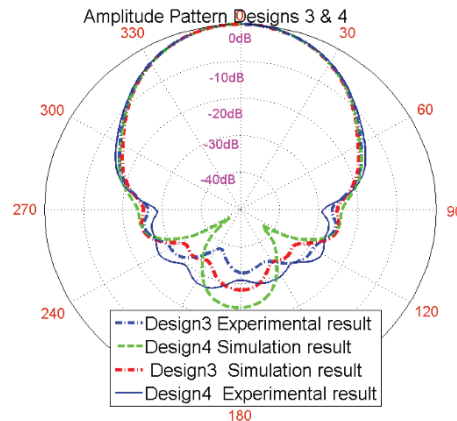


Fig. 13. Amplitude pattern of simulation and experimental results.

VI. CONCLUSION

In this paper, two new methods have been presented for reduction of mutual coupling in CBS antennas, including non-planar ground plane and tuned EM-EBG. Simulations reveal that by utilizing non planar ground plane mutual coupling is decreased by 2.5 dB comparing to planar ground plane. Results show that the depth of holes have a great impact on the surface current suppression.

Two prototypes of non-planar antenna were fabricated. For one of them, tuned EM-EBG had been used. The performance of the fabricated antennas were compared with each other. The measurements confirmed that a tuned-EM-EBG improves the mutual coupling and FBR by about 7 dB and 8 dB respectively.

REFERENCES

- [1] S. V. Georgakopoulos, A. C. Polycarpou, C. A. Balanis, and C. Birtche, "Analysis of coupling between cavity-backed slot antennas: FDTD, FEM & measurements," *Antennas and Propagation IEEE Society International Symposium*, vol. 1, pp. 582-585, July 1999.
- [2] S. V. Georgakopoulos, C. R. Birtcher, and C. A. Balanis, "Coupling, modeling and reduction

- techniques of cavity-backed slot antennas: FDTD versus measurements,” *IEEE Trans. on Electromagnetic Compatibility*, vol. 43, no. 3, Aug. 2001.
- [3] D. Sievenpiper, “High-impedance electromagnetic surfaces,” Ph.D. dissertation, Dep. Elect. Eng., Univ. of California, Los Angeles, 1999.
- [4] D. Sievenpiper, L. Zhang, R. F. J. Broas, N. G. Alexopolous, and E. Yablonovitch, “High impedance electromagnetic surfaces with a forbidden frequency band,” *IEEE Trans. Microw. Theory Tech.*, vol. 47, no. 11, pp. 2059-2074, Nov. 1999.
- [5] F. Yang and Y. Rahmat-Samii, “Mutual coupling reduction of microstrip antennas using electromagnetic band-gap structure,” *Proc. IEEE Antenna and Propagat. Soc. Int. Symp.*, vol. 2, pp. 478-481, 2001.
- [6] R. Abhari and G. V. Eleftheriades, “Metallodielectric electromagnetic band gap structures for suppression and isolation of the parallel plate noise in high-speed circuits,” *IEEE Trans. Microw. Theory Tech.*, vol. 51, no. 6, pp. 1629-1639, June 2003.
- [7] R. Cocciolo, F. R. Yang, K. P. Ma, and T. Itoh, “Aperture-coupled patch antenna on UCPBG substrate,” *IEEE Trans. Microw. Theory Tech.*, vol. 47, no. 11, pp. 2123-2130, Nov. 1999.
- [8] M. Coulombe, S. Farzaneh Koodiani, and C. Caloz, “Compact elongated mushroom (EM)-EBG structure for enhancement of patch antenna array performances,” *IEEE Trans. Antennas Propagat.*, vol. 58, pp. 1076-1086, 2010.
- [9] S. Manshari and M. N. Azarmanesh, “Novel design of cavity-backed slot antenna by reformed ground plane (corner notch and stepped) and elongated mushroom (EM)-EBG,” *Applied Computational Electromagnetics Society*, Aug. 2014.
- [10] A. A. Eldek, “Design of a high-gain cavity-backed slot antenna with mushroom cells and bent ground walls,” *Progress in Electromagnetics Research Letters*, vol. 20, pp. 69-76, 2011.
- [11] B. Mohajer-Iravani, S. Shahparnia, and O. M. Ramahi, “Coupling reduction in enclosures and cavities using electromagnetic band gap structures,” *IEEE Trans. Electromagn. Compat.*, vol. 48, no. 2, pp. 292-303, 2006.
- [12] A. Habashi, J. Nourinia, and C. Ghobadi, “Mutual coupling reduction between very closely spaced patch antennas using low-profile folded split-ring resonators (FSRRs),” *IEEE Antennas and Wireless Propagation Letters*, vol. 10, pp. 862-865, Oct. 2011.
- [13] Ansoft High Frequency Structure Simulation (HFSS), ver. 14, Ansoft Corporation, Pittsburgh, PA, 2005.
- [14] Peter A. Rizzi, *Microwave Engineering: Passive Circuits*. Englewood Cliffs, NJ: Prentice-Hall, 1988.

Artificial Neural Network based Design of RF MEMS Capacitive Shunt Switches

Zlatica Marinković¹, Taeyoung Kim², Vera Marković¹, Marija Milijić¹,
Olivera Pronić-Rančić¹, Tomislav Ćirić¹, and Larissa Vietzorreck²

¹ University of Niš, Faculty of Electronic Engineering
Aleksandra Medvedeva 14, 18000 Niš, Serbia
zlatica.marinkovic@elfak.ni.ac.rs, vera.markovic@elfak.ni.ac.rs, olivera.pronic@elfak.ni.ac.rs,
marija.milijic@elfak.ni.ac.rs, cirict@live.com

² Lehrstuhl für Hochfrequenztechnik, TU München
Arcisstrasse 21, 80333 München, Germany
kim@tum.de, vietzorreck@tum.de

Abstract — Artificial neural networks (ANNs) have appeared as a very efficient alternative to time consuming full-wave simulations of electrical characteristics of RF MEMS. In this paper, a new ANN based method to be used in the design of RF MEMS devices is proposed. ANNs are trained to model dependence of the scattering parameters and the resonant frequency of an RF MEMS switch on the switch geometrical parameters, as well as to perform the opposite procedure, i.e., to determine values of the geometrical parameters to achieve the desired electrical resonant frequency. The developed models can be used for fast simulation and optimization of the switch characteristics replacing time consuming procedures in full-wave simulators, which leads to a significant reduction of time needed for the device design.

Index Terms — Artificial neural networks, computer aided design, RF MEMS.

I. INTRODUCTION

RF MEMS switches are of growing interest for use in various communication and measurement systems, as they possess some properties superior to their mechanical or electronic counterparts [1-4]. They are lightweight, small, extremely linear, can be integrated and allow easy re-configurability or tunability of a system. A simulation of electrical parameters of RF MEMS components can be performed using standard commercial electromagnetic simulators. However, due to the aspect ratio of the vertical and lateral dimensions and the 3D topology, a full-wave simulation becomes time consuming. If the switch is integrated in a larger system, the desired overall system performance requires a certain behavior of the switch, e.g., in case of the capacitive shunt switch it is the position of the

resonance in a given frequency range. To achieve the required performance, time consuming optimizations should be performed, i.e., calculations of the switch with varying parameters have to be repeated. This paper demonstrates how the synthesis of the required switch performance can be accelerated by developing an ANN based model of the switch.

ANNs have been already applied to model some electrical or mechanical characteristics of different RF MEMS devices [5-11]. They have been applied mostly to the models of RF MEMS resonators [5, 9], and to the RF MEMS switches [6-8, 10, 11]. As far as the RF MEMS switch electrical characteristics are concerned, the ANNs have been applied for developing ANN models of the switch scattering parameters based on the frequency and switch geometrical parameters [6, 7], or for modeling the resonant frequency dependence on the switch geometrical parameters [11]. Also, it has been shown how some of the developed ANN models can be used in the design of circuits containing the modeled devices [10].

This contribution presents a neural modeling approach of a capacitive coplanar shunt switch. For the considered device, neural models for dependence of the switch electrical characteristics, i.e., the scattering parameters and resonant frequency, on the switch dimensions are developed. Also, a new approach for the inverse process, i.e., determination of the switch dimensions to achieve the desired switch performance, avoiding full-wave optimization procedures is proposed.

The paper is organized as follows: after introduction, in Section II the considered device is described. In Section III, a brief background on ANNs is given. In the following section the ANN based feed-forward models for determination of switch electrical characteristics for the given switch geometrical parameters are described, as

some of them are further used for building the inverse models. The proposed inverse models are described in Section V. Further, details of the proposed modeling technique and the obtained numerical results are presented and discussed in Section VI. Finally, Section VII contains concluding remarks.

II. DEVICE DESCRIPTION

The considered device is an RF MEMS capacitive coplanar shunt switch, depicted in Fig. 1, fabricated at Fondazione Bruno Kessler (FBK) in Trento, Italy in an 8 layer Silicon micromachining process [12]. The signal line below the bridge is realized as a thin aluminum layer. Adjacent to the signal line the DC actuation pads made of polysilicon are placed. The bridge is a thin membrane connecting both sides of the ground. The inductance of the bridge and the fixed capacitance between signal line and bridge form a resonant circuit to ground. The resonant frequency can be changed by varying the length of the fingered part, L_f , close to the anchors and the solid part, L_s . At the series resonance the circuit acts as a short circuit to ground, in a certain frequency band around the resonant frequency the transmission of the signal is suppressed. The bridge can be closed by applying the actuation voltage of around 45 V.

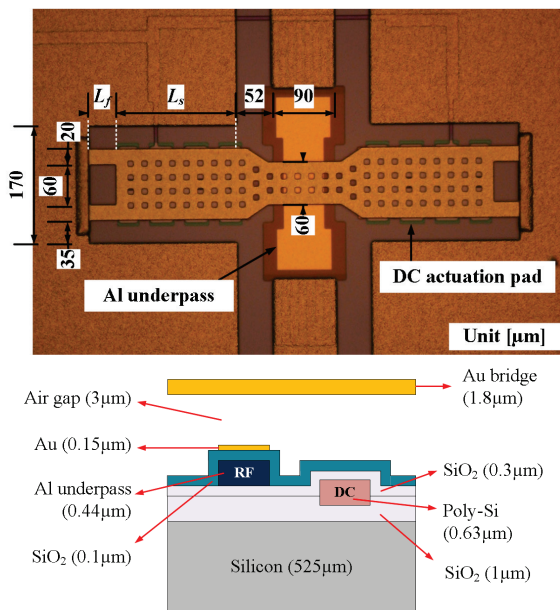


Fig. 1. Top-view of the realized RF MEMS switch and schematic of the cross-section with 8 layers in FBK technology [12].

III. ARTIFICIAL NEURAL NETWORKS

In this work standard multilayer perceptron (MLP)

neural networks are exploited. An MLP ANN consists of basic processing elements (neurons) grouped into layers: an input layer (IL), an output layer (OL), as well as several hidden layers (HL) [13]. Each neuron is connected to all neurons from the adjacent layers, whereas there are no connections among neurons belonging to the same layer. A neuron is characterized by a transfer function and each connection is weighted. In this work the following neuron transfer functions are used: linear transfer function for the input and output neurons and sigmoid transfer function for the hidden neurons. Information flows forward from the input layer to the output layer. An ANN learns relationship among sets of input-output data (training sets) by adjusting network connection weights and thresholds of activation functions. There is a number of algorithms for training of ANNs. The most frequently used are backpropagation algorithm and its modifications, as the Levenberg Marquardt algorithm [13], used in the present work. Once trained, the network provides fast response for various input vectors without changes in its structure and without additional optimizations. The most important feature of ANNs is their generalization ability, i.e., ability to generate a correct response even for the input parameter values not included in the training set. The generalization ability has qualified ANNs to be used as an efficient tool for modeling in the field of RF and microwaves [5-9, 13-24]. As examples, ANNs could be used as an alternative to time-consuming electromagnetic simulations [7, 13, 20, 23] or an alternative to the conventional modeling of microwave devices [14, 17, 22, 24].

IV. FEED-FORWARD RF MEMS SWITCH MODELING

As mentioned in the introductory section, ANNs can be applied to develop models of the electrical characteristics of RF MEMS switches. It should be noted that in the work of the other authors, the simple rectangular shape membrane has been studied. This is the first time that a membrane with complex structure and shape is considered to be modeled by ANNs.

Two types of the models are developed here. The first type of the models is based on ANNs trained to predict the switch scattering parameters dependence on the switch geometrical parameters and frequency, whereas in the second type of the models ANNs are exploited to model dependence of the switch electrical resonant frequency on the switch geometrical parameters. Figures 2 and 3 show the mentioned ANN models developed for the considered capacitive shunt switch.

The considered geometrical parameters are the lengths of the fingered and solid parts, L_f and L_s , as illustrated in Fig. 1.

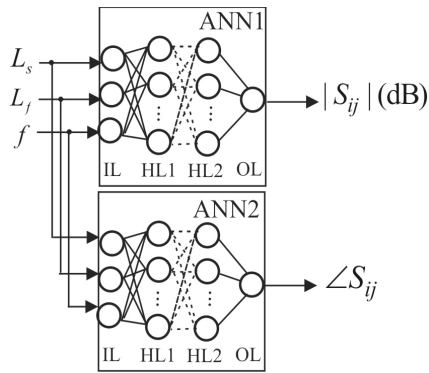


Fig. 2. ANN model of RF MEMS switch S-parameters.

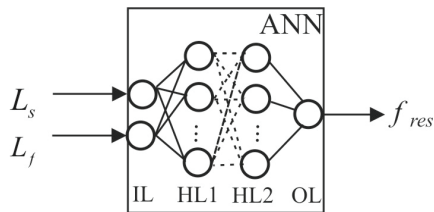


Fig. 3. ANN model of RF MEMS switch resonant frequency.

As far as an RF MEMS switch is a symmetric and reciprocal device, i.e., $S_{22}=S_{11}$ and $S_{12}=S_{21}$, it is enough to develop only models for S_{11} and S_{21} . For each of the modeled parameters, two ANNs are trained, one to model the magnitude ($|S_{ij}|$) and the other to model the phase ($\angle S_{ij}$). As the training data, the S-parameters calculated in numerical full-wave simulations in an electromagnetic simulator are used. Each ANN has three input neurons corresponding to the two lateral dimensions of the switch and the frequency, and one output neuron corresponding to the modeled parameter. The model is validated by comparing the ANN response and the full-wave simulation results for the combination of dimensions not seen by the ANN during the training. Once the ANNs are trained, the S-parameters of the switch can be easily calculated in a very short time by finding the ANN response. In order to use the developed ANN model in a circuit simulator for the switch S-parameter simulation and optimization, the expressions describing the ANNs are implemented in the simulator. Namely, the switch is represented by a two-port expression defined device. The expressions describing the ANNs are put into variable and equation blocks (VAR) having the switch lateral dimensions and frequency as input parameters and switch S-parameters as outputs. The S-parameters calculated in the VAR blocks are assigned to the two-port device S-parameters. Therefore, the two-port device and the corresponding VAR blocks represent the ANN model of switch with

included dependence on the geometrical parameters. The overall procedure of model development and implementation is shown in Fig. 4. Once the ANN model of the switch scattering parameters is implemented in a circuit simulator, further simulations and optimizations are performed in a standard way, but in significantly shorter time, as will be illustrated later.

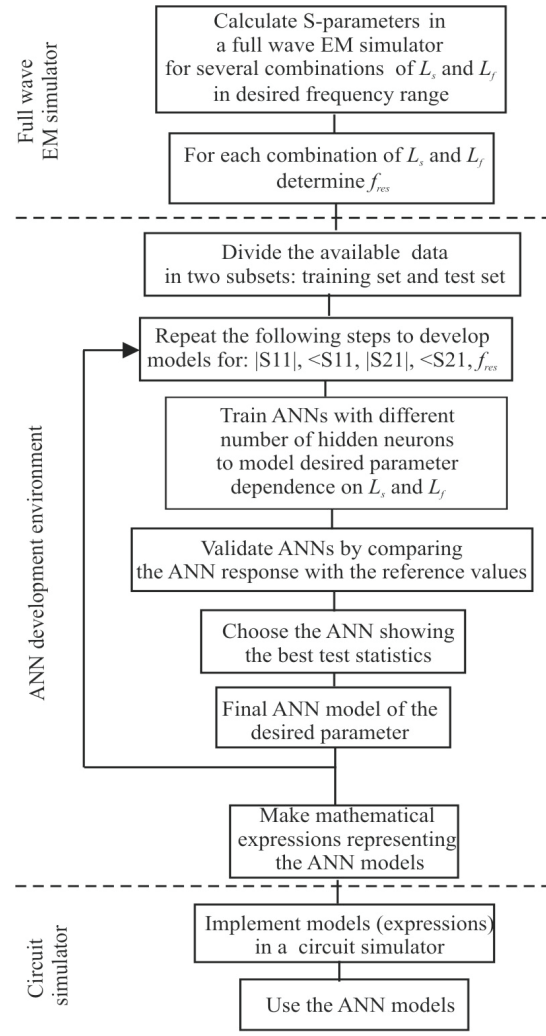


Fig. 4. ANN model development and implementation.

The neural model for the switch resonant frequency consists of an ANN trained to model the switch resonant frequency dependence on the two mentioned lateral dimensions. Therefore, the ANN has two neurons in the input layer and one neuron in the output layer. As in the previous case, the data used for training and validation of the ANN are obtained by the full-wave numerical simulations.

The developed model can be further used to determine the resonant frequency for given values of the lateral dimensions in a very short time or to

optimize the dimensions to achieve the desired resonant frequency.

It is worth to mention that the ANN models are valid for the values of the lateral dimensions falling within their ranges used in the training set.

V. INVERSE RF MEMS SWITCH MODELING

With the aim to avoid optimization procedures in full-wave electromagnetic or circuit simulators, the inverse RF MEMS switch modeling approach based on ANNs is also proposed here. This gives the possibility to directly determine the necessary geometrical dimensions for a desired resonant frequency. The idea is to train ANNs with the aim to directly predict one of the switch geometrical parameters in order to satisfy working conditions around the resonance when the other parameter is fixed, as shown in Fig. 5. Namely, ANNs are trained to learn the relationship between the chosen lateral switch dimension and resonant frequency and the other switch dimension. Therefore, the ANNs have two input neurons and one output neuron. The training and test data are obtained by standard full-wave simulations. By using the trained ANNs, the considered geometrical parameter values could be determined by a simple calculation of the ANN response. In that way design of the RF MEMS switch becomes more efficient.

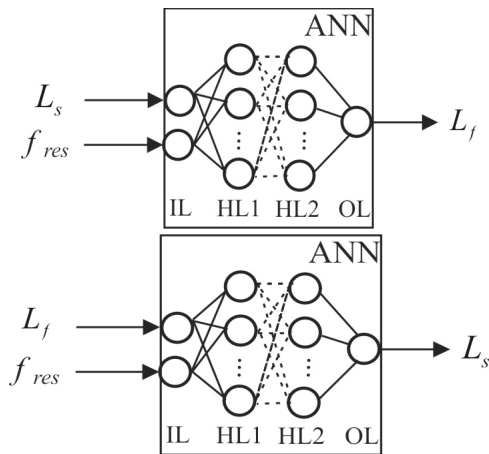


Fig. 5. ANN based determination of RF MEMS switch geometrical parameters.

VI. NUMERICAL RESULTS

The data used for the ANN model development and validation was obtained by full-wave simulations within ADS software package (ADS momentum) [25] for the frequencies up to 40 GHz. As the number of hidden neurons could not be determined prior to the training process, for each ANN, ANNs with different number of hidden neurons were trained and then the

ANN showing the best modeling results was chosen as the final one.

A. Feed-forward RF MEMS switch models

The S-parameters used for the model development were simulated in ADS momentum for 23 combinations of geometrical parameters L_f and L_s . The data referring to 17 combinations was used for training and the data referring to the rest of 6 combinations was used for validation of the model generalization. As mentioned above, for each of the modeled parameters ANNs with different number of hidden neurons were trained and compared. The ANN accuracy was compared by assessing the errors obtained for the test values not used for training. It was found that among the trained ANNs the best test statistics gave the following two-hidden-layer ANNs: for the magnitude of S_{11} : the ANN having 8 neurons in the first layer and 6 neurons in the second hidden layer, and for the magnitude of S_{21} : the ANN with 8 neurons in both hidden layers. For models of the phases in both cases the best results were obtained by the two hidden-layer ANNs containing 10 neurons in each hidden layer. As illustration, Figs. 6 and 7 show comparison of the ANN simulated scattering parameters (lines) and the corresponding reference values obtained by the full-wave simulations in ADS (symbols). It can be concluded that the ANN responses match very well with the simulated values. As the ANN model directly relates the switch lateral dimensions to the scattering parameters over frequency, the S-parameters of a varied geometry can be calculated within seconds.

Optimization of the dimensions for the given requirements in the desired frequency band lasts less than a second when performed by using the neural model implemented in the ADS circuit simulator in a way described in the previous section, which is significantly faster than the optimization in a full wave simulator, which lasts around 2 hours.

To confirm further the achieved good modeling accuracy, magnitude of the transmission coefficient of the fabricated device ($L_s = 174 \mu\text{m}$ and $L_f = 40 \mu\text{m}$) optimized for a resonant frequency of 15 GHz is depicted in Fig. 8. The plot shows the measured data (dashed line) in comparison with the results of the ANN model (line) and the full-wave simulations (symbols).

To develop a model for the resonant frequency, first the resonant frequency for all the combinations of dimensions of the geometrical parameters L_s and L_f considered in the previous case was determined. The resonant frequency was found as the frequency corresponding to the minimum value of magnitude of S_{21} simulated in a full-wave simulator. The training and test set correspond to the same geometrical parameter combinations as in the previous case. Among the trained ANNs with different number of hidden

neurons, the best results were obtained by the ANN having only one hidden layer containing five neurons. Table 1 shows the resonant frequency determined by the ANN model for several combinations of the geometrical parameters not used for the training. It can be seen that the resonant frequency values simulated by the ANN are very close to the target values, as confirmed by the relative percentage error less than 1%.

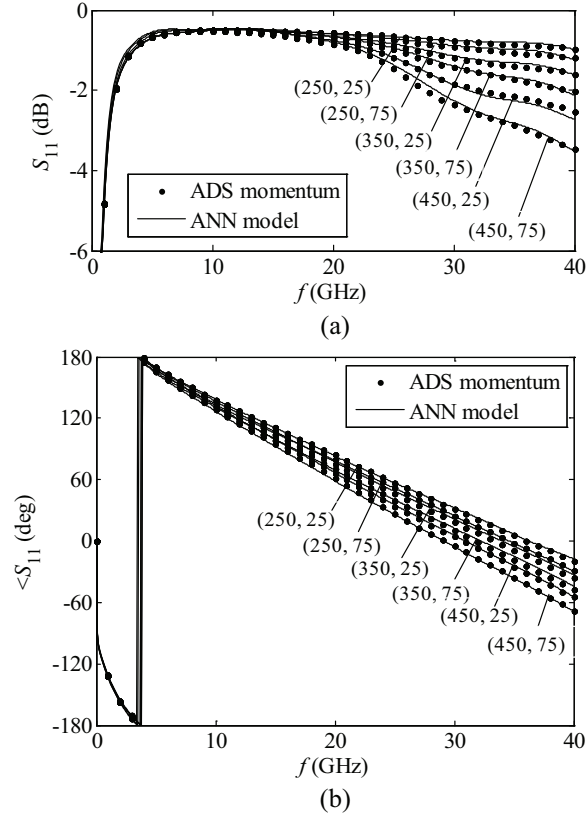


Fig. 6. Parameter S_{11} for six $(L_s [\mu\text{m}], L_f [\mu\text{m}])$ combinations not used for the model development: (a) magnitude and (b) phase.

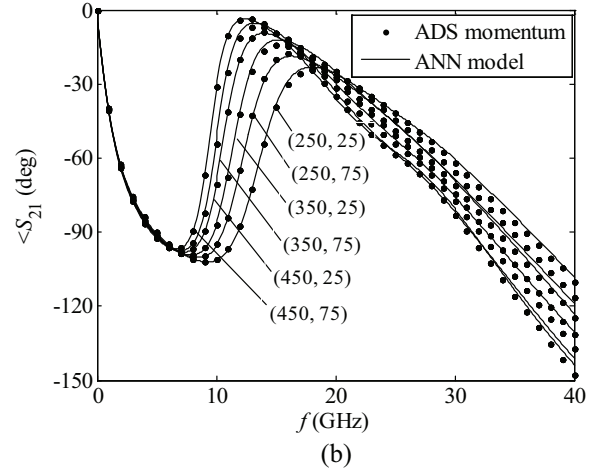
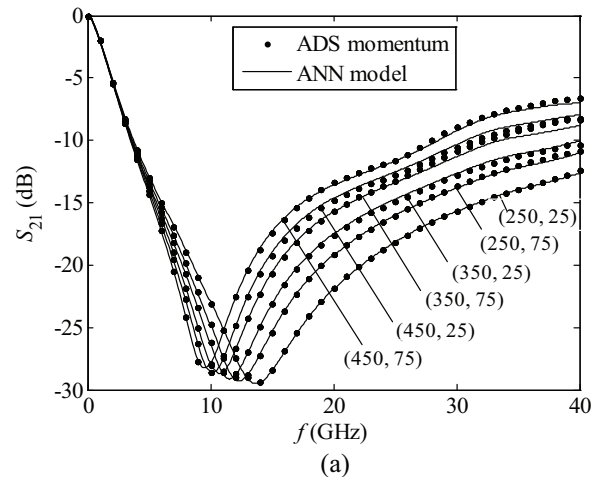


Fig. 7. Parameter S_{21} for six $(L_s [\mu\text{m}], L_f [\mu\text{m}])$ combinations not used for the model development: (a) magnitude and (b) phase.

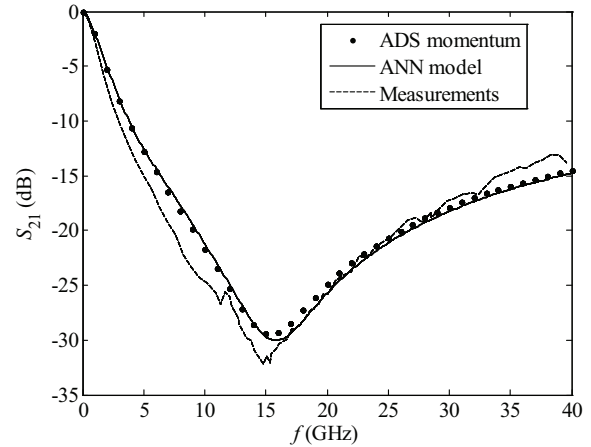


Fig. 8. Isolation of the fabricated RF MEMS switch ($L_s = 174 \mu\text{m}$ and $L_f = 40 \mu\text{m}$).

Table 1: RF MEMS switch resonant frequency

L_s (μm)	L_f (μm)	$f_{res-Target}$ (GHz)	$f_{res-ANN}$ (GHz)	Rel. Error (%)
250	25	13.7	13.689	0.08
250	75	12.4	12.403	0.02
350	25	11.6	11.550	0.43
350	75	10.7	10.638	0.58
450	25	10.2	10.127	0.71
450	75	9.5	9.499	0.01

B. Inverse RF MEMS switch models

The inverse models described in Section V were developed using the full-wave simulated data referring to the same 23 combinations of the switch lateral dimensions as used for the development of the feed-forward models. It appeared that the accuracy of the

modeling was not satisfactory, as the errors during the model validation achieved even several tens percent. This indicates that a larger training set should be used to build reliable inverse ANN models. Acquiring more training data needed for the inverse ANN models assumes new full-wave simulations, as the resonant frequency for each new combination of input geometrical parameters is determined by a full-wave simulation. To make a larger training set, but without significant increase of the model development time, the feed-forward ANN model for the resonant frequency described above was used. As this ANN model gives a response almost in a moment, building a larger data set does not increase significantly the duration of the model development procedure. For building a new larger training dataset, a non-uniform distribution of combinations of the dimensions was used. The number of data in the areas of the input parameter space where the ANN models showed higher error values was increased until the satisfactory accuracy of the inverse ANNs model was reached. The final training dataset referred to 814 input-output pairs. During the ANN model development procedure, the ANNs with different number of hidden neurons were trained and validated on the set of data not used for the training purpose. Among the trained ANNs, the ANNs with two hidden layers with 15 neurons in each hidden layer were chosen for the both lateral dimensions determination.

To illustrate the accuracy of the inverse RF MEMS ANN models, in Tables 2 and 3 there are results of the model testing for the input combinations not used for the ANN training. It should be noted that the resonant frequency values given in the tables are calculated in the full-wave simulator for the combination of input dimension and target output dimension.

It can be seen that the absolute difference of the predicted and expected values is less than 3 μm (which is already close to fabrication tolerances) in the case of modeling the length of fingered part, and less than 3.5 μm , in the case of modeling the length of solid part. The relative errors are in most cases less than 3%.

Table 2: RF MEMS switch inverse modeling: L_f

L_s (μm)	f_{res} (GHz)	L_f (Target) (μm)	L_f (ANN) (μm)	Relative Error (%)
75	22.78	25	24.9	0.4
75	19.17	65	65.4	0.6
75	17.92	85	85.3	0.3
100	17.5	75	73.6	1.9
200	13.13	85	86.8	2.1
350	11.67	25	23.4	6.4
350	10.83	65	62.2	4.3
400	10	85	87.4	2.9

Table 3: RF MEMS switch inverse modeling: L_s

L_f (μm)	f_{res} (GHz)	L_s (target) (μm)	L_s (ANN) (μm)	Relative Error (%)
25	22.78	75	74.9	0.1
65	19.17	75	75.5	0.7
85	17.92	75	75.3	0.4
75	17.5	100	97.9	2.1
85	13.13	200	202.7	1.4
25	11.67	350	347.8	0.6
65	10.83	350	348.0	0.6
85	10	400	403.4	0.9

VII. CONCLUSION

At the example of a capacitive coplanar shunt switch in RF MEMS technology, efficient ways for determination of the switch geometrical parameters based on the ANNs were presented. Usage of the proposed ANN models can be an efficient alternative to the standard optimization of the switch dimensions in the full-wave simulators. First, feed-forward models based on ANNs were trained to determine the switch electrical characteristics for the given values of the considered geometrical parameters. Then, inverse ANN models for determination of the switch geometrical parameters for the given switch resonant frequency were developed.

Once developed the proposed ANN models can be used for obtaining further results within seconds, which is much faster than full-wave EM simulations and optimizations lasting up to 2 hours. Having in mind that training a number of ANNs with different number of hidden neurons and long numerical simulations performed to obtain the training data take time comparable to the time needed for the optimization of the single switch, the efficiency of the proposed method is not obvious for a single switch simulation and optimization. However, the speed of the ANN models comes out as an advantage for a settled technology, when a number of switches with slight variations have to be adjusted to fulfill requirements for different applications without using heavy and time-consuming full-wave simulators, thus speeding up significantly the fabrication cycle.

ACKNOWLEDGMENT

Authors would like to thank FBK Trento, Thales Alenia Italy, CNR Rome and University of Perugia, Italy for providing RF MEMS data. This work was funded by the bilateral Serbian-German project ‘‘Smart Modeling and Optimization of 3D Structured RF Components’’ supported by the DAAD foundation and Serbian Ministry of Education, Science and Technological Development. The work was also

supported by the project TR-32052 of the Serbian Ministry of Education, Science and Technological Development.

REFERENCES

- [1] G. M. Rebeiz, *RF MEMS Theory, Design, and Technology*. New York, USA, Wiley, 2003.
- [2] T. Itoh, G. Haddad, and J. Harvey, "Microelectromechanical switches for RF applications," *RF Technologies for Low Power Wireless Communications*, pp. 349-382, 2001.
- [3] R. Ramadoss, S. Lee, Y. C. Lee, V. M. Bright, and K. C. Gupta, "MEMS capacitive series switch fabricated using PCB technology," *International Journal of RF and Microwave Computer-Aided Engineering*, vol. 17, no. 4, pp. 387-397, July 2007.
- [4] M. Daneshmand, A. A. Fomani, M. M. Fahmi, J. A. Ruiz-Cruz, and R. R. Mansour, "MEMS multiport switches and switch matrices for satellite applications," *IEEE MTT-S International Microwave Symposium Digest*, Montreal, Canada, pp. 1-3, June 2012.
- [5] Y. Lee, Y. Park, F. Niu, B. Bachman, K. C. Gupta, and D. Filipovic, "Artificial neural network modeling of RF MEMS resonators," *International Journal of RF and Microwave Computer-Aided Engineering*, vol. 14, no. 4, pp. 302-316, July 2004.
- [6] Y. Lee and D. S. Filipovic, "Combined full-wave/ANN based modeling of MEMS switches for RF and microwave applications," *IEEE Antennas and Propagation Society International Symposium*, Washington DC, pp. 85-88, July 2005.
- [7] Y. Lee and D. S. Filipovic, "ANN based electromagnetic models for the design of RF MEMS switches," *IEEE Microwave Wireless Component Letters*, vol. 15, no. 11, pp. 823-825, Nov. 2005.
- [8] Y. Mafinejad, A. Z. Kouzani, and K. Mafinezhad, "Determining RF MEMS switch parameter by neural networks," *IEEE Region 10 Conference TENCON 2009*, Singapore, pp. 1-5, Jan. 2009.
- [9] Y. Lee, Y. Park, F. Niu, and D. Filipovic, "Artificial neural network based macromodeling approach for two-port RF MEMS resonating structures," *IEEE Proceedings of Networking, Sensing and Control*, Tucson, pp. 261-266, Mar. 2005.
- [10] Y. Lee, Y. Park, F. Niu, and D. Filipovic, "Design and optimization of RF ICs with embedded linear macromodels of multiport MEMS devices," *International Journal of RF and Microwave Computer-Aided Engineering*, vol. 17, no. 2, pp. 196-209, Mar. 2007.
- [11] Y. Gong, F. Zhao, H. Xin, J. Lin, and Q. Bai, "Simulation and optimal design for RF MEMS cantilevered beam switch," *International Conference on Future Computer and Communication (FCC '09)*, Wuhan, pp. 84-87, June 2009.
- [12] S. DiNardo, P. Farinelli, F. Giacomozzi, G. Mannocchi, R. Marcelli, B. Margesin, P. Mezzanotte, V. Mulloni, P. Russer, R. Sorrentino, F. Vitulli, and L. Vietzorreck, "Broadband RF-MEMS based SPDT," *European Microwave Conference*, Manchester, pp. 1727-1730, Sep. 2006.
- [13] Q. J. Zhang and K. C. Gupta, *Neural Networks for RF and Microwave Design*. Boston, MA, USA, Artech House, 2000.
- [14] C. Christodoulou and M. Gerogiopoulos, *Applications of Neural Networks in Electromagnetics*. Artech House, Inc. Norwood, MA, USA, 2000.
- [15] P. Burrascano, S. Fiori, and M. Mongiardo, "A review of artificial neural network applications in microwave computer-aided design," *International Journal of RF and Microwave Computer-Aided Engineering*, vol. 9, no. 3, pp. 158-174, May 1999.
- [16] S. S. Gultekin, K. Guney, and S. Sagiroglu, "Neural networks for the calculation of bandwidth of rectangular microstrip antennas," *Applied Computational Electromagnetics Society Journal*, vol. 18, no. 2, pp. 110-120, July 2003.
- [17] Z. Marinković and V. Marković, "Temperature dependent models of low-noise microwave transistors based on neural networks," *International Journal of RF and Microwave Computer-Aided Engineering*, vol. 15, no. 6, pp. 567-577, Nov. 2005.
- [18] R. Ghayoula, N. Fadlallah, A. Gharsallah, and M. Rammal, "Design, modeling, and synthesis of radiation pattern of intelligent antenna by artificial neural networks," *Applied Computational Electromagnetics Society Journal*, vol. 23, no. 4, pp. 336-344, Dec. 2008.
- [19] Z. Marinković, G. Crupi, A. Caddemi, and V. Marković, "Comparison between analytical and neural approaches for multibias small signal modeling of microwave scaled FETs," *Microwave and Optical Technology Letters*, vol. 52, no. 10, pp. 2238-2244, Oct. 2010.
- [20] J. E. Rayas-Sanchez, "EM-based optimization of microwave circuits using artificial neural networks: The state-of-the-art," *IEEE Transactions on Microwave Theory and Technique*, vol. 52, no. 1, pp. 420-435, Jan. 2004.
- [21] H. Kabir, Y. Cao, and Q. Zhang, "Advances of neural network modeling methods for RF/

microwave applications,” *Applied Computational Electromagnetics Society Journal*, vol. 25, no. 5, pp. 423-432, May 2010.

- [22] Z. Marinković, G. Crupi, D. Schreurs, A. Caddemi, and V. Marković, “Microwave FinFET modeling based on artificial neural networks including lossy silicon substrate,” *Microelectronic Engineering*, vol. 88, no. 10, pp. 3158-3163, Oct. 2012.
- [23] M. Agatonović, Z. Marinković, and V. Marković, “Application of ANNs in evaluation of microwave pyramidal absorber performance,” *Applied Computational Electromagnetics Society Journal*, vol. 27, no. 4, pp. 326-333, Apr. 2012.
- [24] Z. Marinković, O. Pronić-Rančić, and V. Marković, “Small-signal and noise modeling of class of HEMTs using knowledge-based artificial neural networks,” *International Journal of RF and Microwave Computer-Aided Engineering*, vol. 23, no. 1, pp. 34-39, Jan. 2013.
- [25] Advanced Design System 2009, Agilent Technologies.



Zlatica Marinković received the Dipl.-Ing. degree in Electrical Engineering from the University of Niš, Faculty of Electronic Engineering, Serbia in 1999 and the M.Sc. and Ph.D. degrees from same University in 2003 and 2007, respectively. She is an Assistant

Professor at the Department for Telecommunications of the Faculty of Electronic Engineering Niš. She is an IEEE Senior Member and serves as the IEEE MTT-S Undergraduate Scholarships Chair and Chair of the IEEE MTT-S Chapter of Serbia and Montenegro. Her research areas are: microwave electronics and artificial neural networks and their application in the field of microwaves and telecommunications. She has authored/co-authored more than 90 scientific papers and two book chapters.



Taeyoung Kim received the M.Sc. degree in Microwave Engineering from the Technische Universität München, Germany in 2008. Since 2008, he has worked as a Research Engineer and the Ph.D. student at the Institute for High-Frequency Engineering in München. His

research interest includes the RF MEMS switch system design for space application, the smart antenna design using RF MEMS and metamaterials technologies and the electromagnetic modeling of RF MEMS switches. He has authored/co-authored more than 10 conference or journal papers.



Vera Marković received a Dipl.-Ing degree in Electrical Engineering in 1980, the M.Sc. degree in 1985 and Ph.D. degree in 1992, all from the Faculty of Electronic Engineering, University of Niš. She is currently a Full Professor at the Department for Telecommunications of the Faculty of Electronic Engineering of University of Niš and Vice-Chair of IEEE Serbia & Montenegro section. Her current research interests include the modeling of microwave devices for wireless communications, application of neural networks in microwave CAD techniques, the investigation of biological effects of microwave radiation, etc. Marković has authored or co-authored a monograph, two textbooks and more than 250 conference or journal papers.



Marija Milijć received the Dipl.-Ing. degree in Electrical Engineering from the University of Niš, Faculty of Electronic Engineering, Serbia in 2003 and the M.Sc. degree from same University in 2007. She is a Teaching and Research Assistant with the University of Niš, Faculty of Electronic Engineering, Serbia. Her research areas are: antennas and artificial neural networks and their application in the field of microwaves. She has authored/co-authored more than 40 scientific papers.



Olivera Pronić - Rančić received the Dipl.-Ing. degree in Electrical Engineering from the Faculty of Electronic Engineering, University of Niš, Serbia, in 1993, and M.Sc. degree and Ph.D. from the same university in 1998 and 2002, respectively. She is currently an

Associate Professor at the Department of Telecommunications, at Faculty of Electronic Engineering. Her research interests include modeling of active microwave devices and artificial neural networks and their application in the field of microwaves. Pronić - Rančić has authored/co-authored two textbooks and more than 100 scientific papers.



Tomislav Ćirić received the Dipl.-Ing. degree in Electrical Engineering in 2001. In 2014 he completed a M.Sc. degree at the Faculty of Electronic Engineering, University of Niš, Serbia, where is currently a Ph.D. student in Telecommunications. His research areas are artificial neural networks and their applications for modeling and optimization of RF MEMS devices.



Larissa Vietzorreck received a Dipl.-Ing. degree in Electrical Engineering from Ruhr-Universität Bochum and a Ph.D. from Fernuniversität Hagen, both in Germany. Since 1998 she works as Assistant Professor at Technische Universität München at the Institute for High-Frequency Engineering. In summer 2013 she

was a Visiting Professor at Friedrich-Alexander Universität Erlangen-Nürnberg, Germany. Her research areas comprise the development of numerical modeling tools for electromagnetic and mechanical simulation as well as design and development of RF MEMS and other passive components and circuits. She has authored/co-authored more than 100 scientific papers.

Vector Hysteresis Modeling in Arbitrarily Shaped Objects Using an Energy Minimization Approach

Amr A. Adly¹ and Salwa K. Abd-El-Hafiz²

¹Electrical Power and Machines Department

²Engineering Mathematics and Physics Department
Faculty of Engineering, Cairo University, Giza 12613, Egypt
amradly@ieee.org, salwa@computer.org

Abstract — It is known that proper and efficient modeling of vector hysteresis is crucial to the precise design and performance estimation of electric power devices and magnetic recording processes. Recently, discrete Hopfield neural networks have been successfully utilized in the construction of vector hysteresis models. This paper presents a novel energy-minimization Hopfield neural network approach to implement Stoner-Wohlfarth-like vector hysteresis operators in triangular sub-regions. Advantages of the approach stem from the non-rectangular nature of such operators, which could mimic major hysteresis loops as well as their implementation in the most commonly used triangular discretization sub-domains. Details of the approach are given in the paper.

Index Terms — Discrete Hopfield neural network, energy minimization, shape anisotropy, vector Hysteresis.

I. INTRODUCTION

Electromagnetic field computation in nonlinear media and media exhibiting hysteresis is, in general, a crucial activity to a wide variety of applications such as those involving analysis of magnetic recording processes and determination of core losses in power devices (see, for instance, [1-4]). In this context, only computationally efficient vector hysteresis models may be practically utilized in numerical field computation methodologies, which are indispensable for handling complicated device geometries and excitation schemes.

In the past, substantial efforts focusing on the efficiency enhancement of typical vector hysteresis models have been reported (refer, for instance, to [5]). The notion of implementing an arbitrary elementary hysteresis operator using a dual-node discrete Hopfield neural network (HNN) having positive feedback values was first introduced in [6]. In this approach, switching thresholds of the operator were easily manipulated through the feedback factor as well as an input offset term. Later on, discrete HNNs have been successfully configured to construct scalar – as well as coupled pairs of – hysteresis operators [7-9]. Moreover, an enhancement

of the aforementioned HNN configuration was carried out in [10] for the implementation of Stoner-Wohlfarth-like operators. An important advantage of this enhancement stems from the non-rectangular nature of the generated operators which minimizes the number of operators required to mimic a specific loop.

This paper presents an energy minimization HNN approach to model vector hysteresis in triangular sub-regions. More specifically, the approach further generalizes the work in [10] by correlating a triangular geometrical configuration to the coupling coefficients of a corresponding 3-node HNN. Using this approach, it is possible to account for shape anisotropy implications on vector hysteresis. The approach could also be utilized in field computation in media exhibiting hysteresis.

II. REALIZATION OF A TRIANGULAR SUB-REGION INVOLVING MEDIA EXHIBITING HYSTERESIS

The proposed 2D methodology is based on the utilization of the hybrid discrete-continuous activation function proposed in [10] in a 3-node HNN with positive feedbacks, as shown in Fig. 1. It should be pointed out that this configuration is genuinely proposed in this work to realize the primitive scalar and vector hysteresis properties for a triangular sub-region u having arbitrary geometry. Within this proposed configuration, the orientation of every node is assumed to be along the line joining the u^{th} triangle center point to its corresponding vertex. Positive feedbacks $k_{i,j}^{(u)}$ between different triangle nodes i and j are assumed to be given by:

$$k_{i,j}^{(u)} = k_{copl} \left| \cos(\phi_{ij}^{(u)}) \right|, \quad (1)$$

where, k_{copl} is a pre-selected coupling factor ≤ 1 and $\phi_{ij}^{(u)}$ is the angle subtended between nodes i and j orientations as shown in Fig. 2.

Assuming a hybrid activation function $f(x)$ [10] given by:

$$f(x) = c f_c(x) + (1-c) f_d(x), \quad (2)$$

where, c is a positive constant ≤ 1 while $f_c(x)$ and $f_d(x)$ are the sigmoid continuous and signum discrete activation functions, respectively, given by:

$$f_c(x) = \tanh(ax), \quad a > 0, \quad (3)$$

$$f_d(x) = \begin{cases} +1 & \text{if } x > 0 \\ -1 & \text{if } x < 0 \\ \text{unchanged} & \text{if } x = 0 \end{cases} \quad (4)$$

The new hybrid activation rule for, say, node i thus becomes:

$$m_i^{(u)}(t+1) = c f_c(\text{net}_i^{(u)}(t)) + (1-c) f_d(\text{net}_i^{(u)}(t)), \quad (5)$$

where $m_i^{(u)}$ is the node output while $\text{net}_i^{(u)}$ maybe defined, in accordance with (1) and Fig. 1, by:

$$\text{net}_i^{(u)}(t) = \bar{h}^{(u)}(t) \bullet \left(\frac{\bar{m}_i^{(u)}}{m_i^{(u)}} \right) + \sum_{j=1, j \neq i}^3 k_{i,j}^{(u)} m_j^{(u)}(t), \quad (6)$$

where $\bar{h}^{(u)}$ is the external input applied to the u^{th} triangle.

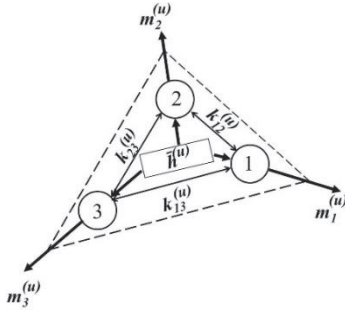


Fig. 1. Realization of a basic vector hysteresis operator representing a triangular sub-region using a tri-node HNN.

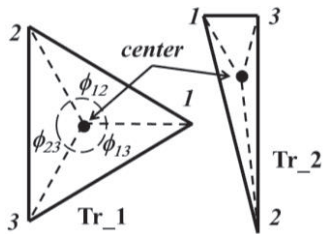


Fig. 2. Examples of two triangular sub-regions having different aspect ratios.

The state of this network converges to the minimum of the following energy function:

$$E^{(u)} = - \sum_{i=1}^3 \left\{ \bar{h}^{(u)} \bullet \bar{m}_i^{(u)} + \frac{1}{2} \sum_{j=1, j \neq i}^3 k_{i,j}^{(u)} m_i^{(u)} m_j^{(u)} \right\}. \quad (7)$$

For every applied external input $\bar{h}^{(u)}$, well established HNN time-stepping algorithms are utilized in accordance with (5)-(7) to achieve a minimum value for the u^{th} triangle energy $E^{(u)}$ (see, for instance, [11, 12]). From the superposition principle, overall triangle output $\bar{m}^{(u)}$ may be computed from:

$$\bar{m}^{(u)} = \sum_{i=1}^3 \bar{m}_i^{(u)}. \quad (8)$$

In order to demonstrate the effect of the geometrical configuration on a triangle's primitive scalar and vector hysteresis properties, consider the 3 triangles whose geometrical details are given in Fig. 3 and Table 1. x-axis scalar and rotational M - H curves corresponding to the three triangles under consideration are shown in Figs. 4 and 5, respectively.

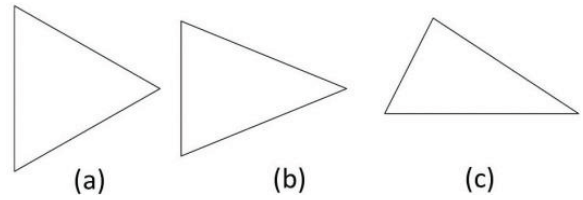


Fig. 3. Three arbitrary chosen triangles having different geometrical configurations: (a) Tr_1, (b) Tr_2, and (c) Tr_3.

Table 1: Geometrical details of the triangles shown in Fig. 3

Triangle	Orientation of the Lines Joining Center Point and Vertices
Tr_1	$0^\circ, +120^\circ, -120^\circ$
Tr_2	$0^\circ, +135^\circ, -135^\circ$
Tr_3	$-15.94^\circ, +116.56^\circ, -158.2^\circ$

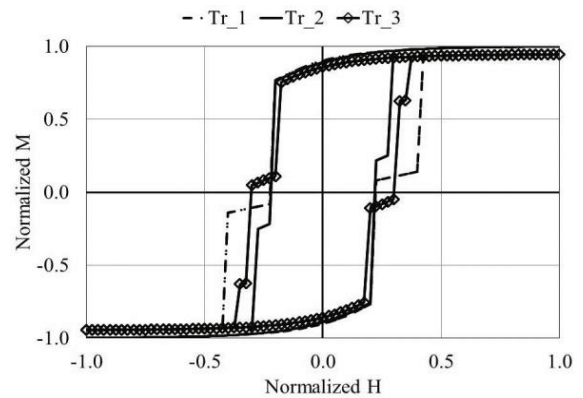


Fig. 4. Normalized scalar M - H curves along the x-axis corresponding to the three triangles shown in Fig. 3 for $k_{copl} = 0.3$, $a = 3$ and $c = 0.7$.

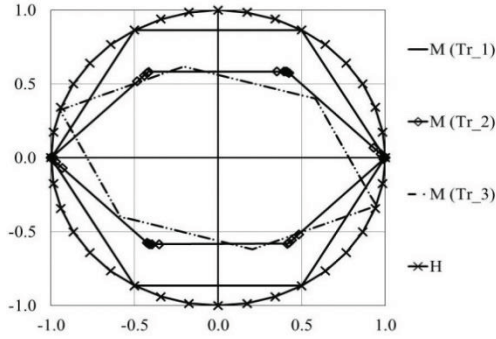


Fig. 5. Normalized rotational M - H curves corresponding to the three triangles shown in Fig. 3 for $k_{copl} = 0.3$, $a = 3$ and $c = 0.7$.

Few important observations, which are in full harmony with magnetism physical principles, may be drawn from these figures [13]. For instance, Fig. 4 suggests that the triangle having the least stretch towards the x-axis (i.e., Tr_1) is the one having the widest (hardest) scalar x-axis M - H curve. Moreover, for the triangle which does not have a vertex orientation along the x-axis (i.e., Tr_3) it is not easy to achieve full saturation. Furthermore, Fig. 5 clearly demonstrates the tri-axis anisotropy associated with a triangular sub-region. In addition, the impact of the geometrical configuration on the rotational M - H curves symmetry as well as tilting is clearly demonstrated in Fig. 5.

More importantly, the ability of the proposed approach to realize different M - H curve width and squareness for a particular triangle is clearly demonstrated in Figs. 6 and 7. In these two figures, different scalar M - H curves are generated for triangle Tr_1 by varying k_{copl} and c , respectively. Likewise, it could be demonstrated that the scalar M - H curves may be modified by varying a . This fact highlights the ability of the approach to custom fit specific hysteresis curves.

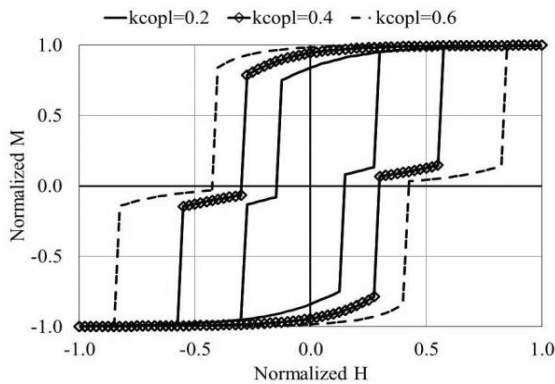


Fig. 6. Normalized scalar M - H curves along the x-axis corresponding to the triangle Tr_1 for $a = 3$, $c = 0.7$ and $k_{copl} = 0.2, 0.4, 0.6$.

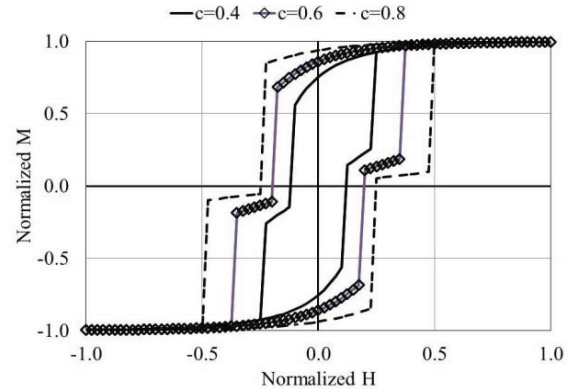


Fig. 7. Normalized scalar M - H curves along the x-axis corresponding to the triangle Tr_1 for $k_{copl} = 0.3$, $a = 3$ and $c = 0.4, 0.6, 0.8$.

III. VECTOR HYSTERESIS MODELING FOR ARBITRARILY SHAPED OBJECTS

As previously stated, any two-dimensional geometrical arbitrary shape may be approximated by an ensemble of triangular sub-regions. Obviously, no shape anisotropy is introduced for circular configurations. In order to demonstrate the applicability of the proposed approach, the circular geometrical configuration shown in Fig. 8 (a) is considered to fit experimentally measured hysteresis loop of an isotropic magnetic sample. More specifically, this circular configuration is assumed to be composed of an ensemble of 36 triangular sub-regions. Identification of the model is achieved through the determination of unknowns k_{copl} , c and a that result in best fit with the experimental data.

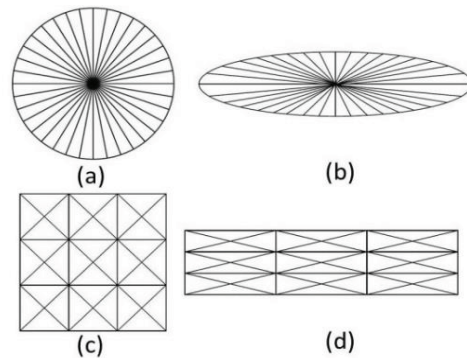


Fig. 8. Four geometrical configurations each comprising 36 triangular sub-regions and corresponding to: (a) a circle, (b) an ellipse, (c) a square, and (d) a rectangle.

For the case under consideration, the method of least square errors was utilized to carry out this process. As a result, values $k_{copl} = 0.38$, $a = 1.2$ and $c = 0.3$ were found to give the best possible qualitative and quantitative

fit for the experimentally measured loop as shown in Fig. 9. Rotational M - H curves of the overall ensemble demonstrating the expected isotropic nature is also shown in Fig. 10 (a). Moreover, a comparison between measured and computed M rotational component phase lag corresponding to different rotating H amplitudes is shown in Fig. 10 (b). This figure demonstrates the good qualitative and quantitative values achieved while using an extremely low number of hysteresis operators.

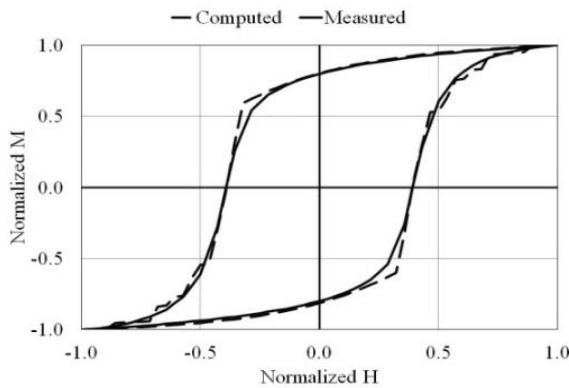


Fig. 9. Comparison between measured and computed hysteresis loop for the 36 triangular sub-region geometrical configuration shown in Fig. 8 (a) corresponding to $k_{copl} = 0.38$, $a = 1.2$ and $c = 0.3$.

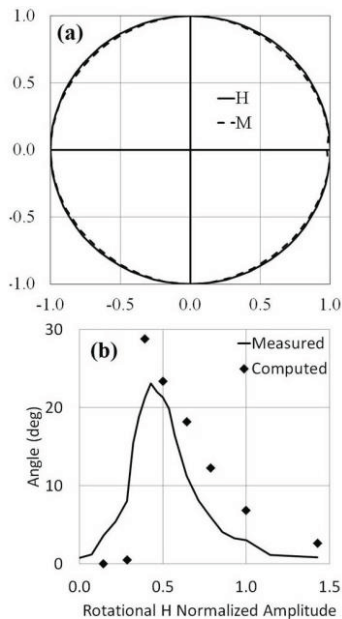


Fig. 10. (a) Rotational M - H curves for the geometrical configuration shown in Fig. 8 (a) and corresponding to $k_{copl} = 0.38$, $a = 1.2$ and $c = 0.3$, and (b) phase lag of M rotational components for different rotational H amplitudes.

In order to demonstrate the proposed approach ability to account for scalar and vector hysteresis properties variations as a result of introduced shape anisotropy, three additional geometrical configurations were considered. In specific, a square as well as a rectangle and an ellipse both having an aspect ratio of 4 were considered as shown in Figs. 8 (b)-(d).

For consistency purposes, each of these geometrical configurations was assumed to be comprised of 36 triangular sub-regions and to have the same overall unity area. Results given in Figs. 11-13 clearly suggest that the proposed approach could be successfully utilized in predicting overall hysteresis properties variations resulting from shape-introduced anisotropy. For instance, while the scalar hysteresis loop of a square object deviates from that of a circular object, loops along the x - and y -directions are identical. Nevertheless, square nature of the object may be easily inferred from its rotational M - H curve. On the other hand, the double aspect ratio assumed for each of the ellipsoidal and rectangular objects introduces an anisotropic behavior demonstrated by the clear deviation between generated scalar hysteresis loops along x - and y -directions. Scalar loops for the aforementioned two objects are not the same. This is also demonstrated by their different rotational M - H curves.

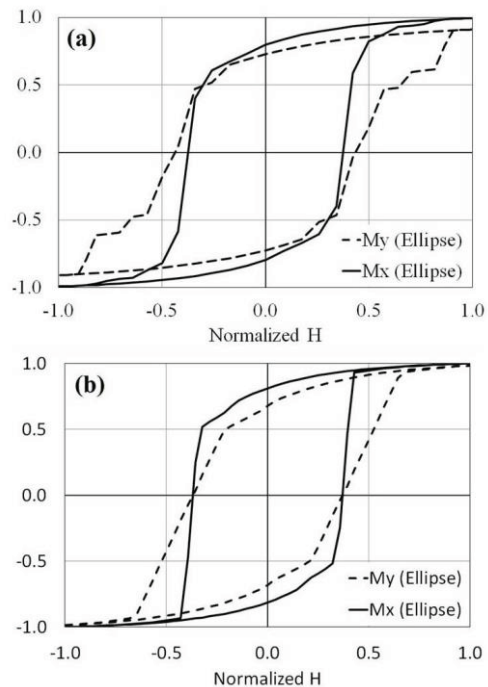


Fig. 11. Scalar M - H curves along the x - and y -axes corresponding to Fig. 8 (b) and computed using: (a) the proposed approach for $k_{copl} = 0.38$, $a = 1.2$ and $c = 0.3$, and (b) using standard demagnetization factors.

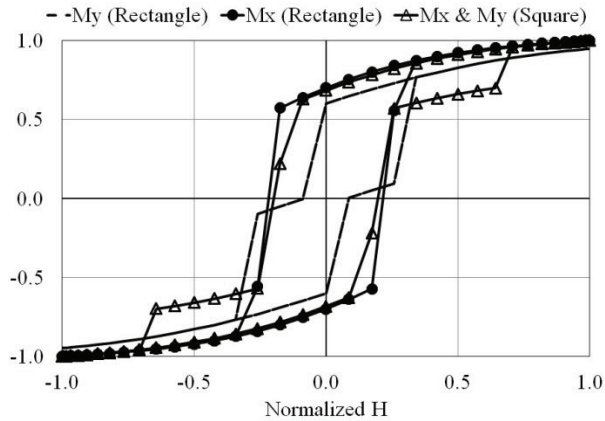


Fig. 12. Scalar M - H curves along the along the x - and y -axes corresponding to Figs. 8 (c)-(d) for $k_{copl} = 0.38$, $a=1.2$ and $c=0.3$.

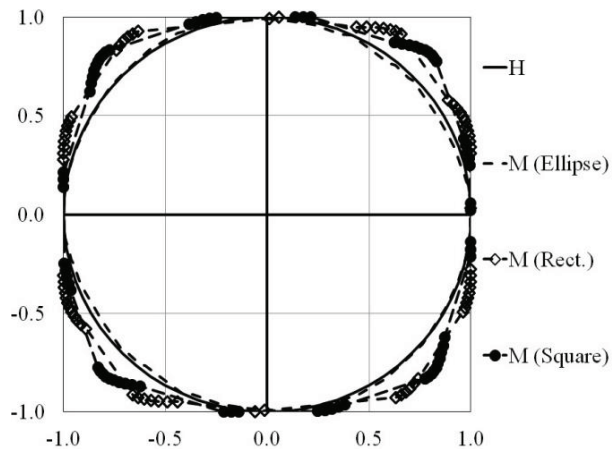


Fig. 13. Rotational M - H curves corresponding to Figs. 8 (b)-(d) for $k_{copl} = 0.38$, $a=1.2$ and $c=0.3$.

For a closer look at the total magnetization orientation for every triangular sub-region in each of the four geometrical configurations, please refer to Fig. 14. In this figure a snapshot of the above-mentioned magnetization magnitudes and orientations is shown for the instant when the applied field is maximum along the positive x -axis direction. Results given in this figure provide a somewhat detailed view of how individual triangular sub-region magnetizations tend to orient in the direction of the applied field. Those results are especially important as they demonstrate that local hysteresis losses may be accounted for and – by incorporating inter-domain interactions – could be extended for field computation purposes in media exhibiting hysteresis.

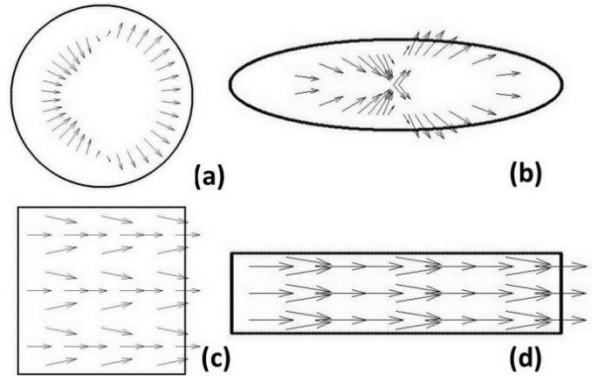


Fig. 14. Local magnetization magnitudes and orientations – on the triangular sub-region scale – corresponding to peak x -axis applied field for the regions shown in Fig. 8.

IV. CONCLUSIONS

It can be concluded from the previous analysis, discussion and results that a tunable efficient approach to mimic scalar and vector hysteresis properties in triangular sub-regions has been proposed. Using an ensemble of triangular sub-regions, it is demonstrated that the proposed approach may be successfully utilized in matching hysteresis properties of symmetrical bodies. It has also been shown that the proposed approach may be utilized to infer shape-anisotropy-introduced hysteresis properties variations. Given that the proposed approach may be utilized to determine the magnetization magnitude and orientation on the local triangular sub-region scale, it may be extended in the future for field computation applications in media exhibiting hysteresis.

REFERENCES

- [1] A. A. Adly and S. K. Abd-El-Hafiz, "Utilizing particle swarm optimization in the field computation of non-linear magnetic media," *Journal of the Applied Computational Electromagnetics Society*, vol. 18, no. 3, pp. 202-209, 2003.
- [2] A. Jacobus, "Nonlinear 3D numerical field calculation of a magnetic recording head," *IEEE Trans. Magn.*, vol. 24, no. 1, pp. 548-551, 1988.
- [3] G. Friedman and I. D. Mayergoyz, "Computation of magnetic field in media with hysteresis," *IEEE Trans. Magn.*, vol. 25, no. 5, pp. 3934-3936, 1989.
- [4] A. A. Adly, I. D. Mayergoyz, R. D. Gomez, and E. R. Burke, "Computation of fields in hysteretic media," *IEEE Trans. Magn.*, vol. 29, no. 6, pp. 2380-2382, 1993.
- [5] E. Dlala, A. Belahcen, K. A. Fonteyn, and M. Belkasim, "Improving loss properties of the Mayergoyz vector hysteresis model," *IEEE Trans.*

- Magn.*, vol. 46, no. 3, pp. 918-924, 2010.
- [6] A. A. Adly and S. K. Abd-El-Hafiz, "Identification and testing of an efficient Hopfield neural network magnetostriction model," *Journal of Magnetism and Magnetic Materials*, vol. 263, no. 3, pp. 301-306, 2003.
- [7] A. A. Adly and S. K. Abd-El-Hafiz, "Efficient implementation of vector Preisach-type models using orthogonally coupled hysteresis operators," *IEEE Trans. Magn.*, vol. 42, no. 5, pp. 1518-1525, 2006.
- [8] A. A. Adly and S. K. Abd-El-Hafiz, "Efficient implementation of anisotropic vector Preisach-type models using coupled step functions," *IEEE Trans. Magn.*, vol. 43, no. 6, pp. 2962-2964, 2007.
- [9] A. A. Adly and S. K. Abd-El-Hafiz, "Efficient vector hysteresis modeling using rotationally coupled step functions," *Physica-B: Condensed Matter*, vol. 407, no. 9, pp. 1350-1353, 2012.
- [10] A. A. Adly and S. K. Abd-El-Hafiz, "Efficient modeling of vector hysteresis using a novel Hopfield neural network implementation of Stoner-Wohlfarth-like operators," *Elsevier Journal of Advanced Research*, vol. 4, no. 4, pp. 403-409, 2013.
- [11] K. Mehrotra, C. K. Mohan, and S. Ranka, *Elements of Artificial Neural Networks*, MIT Press, Cambridge, MA, 1997.
- [12] S. Haykin, *Neural Networks: A Comprehensive Foundation*, Prentice-Hall, Englewood Cliffs, NJ, 1999.
- [13] R. M. Bozorth, *Ferromagnetism*, IEEE Press, New York, 1993.



Amr A. Adly received the B.S. and M.S. degrees in Electrical Power Engineering from Cairo University (CU) in 1984 and 1986, respectively, and the Ph.D. degree in Electrical Engineering from the University of Maryland (UM), College Park, USA, in 1992. He also worked as a Magnetic Measurement Instrumentation Senior Scientist at LDJ Electronics, Michigan, USA, during 1993-1994.

Since 1994, he has been a Faculty Member in the Faculty of Engineering, CU. He also worked in the US as a Visiting Research Prof. at UM, during the summers of 1996-2000. He worked in the period 2003-2004 as a Consultant to the UNESCO Cairo office and in 2006 as an Expert to the EU Commission. He also established and directed the R&D Administration at the Egyptian Industrial Modernization Center in the period 2006-2007. He served as the CU's Faculty of Engineering Vice

Dean in the period 2010-2014. Since July 2014 he has been appointed as the Executive Director of the Science and Technology Development Fund (STDF).

Adly has published more than 120 reviewed papers and holds one U.S. patent. He also served for more than 10 years as a Member of the IEEE Magnetics Society Technical Committee. He reviewed more than 200 papers for international reputable journals, acted as the PI of several international research projects and supervised more than 15 Ph.D. and M.S. students. His research interests include electromagnetic field computation, magnetic materials, superconductivity, energy harvesting, magneto-hydro-dynamics, magnetic recording and power engineering.

Adly has been awarded the 1994 Egyptian State Encouragement Prize, the 2002 Shoman Foundation Young Arab Scientist Prize and the 2006 Egyptian State Excellence Prize. He has been promoted to IEEE Fellow status in 2011 and is currently serving in the Editorial Board of IEEE Transactions on Magnetics and Elsevier's Journal of Advanced Research.



Salwa K. Abd-El-Hafiz received the B.Sc. degree in Electronics and Communication Engineering from Cairo University, Egypt, in 1986 and the M.S. and Ph.D. degrees in Computer Science from the University of Maryland, College Park, Maryland, USA, in 1990 and 1994, respectively.

Since 1994, she has been working as a Faculty Member in the Engineering Mathematics and Physics Department, Faculty of Engineering, Cairo University, and has been promoted to a Full Professor in the same department in 2004. Since August 2014, she has also been working as the Director of the Technical Center for Career Development, Cairo University, Egypt. She co-authored one book, contributed one chapter to another book and published more than 60 refereed papers. Her research interests include software engineering, computational intelligence, numerical analysis, chaos theory and fractal geometry.

Abd-El-Hafiz is a recipient of the 2001 Egyptian State Encouragement Prize in Engineering Sciences, recipient of the 2012 National Publications Excellence Award from the Egyptian Ministry of Higher Education, recipient of the 2014 African Union Kwame Nkrumah Regional Scientific Award for Women in Basic Science, Technology and Innovation, recipient of several international publications awards from Cairo University and an IEEE Senior Member.

Generalized Spectral Decomposition Approach to a Stochastic Finite Integration Technique Electrokinetic Formulation

Lorenzo Codecasa and Luca Di Rienzo

Dipartimento di Elettronica, Informazione e Bioingegneria
Politecnico di Milano, Milano, I-20133, Italy
lorenzo.codecasa@polimi.it, luca.dirienzo@polimi.it

Abstract — In order to efficiently solve the stochastic finite integration technique formulation for electrokinetics, a recently proposed generalized spectral decomposition approach is applied. Compared to the standard approach, the proposed method drastically reduces the computational burden. The results are validated by comparison with those obtained with high order polynomial chaos expansion, taken as the reference solution.

Index Terms — Electrokinetics, finite integration technique, polynomial chaos expansion, resistance welding, uncertainty quantification.

I. INTRODUCTION

The spectral stochastic finite element method (FEM) [1] based on the polynomial chaos expansion (PCE) is a well-established method and has been applied to various electromagnetic problems, e.g., [2]. In order to take advantages of the finite integration technique (FIT), a well-known alternative to the FEM, in [3] the authors presented its spectral stochastic formulation in the case of a prototype problem of electrokinetics type.

The approach in [3] exhibits large computational costs both in the storage requirements and in execution time, due to the large dimensions of the linear systems to be constructed and solved. In order to alleviate these drawbacks, in this paper the benefits of a generalized spectral decomposition approach to the stochastic FIT formulation are shown. Such approach, based on [4], allows to reduce the storage requirement to that of about one deterministic problem and the computational complexity of about one order of magnitude.

These results are validated considering a simplified geometry of a typical system for resistance welding [2, 3]. Here, three aluminium electrodes over a conductive aluminium substrate are considered. The three contact resistances are modelled as sheets of depth equal to d and conductivities σ_1 , σ_2 , and σ_3 . The conductivity of aluminium is indicated with σ_4 . Only the conductive region is discretized. Voltages V_1 , V_2 , and V_3 are imposed as Dirichlet boundary conditions and the three currents I_1 , I_2 , and I_3 are computed from the field solution.

Submitted On: February 24, 2015
Accepted On: November 8, 2015

II. DETERMINISTIC FIT FORMULATION

The stochastic FIT formulation starts from a deterministic FIT formulation, derived discretizing the spatial region of the problem Ω by a pair of three-dimensional oriented dual grids, \mathcal{G} and $\tilde{\mathcal{G}}$. In order to manage boundary conditions, following [5] *unlike* standard FIT, the pair of two-dimensional oriented dual grids, \mathcal{G}_b and $\tilde{\mathcal{G}}_b$ are also introduced, where \mathcal{G}_b is the trace of the primal grid \mathcal{G} onto the boundary $\partial\Omega$ of Ω and $\tilde{\mathcal{G}}_b$ is its dual. The continuity law for currents is discretized, in exact form, as:

$$\tilde{\mathbf{D}}\tilde{\mathbf{i}} + \tilde{\mathbf{D}}_b\tilde{\mathbf{i}}_b = \mathbf{0}, \quad (1)$$

in which $\tilde{\mathbf{i}}$ and $\tilde{\mathbf{i}}_b$ are the vectors of the fluxes of the electric current through the faces of $\tilde{\mathcal{G}}$ and $\tilde{\mathcal{G}}_b$ respectively, $\tilde{\mathbf{D}}$ is the volume-face incidence matrix of $\tilde{\mathcal{G}}$ and $\tilde{\mathbf{D}}_b$ is the incidence matrix between the volumes of $\tilde{\mathcal{G}}$ and the faces of $\tilde{\mathcal{G}}_b$.

The irrotationality of the electric field is expressed, in exact form, as:

$$\mathbf{v} = -\mathbf{G}\boldsymbol{\varphi}, \quad (2)$$

in which \mathbf{v} is the vector with the circulations of the electric field along the edges of \mathcal{G} , $\boldsymbol{\varphi}$ is the vector of the electric potentials at the nodes of \mathcal{G} and \mathbf{G} is the edge-node incidence matrix of \mathcal{G} . As it is well known [5-7], for any pair of dual grids $-\mathbf{G}^T = \tilde{\mathbf{D}}$.

Ohm's law, relating the electric field to the electric current density by means of the electric conductivity σ , assumed to be strictly positive, is discretized in approximate form by means of a discrete material matrix \mathbf{M}_σ , as:

$$\tilde{\mathbf{i}} = \mathbf{M}_\sigma\mathbf{v}. \quad (3)$$

The discrete material matrix \mathbf{M}_σ is assumed to be derived using the energetic approach introduced in [6] for a tetrahedral grid and extended in [7] for generic polyhedral grids. As detailed in [6], in this way this matrix is *symmetric* and *positive definite*. In usual electrokinetics problems it can be assumed that the electric conductivity is uniform and equal to σ_k in each subregion Ω_k composed of a distinct material. As a result, the discrete constitutive matrix takes the form:

$$\mathbf{M}_\sigma = \sum_{k=1}^K \sigma_k \mathbf{M}_k. \quad (4)$$

Lastly boundary conditions are introduced. For a Dirichlet problem, here considered for the sake of simplicity, such conditions can be written in exact form in terms of the incidence matrix $\tilde{\mathbf{D}}_b$ as follows [5]:

$$\tilde{\mathbf{D}}_b^T \boldsymbol{\varphi} = \boldsymbol{\varphi}_b, \quad (5)$$

in which $\boldsymbol{\varphi}_b$ is the vector of the electric potential on the boundary $\partial\Omega$, hence assumed known.

After grouping the unknown electric potentials at the nodes of \mathcal{G} , *not* belonging to \mathcal{G}_b , in the $N \times 1$ vector \mathbf{u} , it can be written:

$$\boldsymbol{\varphi} = \tilde{\mathbf{D}}_b^- \mathbf{u} + \tilde{\mathbf{D}}_b \boldsymbol{\varphi}_b,$$

in which $\tilde{\mathbf{D}}_b^-$ is the matrix mapping the electric potentials of \mathbf{u} onto the electric potentials of $\boldsymbol{\varphi}$. Then eliminating all variables different from \mathbf{u} , (1)-(3), (5) can be reduced to the form:

$$\mathbf{A}\mathbf{u} = \mathbf{b}, \quad (6)$$

in the unknown \mathbf{u} , in which

$$\begin{aligned} \mathbf{A} &= \tilde{\mathbf{D}}_b^T \mathbf{G}^T \mathbf{M}_\sigma \mathbf{G} \tilde{\mathbf{D}}_b^-, \\ \mathbf{b} &= -\tilde{\mathbf{D}}_b^T \mathbf{G}^T \mathbf{M}_\sigma \mathbf{G} \tilde{\mathbf{D}}_b \boldsymbol{\varphi}_b. \end{aligned}$$

In case (4) holds, (6) takes the simplified form:

$$\sum_{k=1}^K \sigma_k \mathbf{A}_k \mathbf{u} = \sum_{k=1}^K \sigma_k \mathbf{b}_k,$$

in which

$$\begin{aligned} \mathbf{A}_k &= \tilde{\mathbf{D}}_b^T \mathbf{G}^T \mathbf{M}_k \mathbf{G} \tilde{\mathbf{D}}_b^-, \\ \mathbf{b}_k &= -\tilde{\mathbf{D}}_b^T \mathbf{G}^T \mathbf{M}_k \mathbf{G} \tilde{\mathbf{D}}_b \boldsymbol{\varphi}_b. \end{aligned}$$

As a consequence of the symmetric, positive definite properties of the discrete material matrix \mathbf{M}_σ , also matrix \mathbf{A} is symmetric, positive definite. Thus, robust sparse numerical methods for symmetric positive definite matrices, both direct and iterative, can be used for solving (6).

III. STOCHASTIC FIT FORMULATION

The electric conductivity is now assumed to depend on a small number Q of random variables ξ_1, \dots, ξ_Q , that can be assumed to be statistically independent and to form a vector $\boldsymbol{\xi} = [\xi_q]$. As a result the constitutive matrix (4) depends on $\boldsymbol{\xi}$ and is indicated by $\mathbf{M}_\sigma(\boldsymbol{\xi})$. Hence, also the coefficient matrix, the right hand vector and unknowns in (6) depend on $\boldsymbol{\xi}$ so that it can be written:

$$\mathbf{A}(\boldsymbol{\xi})\mathbf{u}(\boldsymbol{\xi}) = \mathbf{b}(\boldsymbol{\xi}). \quad (7)$$

A PCE can now be used to approximate the unknown vector $\mathbf{u}(\boldsymbol{\xi})$ in the form:

$$\mathbf{u}(\boldsymbol{\xi}) = \sum_{|\alpha| \leq P} \mathbf{u}_\alpha \psi_\alpha(\boldsymbol{\xi}), \quad (8)$$

in which $\boldsymbol{\alpha} = (\alpha_1, \dots, \alpha_Q)$ are multi-indices of q elements, $|\alpha| = \alpha_1 + \alpha_2 + \dots + \alpha_Q$ and

$$\psi_\alpha(\boldsymbol{\xi}) = \psi_{\alpha_1}^1(\xi_1) \psi_{\alpha_2}^2(\xi_2) \dots \psi_{\alpha_Q}^Q(\xi_Q),$$

where $\psi_j^q(\xi_q)$, with $j = 0, 1, \dots, P$, are polynomials of degree not greater than P , forming an orthonormal basis in the probability space of random variable ξ_q , with $q = 1, \dots, Q$. Thus, the functions $\psi_\alpha(\boldsymbol{\xi})$ are polynomials of degrees not greater than P , forming a basis of dimension:

$$M = \binom{P+Q}{P}, \quad (9)$$

which is orthonormal in the probability space of random vector $\boldsymbol{\xi}$. Equivalently, by defining the column vector $\boldsymbol{\psi}(\boldsymbol{\xi}) = [\psi_\alpha(\boldsymbol{\xi})]$ and the $N \times M$ matrix $\mathbf{U} = [\mathbf{u}_\alpha]$, obtained by juxtaposing \mathbf{u}_α in lexicographic order, it can be written:

$$\mathbf{u}(\boldsymbol{\xi}) = \mathbf{U}\boldsymbol{\psi}(\boldsymbol{\xi}). \quad (10)$$

The spectral stochastic FIT equations are achieved by substituting (10) into (7), multiplying both members on the right by $\boldsymbol{\psi}^T(\boldsymbol{\xi})$ and taking the expected value $E[\cdot]$, so that it results in:

$$E[(\mathbf{A}(\boldsymbol{\xi})\mathbf{U}\boldsymbol{\psi}(\boldsymbol{\xi}) - \mathbf{b}(\boldsymbol{\xi}))\boldsymbol{\psi}^T(\boldsymbol{\xi})] = \mathbf{0}. \quad (11)$$

Using the $\text{vec}(\cdot)$ operator [8], (11) can be written as:

$$\mathcal{A}\mathbf{U} = \mathbf{B}, \quad (12)$$

a linear system of MN equations in the MN unknowns forming column vector $\mathbf{U} = \text{vec}(\mathbf{U})$. The coefficient matrix \mathcal{A} and right-hand vector \mathbf{B} of this system of equations can be written respectively in the form:

$$\begin{aligned} \mathcal{A} &= E[\boldsymbol{\psi}(\boldsymbol{\xi})\boldsymbol{\psi}^T(\boldsymbol{\xi}) \otimes \mathbf{A}(\boldsymbol{\xi})] = \\ &= (\mathbf{1}_n \otimes \tilde{\mathbf{D}}_b^T \mathbf{G}^T) E[\boldsymbol{\psi}(\boldsymbol{\xi})\boldsymbol{\psi}^T(\boldsymbol{\xi}) \otimes \mathbf{M}_\sigma(\boldsymbol{\xi})] (\mathbf{1}_n \otimes \mathbf{G} \tilde{\mathbf{D}}_b^-), \\ \mathbf{B} &= E[\boldsymbol{\psi}(\boldsymbol{\xi}) \otimes \mathbf{b}(\boldsymbol{\xi})] = \\ &= -(\mathbf{1}_n \otimes \tilde{\mathbf{D}}_b^T \mathbf{G}^T) E[\boldsymbol{\psi}(\boldsymbol{\xi}) \otimes \mathbf{M}_\sigma(\boldsymbol{\xi})] (\mathbf{1}_n \otimes \mathbf{G} \tilde{\mathbf{D}}_b \boldsymbol{\varphi}_b). \end{aligned}$$

being \otimes the tensor product.

In case (4) holds, (11) and (12) can be respectively written in the simplified forms:

$$\begin{aligned} \sum_{k=1}^K \mathbf{A}_k \mathbf{U} \mathbf{S}_k &= \sum_{k=1}^K \mathbf{b}_k \mathbf{e}_1^T \mathbf{S}_k, \\ (\sum_{k=1}^K \mathbf{S}_k \otimes \mathbf{A}_k) \mathbf{U} &= \sum_{k=1}^K \mathbf{S}_k \mathbf{e}_1 \otimes \mathbf{b}_k, \end{aligned}$$

being

$$\mathbf{S}_k = E[\sigma_k(\boldsymbol{\xi})\boldsymbol{\psi}(\boldsymbol{\xi})\boldsymbol{\psi}^T(\boldsymbol{\xi})].$$

a symmetric positive definite matrix and being \mathbf{e}_1 the $M \times 1$ vector with all zeros except the first element equal to one.

As a consequence of the symmetric, positive definite properties of the discrete material matrix \mathbf{M}_σ , the coefficient matrix of (12) is symmetric, positive definite. Thus, also for problem (12), the robust sparse numerical methods specific for symmetric positive definite matrices, both direct and iterative can be used. However, as with stochastic FEM, difficulties arise with the solution of this system of equations when the number of independent random variables Q and PCE order P increase, due to the increased dimensionality MN of the problem, as a consequence of (9).

IV. GENERALIZED SPECTRAL DECOMPOSITION

An iterative approach, recently proposed in literature [4], is here adapted to approximate the solution of (12). In this approach, given at step $j-1$ an approximation for $\mathbf{u}(\boldsymbol{\xi})$ in a form analogous to (10),

$$\mathbf{u}_{j-1}(\boldsymbol{\xi}) = \mathbf{U}_{j-1}\boldsymbol{\psi}(\boldsymbol{\xi}), \quad (13)$$

a new approximation $\mathbf{u}_j(\boldsymbol{\xi})$ is obtained as:

$$\mathbf{u}_j(\boldsymbol{\xi}) = \mathbf{u}_{j-1}(\boldsymbol{\xi}) + \sum_{r=1}^R \mathbf{w}_r \lambda_r(\boldsymbol{\xi}), \quad (14)$$

in which a number $R \ll M$ of $N \times 1$ vectors \mathbf{w}_r are searched for together with a number R of functions $\lambda_r(\xi)$ belonging to the space spanned by the $\psi_\alpha(\xi)$ functions expressed as:

$$\lambda_r(\xi) = \sum_{|\alpha| \leq P} l_{r\alpha} \psi_\alpha(\xi), \quad (15)$$

in which $l_{r\alpha}$ are coefficients. Let $\boldsymbol{\lambda}(\xi) = [\lambda_r(\xi)]$ be an $R \times 1$ vector. Also let $\mathbf{W} = [\mathbf{w}_r]$ be an $N \times R$ matrix and let it be $\mathbf{L} = [l_{r\alpha}]$ an $R \times M$ matrix so that $\boldsymbol{\lambda}(\xi) = \mathbf{L}\boldsymbol{\psi}(\xi)$ and (13) can be rewritten in the form:

$$\mathbf{u}_j = \mathbf{u}_{j-1} + \mathbf{W}\mathbf{L}, \quad (16)$$

$$\mathbf{u}_j(\xi) = \mathbf{u}_j\boldsymbol{\psi}(\xi), \quad (17)$$

in which \mathbf{W} and \mathbf{L} have to be determined. In order to compute \mathbf{W} and \mathbf{L} , an iterative procedure is adopted. Precisely, assuming that \mathbf{W} is known, \mathbf{L} is computed by solving the equations obtained substituting (16) into (11) and multiplying on the left by \mathbf{W}^T ,

$$\mathbf{W}^T E[(\mathbf{A}(\xi)(\mathbf{u}_{j-1} + \mathbf{W}\mathbf{L})\boldsymbol{\psi}(\xi) - \mathbf{b}(\xi))\boldsymbol{\psi}^T(\xi)] = 0. \quad (18)$$

After applying the $\text{vec}(\cdot)$ operator, this equation is written in the form of the system of RM equations:

$$E[\boldsymbol{\psi}(\xi)\boldsymbol{\psi}^T(\xi) \otimes \mathbf{W}^T \mathbf{A}(\xi) \mathbf{W}] \mathbf{L} = E[\boldsymbol{\psi}(\xi) \otimes \mathbf{W}^T \mathbf{b}(\xi)] - E[\boldsymbol{\psi}(\xi)\boldsymbol{\psi}^T(\xi) \otimes \mathbf{W}^T \mathbf{A}(\xi)] \mathbf{u}_{j-1}, \quad (19)$$

in the RM unknowns forming the column vector $\mathbf{L} = \text{vec}(\mathbf{L})$. In case (4) holds, Equations (18) and (19) can be respectively rewritten in the simplified forms:

$$\begin{aligned} \sum_{k=1}^K \mathbf{W}^T \mathbf{A}_k \mathbf{W} \mathbf{L} \mathbf{S}_k &= \sum_{k=1}^K \mathbf{W}^T \mathbf{b}_k \mathbf{e}_1^T \mathbf{S}_k - \\ \sum_{k=1}^K \mathbf{W}^T \mathbf{A}_k \mathbf{u}_{j-1} \mathbf{S}_k, & \quad (20) \\ (\sum_{k=1}^K \mathbf{S}_k \otimes \mathbf{W}^T \mathbf{A}_k \mathbf{W}) \mathbf{L} &= \sum_{k=1}^K \mathbf{S}_k \mathbf{e}_1 \otimes \mathbf{W}^T \mathbf{b}_k + \\ -(\sum_{k=1}^K \mathbf{S}_k \otimes \mathbf{W}^T \mathbf{A}_k) \mathbf{u}_{j-1}. & \quad (21) \end{aligned}$$

Then, assuming \mathbf{L} to be known, \mathbf{W} is computed by solving the equations obtained substituting (16) into (11), multiplying on the right by \mathbf{L}^T and using that $\boldsymbol{\lambda}^T(\xi) = \boldsymbol{\psi}^T(\xi)\mathbf{L}^T$, so that

$$E[(\mathbf{A}(\xi)(\mathbf{u}_{j-1} + \mathbf{W}\mathbf{L})\boldsymbol{\psi}(\xi) - \mathbf{b}(\xi))\boldsymbol{\lambda}^T(\xi)] = 0. \quad (22)$$

After applying the $\text{vec}(\cdot)$ operator, this equation is written in the form of the system of RN equations:

$$E[\mathbf{L}\boldsymbol{\psi}(\xi)\boldsymbol{\psi}^T(\xi)\mathbf{L}^T \otimes \mathbf{A}(\xi)] \mathbf{W} = E[\mathbf{L}\boldsymbol{\psi}(\xi) \otimes \mathbf{b}(\xi)] + E[\boldsymbol{\psi}(\xi)\boldsymbol{\psi}^T(\xi)\mathbf{L}^T \otimes \mathbf{A}(\xi)] \mathbf{u}_{j-1}, \quad (23)$$

in the RN variables forming the column vector $\mathbf{W} = \text{vec}(\mathbf{W})$. In case (4) holds, Equations (22) and (23) can be respectively rewritten in the forms:

$$\begin{aligned} \sum_{k=1}^K \mathbf{A}_k \mathbf{W} \mathbf{L} \mathbf{S}_k \mathbf{L}^T &= \sum_{k=1}^K \mathbf{b}_k \mathbf{e}_1^T \mathbf{S}_k \mathbf{L}^T - \\ \sum_{k=1}^K \mathbf{A}_k \mathbf{u}_{j-1} \mathbf{S}_k \mathbf{L}^T, & \quad (24) \end{aligned}$$

$$\begin{aligned} (\sum_{k=1}^K \mathbf{L} \mathbf{S}_k \mathbf{L}^T \otimes \mathbf{A}_k) \mathbf{W} &= \sum_{k=1}^K \mathbf{L} \mathbf{S}_k \mathbf{e}_1 \otimes \mathbf{b}_k + \\ -(\sum_{k=1}^K \mathbf{L} \mathbf{S}_k \mathbf{L}^T \otimes \mathbf{A}_k) \mathbf{u}_{j-1}. & \quad (25) \end{aligned}$$

Equations (21), (23) are iteratively solved until convergence of $\mathbf{W}\mathbf{L}$ in the energy norm. This procedure can be stopped after S iterations, typically in the range $1 \div 4$ [4]. The whole procedure is then repeated, increasing j until the residual of (12) when $\mathbf{U} = \mathbf{u}_j$ is less than a tolerance, as detailed in Algorithm 1.

Algorithm 1: Approximation of \mathbf{U}

```

Set  $i := 0$ 
Set  $j := 0$ 
Set  $\mathbf{u}_j := 0$ 
repeat
  Set  $j := j + 1$ 
  Choose  $\mathbf{L}$  randomly
  repeat  $S$  times
    Set  $i := i + 1$  (total number of iterations)
    Orthonormalize rows of  $\mathbf{L}$ 
    Solve (25) for  $\mathbf{W} = \text{vec}(\mathbf{W})$ .
    Orthonormalize columns of  $\mathbf{W}$ 
    Solve (21) for  $\mathbf{L} = \text{vec}(\mathbf{L})$ 
  end
  Update  $\mathbf{u}_j$  by (16)
until convergence

```

For each step i Algorithm 1 requires the solutions of the systems of RM Equation (24) and the solutions of the systems of RN Equation (20). Since the coefficient matrices of these problems are ensured to be symmetric, positive definite, the same robust numerical methods for solving the deterministic problems, both direct and iterative, can be used.

Using iterative methods the coefficient matrix is not directly constructed, but the product of the coefficient matrix with column vectors are computed. Since (20) and (21) are equivalent, the left-hand-side of (21) can be more efficiently computed as:

$$\text{vec}(\sum_{k=1}^K \mathbf{W}^T \mathbf{A}_k \mathbf{W} \mathbf{L} \mathbf{S}_k).$$

Similarly since (24) and (25) are equivalent, the left-hand-side of (25) can be more efficiently computed as:

$$\text{vec}(\sum_{k=1}^K \mathbf{A}_k \mathbf{W} \mathbf{L} \mathbf{S}_k \mathbf{L}^T).$$

In order to reduce computational complexity, while maintaining satisfactory convergence properties, small values of R are chosen. While in [4] only the case $R=1$ is considered, here it is shown that small values of R greater than 1 can be more effective choices. It is noted that for small numbers Q of random variables and relatively low PCE orders P , as in the cases considered here, M is usually much smaller than N , so that the only computationally demanding problem is problem (25) in RN variables. The orthonormalization of the rows of \mathbf{L} and of the columns of \mathbf{W} is performed in order to ensure robustness, as detailed in [4].

V. NUMERICAL RESULTS

The 3D problem shown in Fig. 1 is chosen as a test case. Conductivities σ_1 , σ_2 , and σ_3 are modelled as uniformly distributed random variables, in the range 1.41 MS/m – 11.3 MS/m. Voltages are imposed with values $V_1=V_3= 1$ V and $V_2=0$. Only the conductive region, without the surrounding air region, is discretized.

Homogeneous Neumann’s boundary conditions are used everywhere, with the exception of the three electrodes at which Dirichlet’s boundary conditions are used, as indicated in Fig. 1.

A set of primal tetrahedral grids is generated. Among these a tetrahedral grid with $n=6441$ nodes is chosen whose further refining introduces variations in the potential distribution lesser than 1% in the energy norm. The energetic approach to FIT is used for constructing discrete material matrices. In particular, the basis functions introduced in [6] for tetrahedral grids are adopted.

The PCE of the electric current I_1 is estimated in the case $P=7$. In the PCE intrusive approach the computational time for solving (12) by the Conjugate Gradient (CG) algorithm is about 152 s on a 2.3 GHz Intel Core i7 with tolerance equal to 10^{-9} . Memory storage requirement is about 120 MB.

In Fig. 2, the probability density function (pdf) of the current I_1 computed following the GSD approach (Algorithm 1) and the one obtained with the standard PCE intrusive approach are compared. In [3] the computation of the same pdf is carried out in about 10 hours by means of 10^5 Monte Carlo simulations using the same computer, validating previous results. A good agreement among the three methods is observed.

The convergence of the approximations to the solution U provided by Algorithm 1 for various choices of R and S is shown in Figs. 3-8, when the relative error is defined as:

$$error = \frac{\|U_{j-1} - U\|}{\|U\|}. \quad (22)$$

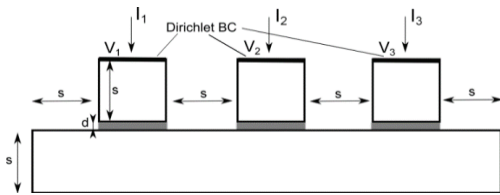


Fig. 1. 2D section of the test case. Depth is equal to s , with $s=10$ mm and $d=1$ mm.

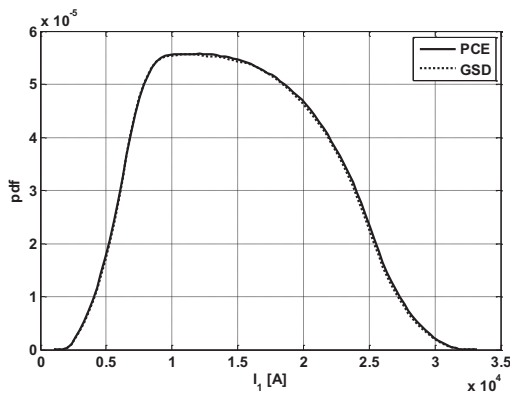


Fig. 2. Probability density function of the current I_1 .

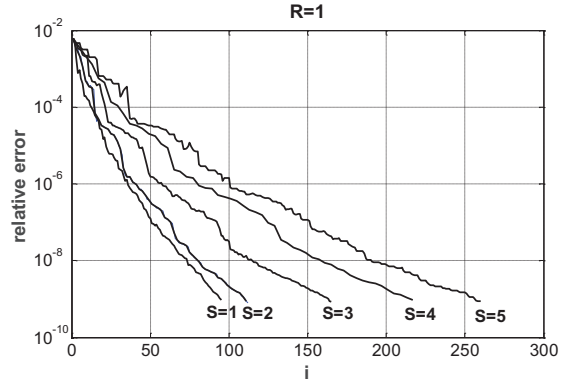


Fig. 3. Relative error (22) vs. number of iterations i of Algorithm 1 when $R=1$, for different values of S .

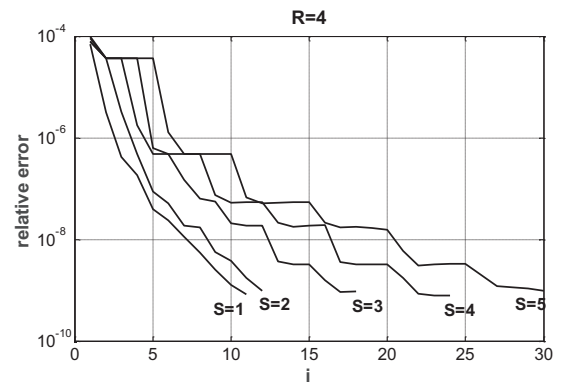


Fig. 4. Relative error vs. number of iterations i when $R=4$, for different values of S .

From these results it follows that for each choice of R the best results in terms of efficiency are obtained for $S=1$; furthermore $R=4$ appears as the optimal value. The computational times for this case ($S=1$ and $R=4$) are reported in Figs. 6-7. The corresponding memory storage requirement is about 1.5 MB, comparable to the 1.3 MB memory storage requirement of a single deterministic electrokinetic problem.

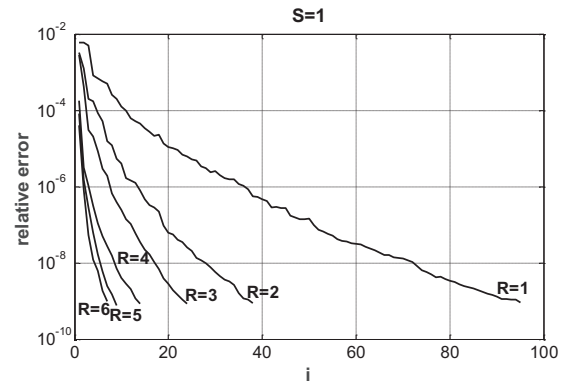


Fig. 5. Relative error vs. number of iterations i when $S=1$, for different values of R .

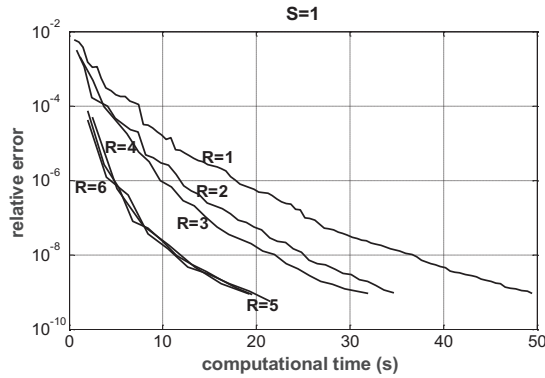


Fig. 6. Relative error vs. computational time of Algorithm 1 when $S=1$, for different values of R .

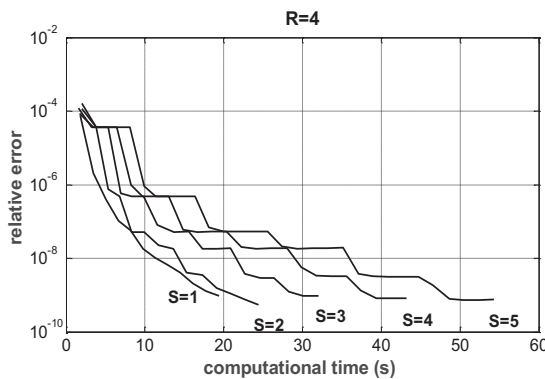


Fig. 7. Relative error vs. computational time of Algorithm 1 when $R=4$, for different values of S .

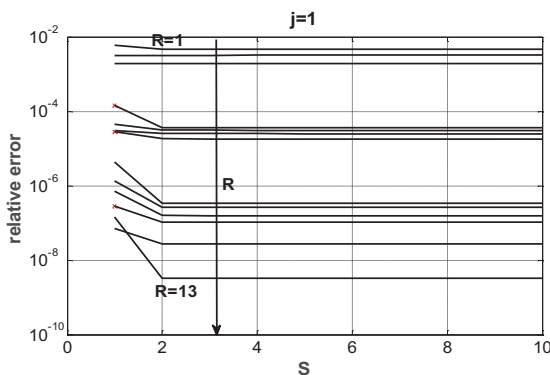


Fig. 8. Relative error for increasing values of R when $j=1$.

VI. CONCLUSION

In this paper it is shown how a generalized spectral decomposition approach can be applied to the spectral stochastic formulation of FIT based on PCE. As an application example, a typical system for resistance welding is analyzed. The results show that the proposed approach allows to drastically reduce the storage requirement and the computational time of the spectral stochastic formulation of FIT based on PCE.

REFERENCES

- [1] D. Xiu, *Numerical Methods for Stochastic Computations: A Spectral Method Approach*, Princeton University Press, 2010.
- [2] S. Clenet and N. Ida, "Error estimation in a stochastic finite element method in electrokinetics," *International Journal for Numerical Methods in Engineering*, vol. 81, no. 11, pp. 1417-1438, 2010.
- [3] L. Codecasa and L. Di Rienzo, "Stochastic finite integration technique formulation for electrokinetics," *IEEE Trans. on Magn.*, vol. 50, no. 2, pp. 573-576, 2014.
- [4] A. Nouy, "A generalized spectral decomposition technique to solve a class of linear stochastic partial differential equations," *Comput. Methods Appl. Mech. Eng.*, vol. 196, pp. 4521-4537, 2007.
- [5] L. Codecasa, "Refoundation of the cell method by means of augmented dual grids," *IEEE Trans. on Magn.*, vol. 50, no. 2, 2014.
- [6] L. Codecasa, V. Minerva, and M. Politi, "Use of barycentric dual grids for the solution of frequency domain problems by FIT," *IEEE Trans. on Magn.*, vol. 40, no. 2, pp. 1414-1419, 2004.
- [7] L. Codecasa, R. Specogna, and F. Trevisan, "A new set of basis functions for the discrete geometric approach," *Journal of Computational Physics*, vol. 229, no. 19, pp. 7401-7410, 2010.
- [8] J. R. Magnus and Heinz Neudecker, *Matrix Differential Calculus with Applications in Statistics and Econometrics*, 2nd Ed., Wiley, 1999.



Lorenzo Codecasa received the M.S. ("cum laude") degree and the Ph.D. degree from Politecnico di Milano, Milan, Italy, both in Electronics Engineering. He is currently with the Department of Electronics, Information, and Bioengineering, Politecnico di Milano, Milan, Italy, as an Associate Professor. His research interests include electro-thermal circuit modeling and simulation and electromagnetic simulation.



Luca Di Rienzo received the M.S. degree (cum laude) and the Ph.D. degrees in Electrical Engineering from Politecnico di Milano, in 1996 and 2001 respectively. From November 2000 to December 2004 he was a Research Assistant with the Department of Electrical Engineering of Politecnico di Milano. In 2005 he became Assistant Professor with the same department (now

named Department of Electronics, Information, and Bioengineering) where since 2015 he has been Associate Professor. At present his research interests are surface

impedance boundary conditions and uncertainty quantification in computational electromagnetics.

Efficient Representation of Multilevel QR Algorithm for Analysis of Microstrip Structures

Zhaoneng Jiang^{1,3} and Ting Wan^{2,3}

¹Hefei University of Technology, Hefei 230009
jiangzhaoneng@hfut.edu.cn

²Nanjing University of Posts and Telecommunications, Nanjing 210003
want@njupt.edu.cn

³State Key Laboratory of Millimeter Waves, Nanjing 210096

Abstract — This paper presents a novel approach for the efficient solution of large-scale microstrip structures with the mixed potential integral equation (MPIE) in conjunction with the method of moments (MoM) based on the conventional Rao-Wilton-Glisson (RWG) basis functions. Although multilevel QR (MLQR) is efficient compared with direct method, it consumes more computation time and storage memory. A novel matrix compression technique is presented to recompress the sub-matrices of MLQR algorithm. The advantages of applying the novel recompression technique are illustrated by numerical results, the computation time as well as the memory requirements are compared to the conventional MLQR algorithm and the matrix decomposition algorithm-singular value decomposition (MDA-SVD). It is demonstrated that the use of proposed method can result in significant savings in computation time and memory requirements, with little or no compromise in the accuracy of the solution.

Index Terms — Compression techniques, microstrip structure, Multilevel QR Algorithm (MLQR).

I. INTRODUCTION

The method of moments (MoM) [1-5] has been widely used for the analysis of microstrip structures. The first kind is the spectral domain MoM which has been used to analyze the electromagnetic problems in [3]. The second kind is the spatial domain MoM which is proposed by Michalski and Hsu in [4] for scattering by microstrip patch antennas in a multilayered medium. However, the conventional MoM using subsectional basis functions and $\lambda/10$ discretization becomes highly inefficient for the analysis of large-scale microstrip structures. This is because the size of the associated MoM matrix grows very rapidly as the dimensions become large in terms of the wavelength, or a fine mesh

is used to model a complex structure to guarantee good solution accuracy, and this in turn places an inordinately heavy burden on the CPU in terms of both memory requirement and computational complexity, which increase with $O(N^2)$ and $O(N^3)$, where N is the number of unknowns. This difficulty can be circumvented by using the Krylov iterative method, which can reduce the operation count to $O(N^2)$.

To make the iterative methods more efficient, many fast algorithms are developed to speed up the matrix-vector product operation, such as the fast multipole method (FMM) [6-7] and the matrix decomposition techniques [8-22], etc. The multilevel fast multi-pole algorithm (MLFMA) [23] has been successfully applied to the free space problem since the memory cost is reduced to the order of $M \log N$. To be noticed, though the FMM is successfully applied to the microstrip problems, the procession is always difficult because of its dependence on the Green's function. At the beginning, FMM is tried to combine with discrete complex image method (DCIM) to solve the static and two-dimensional problems [6]. Unfortunately, it will be lack of accuracy when the frequency is high. Though FMM is employed in [7] for full wave analysis, the implementation is very complicated because the surface-wave poles are extracted in DCIM. The FMM also has been applied to thin layer structures as the thin stratified medium fast multipole algorithm [24] which is adaptive to thin-stratified media. In contrast with FMM, the matrix decomposition technique is purely algebraic and, therefore, independent of the problem of Green's function. It can be easily interfaced to existing MOM codes. QR is a popular matrix decomposition technique, which has been successfully applied in [18-22] to electromagnetic problems.

The aim of this paper is to present a novel representation of MLQR algorithm for analyzing the electromagnetic scattering and radiation problems of

microstrip structures. It utilizes novel recompression technique to recompress the sub-matrices of MLQR. Simulation results show that the proposed method is computationally more efficient than the MLQR and the MDA-SVD algorithm [16-17].

II. NOVEL VERSION OF MLQR ALGORITHM

A. MLQR algorithm

The QR algorithm has been widely used to analyze the scattering/radiation [18-22], which exploits the well known fact that for well separated sub-scatterers, the corresponding sub-matrices are low rank and can be compressed [8-17]. MLQR has been successfully applied in [21-22] to electromagnetic problems. In MLQR implementation, the far-field matrix can be expressed as:

$$[Z_F] = \sum_{l=3}^L \sum_{i=1}^{M(l)} \sum_{j=1}^{Far(l(i))} [Q_{ij}][R_{ij}], \quad (1)$$

where $M(l)$ is the number of on empty groups at level l and, denotes the number of far interaction groups of the i -th nonempty group for each observation group $l(i)$ at level l . The largest boxes not touching each other are at level 3 in the octal tree, while the smallest boxes are at level L . The product $[Q_{ij}][R_{ij}]$ is associated with the interaction between the observer group $l(i)$ and the source group $l(j)$. For a given observation group $l(i)$, it is needed to store the matrix $[R_{ij}]$ for different source group $l(j)$, increasing the memory requirement. A novel recompression technique is utilized to recompress the sub-matrices of MLQR in this paper, which provides a sparser impedance matrix than the MLQR in solving 2-D and 3-D electromagnetic problems.

B. Novel Version of MLQR (NVMLQR)

A novel version of MLQR is proposed in this section, which utilizes matrix recompression technique to transform the far-field matrix into a sparser form. The Equation (1) can be changed into the following form:

$$[Z_F] = \sum_{l=3}^L \sum_{i=1}^{M(l)} [W_{li}]^* \sum_{j=1}^{Far(l(i))} [Y_{ij}][W_{lj}]^*, \quad (2)$$

where the $[W]$ is a unitary matrix, which is also block-diagonal matrix. The $[W]^*$ is the conjugate matrix of $[W]$. It needs to store the matrix $[W_{li}]$ only once for a given the observer group $l(i)$ and the dimensions of matrix $[Y_{ij}]$ are very small. Therefore, the form of Equation (2) is much sparser than that of Equation (1). The following process is used to form the two matrices in the Equation (2):

(i) The formation process of matrix $[W]$

For level l , loop over all level l source groups $l(i)$,

which is not near-neighbors of the group $l(j)$. Extract the corresponding sub-matrix $[Z_{l(i),l(j)}]$, $l(i) \in Far(l(j))$ of impedance matrix $[Z]$, which is approximated by Equation (1). Then concatenate all matrix $[R_{l(i),l(j)}]$ in a row and obtain the matrix A . Maintaining the admissible error ε , use adaptive cross approximation-singular value decomposition (ACA-SVD) [25] (which does need to form the whole information of matrix $[A]$) to decompose the matrix $[A]$:

$$[A_{pm}] = \begin{Bmatrix} \vdots \\ [R_{l(i),l(j)}] \\ \vdots \end{Bmatrix} \xrightarrow{ACA-SVD} [U'_{pk}][V'_{nk}]^*, k < \min(p, m), \quad (3)$$

where n indicates the number of the basis functions in the box $l(j)$. p denotes the sum of the rank r of sub-matrix $[Z_{l(i),l(j)}]$, $l(i) \in Far(l(j))$ in Equation (1), while k indicates the rank of the matrix $[A]$. $[V'_{nk}]^*$ is the j -th diagonal block of $[W]$. Implement the procedure as the above, we can build $[W]$. Using the procedures at all level of octal tree structure, we can obtain the whole matrix of $[W]$.

(ii) The formation process of matrix $[Y]$

The matrix $[Y]$ is formed by using the matrix $[W]$ and Equation (1), which utilizes the matrix $[W]$ multiply both sides of the Equation (1). For level l , the detail process is shown in the following:

$$[Y_l] = \sum_{i=1}^{M(l)} [W_{li}]^* \sum_{j=1}^{Far(l(i))} [Q_{ij}][R_{ij}][W_{lj}]. \quad (4)$$

The dimensions of matrix $[Y_l]$ are very small. Using the procedures at all level of octal tree structure, we can obtain the whole matrix of $[Y]$.

The essential of above procedure is to recompress the far-field matrix of MLQR. The dominant memory usage of the novel version of MLQR is the storage of the matrices $[W]$ and $[Y]$. The forms of the matrices $[W]$ and $[Y]$ are very sparse. Because of recompression of far interactions, the matrix-vector multiplication of proposed method is more efficient than that of MLQR.

III. NUMERICAL RESULTS

To validate and demonstrate the accuracy and efficiency of the proposed novel version of MLQR (NVMLQR), some numerical results are presented in this section. In the implementation of the NVMLQR, the restarted version of generalized minimal residual (GMRES) algorithm [26-27] is used as the iterative method. The restart number of GMRES is set to be 30 and the stop precision for restarted GMRES is denoted to be 10^{-3} . The truncating tolerance of MDA-SVD is 10^{-3} relative to the largest singular value. All experiments are performed on a Core-i5 3350P with 3.1 GHz CPU and

4 GB RAM in double precision.

A. The accuracy of the NVMLQR

The first example is a dual wideband filter shown in Fig. 1 (a). The dimensions of the structure are the same as that presented in [28]. The second example concerns the radiation from microstrip corporate fed planar arrays. The geometry of an 16×16 antenna array is depicted in Fig. 1 (b), where $\epsilon_r = 2.2$ and the substrate thickness is $h = 1.59 \text{ mm}$. The width of rectangular patch is $W = 10.08 \text{ mm}$ with $L = 11.79 \text{ mm}$. The fed line is of the width $d_1 = 1.3 \text{ mm}$, $d_2 = 3.93 \text{ mm}$ with the length $L_1 = 12.32 \text{ mm}$, $L_2 = 18.48 \text{ mm}$. The interval between patches are $D_1 = 23.58 \text{ mm}$ and $D_2 = 22.40 \text{ mm}$, respectively. The frequency is 9.42 GHz . The S -parameter of the dual wideband filter is analyzed in Fig. 2, while the radiation pattern which is observed at $\phi = 90^\circ$ shown in Fig. 3. It can be found that the results of the proposed method agree well with the HFSS and the Ansoft Designer simulation results. The results validate the accuracy of the proposed method.

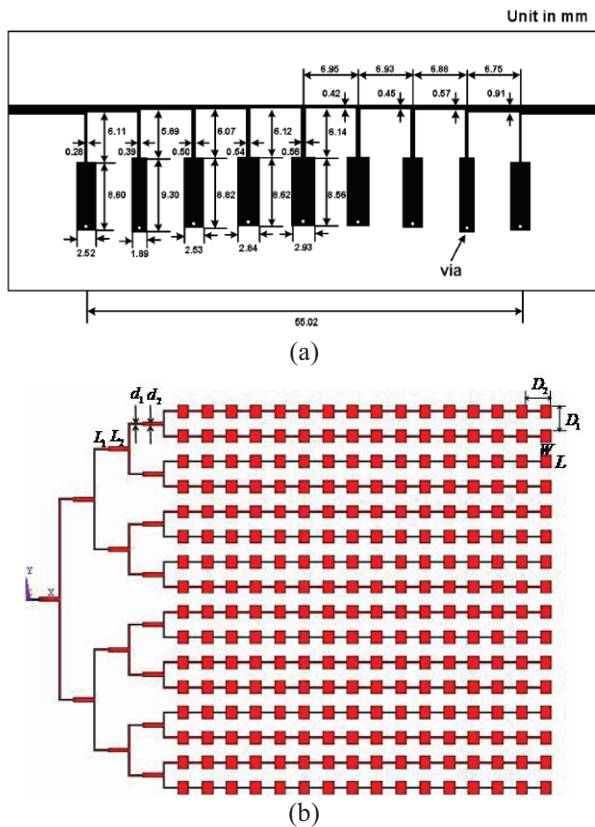


Fig. 1. (a) The topology and dimensions of the dual wideband filter, and (b) the 16×16 series-fed microstrip antenna array.

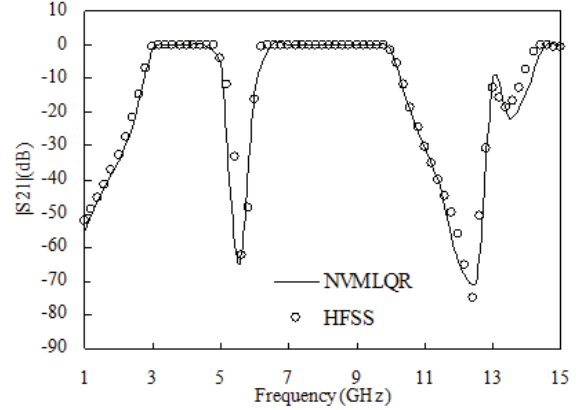


Fig. 2. The S -parameter of the dual wideband filter.

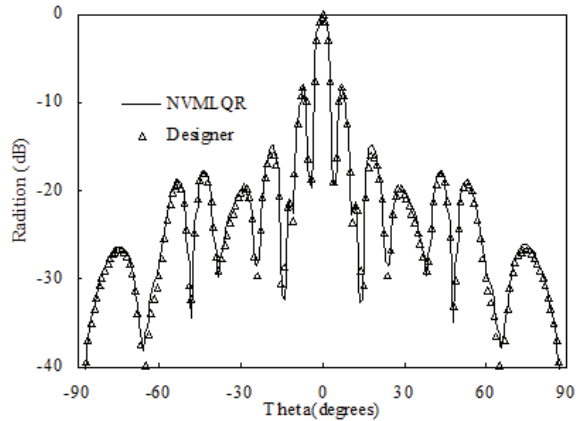


Fig. 3. The radiation pattern of the series-fed microstrip antenna.

The relative errors of the NVMLQR and MDA-SVD and MLQR for the two structures as mentioned above are shown in Table 1. The formulation of the relative error is given by:

$$\text{Relative error} = \|F - E\| / \|E\|, \quad (5)$$

where E denotes the induced current computed using the MoM iterative solution, and F is the induced current computed using the NVMLQR and MDA-SVD and MLQR.

Table 1: The relative errors for the two structures

Structures	NVMLQR	MDA-SVD	MLQR
Dual wideband filter	0.49%	0.44%	0.24%
Series-fed microstrip antenna	0.58%	0.53%	0.31%

B. The efficiency analysis of the NVMLQR

In order to check the efficiency of the algorithm, Fig. 4 and Fig. 5 shows the memory behavior and the CPU

time per iteration of the NVMLQR observed on the series-fed microstrip antenna when the number of unknowns is increased, respectively. MVP indicates one matrix-vector operation in Fig. 5. According to the plots, the memory requirement of the NVMLQR is much less than that of MLQR, while it is much less than sixth of the MDA-SVD's memory and a seventh of the MLQR's memory. The MVP time of the NVMLQR is much less than a quarter of that of MDA-SVD and a fifth of that of MLQR.

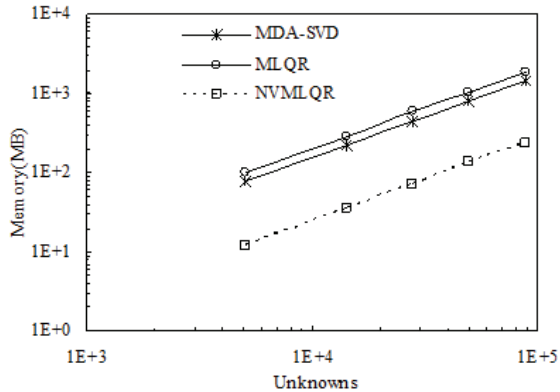


Fig. 4. Plot of the far-field memory consumption for the series-fed microstrip antenna.

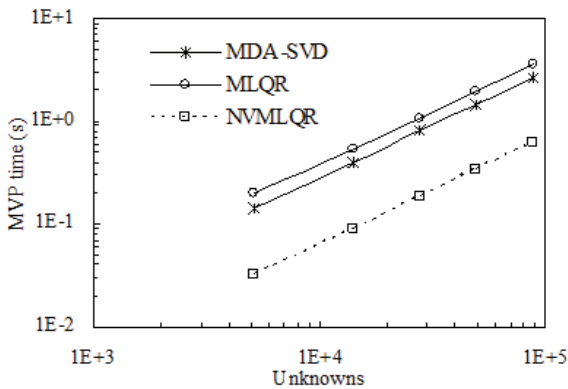


Fig. 5. Plot of the MVP time for the series-fed microstrip antenna.

IV. CONCLUSION

In this paper, a novel version of MLQR (NVMLQR) is applied to analyze the properties of microstrip structures efficiently. It is more convenient than MLFMA for solving the complex Green's functions' problems. Since recompression of far interactions of MLQR, the matrix-vector multiplication of the NVMLQR is much more efficient than MLQR. The numerical results demonstrate that the memory requirement and matrix-vector multiplication time of NVMLQR are much

less than that of MLQR and MDA-SVD, while the accuracy of the NVMLQR is controllable. It can be used to compute monostatic RCS's of complex objects efficiently.

ACKNOWLEDGEMENT

This work was supported in part by HeFei University of Technology Teacher Foundation of JZ2014HGBZ0372, National Natural Science Foundation of China under Contract Number 61501159, Natural Science Foundation of Anhui Province (1608085MF124), the Open Research Program of State Key Laboratory of Millimeter Waves of Southeast University under Contract Number K201602 and K201411.

REFERENCES

- [1] R. F. Harrington, *Field Computation by Moment Methods*. Malabar, Fla.: R. E. Krieger, 1968.
- [2] S. M. Rao, D. R. Wilton, and A. W. Glisson, "Electromagnetic scattering by surfaces of arbitrary shape," *IEEE Trans. Antennas Propagat.*, vol. AP-30, pp. 409-418, May 1982.
- [3] E. H. Newman and D. Forrai, "Scattering from a microstrip patch," *IEEE Trans. Antennas Propagat.*, vol. AP-35, pp. 245-251, Mar. 1987.
- [4] K. A. Michalski and C. G. Hsu, "RCS computation of coax-loaded microstrip patch antennas of arbitrary shape," *Electromagn.*, vol. 14, pp. 33-62, Jan.-Mar. 1994.
- [5] K. A. Michalski and D. L. Zheng, "Electromagnetic scattering and radiation by surfaces of arbitrary shape in layered media, part I: theory," *IEEE Trans. Antennas Propagat.*, vol. 38, no. 3, pp. 335-344, 1990.
- [6] L. Gurel and M. I. Aksun, "Electromagnetic scattering solution of conducting strips in layered media using the fast multipole method," *IEEE Microwave Guided Wave Lett.*, vol. 6, pp. 277-279, Aug. 1996.
- [7] P. A. Macdonald and T. Itoh, "Fast simulation of microstrip structures using the fast multipole method," *Int. J. Numer. Modeling: Electron. Networks, Devices, Fields*, vol. 9, pp. 345-357, 1996.
- [8] E. Michielssen and A. Boag, "A multilevel matrix decomposition algorithm for analyzing scattering from large structures," *IEEE Trans. Antennas Propagat.*, vol. 44, no. 8, pp. 1086-1093, Aug. 1996.
- [9] A. Heldring, J. M. Tamayo, J. M. Rius, and J. Parron, "Multilevel MDA-CBI for fast direct solution of large scattering and radiation problems," *IEEE AP-S International Symposium 2007*, Honolulu, Hawaii, USA, 10-15 June 2007.
- [10] J. M. Rius, J. Parron, E. Ubeda, and J. Mosig, "Multilevel matrix decomposition algorithm for

- analysis of electrically large electromagnetic problems in 3-D,” *Microw. Opt. Technol. Lett.*, vol. 22, no. 3, pp. 177-182, Aug. 1999.
- [11] J. Parron, G. Junkin, and J. M. Rius, “Improving the performance of the multilevel matrix decomposition algorithm for 2.5-d structures application to metamaterials,” in *Proc. Antennas Propag. Soc. Int. Symp.*, pp. 2941-2944, July 2006.
- [12] J. Parron, J. M. Rius, and J. Mosig, “Application of the multilevel decomposition algorithm to the frequency analysis of large microstrip antenna arrays,” *IEEE Trans. Magn.*, vol. 38, no. 2, pp. 721-724, Mar. 2002.
- [13] J. Parron, J. M. Rius, A. Heldring, E. Ubeda, and J. R. Mosig, “Analysis of microstrip antennas by multilevel matrix decomposition algorithm,” in *Proc. Euro. Congress Computational Methods Applied Sciences in Engineering*, Barcelona, Spain, Sept. 2000.
- [14] J. Parron, J. M. Rius, and J. Mosig, “Method of moments enhancement technique for the analysis of sierpinski pre-fractal antennas,” *IEEE Trans. Antennas Propag.*, vol. 51, no. 8, pp. 1872-1876, Aug. 2003.
- [15] J. M. Rius, A. Heldring, J. M. Tamayo, and J. Parron, “New and more efficient formulation of MLMDA for arbitrary 3D antennas and scatterers,” *Antennas Propag., EuCAP The First European Conference on*, pp. 1-6, 2006.
- [16] J. M. Rius, J. Parron, A. Heldring, J. M. Tamayo, and E. Ubeda, “Fast iterative solution of integral equations with method of moments and matrix decomposition algorithm - singular value decomposition,” *IEEE Trans. Antennas Propag.*, vol. 56, no. 8, pp. 2314-2324, Aug. 2008.
- [17] J. M. Rius, A. Heldring, J. M. Tamayo, and J. Parron, “The MDA-SVD algorithm for fast direct or iterative solution of discrete integral equations,” *Antennas Propag., EuCAP The Second European Conference on*, pp. 1-8, 2007.
- [18] N. A. Ozdemir and J. F. Lee, “A low-rank IE-QR algorithm for matrix compression in volume integral equations,” *IEEE Trans. On Magnetics*, vol. 40, no. 2, pp. 1017-1020, Mar. 2004.
- [19] S. M. Seo and J. F. Lee, “A single-level low rank IE-QR algorithm for PEC scattering problems using EFIE formulation,” *IEEE Trans. Antennas Propag.*, vol. 52, no. 8, pp. 2141-2146, Aug. 2004.
- [20] K. Z. Zhao and J. F. Lee, “A single-level dual rank IE-QR algorithm to model large microstrip antenna arrays,” *IEEE Trans. Antennas Propag.*, vol. 52, no. 10, pp. 2580-2585, Oct. 2004.
- [21] D. Gope and V. Jandhyala, “Oct-tree-based multilevel low-rank decomposition algorithm for rapid 3-D parasitic extraction,” *IEEE Trans. Computer-Aided Design*, vol. 23, no. 4, pp. 1575-1580, Nov. 2004.
- [22] D. Gope and V. Jandhyala, “Efficient solution of EFIE via low-rank compression of multilevel predetermined interactions,” *IEEE Trans. Antennas Propag.*, vol. 53, no. 10, pp. 3324-3333, Oct. 2005.
- [23] W. C. Chew, J. M. Jin, E. Michielssen, and J. Song, *Fast Efficient Algorithms in Computational Electromagnetics*. Boston, MA: Artech House, 2001.
- [24] J. S. Zhao, W. C. Chew, C. C. Lu, E. Michielssen, and J. M. Song, “Thin-stratified medium fast-multipole algorithm for solving microstrip structures,” *IEEE Trans. Microwave Theory Tech.*, vol. 46, pp. 395-403, Apr. 1998.
- [25] M. Bebendorf and S. Kunis, “Recompression techniques for adaptive cross approximation,” *J. Integral Equations Appl.*, vol. 21, no. 3, pp. 331-357, 2009.
- [26] Y. Saad and M. H. Schultz, “GMRES: A generalized minimal residual algorithm for solving nonsymmetric linear systems,” *SIAM J. Sci. Statist. Comput.*, vol. 7, pp. 856-869, July 1986.
- [27] Y. Saad, *Iterative Methods for Sparse Linear System*. PWS Publishing Company, 1996.
- [28] A.-S. Liu, T.-Y. Huang, and R.-B. Wu, “A dual wideband filter design using frequency mapping and stepped-impedance resonators,” *IEEE Transaction on Microwave and Theory Technology*, vol. 12, pp. 2921-2929, 2008.

Analytical Solution for Line Source Excitation of a PEMC Cylinder Coated with Multilayer Anisotropic Media

A. Shahi, M. Fallah, and A. Abdolali

Department of Electrical Engineering
Iran University of Science and Technology, Tehran, 1684613114, Iran
a_shahi@alumni.iust.ac.ir, m_fallah@elec.iust.ac.ir, abdolali@iust.ac.ir

Abstract — An analytical solution is presented for line source excitation of a cylinder with perfect electromagnetic conductor (PEMC) core which is coated with multilayer anisotropic materials. Exact solution is presented using analytical relations for scattering from cylindrical structures. For multilayer structures, we have to calculate the inverse of a matrix which is sparse, thus, we use recursive relations to calculate the fields. A recursive relation for solving the problem with PEMC boundary condition is presented. Finally, some examples are given using this method and the results are compared and validated with the simulation results and other works. The advantage of analytical relation proposed in this paper is much less run time compared to numerical simulation.

Index Terms — Line source, multilayer structures, perfect electromagnetic conductor, scattering RCS, special materials/anisotropic.

I. INTRODUCTION

Perfect electromagnetic conductor which was introduced by Lindell and Sihvola [3] is described using the following relations:

$$\vec{H} + M\vec{E} = 0, \quad (1)$$

$$\vec{D} - M\vec{B} = 0, \quad (2)$$

where M is the admittance of PEMC: a more general form of PEC or PMC, which can be simplified to show these boundary conditions.

PEMC is an ideal boundary, since it can be shown that pointing vector has only an imaginary part and no real part; thus, no real power flows into PEMC and it can be described as:

$$\hat{n} \times (\vec{H} + M\vec{E}) = 0. \quad (3)$$

PEMC boundary condition has been widely studied in several works from realization to a variety of scattering problems to applications. In references [6-8], the realization of PEMC boundary condition has been conducted. A grounded ferrite can be designed to have a Faraday rotation and thus show PEMC boundary

condition. In [9-19], scattering problems containing PEMC boundary condition have been worked on. Reflection and transmission obliquely incident plane wave at the interface of a PEMC was considered in [9]. Analytical relations for scattering from a PEMC sphere and cylinder have been considered in [10] and [11], respectively. Scattering from a PEMC cylinder coated with single metamaterial layer was considered in [12]. Also, scattering from a PEMC cylinder buried in a dielectric half space was investigated in [13]. Scattering from two PEMC cylinders was investigated in [14] using iterative methods. In [15], a transformation method was introduced to solve the problems containing PEMC boundary condition and those involving PEMC objects in the air were treated. In [16], an extension to PEMC was introduced as “good electromagnetic conductor”. Plane electromagnetic wave propagation in PEMC was considered in [17]. In [18] and [19] a PEMC cylindrical reflector has been studied and high frequency expressions were used.

Electromagnetic scattering from stratified media is the subject of many research and scientific articles [21]. By using stratified media, we can obtain some advantageous like wideband operation of our structure [22] and increased degree of freedom. Specifically, scattering analysis of anisotropic stratified medium is the subject of interest in many works [23-24]. For example, in [24], a stratified anisotropic medium was used to achieve invisibility. Therefore, it is interesting to investigate the problem of multilayer anisotropic coat with different cores including PEMC core. Solution of electromagnetic scattering from an anisotropic cylinder is studied in many resources. One of which is [20].

Most of the PEMC problems have concentrated on single PEMC core or single layer coated PEMC. For example, in [4], a single anisotropic layer coating a PEMC cylinder was considered and scattering of plane wave was investigated through this structure. Not many papers have investigated the scattering problem of a multilayer structure containing PEMC core. In this paper, this problem is considered for the cylindrical geometry with a simple method.

Organization of the paper is as follows: In the first section, formulation of the problem is stated, general form of the field in each region is introduced, boundary conditions are presented and the problem of sparseness of a matrix which should be inverted to solve the problem is issued.

In the next section, recursive relations are introduced to solve the problem of sparseness of that matrix mentioned in the previous paragraph. The last section presents the results.

II. FORMULATION OF THE PROBLEM

In this section, we investigate the analysis of the above stated problem. Geometry of the problem is shown in Fig. 1. The permittivity and permeability tensors of the problem can be shown as:

$$\bar{\varepsilon} = \begin{bmatrix} \varepsilon_1 & 0 & 0 \\ 0 & \varepsilon_2 & 0 \\ 0 & 0 & \varepsilon_3 \end{bmatrix}_{\rho\phi z}, \quad \bar{\mu} = \begin{bmatrix} \mu_1 & 0 & 0 \\ 0 & \mu_2 & 0 \\ 0 & 0 & \mu_3 \end{bmatrix}_{\rho\phi z}. \quad (4)$$

The form of incident electric and magnetic field for TM polarization is:

$$E_z^i = -\frac{\omega\mu_0}{4} \begin{cases} \sum_{n=-\infty}^{\infty} J_n(k_0\rho) H_n^2(k_0\rho') e^{jn(\phi-\phi')} & \rho < \rho', \\ \sum_{n=-\infty}^{\infty} J_n(k_0\rho') H_n^2(k_0\rho) e^{jn(\phi-\phi')} & \rho > \rho', \end{cases} \quad (5)$$

$$H_\phi^i = \frac{-k_0}{4j} \begin{cases} \sum_{n=-\infty}^{\infty} H_n^{(2)}(k_0\rho') J_n'(k_0\rho) e^{jn(\phi-\phi')} & \rho < \rho', \\ \sum_{n=-\infty}^{\infty} J_n(k_0\rho') H_n^{(2)'}(k_0\rho) e^{jn(\phi-\phi')} & \rho > \rho'. \end{cases} \quad (6)$$

And the form of scattered field would be:

$$E_z^s = -\frac{\omega\mu_0}{4} \sum_{n=-\infty}^{\infty} a_n H_n^{(2)}(k_0\rho) e^{jn(\phi-\phi')}, \quad (7)$$

$$H_z^s = \frac{-k_0}{4j} \sum_{n=-\infty}^{\infty} a_n H_n^{(2)'}(k_0\rho) e^{jn(\phi-\phi')}. \quad (8)$$

Also, the form of field distribution in each anisotropic layer would be:

$$E_z^{(i)} = -\frac{\omega\mu_0}{4} \sum_{n=-\infty}^{\infty} [c_n^i H_{\nu ei}^{(1)}(u_i^\rho) + d_n^i H_{\nu ei}^{(2)}(u_i^\rho)] e^{jn(\phi-\phi')}, \quad (9)$$

$$H_\phi^{(i)} = \frac{-k_0}{4j} Y_{ei} \sum_{n=-\infty}^{\infty} [c_n^i H_{\nu ei}^{(1)'}(u_i^\rho) + d_n^i H_{\nu ei}^{(2)'}(u_i^\rho)] e^{jn(\phi-\phi')}, \quad (10)$$

$$\nu ei = n \sqrt{\frac{\mu_{2i}}{\mu_{1i}}}, \quad u_i^\rho = k_0 \rho \sqrt{\varepsilon_{3i} \mu_{2i}}, \quad Y_{ei} = \sqrt{\frac{\varepsilon_{3i}}{\mu_{2i}}}. \quad (11a-c)$$

And the field distribution for cross-pol components can be stated as:

$$H_z^s = \frac{-k_0}{4j} \sum_{n=-\infty}^{\infty} b_n H_n^{(2)}(k_0\rho) e^{jn(\phi-\phi')}, \quad (12)$$

$$E_\phi^s = \frac{-\omega\mu_0}{4} \sum_{n=-\infty}^{\infty} b_n H_n^{(2)'}(k_0\rho) e^{jn(\phi-\phi')}, \quad (\rho > \rho_N) \quad (13)$$

$$H_z^{(i)} = \frac{-k_0}{4j} \sum_{n=-\infty}^{\infty} [c_{n2}^i H_{\nu mi}^{(1)}(u_i^\rho) + d_{n2}^i H_{\nu mi}^{(2)}(u_i^\rho)] \dots e^{jn(\phi-\phi')}. \quad (14)$$

$$E_\phi^{(i)} = \frac{-\omega\mu_0}{4} Z_{mi} \sum_{n=-\infty}^{\infty} [c_{n2}^i H_{\nu mi}^{(1)'}(u_i^\rho) + d_{n2}^i H_{\nu mi}^{(2)'}(u_i^\rho)] e^{jn(\phi-\phi')}, \quad (15)$$

$$\nu mi = n \sqrt{\frac{\varepsilon_{2i}}{\varepsilon_{1i}}}, \quad Z_{mi} = \sqrt{\frac{\mu_{3i}}{\varepsilon_{2i}}}, \quad u_i^\rho = k_0 \rho \sqrt{\varepsilon_{2i} \mu_{3i}}. \quad (16)$$

Here, ρ_N is radius of the N^{th} layer.

Now, we should apply boundary conditions to complete the formulation of the problem. Boundary conditions involve the continuity of tangential electric and magnetic fields at the boundary between two layers or between the last layer and free space. Since we have two polarizations, as one original polarization and one cross polarization, we should write boundary conditions for each polarization separately and apply PEMC boundary conditions between the field components of co and cross-polarized components of the first layer. In what follows, we have written boundary conditions in each region separately, the first two equations are for general polarization and the last two equations are for cross polarization. One of the two equations is for the electric field and the other is related to the magnetic field:

$$-\frac{\omega\mu_0}{4} [J_n(k_0\rho_N) H_n^2(k_0\rho') + a_n H_n^{(2)}(k_0\rho_N)] = \quad (17)$$

$$-\frac{\omega\mu_0}{4} [c_n^N H_{\nu eN}^{(1)}(u_N^{\rho_N}) + d_n^N H_{\nu eN}^{(2)}(u_N^{\rho_N})],$$

$$\frac{-k_0}{4j} [H_n^{(2)}(k_0\rho') J_n'(k_0\rho_N) + a_n H_n^{(2)'}(k_0\rho_N)] = \quad (18)$$

$$\frac{-k_0}{4j} Y_{eN} [c_n^N H_{\nu eN}^{(1)'}(u_N^{\rho_N}) + d_n^N H_{\nu eN}^{(2)'}(u_N^{\rho_N})],$$

$$\frac{-k_0}{4j} [c_{n2}^N H_{\nu mN}^{(1)}(u_N^{\rho_N}) + d_{n2}^N H_{\nu mN}^{(2)}(u_N^{\rho_N})] = \quad (19)$$

$$\frac{-k_0}{4j} b_n H_n^{(2)}(k_0\rho_N),$$

$$\frac{-\omega\mu_0}{4} Z_{mN} [c_{n2}^N H_{\nu mN}^{(1)'}(u_N^{\rho_N}) + d_{n2}^N H_{\nu mN}^{(2)'}(u_N^{\rho_N})] = \quad (20)$$

$$\frac{-\omega\mu_0}{4} b_n H_n^{(2)'}(k_0\rho_N),$$

$$-\frac{M\omega\mu_0}{4}[c_n^1 H_{\nu e1}^{(1)}(u_1^{\rho_1}) + d_n^1 H_{\nu e1}^{(2)}(u_1^{\rho_1})] - \frac{k_0}{4j}[c_{n2}^1 H_{\nu m1}^{(1)}(u_1^{\rho_1}) + d_{n2}^1 H_{\nu m1}^{(2)}(u_1^{\rho_1})] = 0, \quad (21)$$

$$\frac{-M\omega\mu_0}{4}Z_{m1}[c_n^1 H_{\nu m1}'(u_1^{\rho_1}) + d_{n2}^1 H_{\nu m1}'(u_1^{\rho_1})] - \frac{k_0}{4j}Y_{e1}[c_n^1 H_{\nu e1}'(u_1^{\rho_1}) + d_n^1 H_{\nu e1}'(u_1^{\rho_1})] = 0. \quad (22)$$

Equations (17-20) are boundary conditions between last layer and free space. Equations (21-22) are PEC boundary conditions.

Boundary conditions between the i^{th} and $(i+1)^{\text{th}}$ layers are similar to Equations (17-20) with suitable changes.

After applying the boundary conditions (Equations (17-22)), the formulation of the problem is finished and we should find unknowns of the problem. Result of applying boundary conditions to the problem is a set of $4N$ linear equations with $4N$ unknowns. This system may be described as:

$$CX = D, \quad (23)$$

where X shows unknowns of the problem, C is a matrix containing coefficients of unknowns in the set of linear equations, and D is a vector of known values of the problem.

The matrix C becomes sparse. The reason is that each row has only three or four nonzero elements and others are zero. If we show the element of the matrix with A and B with subscripts \pm and superscripts i, j then A shows coefficient of electric field boundary condition, B shows coefficient of magnetic field boundary condition, i is the layer in which fields exist, j is the layer boundary whose fields are evaluated, and $+$ and $-$ show direction of propagation of field. Consider a simple case where we do not have cross-polarized components in the problem. Thus, the coefficient matrix becomes as follows:

$$\begin{bmatrix} A_{(N+1)N}^+ & A_{NN}^+ & A_{NN}^- & 0 & 0 & \cdots & 0 \\ B_{(N+1)N}^+ & B_{NN}^+ & B_{NN}^- & 0 & 0 & \cdots & 0 \\ 0 & A_{N(N-1)}^+ & A_{N(N-1)}^- & A_{(N-1)(N-1)}^+ & A_{(N-1)(N-1)}^- & \cdots & 0 \\ 0 & B_{N(N-1)}^+ & B_{N(N-1)}^- & B_{(N-1)(N-1)}^+ & B_{(N-1)(N-1)}^- & \cdots & 0 \\ \vdots & \vdots & \vdots & \vdots & \vdots & \vdots & 0 \\ 0 & \cdots & 0 & A_{21}^+ & A_{21}^- & A_{11}^+ & A_{11}^- \\ 0 & \cdots & 0 & B_{21}^+ & B_{21}^- & B_{11}^+ & B_{11}^- \end{bmatrix}. \quad (24)$$

As can be seen, there are so many zeroes in the matrix. The first and second rows have three nonzero elements, other rows have four nonzero elements, and the rest are all zero. For example, for a 3 layer problem, we have 7 unknowns; so, matrix is of order 7. There are 8 zeroes in the first and second rows and each other row has 3 zeroes. Totally, we have 23 zeroes in this matrix and 26

nonzero elements. It is obvious that this matrix is sparse. As the order of the matrix increases, this problem becomes more serious. The problem gets more difficult when we have PEC boundary condition that causes the existence of cross-polarized components, which adds to the unknowns of the problem by the order of N .

Calculation of inverse of a sparse matrix is a tedious task and we want to prevent this difficulty so we use recursive relations instead which is introduced and formulated in the following section

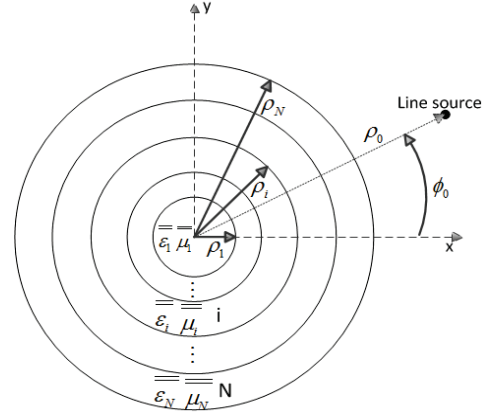


Fig. 1. Geometry of the problem.

III. RECURSIVE RELATIONS

In [2], a layered media was considered and solved using recursive relations. We get this idea and use it for our cylindrically layered media.

According to Equations (19) and (20), we can obtain recursive relations for cross-polarized components as follows:

$$\frac{d_{n2}^N}{c_{n2}^N} = \frac{F_A H_{\nu mN}^{(1)'}(u_N^{\rho_N}) - H_n^{(2)'}(k_0 \rho_N) H_{\nu mN}^{(1)}(u_N^{\rho_N})}{H_n^{(2)'}(k_0 \rho_N) H_{\nu mN}^{(2)}(u_N^{\rho_N}) - F_A H_{\nu mN}^{(2)'}(u_N^{\rho_N})}, \quad (25)$$

$$\frac{d_{n2}^i}{c_{n2}^i} = \frac{F_1 \left(\frac{d_{n2}^{i+1}}{c_{n2}^{i+1}} \right) H_{\nu mi}^{(1)'}(u_i^{\rho_i}) - F_2 \left(\frac{d_{n2}^{i+1}}{c_{n2}^{i+1}} \right) H_{\nu mi}^{(1)}(u_i^{\rho_i})}{F_2 \left(\frac{d_{n2}^{i+1}}{c_{n2}^{i+1}} \right) H_{\nu mi}^{(2)}(u_i^{\rho_i}) - F_1 \left(\frac{d_{n2}^{i+1}}{c_{n2}^{i+1}} \right) H_{\nu mi}^{(2)'}(u_i^{\rho_i})}, \quad (26)$$

$$F_A = Z_{mN} H_n^{(2)}(k_0 \rho_N), \quad (27)$$

$$F_1 \left(\frac{d_{n2}^{i+1}}{c_{n2}^{i+1}} \right) = Z_{mi} [H_{\nu m(i+1)}^{(1)}(u_{i+1}^{\rho_i}) + \frac{d_{n2}^{i+1}}{c_{n2}^{i+1}} H_{\nu m(i+1)}^{(2)}(u_{i+1}^{\rho_i})], \quad (28)$$

$$F_2 \left(\frac{d_{n2}^{i+1}}{c_{n2}^{i+1}} \right) = Z_{m(i+1)} [H_{\nu m(i+1)}^{(1)'}(u_{i+1}^{\rho_i}) + \frac{d_{n2}^{i+1}}{c_{n2}^{i+1}} H_{\nu m(i+1)}^{(2)'}(u_{i+1}^{\rho_i})]. \quad (29)$$

It is observed that we have a certain known value for d_{n2}^N / c_{n2}^N ; thus, we can express $d_{n2}^{N-1} / c_{n2}^{N-1}$ in terms of d_{n2}^N / c_{n2}^N according to 26 and continue it until getting to the first layer and obtain d_{n2}^1 / c_{n2}^1 which is known.

Afterwards, we make a relationship between co and cross-polarized components using the following relation (obtained from PEMC boundary condition):

$$\frac{d_n^1}{c_n^1} = \frac{F_3 \left(\frac{d_{n2}^1}{c_{n2}^1} \right) - \left(\frac{M\omega\mu_0}{4} \right)^2 Z_{m1} H_{ve1}^{(1)}(u_1^{\rho_1}) F_4 \left(\frac{d_{n2}^1}{c_{n2}^1} \right)}{\left(\frac{M\omega\mu_0}{4} \right)^2 Z_{m1} H_{ve1}^{(2)}(u_1^{\rho_1}) F_4 \left(\frac{d_{n2}^1}{c_{n2}^1} \right) - F_B F_3 \left(\frac{d_{n2}^1}{c_{n2}^1} \right)}, \quad (30)$$

$$F_B = \left(\frac{k_0}{4j} \right)^2 Y_{e1} H_{ve1}^{(1)'}(u_2^{\rho_1}), \quad (31)$$

$$F_3 \left(\frac{d_{n2}^1}{c_{n2}^1} \right) = [H_{vm1}^{(1)}(u_1^{\rho_1}) + \frac{d_{n2}^1}{c_{n2}^1} H_{vm1}^{(2)}(u_1^{\rho_1})], \quad (32)$$

$$F_4 \left(\frac{d_{n2}^1}{c_{n2}^1} \right) = [H_{vm1}'(u_1^{\rho_1}) + \frac{d_{n2}^1}{c_{n2}^1} H_{vm1}'(u_1^{\rho_1})]. \quad (33)$$

Now, we move from the first layer to the last layer using recursive relations of co-polarized components of the field. We express d_n^2/c_n^2 in terms of d_n^1/c_n^1 which is known according to Equation (30) and continue to obtain d_n^N/c_n^N . We use the following recursive relation for this task:

$$\frac{d_n^{i+1}}{c_n^{i+1}} = \frac{F_5 \left(\frac{d_n^i}{c_n^i} \right) H_{ve(i+1)}^{(1)'}(u_{i+1}^{\rho_i}) - F_6 \left(\frac{d_n^i}{c_n^i} \right) H_{ve(i+1)}^{(1)}(u_{i+1}^{\rho_i})}{F_6 \left(\frac{d_n^i}{c_n^i} \right) H_{ve(i+1)}^{(2)}(u_{i+1}^{\rho_i}) - F_5 \left(\frac{d_n^i}{c_n^i} \right) H_{ve(i+1)}^{(2)'}(u_{i+1}^{\rho_i})}, \quad (34)$$

$$F_5 \left(\frac{d_n^i}{c_n^i} \right) = Y_{e(i+1)} [H_{vei}^{(1)}(u_i^{\rho_i}) + H_{vei}^{(2)}(u_i^{\rho_i}) \frac{d_n^i}{c_n^i}], \quad (35)$$

$$F_6 \left(\frac{d_n^i}{c_n^i} \right) = Y_{ei} [H_{vei}'(u_i^{\rho_i}) + H_{vei}^{(2)'}(u_i^{\rho_i}) \frac{d_n^i}{c_n^i}]. \quad (36)$$

When we obtain d_n^N/c_n^N , we can use Equations (17) and (18) to obtain a_n as follows:

$$a_n = \frac{F_7 \left(\frac{d_n^N}{c_n^N} \right) H_n^{(2)}(k_0 \rho_N) J_n'(k_0 \rho_N) - F_8 \left(\frac{d_n^N}{c_n^N} \right) J_n(k_0 \rho_N) H_n^2(k_0 \rho')}{F_8 \left(\frac{d_n^N}{c_n^N} \right) H_n^{(2)}(k_0 \rho_N) - F_7 \left(\frac{d_n^N}{c_n^N} \right) H_n^{(2)'}(k_0 \rho_N)}, \quad (37)$$

$$F_7 \left(\frac{d_n^N}{c_n^N} \right) = [H_{veN}^{(1)}(u_N^{\rho_N}) + H_{veN}^{(2)}(u_N^{\rho_N}) \frac{d_n^N}{c_n^N}], \quad (38)$$

$$F_8 \left(\frac{d_n^N}{c_n^N} \right) = Y_{eN} [H_{veN}'(u_N^{\rho_N}) + H_{veN}^{(2)'}(u_N^{\rho_N}) \frac{d_n^N}{c_n^N}]. \quad (39)$$

Thus, the problem is solved completely and we know the scattering coefficient and consequently scattering pattern and total field pattern.

Similar relations might be written for TE polarization. We can briefly describe what we did in this part:

We started from the last layer and used recursive relations of cross-polarized components (Equations (25) and (26)) to move through the layers to the first layer. In the first layer, we used PEMC boundary conditions

(Equations (21) and (22)) and made a relationship between co- and cross-pol components (Equation (30)). Afterwards, we moved through the layers to the last layer using recursive relations of co-polarized components (Equation (34)) and finally obtained scattering coefficient. Thus, our movement was from the last to the first layers in terms of recursive relations of cross-polarized components and from the first to the last layers in terms of recursive relations of co-polarized components. This issue is schematically illustrated in Fig. 2.

Note that, according to Fig. 2, by starting with b_n , we mean that we use Equation (25) to start moving through the layers and there is no dependence on b_n .

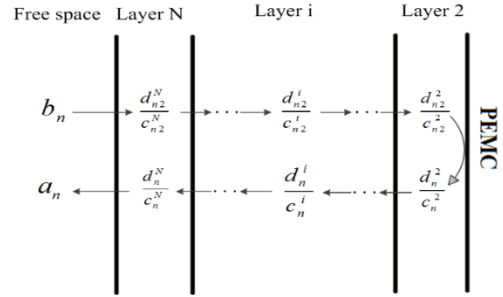


Fig. 2. Movements in layers in order to find scattering coefficient. Layers are cylindrical.

IV. RESULTS

In this section, we are going to illustrate the numerical results of the formulas presented earlier. Some methods are exerted to validate the results. One of them is to compare the results of a simple problem solved using our method with full-wave software like CST microwave studio. A simple problem refers to the one in which the core is PEC and the coat material is isotropic. Thus, we simulate a PEC cylinder coated with several dielectric layers illuminated by plane wave and then observe a near-field pattern. Afterwards, we are sure that our results are true for simple problems and recursive relations are written correctly. Finally, we compare the results with those of some of the previous works for PEMC core.

The result seen in CST is electric in TM polarization case and magnetic field in TE polarization case evaluated on a curve which is a circle concentric with a cylindrical structure.

Therefore, a PEC cylinder coated with 5 dielectric layers illuminated with TM and TE-polarized plane wave is simulated. Comparison is made between our code and CST simulation and then presented in Fig. 3.

As can be seen from Fig. 3, comparisons show that our method has great accuracy and is thus reliable. The next step is to compare the results with other works.

In [4], Montaseri et al. solved the problem for one layer case. Here, we compare our results with those of their work. Two general cases are considered: Isotropic

and Anisotropic. In each case, co and cross-pol results are compared.

The results in [4] are for the plane wave case. Normalized scattering cross-section with the following form is considered:

$$\frac{\sigma_{co}}{\lambda_0} = \frac{2}{\pi} \left| \sum_{n=-\infty}^{+\infty} a_n e^{jn(\phi-\phi_0)} \right|^2, \quad (40)$$

$$\frac{\sigma_{cross}}{\lambda_0} = \frac{2}{\pi} \left| \sum_{n=-\infty}^{+\infty} b_n e^{jn(\phi-\phi_0)} \right|^2, \quad (41)$$

where a_n is scattering coefficient for co-polarized component, b_n is scattering coefficient for cross-polarized coefficient, and ϕ_0 is angle of plane wave incidence.

In Figs. 4 and 5, isotropic dielectric cylinder coating a PEMC cylinder scattering is evaluated.

In Figs. 6 and 7, isotropic dielectric cylinder coating a PEMC cylinder scattering is evaluated.

Finally, we present the field pattern of line source from a 2-layer anisotropic structure with PEMC in the first layer. It is illuminated with electromagnetic fields of a line source and results are shown in Figs. 8 and 9 for co- and cross-pol, respectively.

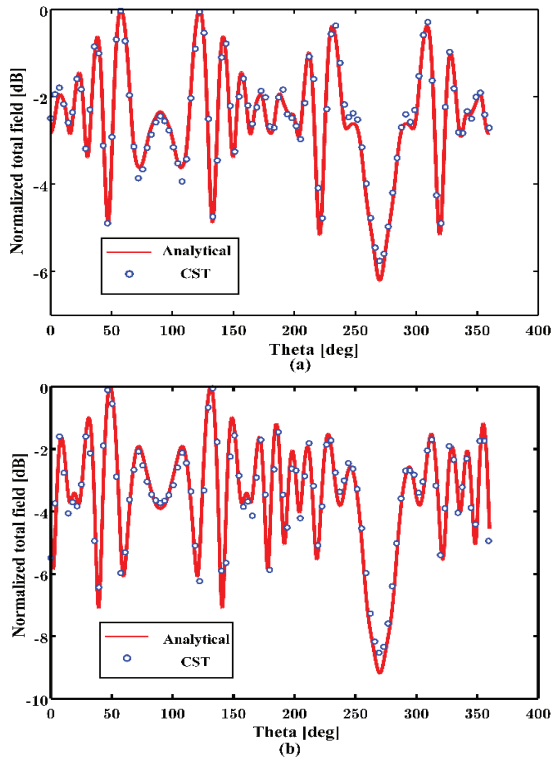


Fig. 3. Comparison between analytical relation stated in the paper and CST full-wave simulation for 5 layer dielectric cylinder with radiuses of layers described as 0.1λ , 0.2λ , 0.3λ , 0.4λ , 0.5λ with dielectric constants $\epsilon_r = 2$, $\epsilon_r = 3$, $\epsilon_r = 4$, $\epsilon_r = 5$, $\epsilon_r = 6$ illuminated by a plane wave with angle of $\pi/2$ relative to x-axis. Near field is observed at: (a) TM polarization and (b) TE polarization.

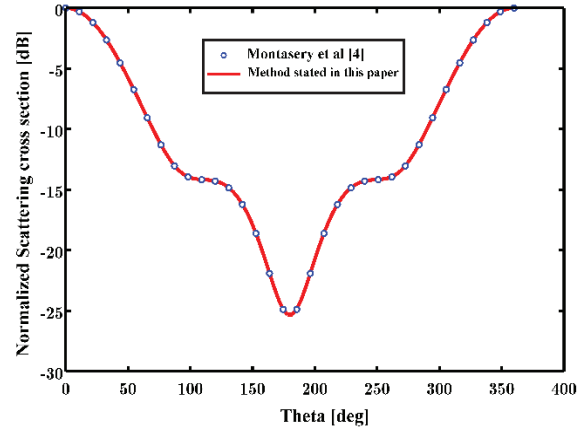


Fig. 4. Normalized co-polarization scattering cross section with parameters $\epsilon_1 = \epsilon_2 = \epsilon_3 = 9.8$, $\mu_1 = \mu_2 = \mu_3 = 1$, $\phi_0 = \pi/2$, $M\eta_0 = \pm 1$, $a = \lambda/6$, $b = \lambda/3$.

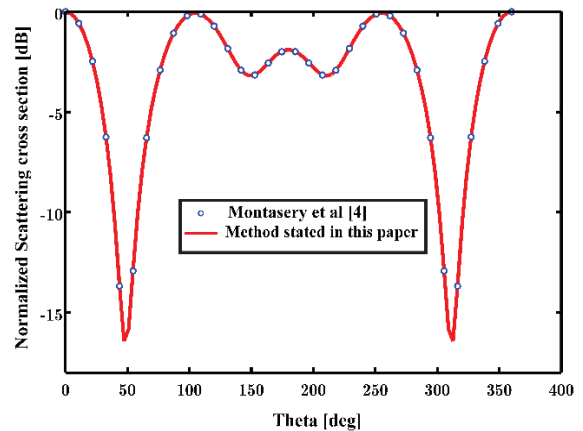


Fig. 5. Normalized cross-polarization scattering cross section with parameters $\epsilon_1 = \epsilon_2 = \epsilon_3 = 9.8$, $\mu_1 = \mu_2 = \mu_3 = 1$, $\phi_0 = \pi/2$, $M\eta_0 = \pm 1$, $a = \lambda/6$, $b = \lambda/3$.

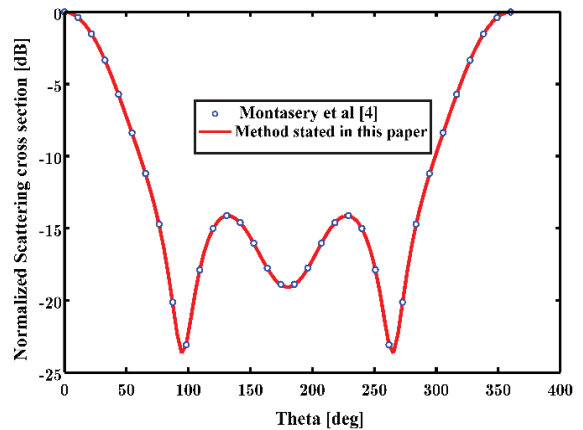


Fig. 6. Normalized co-polarization scattering cross-section with parameters $\epsilon_1 = \epsilon_2 = \epsilon_3 = 9.8$, $\mu_1 = 1$, $\mu_2 = 19$, $\mu_3 = 6$, $\phi_0 = \pi/2$, $M\eta_0 = \pm 1$, $a = \lambda/6$, $b = \lambda/3$.

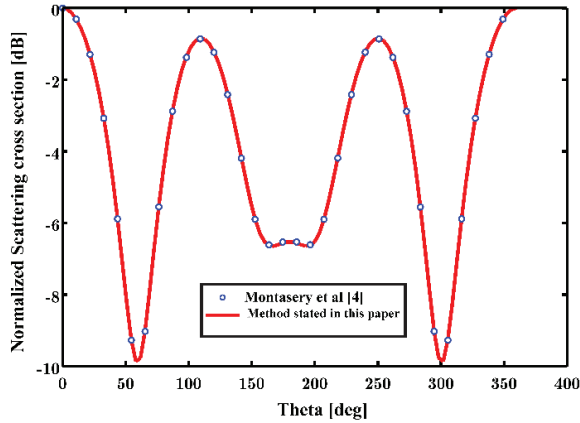


Fig. 7. Normalized cross-polarization scattering cross-section with parameters $\epsilon_1 = 9.8$, $\epsilon_2 = 16$, $\epsilon_3 = 7$, $\mu_1 = 1$, $\mu_2 = 19$, $\mu_3 = 6$, $\varphi_0 = \pi/2$, $M\eta_0 = \pm 1$, $a = \lambda/6$, $b = \lambda/3$.

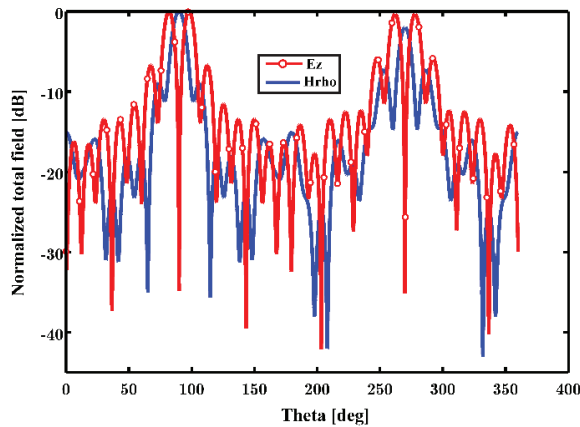


Fig. 8. Co-pol case with parameters described as $\epsilon_{11} = 6.4$, $\epsilon_{12} = 9.8$, $\epsilon_{13} = 5.3$, $\epsilon_{21} = 7$, $\epsilon_{22} = 1.1$, $\epsilon_{23} = 4$, $\mu_{ij} = 1$, $i = 1, 2$, $j = 1, 2$, $r_0 = \lambda/6$, $r_1 = \lambda/3$, $r_2 = \lambda/2$, $M\eta_0 = \pm 1$, $\rho_0 = 20\lambda$, $\varphi_0 = \pi/2$.

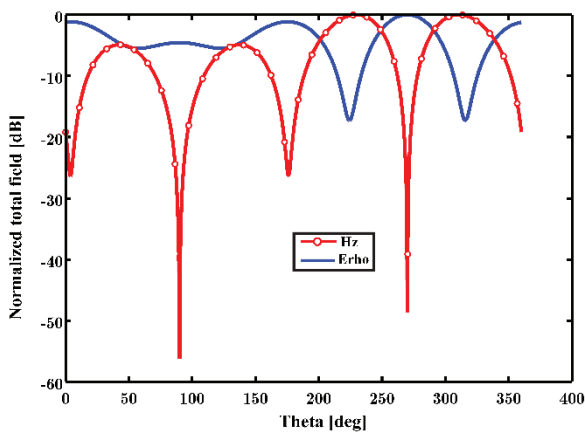


Fig. 9. Cross-pol case for the structure described in Fig 8.

V. CONCLUSION

In this paper, we analyzed line source scattering from a multilayer cylinder with a PEMC boundary condition at the first layer. Formulation of the problem was stated and boundary conditions were obtained. For the multilayer problems, the-inverse of a matrix that was sparse was calculated. Thus, we introduced a novel recursive method for the calculation of scattering coefficient for PEMC boundary condition. Finally, we illustrated the validation of the results using CST microwave studio and comparison with previous works and one case of multilayer problem was evaluated.

REFERENCES

- [1] C. A. Balanis, *Advanced Engineering Electromagnetics*. vol. 20, New York: Wiley, 1989.
- [2] J. A. Kong, "Theory of electromagnetic waves," *New York, Wiley-Interscience*, 348, pp. 1, 1975.
- [3] I. V. Lindell and A. H. Sihvola, "Perfect electromagnetic conductor," *Journal of Electromagnetic Waves and Applications*, vol. 19, no. 7, pp. 861-869, 2005.
- [4] N. Montaseri, A. Abdolali, M. Soleimani, and V. Nayyeri, "Plane wave scattering by a circular PEMC cylinder coated with anisotropic media," *International Journal of RF and Microwave Computer-Aided Engineering*, vol. 23, no. 2, pp. 225-231, 2013.
- [5] S. Ahmed and A. N. Qaisar, "Directive EM radiation of a line source in the presence of a coated PEMC circular cylinder," *Progress In Electromagnetics Research*, vol. 92, pp. 91-102, 2009.
- [6] N. Montaseri, M. Soleimani, and A. Abdolali, "Realization of the perfect electromagnetic conductor circular cylinder using anisotropic media," *Progress In Electromagnetics Research M*, vol. 25, pp. 173-184, 2012.
- [7] I. V. Lindell and A. H. Sihvola, "Realization of the PEMC boundary," *IEEE Trans Antennas Propag.*, vol. 53, pp. 3012-3018, 2005.
- [8] A. Shahvarpour, T. Kodera, A. Parsa, and C. Caloz, "Realization of the perfect electromagnetic conductor (PEMC) boundary by a grounded ferrite slab using Faraday rotation," *Proceedings of the 39th European Microwave Conference*, pp. 731-734, 2009.
- [9] I. V. Lindell and A. H. Sihvola, "Reflection and transmission of waves at the interface of perfect electromagnetic conductor (PEMC)," *Progress in Electromagnetic Research B*, vol. 5, pp. 169-183, 2008.
- [10] R. Ruppim, "Scattering of electromagnetic radiation by a perfect electromagnetic conductor sphere," *Journal of Electromagnetic Waves and Application*, vol. 20, pp. 1569-1576, 2006.

- [11] R. Ruppin, "Scattering of electromagnetic radiation by a perfect electromagnetic conductor cylinder," *Journal of Electromagnetic Waves and Application*, vol. 20, pp. 1553-1860, 2006.
- [12] S. Ahmed and Q. A. Naqvi, "Electromagnetic scattering from a perfect electromagnetic conductor cylinder coated with a metamaterial having negative permittivity and/or permeability," *Opt. Commun.*, vol. 281, pp. 5664-5670, 2008.
- [13] S. Ahmed and Q. A. Naqvi, "Electromagnetic scattering from a perfect electromagnetic conductor cylinder buried in a dielectric half space," *Progress in Electromagnetic Research*, vol. 78, pp. 25-38, 2008.
- [14] S. Ahmed and Q. A. Naqvi, "Electromagnetic scattering from parallel perfect electromagnetic conductor cylinders of circular cross-sections using iterative procedure," *Journal of Electromagnetic Waves and Application*, vol. 22, pp. 987-1003, 2008.
- [15] I. V. Lindell and A. H. Sihvola, "Transformation method for problems involving perfect electromagnetic conductor (PEMC) structures," *IEEE Trans. Antennas Propag.*, vol. 53, no. 9, pp. 3005-3011, 2005.
- [16] I. V. Lindell and A. H. Sihvola, "Losses in PEMC boundary," *IEEE Trans. Antennas Propag.*, vol. 54, no. 9, pp. 2553-2558, 2006.
- [17] B. Jancewicz, "Plane electromagnetic wave in PEMC," *Journal of Electromagnetic Waves and Applications*, vol. 20, no. 5, pp. 647-659, 2006.
- [18] M. A. Fiaz, A. Ghaffar, and Q. A. Naqvi, "High frequency expressions for the field in the caustic region of a PEMC cylindrical reflector using Maslov's method," *Journal of Electromagnetic Waves and Applications*, vol. 22, pp. 358-397, 2008.
- [19] I. V. Lindell and A. H. Sihvola, "High frequency expressions for the field in the caustic region of a PEMC Gregorian system using Maslov's method," *Progress In Electromagnetics Research*, vol. 81, pp. 135-148, 2008.
- [20] Y. L. Li and J. Li, "Investigation of scattering property for an anisotropic dielectric circular cylinder," *arXiv preprint arXiv: 1009.2550*, 2010.
- [21] K. Li, *Electromagnetic Fields in Stratified Media*. Springer Science & Business Media, 2009.
- [22] H. Oraizi and A. Abdolali, "Ultra wide band RCS optimization of multilayered cylindrical structures for arbitrarily polarized incident plane waves," *Progress In Electromagnetics Research*, vol. 78, pp. 129-157, 2008.
- [23] A. H. Nayfeh, "Wave propagation in layered anisotropic media: With application to composites," *Elsevier*, 1995.
- [24] N. Yaxian, G. Lei, and W. Q. Cheng, "Achieving invisibility of homogeneous radially anisotropic cylinders by effective medium theory," *arXiv preprint arXiv: 0905.1503*, 2009.
- [25] CST Microwave Studio, ver. 2013, Computer Simulation Technology, Framingham, MA, 2013.



Ali Shahi was born in Isfahan, Iran. He received his Bs.C. of Science in Electrical Engineering from Isfahan University of Technology (IUT) in 2013 and from 2013 to present. He is M.Sc. student at Iran University of Science and Technology (IUST). His research interests include analytical methods in electromagnetic theory, electromagnetic wave scattering theory and wave propagation in complex media.



Mahmoud Fallah was born in Iran. He received his M.Sc. from Iran University of Science and Technology (IUST) in 2012. His research interests include wave propagation in Anisotropic, Inhomogeneous media, Periodic Structures (FSS, metamaterial), Scattering, Artificial Magnetic Conductor (AMC).



Ali Abdolali was born in Tehran, Iran, on May 3, 1974. He received B.Sc. degree from the University of Tehran, and M.S. degree from the University of Tarbiat Modares, Tehran, and the Ph.D. degree from the Iran University of Science and Technology (IUST), Tehran Ann Arbor, all in Electrical Engineering, in 1998, 2000, and 2010, respectively. In 2010, he joined the Department of Electrical Engineering, Iran University of Science and Technology, Tehran, Iran, where he is an Assistant Professor of Electromagnetic Engineering. His research interests include electromagnetic wave scattering, Radar Cross Section (RCS) & RCSR, Radar Absorbing Materials (RAM), cloaking, Metamaterials, Wave Propagation in composite media (anisotropic, inhomogeneous, dispersive media), Frequency Selective Surfaces (FSS), Bio electromagnetism (BEM). He has authored or co-authored over 80 papers in international journals & conferences.

A Compact Design of Planar Array Antenna with Fractal Elements for Future Generation Applications

Naser Ojaroudiparchin, Ming Shen, and Gert Frølund Pedersen

Antennas, Propagation, and Radio Networking (APNet) Section
Department of Electronic Systems, Faculty of Engineering and Science
Aalborg University, DK-9220, Aalborg, Denmark
naser@es.aau.dk, mish@es.aau.dk, gfp@es.aau.dk

Abstract — In this paper, a planar phased array fractal antenna for the future fifth generation (5G) applications is presented. The proposed array antenna is designed to operate at 22 GHz. 64 patch antenna elements with coaxial-probe feeds have been used for the proposed design. The antenna elements are based on Vicsek fractal geometry where the third iteration patches operate over a wide bandwidth and contribute to improve the efficiency and realized gain performance. The designed planar array has more than 22 dB realized gain and -0.3 dB total efficiency when its beam is tilted to 0° elevation. The antenna configuration is simple, easy to fabricate and can be integrated into 5G devices. Simulated and measured results are presented to validate the usefulness of the proposed phased array antenna for 5G applications.

Index Terms — 5G wireless communications, fractal antenna, patch antenna, planar phased array.

I. INTRODUCTION

Due to the increasing need for future applications requiring even higher data rates (such as wireless broadband connections, massive machine type communications and highly reliable networks), the research and development of fifth-generation (5G) mobile communication systems have started. It is predicted that the commercial deployment of 5G will be approximately in the early of 2020s [1-3]. One major difference in the enabling technologies for 4G and 5G communication is the use of millimeter wave (mm-Wave) frequencies, aiming for wider bandwidth and higher spectral efficiency [4]. However, moving from the cellular carrier frequencies used today (<4 GHz) up towards the mm-Wave bands introduces new aspects that need careful consideration [5-7].

As a solution to minimizing the antenna size while keeping high radiation efficiency, fractal antennas have drawn special attention in microwave engineering. In many cases, the use of fractal element antennas can simplify circuit design. Another benefit of fractal

antennas is that, fractal antennas are in form of a printed circuit board (PCB), which can reduce fabrication costs.

Basically, a fractal is a rough or fragmented geometric shape that can be subdivided in parts, each of which is a reduced-size copy of the whole. Fractals are generally self-similar and independent of scale. Fractal antenna theory uses a modern (fractal) geometry that is a natural extension of Euclidian geometry [8-10].

This paper focuses on the design and implementation of a planar phased array fractal antenna for millimeter-wave 5G mobile applications. The proposed design shown in Fig. 1 consists of 64-elements of 22 GHz Vicsek fractal patch antenna elements with coaxial-probe feed. The proposed phased array antenna has high efficiencies, high gains and good beam steering characteristics. The analysis and performance of the antenna are obtained by using CST software [11].

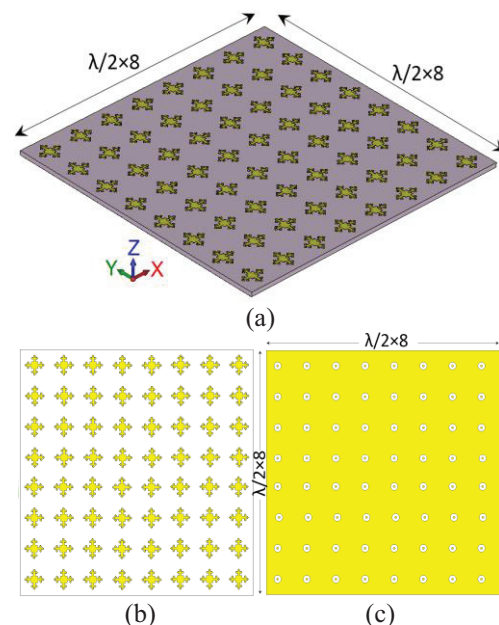


Fig. 1. Proposed antenna configuration: (a) side view, (b) top layer, and (c) bottom layer.

II. ANTENNA DESIGN

The fractal geometries are generated by an iterative process performed on a simple starting topology. As can be observed in Fig. 2 (a), the proposed fractal shape begins as a simple square (0th order). Next, divide the square into nine equal small squares and move the four at comers [9].

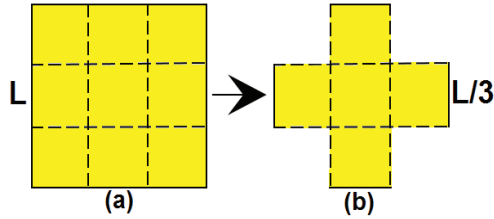


Fig. 2. Generating rules of Vicsek shape: (a) the 0th order and (b) the 1st order.

According to the properties of self-similarity, the fractal dimension D_s is defined as:

$$D_s = \frac{\log(N)}{\log(R)}, \quad (1)$$

where N is the total number of distinct copies similar to (1), which is scaled down by a ratio of $1/r$. For the Vicsek shape, $N=5$ and $r=3$. So the fractal dimension is:

$$D_s = \frac{\log 5}{\log 3} = 1.4650.$$

The resonant frequencies can be carried out using the following equation [12]:

$$(f_r)_{mn} = \frac{1}{2\pi\sqrt{\left(\frac{m\pi}{l}\right)^2 + \left(\frac{n\pi}{w}\right)^2}} \Big|_{l=w} = \frac{c}{2l\sqrt{\epsilon_r}} \sqrt{m^2 + n^2}, \quad (2)$$

where (f_r) is the mn mode resonant frequency, l , w are the two dimensions ($w=l$) of the square, and c is the velocity of light. The fundamental frequency corresponds to 22 GHz by using the equation above.

As illustrated in Fig. 1, 64-elements of Vicsek fractal patch antenna have been used for the proposed design. For beam forming array, the distance between antenna elements (d) is calculated near $\lambda/2$ ($f_0=22$ GHz). The overall dimension of the proposed planar phased array antenna is $8\lambda/2 \times 8\lambda/2$.

III. SINGLE ELEMENT FRACTAL PATCH ANTENNA

In this section the fundamental properties of the designed Vicsek fractal patch antenna have been investigated. The geometry of the single element patch antenna is illustrated in Fig. 2. A microstrip patch antenna is basically a conductor printed on the top layer of the substrate with a full ground plane. It can be fed in a variety of ways such as microstrip feed, coaxial feed, aperture coupled feed, and proximity coupled feed [13].

In this paper, the coaxial probe feeding technique has been used. The basic geometry of the radiation patch is a square of length L , on which repeated iterations lead to the Vicsek snowflake geometry as shown in Fig. 3.

As illustrated, the fractal shape begins as a simple square which its iteration order is zero [Fig. 4 (a)]. Next, divide the square into nine equal small squares and move the four at comers [Fig. 4 (b)]. In order to obtain the second and third iteration [Figs. 4 (c) and (d)], the same process is applied for the small squares located at the corners of radiation patch. The values of the antenna parameters are listed in Table 1.

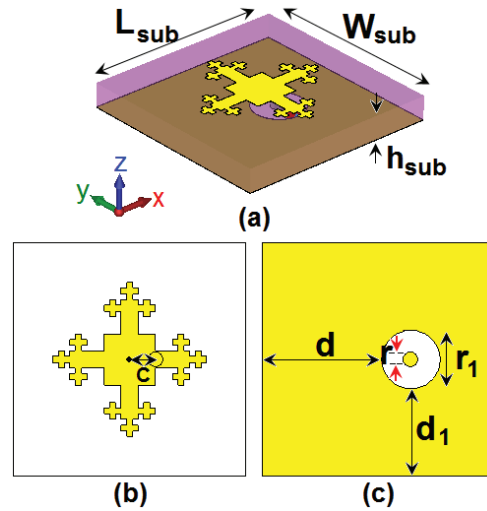


Fig. 3. Configuration of single element antenna: (a) side view, (b) top layer, and (c) bottom layer.

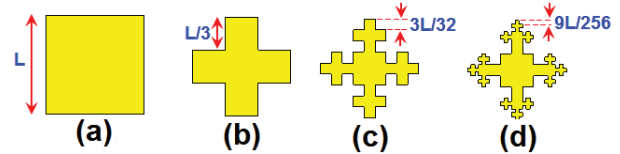


Fig. 4. Vicsek snowflake in its different iteration stages: (a) basic geometry, (b) first iteration, (c) second iteration, and (d) third iteration.

Table 1: Dimensions of the antenna parameters

Parameter	W_{sub}	L_{sub}	h_{sub}	L
Value (mm)	6.8	6.8	0.8	4.5
Parameter	r_1	d	d_1	C
Value (mm)	0.5	3.4	2.75	0.75

Figure 5 illustrates the simulated S_{11} characteristics of the patch antenna for iteration stages of the fractal geometry. It is observed that the Vicsek fractal geometry improves the impedance matching characteristic of the antenna at 22 GHz along the bandwidth enhancement of the antenna [14].

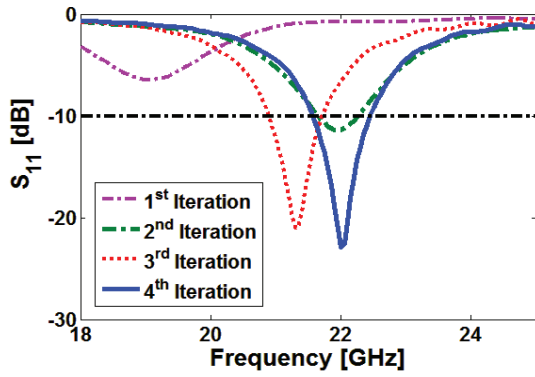


Fig. 5. Simulated S_{11} characteristics of the Vicsek fractal antenna for different iterations stages.

Figure 6 shows the simulated radiation patterns of the antennas shown in Fig. 4 at resonance frequencies. As illustrated, by using the proposed fractal structure, the efficiency and realized gain characteristics can be improved. It can be seen, the single element 22 GHz Vicsek patch has values of -0.1 dB and 6.8 dB for radiation efficiency and realized gain characteristics respectively.

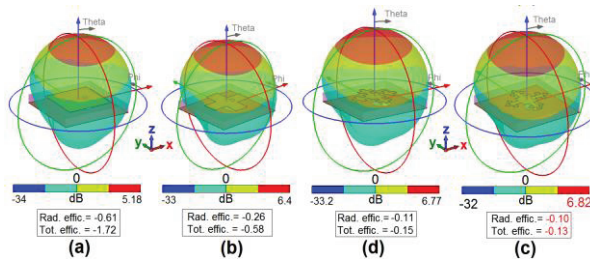


Fig. 6. Simulated radiation patterns at resonance frequencies of the antennas for different iteration stages shown in Fig. 4.

Figure 7 shows the simulated surface current distribution for the antenna at 22 GHz. As illustrated, the currents flow around the Vicsek fractal radiator. It can be seen, the distribution of the current around the radiation patch is almost uniform due to symmetrical configuration of the radiator. One of the important parameters of the proposed design is the feeding point. Its main effect occurs on the operation frequency of the antenna.

Figure 8 illustrates the simulated S_{11} characteristics with various values of C (distance between feeding point and center of the radiator). As the distance between feeding point and center of antenna increases from 0.6 to 0.8 mm, the operation frequency of antenna is varied from 21.6 to 22.2 GHz. From this result, we can conclude that the antenna operation frequency can be controlled by changing the antenna feeding point. For $C=0.75$ mm, the antenna has a good impedance

matching at the desired frequency (22 GHz).

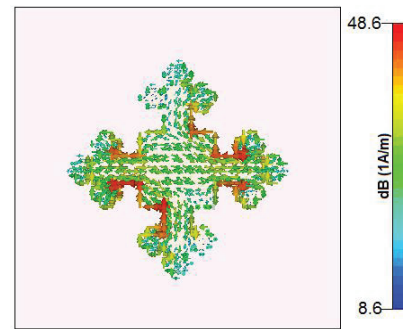


Fig. 7. Simulated surface current distribution of the single antenna element at 22 GHz.

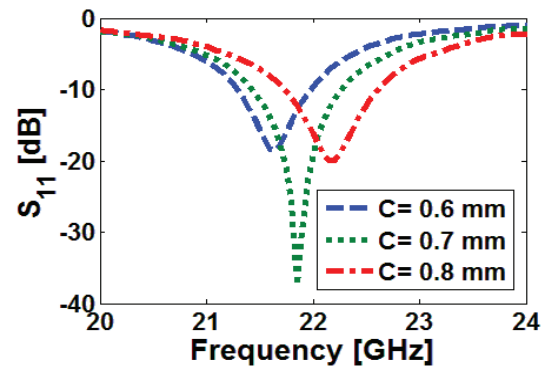


Fig. 8. Simulated S_{11} characteristics of the antenna for different values of C .

Simulated maximum gain, radiation and total efficiencies of the single element patch antenna over operation frequency range are illustrated in Fig. 9. As seen, the antenna radiation and total efficiencies are better than -0.2 and -1 dB, respectively. In addition, the antenna has more than 6.7 dBi maximum gain.

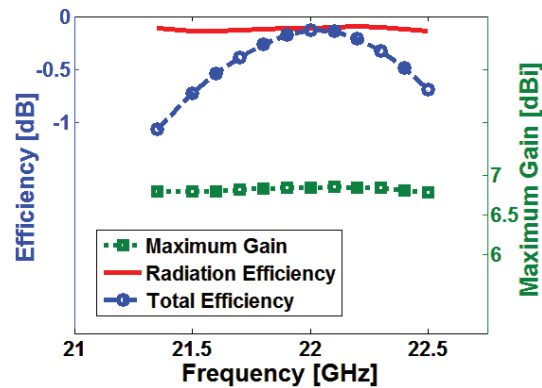


Fig. 9. Simulated maximum gain, radiation and total efficiencies of the antenna over the operation frequency range.

IV. 1×8 LINEAR ARRAY USING THE PROPOSED FRACTAL STRUCTURE

Figure 10 shows the configuration of the 1×8 linear array with eight elements of 22 GHz patch antennas. For beam forming array, the distance between elements is calculated $\lambda/2=6.8$ mm. The simulated S-parameters of the linear array are illustrated in Fig. 11.

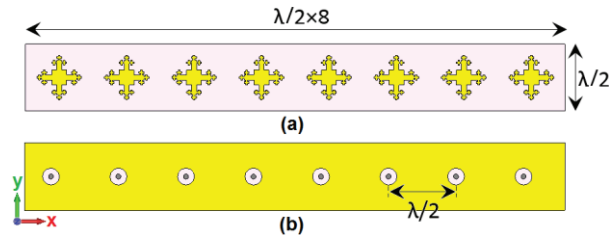


Fig. 10. Geometry of the linear array: (a) top layer and (b) bottom layer.

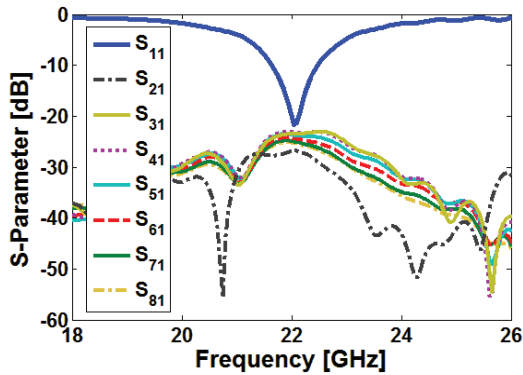


Fig. 11. Simulated S-parameters of the linear array.

As illustrated, the antenna can operate at the frequency range of 21.6 to 22.4 GHz. It can be seen that the antenna has -22 dB return loss and the highest mutual-coupling between the elements is less than -23 dB which is sufficient for beam steering issue.

3D beam steering characteristic of the array radiation patterns with realized gain values at different scanning angles (0° , 30° , and 60°) at 22 GHz are shown in Fig. 12. The analysis and performance of the antenna beams are obtained by post-processing using CST software. The shape and direction of the array beams are determined by relative phases amplitudes applied to each radiating element as below:

$$\psi = 2\pi(d/\lambda) \sin \theta, \quad (3)$$

where d is the distance between the radiation elements and θ is the angle of incidence. In order to see the radiation beam of the array at 30° (by considering that the elements are arranged on a linear array with distance of $\lambda/2$), the phase shift between adjacent sources will be calculated $\Psi=90^\circ$. The next step is applying 90° phased-shifting with same values of the

amplitude=1 for the radiation elements, respectively. Same process of the phase shifting could be used of the planar phased arrays.

As seen, the proposed antenna has a good beam steering property which is highly effective to cover the spherical beam-coverage for 5G devices. The beam-steering characteristic of the proposed antenna for plus/minus (+/-) scanning angles are expected to be the same.

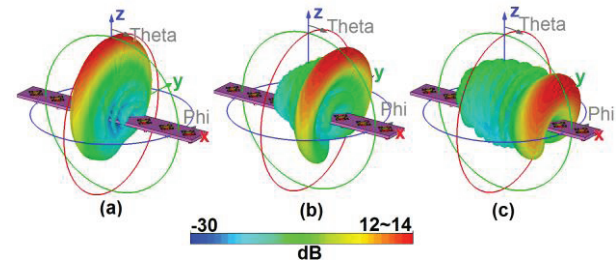


Fig. 12. 3D Radiation patterns of the linear array at different scanning angles: (a) 0° , (b) 30° , and (c) 60° .

Figure 13 illustrates the simulated directivity, radiation efficiency and total efficiency characteristics of the proposed antenna in the scanning range of 0 to 70 degree. As seen, the antenna radiation and total efficiencies are better than -0.5 dB (90%). Furthermore, as can be seen, when the scanning angle of beam-steering characteristic is ≤ 60 , the proposed antenna has more than 12 dBi directivity.

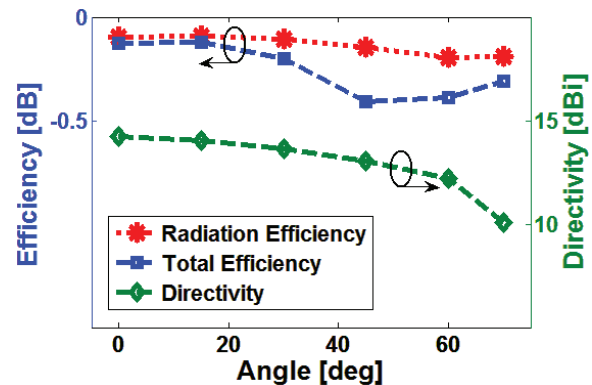


Fig. 13. Simulated directivity, radiation efficiency and total efficiency characteristics of the antenna at different scanning angles.

V. THE PROPOSED PLANAR PHASED ARRAY 5G ANTENNA

64 Vicsek patches have been used to design the final planar 5G antenna. The proposed planar array with final design has been fabricated to validate the performance. Figure 14 shows the photograph of fabricated antenna. The simulated and measured S_{11}

characteristics of the antenna element are shown in Fig. 15. As illustrated, the antenna has a good response in the frequency range of 21.5 to 22.5 GHz.

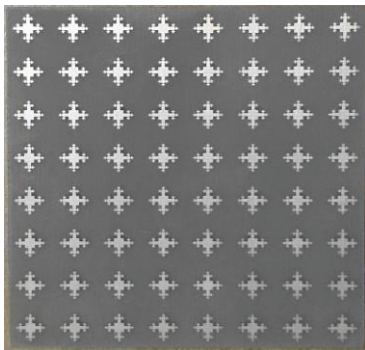


Fig. 14. Fabricated prototype (top-view).

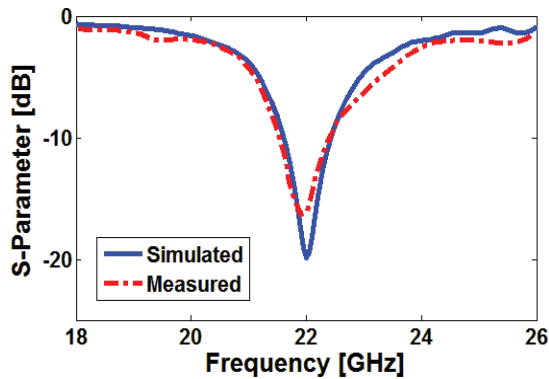


Fig. 15. Measured and simulated S_{11} characteristics of the proposed antenna.

Simulated surface-current distribution for the antenna at 22 GHz (resonance frequency) is shown at Fig. 16. As illustrated, the current flows are distributed around the fractal patch elements and the effect of the full ground plane to reduce the power of radiation is insignificant.

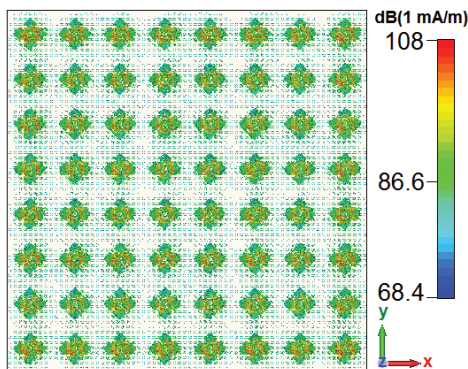


Fig. 16. Simulated current distribution of the proposed planar phased array at 22 GHz (resonance frequency).

Figure 17 shows the radiation beams of the proposed 8×8 phased array antenna with realized gain values for different scanning angles at 22 GHz. It can be seen, the antenna has a good beam steering characteristic with high-level gains at different scanning angles. In addition the proposed array has high efficiencies at different scanning angles.

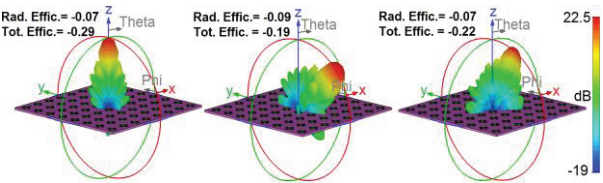


Fig. 17. 3D radiation patterns of the proposed planar array at different scanning angles.

Figure 18 shows the directivity characteristics of the single element, linear, and planar arrays of the proposed fractal patch antenna. It can be seen that the designed arrays have good performances. More than 7, 13, and 23 dBi directivity values with good radiation behaviors and low back lobes have been achieved for the arrays.

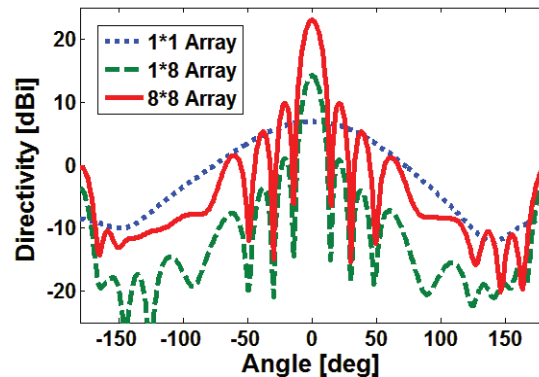


Fig. 18. Simulated directivity characteristics of the single element, linear, and planar array antennas at 0° scanning angle.

As can be observed in Fig. 1, eight 1×8 uniform linear arrays are used where each radiating element of them is excited by signals with equal magnitude. One of the most important system blocks to achieve a functional array antenna is the feed network. There are various feed network techniques that could be used for this purpose (such as the corporate feed network shown in Fig. 19). The power dividers (such as Wilkinson) divide the power to equally 1:N and also unequally by changing the input and output. The feed network of proposed phased array can be implemented using low loss phase shifters (such as HMC933LP4E) for beam steering issue. The HMC933LP4E phase shifter [15] is

controlled via an analog-control voltage from 0 to +13V. It has a low insertion loss characteristic in the operation frequency of 18-24 GHz.

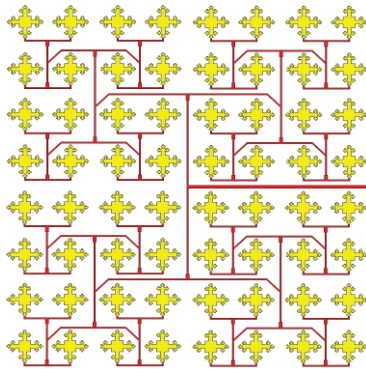


Fig. 19. Schematic of the corporate feed network for the planar phased arrays.

Compared with previous works [16-20], the proposed phased array antenna provides attractive features such as high-gain/high-directivity, low-profile/symmetric structure, high efficiency and easy to fabricate. Vicsek fractal radiation elements have been used as a solution to minimizing the antenna overall size while keeping high radiation efficiency. The overall dimension of the proposed design is $55 \times 55 \text{ mm}^2$. Using the fractal elements instead of conventional structure, the antenna provides superior antenna fundamental radiation performance. The values of the antenna gain, directivity and efficiency characteristics when its beam is tilted to 0° are 22.5 dB, 23 dBi, and -0.29 (93%).

The design and its radiation elements have symmetrical configurations which causes the antenna provides directional and symmetrical radiation patterns. Furthermore, the antenna has good beam-steering property with high-gain values and low side/back lobes at different angles. It also has wide-angle scanning which makes it suitable for phased array applications.

VI. INVESTIGATION ON THE ARRAY PERFORMANCE WITH DIFFERENT NUMBER OF RADIATORS

In this section, the investigation on the performance of the proposed 22 GHz planar array with different number of the patch antennas has been done.

Figure 20 shows the configurations of the arrays with 2×2 , 4×4 , and 8×8 numbers of antenna elements. The spacing between the elements of the arrays is $\lambda/2$ of 22 GHz. Figure 21 shows the simulated S-parameters (S_{11} & S_{21}) of the arrays. It can be seen that the designed arrays have good and similar performances.

As illustrated in Fig. 21 (a), -25, -28, and -35 dB reflection coefficients (S_{11}) are achieved for the 2×2 ,

4×4 , and 8×8 planar arrays. Figure 22 (b) shows the highest mutual couplings (S_{21}) between antenna elements for the proposed arrays. As can be observed, the designed arrays have sufficient mutual couplings between the radiation elements (less than -24 dB).

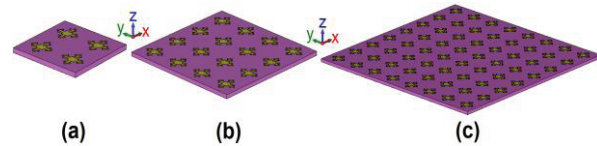


Fig. 20. Configuration of the planar arrays: (a) 2×2 , (b) 4×4 , and (c) 8×8 .

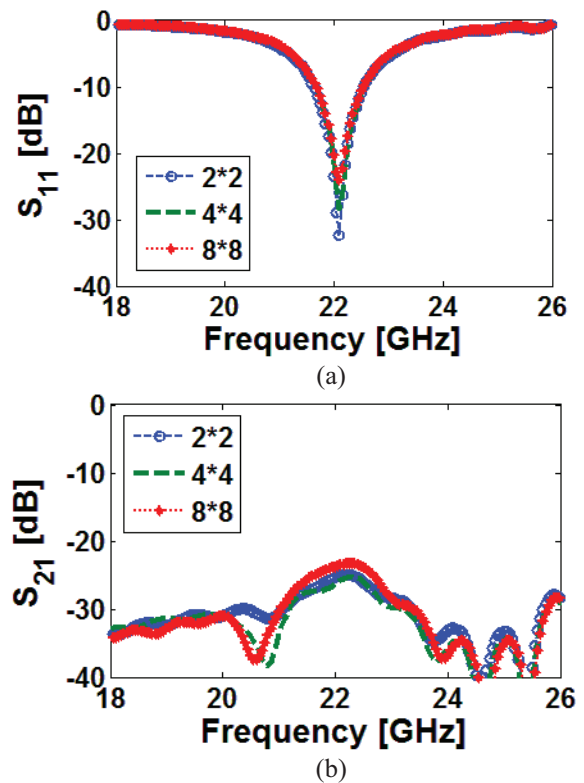


Fig. 21. (a) S_{11} and (b) S_{21} of the planar arrays.

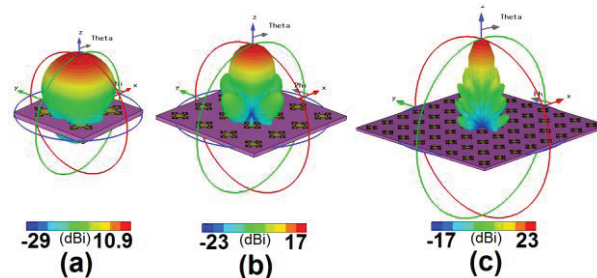


Fig. 22. 3D radiation beams of the planar arrays at 0° scanning angle for: (a) 2×2 , (b) 4×4 , and (c) 8×8 .

3D directional radiation beams of the arrays when their beams are tilted to 0° elevation are shown in Fig. 22. More than 10.9, 16.5, and 23 dBi directivity values with good radiation behaviors and low back/side lobes have been achieved for the planar arrays.

Table 2 summarizes the performances of the designed arrays in terms of realized gain, efficiency, bandwidth (BW), reflection coefficient (RC) and mutual coupling (MC). As seen, the arrays exhibit good performance in in different terms of the antenna parameters.

Table 2: Characteristics of the planar arrays at 0°

Param.	Gain	Effic.	BW	RC	MC
1×1	6.82 dB	-0.13 dB	1 GHz	-23 dB	N/A
2×2	10.7 dB	-0.23 dB	0.9 GHz	-35 dB	-26 dB
4×4	16.7 dB	-0.28 dB	0.9 GHz	-28 dB	-26 dB
8×8	22.7 dB	-0.29 dB	0.9 GHz	-25 dB	-24 dB

VII. CONCLUSION

An 8×8 phased array 5G antenna with fractal patch elements is designed and investigated in this study. The antenna elements are designed based on Vicsek fractal geometry to operate at 22 GHz. The proposed antenna has good performance in terms of impedance matching, antenna gain, efficiency, and beam steering characteristics. The antenna also features compact and symmetric structure. The results show that the proposed antenna could be used in high speed wireless communication systems in particular for use in 5G mobile devices. In addition, the radiation characteristics of the proposed planar phased array with different number of the radiators have been investigated.

REFERENCES

- [1] P. Zhouyue and F. Khan, "An introduction to millimeter-wave mobile broadband systems," *IEEE Communications Magazine*, vol. 49, pp. 101-107, 2011.
- [2] T. S. Rappaport, et al., "Millimeter wave mobile communications for 5G cellular: It will work!," *IEEE Access*, vol. 1, pp. 335-349, 2013.
- [3] W. Roh, et al., "Millimeter-wave beamforming as an enabling technology for 5G cellular communications: Theoretical feasibility and prototype results," *IEEE Commun. Mag.*, vol. 52, pp. 106-113, 2014.
- [4] Y. Wang, et al., "5G mobile: Spectrum broadening to higher-frequency bands to support high data rates," *IEEE Vehicular Technology Magazine*, vol. 9, pp. 39-46, 2014.
- [5] S. Rajagopal, et al., "Antenna array design for multi-Gbps mm-wave mobile broadband communication," in *IEEE Globecom*, Dec. 2011.
- [6] T. S. Rappaport, et al., "Broadband millimeter-wave propagation measurements and models using adaptive-beam antennas for outdoor urban cellular communications," *IEEE Transactions on Antennas and Prop.*, vol. 61, no. 4, pp. 1850-1859, 2013.
- [7] T. Bai and R. Heath, "Coverage and rate analysis for millimeter wave cellular networks," *IEEE Transactions on Wireless Communications*, vol. 14, pp. 110-1114, 2015.
- [8] D. H. Werner and S. Ganguly, "An overview of fractal antenna engineering research," *IEEE Antennas and Propagation Magazine*, vol. 45, pp. 38-57, 2003.
- [9] W. Hongjian and G. Benqing, "The full wave analysis of fractal antenna," *3rd International Symposium on Electromagnetic Compatibility*, pp. 135-138, 2002.
- [10] B. B. Mandelbort, *The Fractal Geometry of Nature*. New York, W. H. Freeman, 1983.
- [11] CST Microwave Studio, ver. 2014, CST, Framingham, MA, USA, 2014.
- [12] C. A. Balanis, *Antenna Theory: Analysis and Design*. Wiley, New York, 1982.
- [13] R. Garg, P. Bhartia, I. Bahl, and A. Ittipiboon, *Microstrip Antenna Design Handbook*. Norwood, MA: Artech House, 2000.
- [14] C. Puente, J. Ponmeu, R. Pous, and A. Cardama, "On the behavior of the Sierpinski multiband antenna," *IEEE Transactions on Antennas and Propagation*, vol. 46, pp. 517-524, 1998.
- [15] HMC933LP4E, "Analog phase shifter," Hittite Microwave Company.
- [16] S. E. Valavan, D. Tran, A. G. Yarovoy, and A. G. Roederer, "Dual-band wide-angle scanning planar phased array in X/Ku-bands," *IEEE Trans. Antennas and Propagation*, vol. 62, pp. 2514-2521, 2014.
- [17] J. Wu, Y. J. Cheng, and Y. Fan, "Millimeter-wave wideband high-efficiency circularly polarized planar array antenna," *IEEE Trans. Antennas and Propagation*, vol. 64, pp. 535-542, 2014.
- [18] D. L. Lavanya, "Design of 8×8 circularly polarized planar array antenna for ISM band," *2012 International Conference on Radar, Communication and Computing (ICRCC)*, SKP Engineering College, Tiruvannamalai, TN, India, pp. 112-116, 21-22 Dec. 2012.
- [19] P. Padilla de la Torre and M. Sierra Castafiort, "Transmitarray for Ku band," *The Second European Conference on Antennas and Propagation (EuCAP)*, Edinburgh, UK, 11-16 Nov. 2007.
- [20] S. E. Valavan, D. Tran, A. G. Yarovoy, and A. G. Roederer, "Planar dual-band wide-scan phased array in X-band," *IEEE Trans. Antennas and Propagation*, vol. 62, pp. 5370-5375, 2014.



Naser Ojaroudiparchin was born in 1986 in Iran. He received M.Sc. degree in Telecommunication Engineering from Shahid Rajaei University (SRITU), Tehran, Iran in 2013. Since Nov. 2014, he is working as a Guest Researcher in Antennas, Propagation and Radio Networking (APNet) section, Department of Electronic Systems, Aalborg University, Aalborg, Denmark. His research interests include multi-band/UWB antennas, mm-Wave phased array 5G antennas, band-stop/band-pass microwave filters, and reconfigurable structure.



Ming Shen received the Master and Ph.D. degrees in Electrical Engineering from the University of Chinese Academy of Sciences, China in 2005, and from Aalborg University, Denmark in 2010, respectively. Since 2007, he has been with the Department of Electronic Systems, Aalborg University, where he is currently an Assistant Professor. He is the author of more than 30 technical papers and book chapters. His current research interests include: energy harvesting and battery-less low power circuits and systems, 5G mm-Wave circuits and antennas, remote patient monitoring, and wireless power transfer technologies.



Gert Frølund Pedersen received the B.Sc. E.E. degree, with honor, in Electrical Engineering from College of Technology in Dublin, Ireland in 1991, and the M.Sc. E.E. degree and Ph.D. from Aalborg University in 1993 and 2003. He has been with Aalborg University since 1993 where he is a Full Professor heading the Antenna, Propagation and Networking LAB with 36

researchers. Further he is also the Head of the doctoral school on wireless communication with some 100 Ph.D. students enrolled. His research has focused on radio communication for mobile terminals especially small Antennas, Diversity systems, Propagation and Biological effects and he has published more than 175 peer-reviewed papers and holds 28 patents. He has also worked as consultant for developments of more than 100 antennas for mobile terminals including the first internal antenna for mobile phones in 1994 with lowest SAR, first internal triple-band antenna in 1998 with low SAR and high TRP and TIS, and lately various multi antenna systems rated as the most efficient on the market. He has worked most of the time with joint university and industry projects and have received more than 12 M\$ in direct research funding. Latest he is the project leader of the SAFE project with a total budget of 8 M\$ investigating tunable front end including tunable antennas for the future multiband mobile phones. He has been one of the pioneers in establishing Over-The-Air (OTA) measurement systems. The measurement technique is now well established for mobile terminals with single antennas and he was chairing the various COST groups (swg2.2 of COST 259, 273, 2100 and now ICT1004) with liaison to 3GPP for over-the air test of MIMO terminals.

A Compact Design and New Structure of Monopole Antenna with Dual Band Notch Characteristic for UWB Applications

S. Hoseyni¹, J. Nourinia², Ch. Ghobadi², Sv. Masumina², and B. Mohammadi²

¹ Sciences and Researches
Urmia Kamal Institute of Higher Education, Urmia, Iran
saeednorton1@gmail.com

² Department of Electrical Engineering
Urmia University, Urmia, Iran
j.nourinia@urmia.ac.ir, ch.ghobadi@urmia.ac.ir, sv.masumina@urmia.ac.ir, b.mohammadi@urmia.ac.ir

Abstract — In this paper, a compact design and new structure of monopole antenna with dual band notch characteristics for UWB applications has been presented. The antenna consists of a triangular patch with C-shaped slot, two L-shaped and one split ring shaped parasitic backplane elements structure. By inserting three slots in the rectangular truncated ground plane as defected ground structures (DGSs), much wider impedance bandwidth can be produced, and moreover to improve the input matching quality of the antenna at all its operating bands which are spread in a vast frequency range, a modified stepped feed-line is employed. These changes much improves the antenna's impedance bandwidth by 112% which covers the entire UWB bandwidth range. In order to generate single band notch characteristic, split ring shaped parasitic element backplane structure is utilized on the ground plane side of the substrate. In addition, by etching a C-shaped slot on the radiating patch, a dual band notch function is achieved. The measured frequency results show an impedance bandwidth of 3.15-10.78 GHz for a Voltage Standing Wave Ratio (VSWR) less than 2 with two eliminated bands placed at 3.49-3.81 GHz (320 MHz, 8.8%) and 5.24-6.22 GHz (980 MHz, 17%), which reject the WiMAX band, and Wireless Local Area Network (WLAN) band, respectively. A prototype was fabricated and measured based upon optimal parameters and experimental results show consistency with simulation results. The measured radiation patterns of proposed antenna for most frequencies are omnidirectional and this antenna as wide impedance bandwidth.

Index Terms — C-shape slot, dual band notch, monopole antenna, split ring shaped parasitic element, ultra wideband (UWB).

I. INTRODUCTION

In 2002, Federal Communications Commission (FCC) of US declares the frequencies from 3.1 to 10.6 GHz as an unlicensed band for wireless radio communication [1]. This technology uses short duration pulses that result in very large or wideband transmission bandwidths. With proper technical standards, UWB devices can be operated using spectrum, occupied by existing radio services without causing interference, thereby permitting scarce spectrum resources to be used more efficiently [2]. One key component, necessary to fulfill these requirements in UWB system, is a planar antenna that is capable of providing a wide impedance bandwidth. The antenna needs to work over the UWB, as it is defined by the FCC. In addition, it needs to give omnidirectional radiation coverage over the entire UWB frequency range [3]. A lot of effort has been put into designing new antennas which can satisfy the requirements of modern communication systems. As a result of accelerating growth of UWB technology, there has been a vast body of literature introducing novel antennas for UWB applications and systems [4-13].

UWB systems have met a hostile radio environment which may cause potential interferences to the UWB band. For instance, IEEE 802.16 WIMAX system operates at 3.3–3.7 GHz and IEEE 802.11a WLAN system operates at 5.15–5.825 GHz [6-10]. However, the use of filters increases the complexity and cost of the UWB system. The frequency band notch characteristics can be essentially achieved using one of the two common methods [13]. Two common methods to creation the band notch are using C-shaped, T-shaped, H-shaped, U-shaped, L-shaped slots [4-8], on the radiation patch or on the ground plane and the parasitic elements with various geometric shapes on the back-plane of antenna or in the

vicinity of the patch [12].

In this paper, a dual band notch compact monopole antenna has been presented. In the proposed structure to improve the bandwidth, three slots in the rectangular truncated ground plane and a modified stepped feed-line is used which creates an extra resonance, and hence, much wider impedance bandwidth can be produced. This change much improves the antenna's impedance bandwidth up to 112%. Adding a split ring-shape as a parasitic element on the back-plane of the antenna structure leads to a single band notch function which occurs at frequencies near 5.5 GHz, and then cutting a C-shaped slot on the antenna radiating patch creates an added band notch function at frequencies next to 3.7 GHz. The designed antenna has a small size of $20 \times 18 \times 1.6 \text{ mm}^3$. Good VSWR and radiation pattern characteristics are obtained in the frequency band of interest. Also, the antenna is provided for parametric analysis. The finally design of the proposed antenna has been fabricated and tested and the results are acceptable.

II. ANTENNA DESIGN

The dual band notch compact monopole antenna with C-shaped slot and split ring shaped parasitic element fed by a $50\text{-}\Omega$ microstrip line is shown in Fig. 1, which is printed on a FR4 substrate with thickness of 1.6 mm, permittivity of 4.4, and loss tangent of 0.018. The basic antenna structure consists of a radiating triangular patch, a $50\ \Omega$ microstrip modified stepped feed-line, and three slots in the rectangular truncated ground plane. The radiating stub is connected to the feed-line of width W_F (2.8 mm), as shown in Fig. 1 (b). Proposed antenna is connected to a $50\ \Omega$ SMA connector for signal transmission. A single band notch function is provided by inserting a split ring shaped parasitic element backplane and a dual band notch characteristic is obtained by using a C-shaped slot in the triangular radiating patch. The planar monopole antenna with its final design parameters was constructed, and the numerical and experimental results of the input impedance and radiation characteristics are presented and discussed. The parameters of this proposed antenna are studied by changing one parameter at a time while others were kept fixed. Simulated results are obtained using Ansoft simulation software High-Frequency Structure Simulator (HFSS) [14]. Final design parameters values of the presented antenna are specified in Table 1.

Figure 2 shows the structure of various antennas which were used for simulation studies of UWB antenna without notch bands. VSWR characteristics for ordinary triangular patch antenna (Fig. 2 (a)), triangular patch antenna with three slots in the rectangular truncated ground plane (Fig. 2 (b)), proposed UWB antenna without split ring-shape parasitic element and C-shape slot (Fig. 2 (c)) are compared in Fig. 3. As shown in Fig. 3, three slots in the rectangular truncated ground plane directly

influence both the upper and lower band edge frequencies. As illustrated in Fig. 3, the rectangular slots on the ground plane conductor play an important role in the broadband characteristic of the proposed antenna and also in determining the impedance matching sensitivity of this antenna [7-9]. It is found that by etching steps on the feed-line additional resonance (at 9 GHz) is excited, and hence, much wider impedance bandwidth can be produced, because of multi-resonance characteristics.

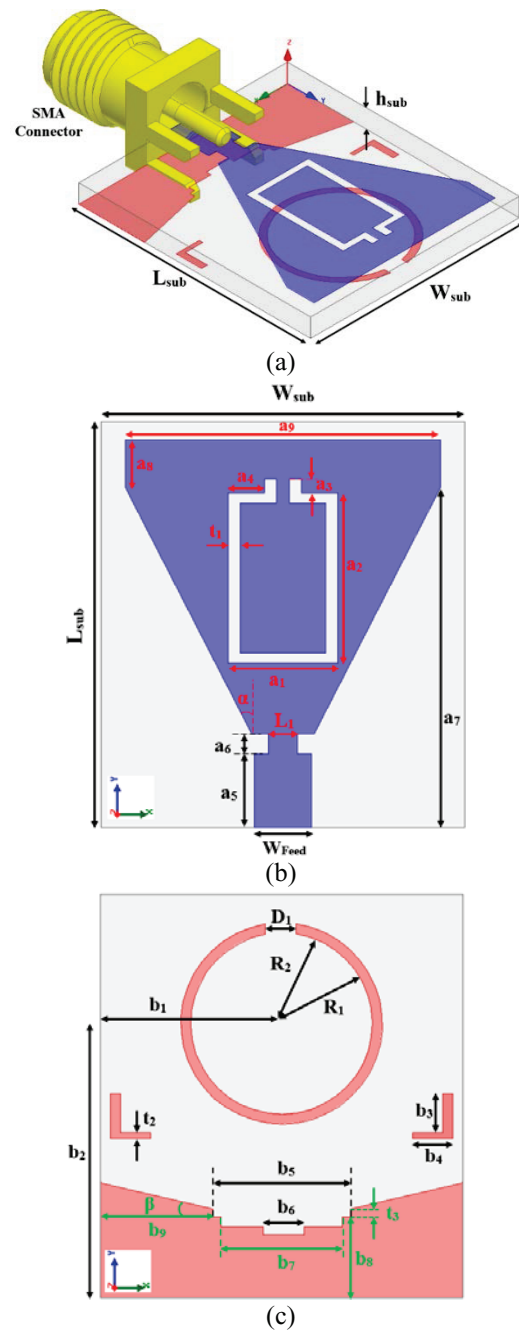


Fig. 1. Geometry of the proposed monopole antenna: (a) side view, (b) top view, and (c) bottom view.

Table 1: The final dimensions of the designed monopole antenna

Param.	mm	Param.	mm	Param.	mm
a ₁	5	b ₁	9	W _{sub}	18
a ₂	8.1	b ₂	13.7	L _{sub}	20
a ₃	0.6	b ₃	1.8	R ₁	4.5
a ₄	1.5	b ₄	2	R ₂	5
a ₅	3.5	b ₅	6.8	D ₁	1.5
a ₆	1	b ₆	2	L ₁	1.5
a ₇	16.7	b ₇	6	t ₁	0.5
a ₈	2.3	b ₈	4.3	t ₂	0.3
a ₉	15.5	b ₉	5.6	t ₃	0.9

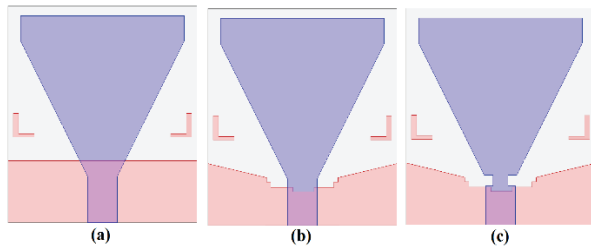


Fig. 2. (a) Ordinary triangular patch antenna, (b) triangular patch antenna with three slots in the rectangular truncated ground plane, and (c) proposed UWB antenna without the split ring-shape parasitic element and C-shape slot.

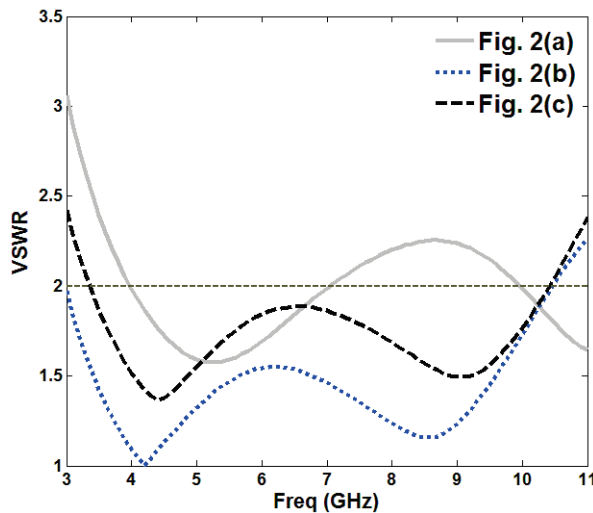


Fig. 3. Simulated VSWR characteristics for antennas shown in Fig. 2.

To understand the phenomenon behind this new excited resonance performance by modified stepped feed-line, the simulated current distributions on the triangular patch at 9 GHz for the antennas with and without etching steps on the feed line are compared in Fig. 4. As it can be observed in Fig. 4, at 9 GHz the current is more

dominate along the edges of the modified stepped feed-line, and therefore, the antenna impedance changes at this frequency due to the resonant properties of these etching [10-12].

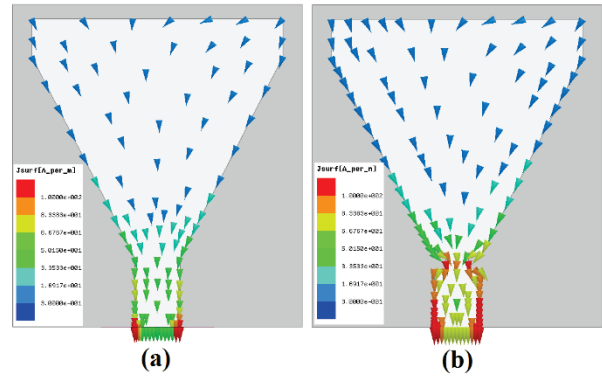


Fig. 4. Simulated surface current distribution on the triangular patch antenna with: (a) the simple feed-line at 9 GHz, and (b) the modified stepped feed-line at 9 GHz.

Figure 5 shows the structure of various antennas used for band notch function simulation studies. The VSWR characteristics for the triangular patch antenna without split ring-shape parasitic element and C-shape slot (Fig. 5 (a)), antenna with C-shaped slot on the radiating patch (Fig. 5 (b)), and the proposed antenna (Fig. 5(c)) are compared in Fig. 6. As it is observed in Fig. 6, adding C-shaped slot on the radiating patch of the antenna structure generates single band notch characteristics. In order to eliminate interferences from WiMAX system line break operating at 3.5-3.7 GHz, a C-shaped slot with a width of 0.5 mm is etched on the radiation patch to generate band notch function. The total length of the C-shaped slot on the radiation patch is $L_{Notch}=a_1+2[a_2+a_3+a_4]$ [10-11]. Besides WiMAX system, WLAN operating from 5.3 to 6 GHz may cause interferences to the UWB system too. By printing a split ring-shape as a parasitic element, on the backplane of proposed antenna, 5.7 GHz band-notched function is realized [7].

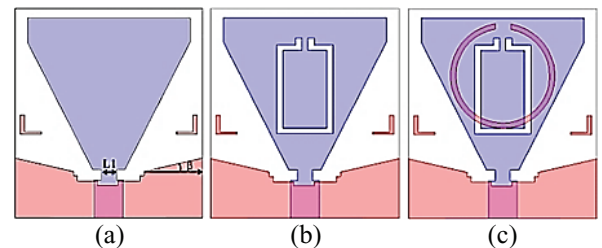


Fig. 5. (a) Primary antenna without split ring-shape parasitic element and C-shape slot, (b) antenna with C-shape slot, and (c) proposed antenna.

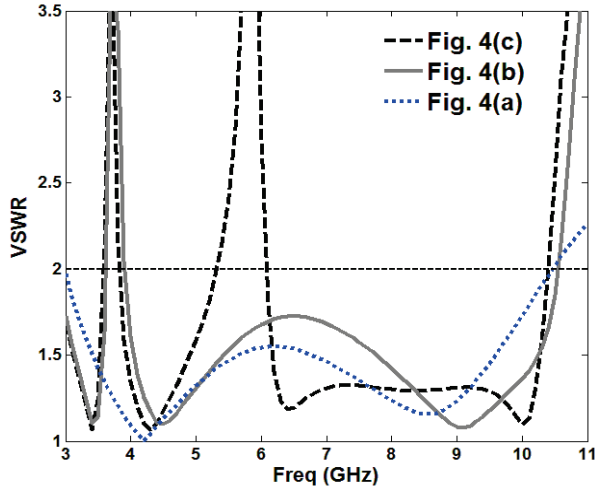


Fig. 6. Simulated VSWR characteristics for antennas shown in Fig. 5.

To understand the phenomenon behind this dual band notch performance, the simulated current distribution for the proposed antenna at the notched center frequencies of 3.6 GHz and 5.7 GHz is presented in Fig. 7 (a) and Fig. 7 (b), respectively. The large current distribution with red vector and small current distribution with blue vector is shown in Fig. 7. As it can be observed from Fig. 7 (a), at the lower notched center frequency (3.6 GHz), the current flows are more dominant around the C-shaped slot and they are oppositely directed between the slot edges [8]. Therefore, the antenna impedance changes at this frequency due to the band notch properties of the proposed structure, and as a result the desired high attenuation is achieved. According Fig. 7 (b), at the upper notched center frequency (5.7 GHz), the current flows are more dominant around the parasitic element, the surface currents are oppositely directed between this parasitic element and the radiating patch [9]. Therefore, the resultant radiation fields cancel, and high attenuation near the notched frequencies is produced, and as a result, the antenna does not radiate efficiently at the notched frequencies [13].

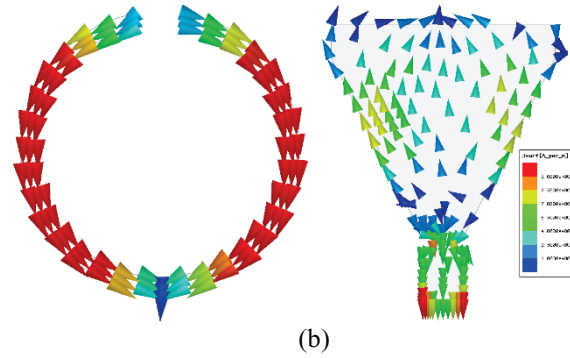
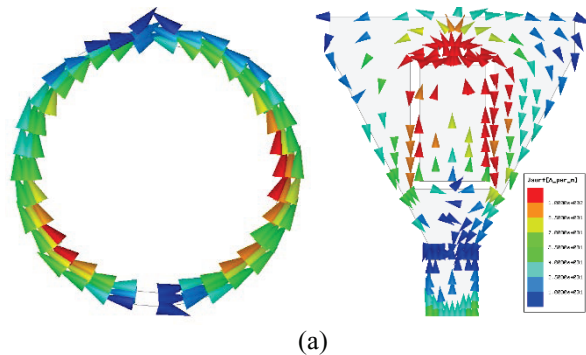


Fig. 7. Simulated surface current distributions for the proposed antenna at its notched band center frequencies: (a) at 3.6 GHz and (b) at 5.7 GHz.

III. RESULTS AND DISCUSSIONS

In this section, the monopole antenna with a new dual band-notched structure with various design parameters was constructed, and the experimental results are presented and discussed. The parameters of this proposed antenna are studied by changing one parameter at a time and fixing the others. Figure 8 shows the VSWR to change in the L_1 , without the parasitic element and C-shape slot of proposed antenna (Fig. 2(c)). According to Fig. 8, choose the size $L_1=1.5$ mm to increase the upper bandwidth of the antenna. Figure 9 shows the VSWR to change in the parameter β , without the parasitic element and C-shape slot of proposed antenna (Fig. 1 (b)). By choose the $\beta = 12.9^\circ$ selecting the primary antenna bandwidth is between 3.2-10.6 GHz. Three slots (air gaps) on the rectangular truncated ground plane, increases the bandwidth and relatively good matching with UWB.

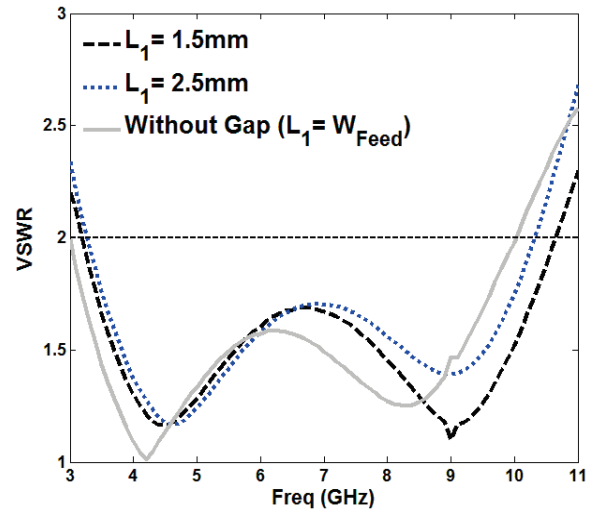


Fig. 8. Simulated VSWR characteristic for various size of L_1 .

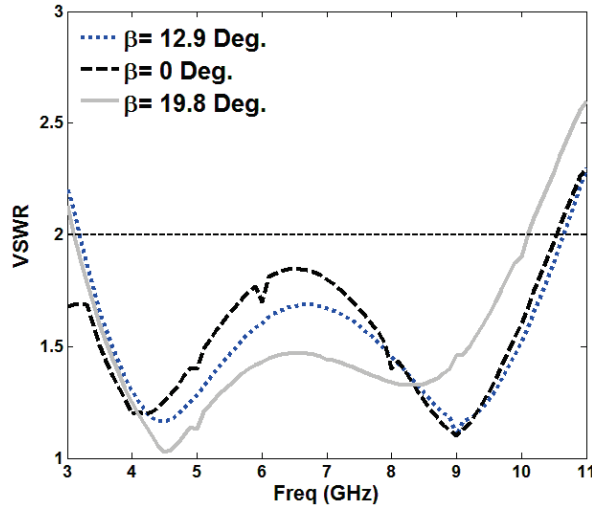


Fig. 9. Simulated VSWR characteristic for various of β angle.

As can be seen in Fig. 10, choice three slots (air gaps) on the rectangular truncated ground plane, improving the bandwidth of the primary antenna. The truncated ground plane plays an important role in the broadband characteristics of this antenna, because it helps to match the patch with the feed line in a wide range of frequencies. This is because the truncation creates a capacitive load that neutralizes the inductive nature of the patch to produce nearly pure resistive input impedance [5-7].

In the proposed antenna length of the C-shape slot on the radiation patch, and width of the split ring-shape parasitic element on the backplane, as control parameters for choose band notch. Following the analysis each of the parameter will be discussed. By changing the length of the C-shape slot, the notched frequency will change. According to Fig. 11, with the choice of $L_{\text{Notch}} = 26.4$ mm, between 3.5-3.7 GHz amount VSWR is bigger than 2. Therefore, the WiMAX frequency band can be notched. The place, length and width of the C-shaped slot have great effects on the band notch performance and should be tuned carefully. In the next phase of the proposed antenna design, changes in the width of the parasitic element alter the band notched. Parasitic element is formed of the inner radius (R_1) and the outer radius (R_2). The width of the split ring-shaped conductor changes with constant outer radius and inner radius shift. Figure 12 shows simulated VSWR for different values of R_1 with other parameters fixed and also shows the effect of R_1 parameter in the VSWR parameter on the frequency bandwidth, impedance matching, higher and lower operating frequency. It is observed that the VSWR at the $R_1 = 4.5$ mm for 5.3-6 GHz is bigger 2, actually the WLAN band notched. In other words, the band-notch for WLAN can be controlled by the radius of the split ring-

shaped. Actually, changes in the width of the split ring-shape due to the frequency-notched change.

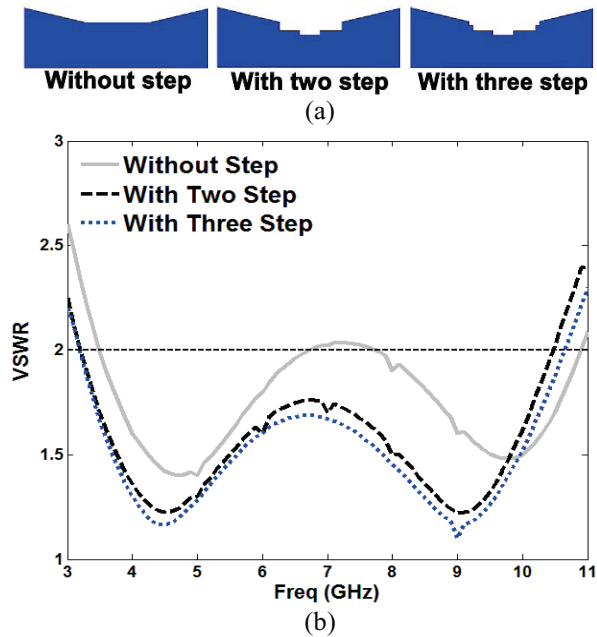


Fig. 10. (a) Various slot number (air gaps) on the rectangular truncated ground, and (b) simulated SWR characteristic.

In the proposed antenna length of the C-shape slot on the radiation patch, and width of the split ring-shape parasitic element on the backplane, as control parameters for choose band notch. Following the analysis each of the parameter will be discussed. By changing the length of the C-shape slot, the notched frequency will change. According to Fig. 11, with the choice of $L_{\text{Notch}} = 26.4$ mm, between 3.5-3.7 GHz amount VSWR is bigger than 2. Therefore, the WiMAX frequency band can be notched. The place, length and width of the C-shaped slot have great effects on the band notch performance and should be tuned carefully. In the next phase of the proposed antenna design, changes in the width of the parasitic element alter the band notched. Parasitic element is formed of the inner radius (R_1) and the outer radius (R_2). The width of the split ring-shaped conductor changes with constant outer radius and inner radius shift. Figure 12 shows simulated VSWR for different values of R_1 with other parameters fixed and also shows the effect of R_1 parameter in the VSWR parameter on the frequency bandwidth, impedance matching, higher and lower operating frequency. It is observed that the VSWR at the $R_1 = 4.5$ mm for 5.3-6 GHz is bigger 2, actually the WLAN band notched. In other words, the band-notch for WLAN can be controlled by the radius of the split ring-shape. Actually, changes in the width of the split ring-shape due to the frequency-notched change.

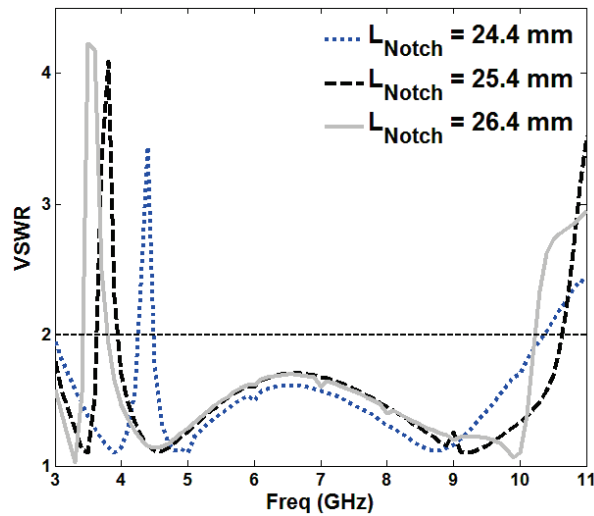


Fig. 11. Simulated VSWR characteristic for various length C-shaped slot.

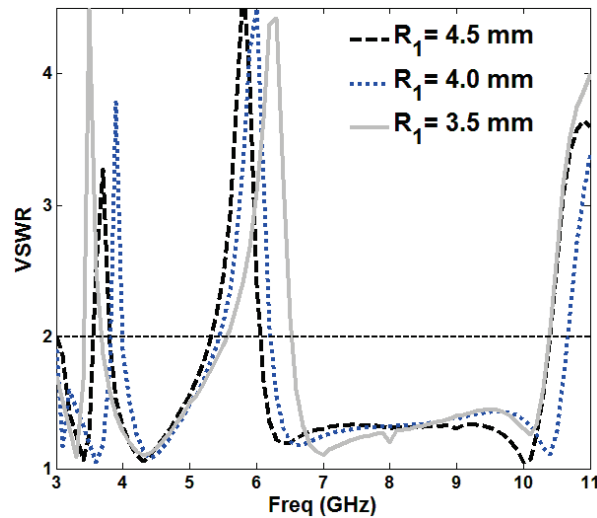


Fig. 12. Simulated VSWR characteristic for various R_1 .

A prototype of the proposed dual band-notched antenna was fabricated and its radiation characteristics have been measured and investigated. The photograph of the fabricated antenna is shown in Fig. 13 and its measured and simulated VSWR characteristics are compared in Fig. 14. The fabricated antenna provides a wide usable fractional bandwidth of more than 112% (3.15 to 10.78 GHz) also band notched 8.8% (3.49 to 3.81) and 17% (5.24 to 6.22 GHz). In simulated of proposed antenna with dual band-notched fractional bandwidth of more than 111% (3 to 10.6 GHz) also band notched 5.5% (3.4 – 3.7) and 12% (5.3 – 6 GHz). As shown in Fig. 14, there exists a discrepancy between measured data and the simulated results. This discrepancy between measured and simulated results is mostly due to

a number of parameters such as the fabricated antenna dimensions as well as the thickness and dielectric constant of the substrate, in other words FR4 substrate quality on which the antenna is fabricated, the wide range of simulation frequencies and also the effect of SMA soldering [15-16].

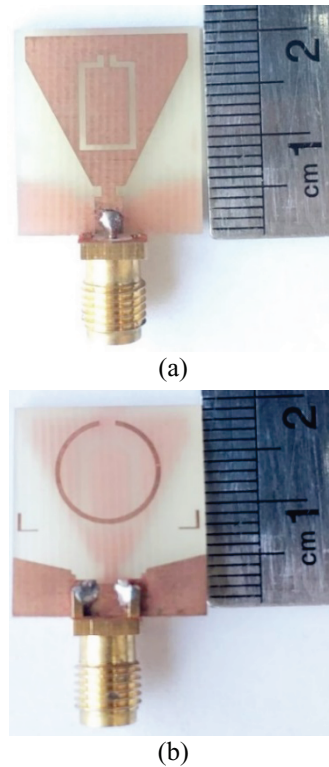


Fig. 13. Fabricated antenna: (a) top view and (b) bottom view.

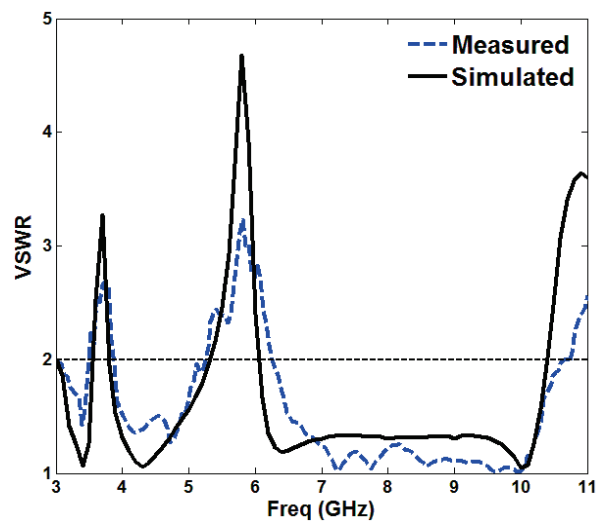


Fig. 14. Measured and simulated VSWR characteristics of the proposed antenna.

Figure 15 shows the measured radiation patterns including the co- and cross-polarization in the H- and E-planes. The main purpose of the radiation patterns is to demonstrate that the antenna actually radiates over a wide range of frequencies. From an overall view of these radiation patterns, the antenna behaves similarly to the typical printed monopoles. It can be seen that the radiation patterns in the H-plane are nearly omnidirectional for the three frequencies. The omnidirectional patterns can enhance and increase the channel capacity [10]. As shown in Fig. 15 (c), the 10 GHz, H-plane pattern has a larger cross polarization compared to similar UWB antennas. This discrepancy between measured and expected results is mostly due to the small ground plane effects and the change of excited surface current distributions on the system ground plane at high frequencies [12].

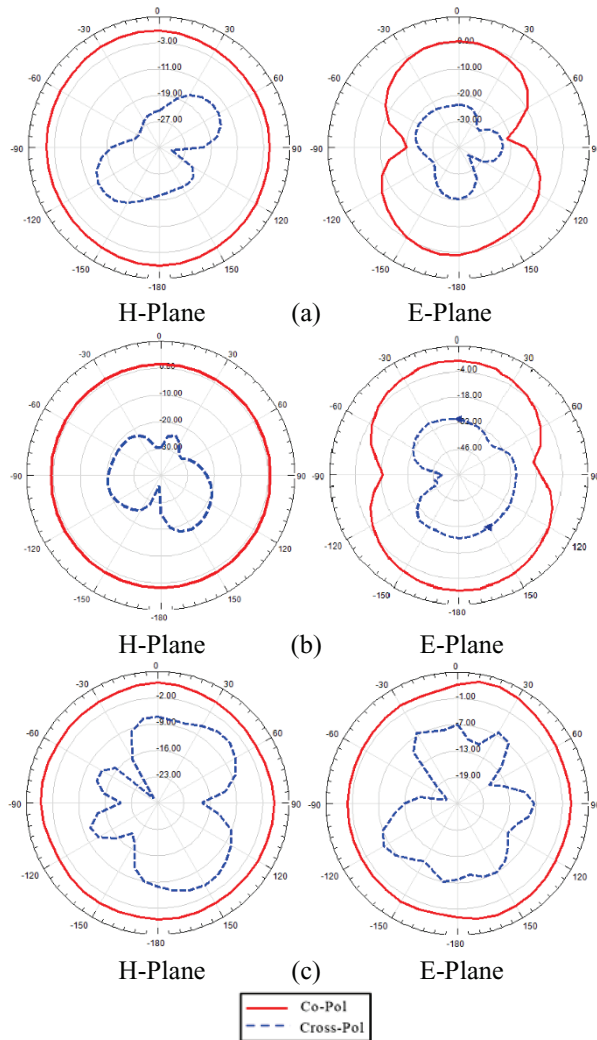


Fig. 15. Measured E- and H-planes radiation pattern for the proposed antenna at: (a) 4.7 GHz, (b) 7 GHz, and (c) 10 GHz.

Figure 16 presents the measured peak gains of the proposed antenna with dual band notch within its working frequency band. The proposed antenna has a gain variation between 2.3 dBi and 3.2 dBi in the UWB. A sharp decrease of maximum gain in the notched frequency band at 3.6 and 5.7 GHz is shown. For other frequencies outside the notched frequency band, the antenna gain with the filter is similar to those without it.

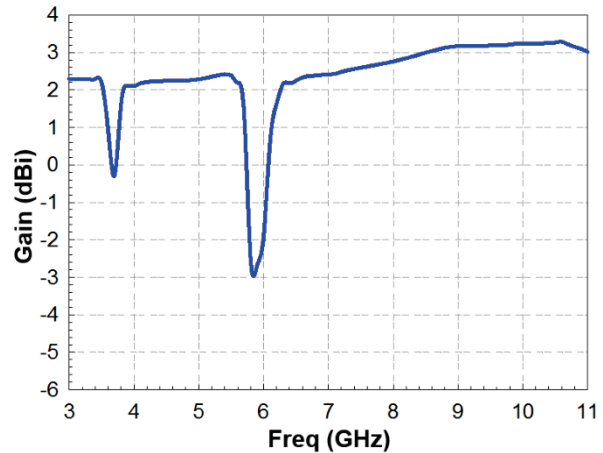


Fig. 16. The measured peak gain of the proposed antenna with dual band notch.

IV. CONCLUSION

In this paper, a compact design and new structure of monopole antenna with dual band notch characteristics for UWB applications is presented. In this design, the proposed antenna can work from 3 GHz to 10.6 GHz with $VSWR < 2$. Moreover, by inserting a C-shaped slot on the radiating patch and a split ring-shaped parasitic element on the other side of the substrate, a dual band notch characteristic is generated. In other word, WiMAX and WLAN band is notched in this antenna. The proposed antenna has advantages of low cost, compact size, and ease of fabrication. The experimental results show that the realized antenna with a very compact size, simple structure, and wide bandwidth can be a good candidate for UWB application.

ACKNOWLEDGMENT

The authors thank the Northwest Antenna and Microwave Research Laboratory (NAMRL) for their beneficial and professional help.

REFERENCES

- [1] Federal Communications Commission. Revision of Part 15 of the Commission's Rules Regarding Ultra-Wideband Transmission System From 3.1 to 10.6 GHz. Washington, DC, USA: Federal Communications Commission, T-Docket, 2002.
- [2] P. Beigi, J. Nourinia, B. Mohammadi, and A.

- Valizade, "Bandwidth enhancement of small square monopole antenna with dual band notch characteristics using U-shaped slot and butterfly shape parasitic element on backplane for UWB applications," *Applied Computational Electromagnetics Society Journal (ACES)*, vol. 30, no. 1, pp. 78-85, Jan. 2015.
- [3] A. Siahcheshm, J. Nourinia, Y. Zehforoosh, and B. Mohammadi, "A compact modified triangular CPW-fed antenna with multioctave bandwidth," *Microwave and Optical Technology Letters*, vol. 57, no. 1, pp. 69-72, Jan. 2015.
- [4] S. Barbarino and F. Consoli, "UWB circular slot antenna provided with an inverted-L notch filter for the 5 GHz WLAN band," *Progress in Electromagnetics Research*, vol. 104, pp. 1-13, 2010.
- [5] J. W. Jayasinghe and D. N. Uduwawala, "A novel miniature multi-frequency broadband patch antenna for WLAN applications," *Proceedings of the IEEE 8th International Conference on Industrial and Information Systems (ICIIS '13)*, Peradeniya, Sri Lanka, pp. 361-363, Aug. 2013.
- [6] M. A. Habib, A. Bostani, A. Djaiz, M. Nedil, M. C. E. Yagoub, and T. A. Denidni, "Ultra wideband CPW-fed aperture antenna with WLAN band rejection," *Progress in Electromagnetics Research*, vol. 106, pp. 17-31, 2010.
- [7] R. Zaker, C. Ghobadi, and J. Nourinia, "A modified microstrip-fed two-step tapered monopole antenna for UWB and WLAN applications," *Progress in Electromagnetics Research, PIER*, vol. 77, pp. 137-148, 2007.
- [8] T. N. Chang and M. C. Wu, "Band-notched design for UWB antennas," *IEEE Antennas and Wireless Propagation Letters*, vol. 7, pp. 636-640, 2008.
- [9] Q. Luo, J. R. Pereira, and H. M. Salgado, "Reconfigurable dual band C-shaped monopole antenna array with high isolation," *Electronics Letters*, vol. 46, no. 13, pp. 888-889, Jun. 2010.
- [10] M. Ojaroudi, N. Ojaroudi, and Y. Ebazadeh, "Dual band-notch small square monopole antenna with enhanced bandwidth characteristics for UWB applications," *Applied Computational Electromagnetics Society (ACES) Journal*, vol. 27, no. 5, pp. 420-426, May 2012.
- [11] A. Valizade, C. Ghobadi, J. Nourinia, N. Ojaroudi, and M. Ojaroudi, "Band-notch slot antenna with enhanced bandwidth by using Ω shaped strips protruded inside rectangular slots for UWB applications," *Applied Computational Electromagnetics Society (ACES) Journal*, vol. 27, no. 10, pp. 816-822, Oct. 2012.
- [12] R. Zaker, C. Ghobadi, and J. Nourinia, "Novel modified UWB planar monopole antenna with variable frequency band-notch function," *IEEE Antennas and Wireless Propagation Letters*, vol. 7, pp. 112-114, Oct. 2008.
- [13] E. Pancera, J. Timmermann, T. Zwick, and W. Wiesbeck, "Time domain analysis of band notch UWB antennas," *Proc. of European Conference on Antenna and Propagation*, pp. 3658-3662, 2009.
- [14] Ansoft High Frequency Structure Simulation (HFSS), ver. 15, Ansoft Corporation, Pittsburgh, PA, 2013.
- [15] B. Mohammadi, J. Nourinia, C. Ghobadi, and A. Valizade, "Design and analysis of the stub and radial-stub loaded resonator bandpass filter with cross-shaped coupled feed-lines for UWB applications," *Applied Computational Electromagnetic Society (ACES) Journal*, vol. 28, no. 9, pp. 851-857, Sep. 2013.
- [16] P. Zibadoost, J. Nourinia, C. Ghobadi, S. Mohammadi, A. Mousazadeh, and B. Mohammadi, "Full band MIMO monopole antenna for LTE systems," *Applied Computational Electromagnetics Society Journal (ACES)*, vol. 29, no. 1, pp. 54-61, Jan. 2014.



Saeed Hoseyni was born in 1981 in Urmia, Iran. He received his B.Sc. degree in Electronic Engineering from Azad University, Urmia Branch and his M.Sc. degree in Electrical Engineering from the Department of Electrical Engineering, Science and Research Kamal Institute of Higher Education, West Azerbaijan, Iran. His research interests include monopole antenna, microstrip antennas with band-notch, and small antennas for wireless communications.



Javad Nourinia received his B.Sc. degree in Electrical and Electronic Engineering from Shiraz University and his M.Sc. degree in Electrical and Telecommunication Engineering from Iran University of Science and Technology, and his Ph.D. degree in Electrical and Telecommunication from University of Science and Technology, Tehran Iran in 2000. From 2000, he was an Assistant Professor and now he is a Professor in the Department of Electrical Engineering of Urmia University, Urmia, Iran. His primary research interests are in antenna design, numerical methods in electromagnetic, microwave circuits.



Changiz Ghobadi received his B.Sc. in Electrical Engineering Electronics and M.Sc. degrees in Electrical Engineering Telecommunication from Isfahan University of Technology, Isfahan, Iran and Ph.D. degree in Electrical Telecommunication from University of Bath, Bath, UK in 1998. From 1998 he was an Assistant Professor and now he is a Professor in the Department of Electrical Engineering of Urmia University, Urmia Iran. His primary research interests are in antenna design, radar and adaptive filters.



Sayed Vahid Masuminia was born in Urmia, Iran 1976. He received his B.Sc. in Electrical Engineering from Azad University of Urmia, Iran, in 1994 and M.Sc. degrees in Electrical Engineering Telecommunication from Azad University of Tehran, Iran, in 1999, and he is currently Ph.D. student at Urmia University, Urmia, Iran. His primary research interests are in radar, microwave circuits, MIMO systems.



Bahman Mohammadi received the B.S. degree in Electrical Engineering-Telecommunication from Tabriz University, Tabriz, Iran, in 2011 and M.Sc. degrees in Electrical Engineering- Microwave, Antenna and Propagation from Urmia University, Urmia, Iran, in 2013, where he is currently working as a Research Assistant in the Northwest Antenna and Microwave Research Laboratory (NAMRL) in Urmia University, Urmia, Iran. His research interests include Periodic Structures, Microwave Components, Optimization, MIMO and Measurement.

A Compact and Miniaturized Broadband Phase Shifter Using Coupled-lines

Yongle Wu*, Siyue Zhou, Xiaochuan Shen, and Yuanan Liu

School of Electronic Engineering, Beijing Key Laboratory of Work Safety Intelligent Monitoring
Beijing University of Posts and Telecommunications, P.O. Box. 282, 100876, Beijing, China
wuyongle138@gmail.com*, zsy.amanda@gmail.com, shenxc188@gmail.com, yuliu@bupt.edu.cn

Abstract — In this paper, a compact and miniaturized broadband phase shifter using coupled-lines (CL) is proposed. This broadband phase shifter merely consists of two sections, one pair of CL as the reference and another two parallel CLs as the main body. An analysis of even-odd mode on the theoretical circuit is shown to explain the basic principle of the proposed phase shifter. For demonstration of this novel configuration, a broadband 90° phase shifter was designed and fabricated. The measured results present that the proposed phase shifter can provide a stable wide bandwidth (over 80%) of 90° phase difference with deviation less than 6.7°, good return losses more than 10 dB and low insertion losses less than 0.53 dB.

Index Terms — Broadband, coupled-line (CL), phase shifter.

I. INTRODUCTION

Differential phase shifter is a key component to various communication systems. It is often designed as a four-port passive component comprised of two paths, the main body for phase delay and the reference section for phase adjustment. There are two phase shifts: $\angle S_{21}$ from reference part, and $\angle S_{43}$ from main body. The purpose of this configuration is to create a stable phase difference between the two sections, namely $\Delta\Phi = \angle S_{43} - \angle S_{21}$, over a wide bandwidth. The values of shifted phase rely on the different circuit parameters of the differential phase shifter.

The classic Schiffman phase shifter in [1, 2] achieved an 80% of bandwidth with a phase error of 10°. From then on, a serial of designs aimed at broadening the bandwidth with lower phase deviation were proposed. One approach by adding a T-shaped open stub on the main line was invented in [3], which yielded a wide bandwidth of 82% and phase inaccuracy of 6.4°. Based on these designs, the reference part was developed with some parallel multi-section coupled-lines in [4]. Another structure utilized multi-section radial stubs on the main line [5], which leads to an ultra-wideband frequency with a phase deviation of 9.02°. In addition, the multi-layer structure used broadside-coupled microstrip patches [6], achieving various shifted phase ranging from -180° to

180°. On the other hand, a T-type bandpass network for the main body merely depending on the L/C components was designed in [7]. It accomplished a better bandwidth larger than 125%. However, the circuits in [3-6] often require a complicated technique of fabrication, especially the multi-layer structure which is not suitable for the single-layer components. Meanwhile, the L/C components in [7] limit the performance when operating at a higher frequency.

This paper proposes a novel broadband phase shifter using *coupled-lines* with a *compact* structure. A theoretical model was analyzed via even-odd mode and kinds of circuit parameters for different shifted phase were provided and simulated as well. For experimental validations, an example of a broadband 90° phase shifter was simulated, fabricated, and measured.

II. PHASE SHIFTER DESIGN

The schematic of the proposed differential phase shifter with four ports is shown in Fig. 1 (a). It contains two paths: Path 1 employs only one coupled-line with an interconnected point as the reference section; Path 2 utilizes two pair of parallel CLs as main body.

Compared to the previously reported phase shifters, the circuit of this novel phase shifter is compact and miniaturized since it simply consists of some coupled-lines maintaining wide-band feature. Besides, this main body includes two connected sections with one connecting point shorted to ground by two vias. The electrical parameters of the ideal circuit are defined as follow: the even-mode and odd-mode characteristic impedances are Z_{ei} and Z_{oi} ($i = 1, 2, 3$), respectively; while, θ_j ($j = 1, 2$) corresponds to the electrical lengths of the reference part and the main body. The electrical lengths θ_j ($j = 1, 2$) at the frequency f are defined as:

$$\theta_1 = \theta_{1o} \frac{f}{f_0}, \quad \theta_2 = \theta_{2o} \frac{f}{f_0}, \quad (1)$$

where θ_{jo} ($j = 1, 2$) are the electrical lengths of the reference part and the main body at the designed frequency f_0 . In addition, Z_0 stands for the characteristic impedance of each port.

Since the topology of the schematic is symmetric, as illustrated in Fig. 1 (a), it means that the theoretical

analysis can be simplified with the even-odd mode method displayed in [8]. Figure 1 (b) and Fig. 1 (c) present the symmetric equivalent circuits of the main body (Path 2) when separately motivated by even-mode source or odd-mode source.

As for the Fig. 1 (b) and Fig. 1 (c), the input impedances of the Path 2 both for the even- and odd-mode equivalent circuits can be expressed as:

$$Z_{ine} = \frac{Z_{e2}Z_{e3}}{j[Z_{e3} \tan(\theta_2) - Z_{e2} \cot(\theta_2)]}, \quad (2a)$$

$$Z_{ino} = -\frac{Z_{o2}Z_{o3} \tan(\theta_2)}{j(Z_{o3} + Z_{o2})}. \quad (2b)$$

Based on the Equations (2a) and (2b), the reflection coefficients of the Path 2 for each mode excitations S_{33e} and S_{33o} can be obtained by:

$$S_{33e} = \frac{Z_{ine} - Z_0}{Z_{ine} + Z_0} = \frac{Z_{e2}Z_{e3} - jZ_0[Z_{e3} \tan(\theta_2) - Z_{e2} \cot(\theta_2)]}{Z_{e2}Z_{e3} + jZ_0[Z_{e3} \tan(\theta_2) - Z_{e2} \cot(\theta_2)]}, \quad (3a)$$

$$S_{33o} = \frac{Z_{ino} - Z_0}{Z_{ino} + Z_0} = \frac{-Z_{o2}Z_{o3} \tan(\theta_2) - jZ_0(Z_{o2} + Z_{o3})}{-Z_{o2}Z_{o3} \tan(\theta_2) + jZ_0(Z_{o2} + Z_{o3})}. \quad (3b)$$

Furthermore, by using (3a) and (3b), the scattering parameters of the return loss S_{33} and the insertion loss S_{43} in the Path 2 can be derived as:

$$S_{33} = \frac{S_{11e} + S_{11o}}{2} = \frac{Z_{e2}Z_{e3} - jZ_0[Z_{e3} \tan(\theta_2) - Z_{e2} \cot(\theta_2)]}{2Z_{e2}Z_{e3} + j2Z_0[Z_{e3} \tan(\theta_2) - Z_{e2} \cot(\theta_2)]} + \frac{-Z_{o2}Z_{o3} \tan(\theta_2) - jZ_0(Z_{o2} + Z_{o3})}{-2Z_{o2}Z_{o3} \tan(\theta_2) + j2Z_0(Z_{o2} + Z_{o3})}, \quad (4)$$

$$S_{43} = \frac{S_{11e} - S_{11o}}{2} = \frac{Z_{e2}Z_{e3} - jZ_0[Z_{e3} \tan(\theta_2) - Z_{e2} \cot(\theta_2)]}{2Z_{e2}Z_{e3} + j2Z_0[Z_{e3} \tan(\theta_2) - Z_{e2} \cot(\theta_2)]} - \frac{-Z_{o2}Z_{o3} \tan(\theta_2) - jZ_0(Z_{o2} + Z_{o3})}{-2Z_{o2}Z_{o3} \tan(\theta_2) + j2Z_0(Z_{o2} + Z_{o3})}. \quad (5)$$

The ideal situation that the scattering parameter should satisfy at the center frequency is $S_{33}=0$. Thus, (4) can be transformed into Equation (6):

$$Z_0^2 (Z_{o2} + Z_{o3}) [Z_{e3} \tan^2(\theta_2) - Z_{e2}] - Z_{e2}Z_{e3}Z_{o2}Z_{o3} \tan^2(\theta_2) = 0. \quad (6)$$

In addition, if the value of the θ_2 becomes 90° , the scattering parameter of the proposed phase shifter will automatically meet the conditions $S_{33}=0$. Besides, the phase constant ϕ of the Path 2 can be derived from:

$$\tan \phi = \frac{AB(C^2 + D^2) - CD(A^2 + B^2)}{A^2D^2 - B^2C^2}, \quad (7)$$

where

$$A = Z_{e2}Z_{e3}, \quad (8a)$$

$$B = Z_0 \left[\frac{Z_{e2} - Z_{e3} \tan^2(\theta_2)}{\tan(\theta_2)} \right], \quad (8b)$$

$$C = Z_{o2}Z_{o3} \tan(\theta_2), \quad (8c)$$

$$D = Z_0 (Z_{o2} + Z_{o3}). \quad (8d)$$

Subsequently, considering the reference line (Path 1), the ideal circuit parameters and the phase constant, φ are expressed in [1], in terms of even-mode Z_{e1} , and odd-mode Z_{o1} impedances and its electrical length of the interconnected coupled-line,

$$Z_0 = \sqrt{Z_{e1}Z_{o1}}, \quad (9)$$

and

$$\cos \varphi = \frac{Z_{e1}/Z_{o1} - \tan^2 \theta_1}{Z_{e1}/Z_{o1} + \tan^2 \theta_1}. \quad (10)$$

Consequently, by combining (7) and (10), the differential phase shift δ between Path 1 and Path 2 for this schematic can be calculated as below:

$$\delta = \angle(S_{43}) - \angle(S_{21}) = \tan^{-1}(\phi) - \cos^{-1}(\varphi). \quad (11)$$

For instance, we have assumed that all the electrical lengths of the coupled-lines work under the frequency $f_0=2.6$ GHz. All the circuit parameters of the proposed design parameters can be identified by using Equations (1)-(11). To validate the capability of the proposed broadband phase shifter, five typical examples with the differential shifted phase of 70° , 85° , 100° , 120° and 135° have been designed and simulated.

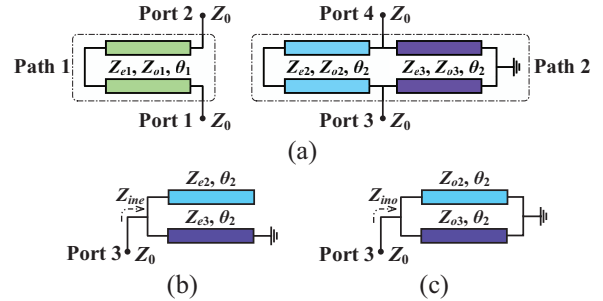
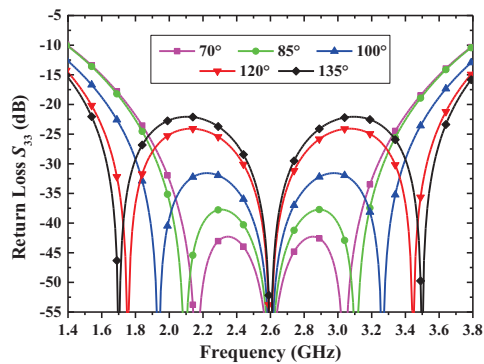


Fig. 1. (a) Circuit configuration of the proposed phase shifter, (b) the even-mode and (c) the odd-mode symmetric equivalent circuit of the Path 2.

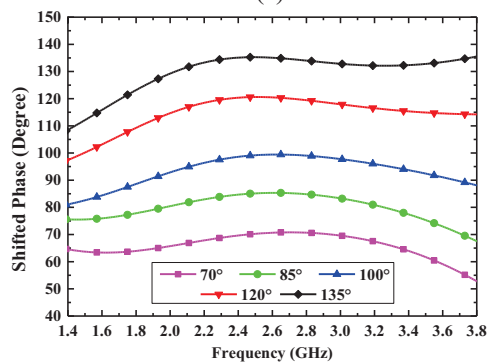
Table 1 lists the corresponding circuit parameters and operating bandwidth in terms of the ideal simulated return losses S_{33} for their amplitude ($f_0=2.6$ GHz) and phase feature as well, which is also exhibited in Fig. 2. In contrast to [3-6], the proposed structure with a single-layer structure leads to a compact and miniaturized topology, which is easier to be implemented. Meanwhile, it can maintain a wide-band operating properties at a higher frequency band compared with the L/C components in [7].

Table 1: The calculated optimum ideal circuit parameters of five examples for different shifted phase values

Examples	Shifted Phase	Circuit Parameters	Bandwidth (GHz) of $ \text{Return Losses} \leq 10 \text{ dB}$ and $ \text{phase error} \leq 5\%$
I	70°	$Z_{e1}=59\Omega, Z_{o1}=42.4\Omega,$ $Z_{e2}=69\Omega, Z_{o2}=60\Omega,$ $Z_{e3}=95\Omega, Z_{o3}=83\Omega,$ $\theta_1=121^\circ, \theta_2=90^\circ$	2.03-3.27 ($70^\circ \pm 3.89^\circ$)
II	85°	$Z_{e1}=59\Omega, Z_{o1}=42.4\Omega,$ $Z_{e2}=69\Omega, Z_{o2}=55\Omega,$ $Z_{e3}=95\Omega, Z_{o3}=83\Omega,$ $\theta_1=128^\circ, \theta_2=90^\circ$	2.03-3.25 ($85^\circ \pm 4.72^\circ$)
III	100°	$Z_{e1}=59\Omega, Z_{o1}=42.4\Omega,$ $Z_{e2}=69\Omega, Z_{o2}=50\Omega,$ $Z_{e3}=110\Omega, Z_{o3}=90\Omega,$ $\theta_1=135^\circ, \theta_2=90^\circ$	2.02-3.34 ($100^\circ \pm 5.56^\circ$)
IV	120°	$Z_{e1}=59\Omega, Z_{o1}=42.4\Omega,$ $Z_{e2}=69\Omega, Z_{o2}=43\Omega,$ $Z_{e3}=110\Omega, Z_{o3}=90\Omega,$ $\theta_1=146^\circ, \theta_2=90^\circ$	1.95-3.85 ($120^\circ \pm 6.67^\circ$)
V	135°	$Z_{e1}=59\Omega, Z_{o1}=42.4\Omega,$ $Z_{e2}=69\Omega, Z_{o2}=43\Omega,$ $Z_{e3}=110\Omega, Z_{o3}=80\Omega,$ $\theta_1=154^\circ, \theta_2=90^\circ$	1.93-3.97 ($135^\circ \pm 7.5^\circ$)



(a)

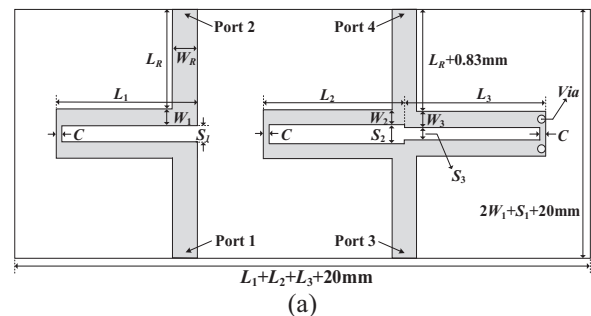


(b)

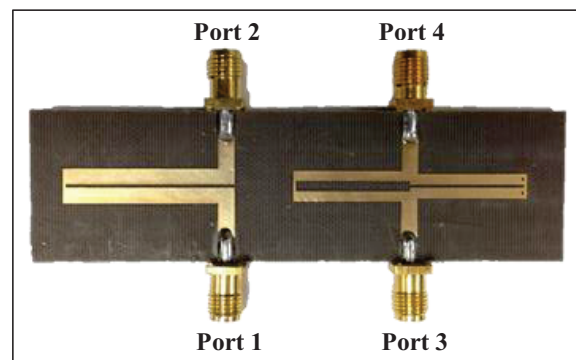
Fig. 2. (a) Simulated responses of the proposed phase shifter for the different shifted phase values under the ideal transmission-line models return loss of S_{33} , and (b) different values of shifted phase.

III. RESULTS AND DISCUSSIONS

To demonstrate the proposed model and theoretical analysis, a 90° broadband phase shifter was simulated, fabricated, and tested as an instance. This circuit was designed on F4B substrate with the relative permittivity of 2.65 and the thickness of 1 mm. Based on the working principle as mentioned before, this instance can be easily realized. The circuit structure of the specified shifted phase and the photograph of the fabricated entity are given in Fig. 3 (a) and Fig. 3 (b). The impedance values of the coupled-lines can be extracted from Equation (1)-(11). The selected characteristic impedances and electrical lengths are as follow: $Z_{e1}=59 \Omega$, $Z_{o1}=42.4 \Omega$, $Z_{e2}=70 \Omega$, $Z_{o2}=60 \Omega$, $Z_{e3}=75 \Omega$, $Z_{o3}=50 \Omega$, $\theta_1=131^\circ$ and $\theta_2=90^\circ$ at 2.6 GHz. Moreover, for the feasibility of the measurement, the impedance Z_0 of the four ports is defined to 50Ω . After the line-calculation and optimization of the model, all the physical dimensions are (unit: mm): $W_R=2.72$, $W_1=2.59$, $W_2=1.7$, $W_3=1.8$, $L_1=28.67$, $L_2=19.8$, $L_3=19.88$, $S_1=0.63$, $S_2=1.8$, $S_3=0.56$ and $C=0.4$. It should be pointed out that, the size of the interconnected sections at each coupled-line have tiny influence on the performance of the proposed phase shifter due to the simulated process.



(a)



(b)

Fig. 3. (a) The optimized dimensions, and (b) the photograph of the fabricated 90° phase shifter.

The simulation on the EM model was achieved by HFSS and the measurement was done by an Agilent Network Analyzer. The scattering parameters for both simulation and measurement are exhibited in Fig. 4. A

close agreement between the measurement and the simulation was fulfilled with the return losses better than 10 dB and the insertion losses lower than 0.53 dB (containing the loss imported by SMA connectors). Besides, the operating frequency band can cover a wide bandwidth from 1.34 GHz to 3.20 GHz (over 80%) with a small inaccuracy of shifted phase within $90 \pm 6.7^\circ$. Simultaneously, the main body occupied a miniaturized size smaller in terms of the guided wavelength

$[0.51\lambda_g \times 0.33\lambda_g$ (including port lines), $\lambda_g=77.64$ mm]. In addition, the slight deviation between the simulation and the experiment probably results from simulated algorithm and the calibrated errors from measurement as well. In order to further explain the novelty and advantages of this proposed phase shifter, Tables 2 and 3 summarize the compared characteristics and measured performance between this proposed phase shifter and the other ones in [3-7].

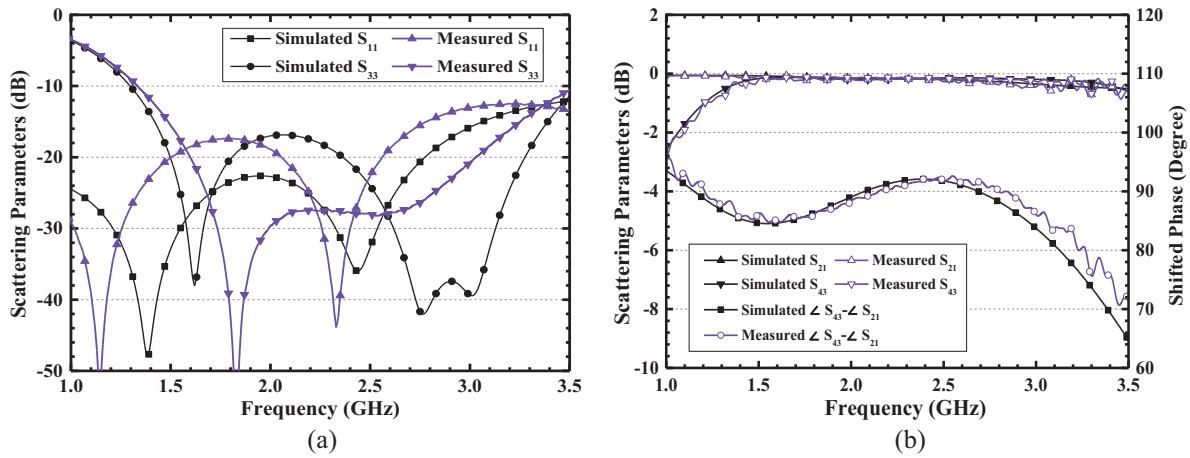


Fig. 4. (a) Simulated and measured results: return losses, and (b) insertion losses and the shifted phase between two outputs of the fabricated 90° phase shifter.

Table 2: The comparison between the proposed phase shifter and previous ones

References	Layer	Type	Symmetry	Substrate	Refer. Line	Main Line	Features	Described Shifting Phases
[3]	Single	Microstrip lines	√	PCB	A 50-Ω transmission line	T-shaped open stub	Easily implemented	$60^\circ, 75^\circ, 90^\circ, 105^\circ, 120^\circ$
[4]	Single	Microstrip lines	√	PCB	Phase correcting network using multi-sections of CLs	T-shaped open stub	Complicated, and large size	90°
[5]	Single	Microstrip lines	√	PCB	A 50-Ω transmission line	Multi-section radial stubs and open stub	Inconvenient fabricated and UWB	90°
[6]	Multi-layer	Microstrip patches	×	RO4003C	A 50-Ω transmission line	Broadside-coupled microstrip patches at the top and bottom layer	Inconvenient fabricated, small size and UWB	$-180^\circ, -90^\circ, 90^\circ, 180^\circ$
[7]	Single	L/C components	×	FR4	A 50-Ω transmission line	L/C components	Small size and limitation of higher frequency	$22.5^\circ, 45^\circ, 90^\circ$
This work	Single	Microstrip lines	√	PCB	A pair of coupled-line	Two pair of Coupled-lines	Convenient fabricated, compact and a small size	$70^\circ, 85^\circ, 100^\circ, 120^\circ, 135^\circ$

Table 3: The comparison of the measured results between the proposed phase shifter and previous ones

References	Bandwidth (GHz)	Shifting Phase	Phase Error	BW (%)	Return Loss (dB)	Insertion Loss (dB)	Size of Main Body Without Port Line (Wavelength $\lambda_g \times \lambda_g$)
[3]	2.30-5.50	90°	6.4°	82.1	>10	<0.6	0.48×0.35
[4]	2.50-5.43	90°	2.54°	81	>10	<0.8	0.48×0.35
[5]	3.10-10.6	90°	9.02°	109	>10	<0.96	0.81×0.54
[6]	3-11	-180°, -90°, 90°, 180°	6°, 2°, 5°, 7°	114.3	>10	<0.7, <1.4, <0.6, <1.2	0.2×0.45
[7]	0.58-2.52	90°	5.5°	125	>18.1	<0.16	N. A.
This work	1.34-3.20	90°	6.72°	81.9	>10	<0.53	0.51×0.06

IV. CONCLUSION

This paper reports a novel circuit configuration for the wideband differential phase shifter only comprised of coupled-lines. The circuit of the proposed phase shifter makes it easier to design and fabrication with a compact and miniaturized structure. It can provide a stable shifting phase in a wide bandwidth with low phase deviation. Besides, the theoretical analysis and the various configurations for different shifted phase values are given. For the verification of this novel structure, an example of a broadband 90° phase shifter with coupled-lines was simulated, fabricated, and measured. The measured results validated that it could accomplish a stable wide bandwidth (over 80%) with phase error 90° ± 6.72°, return losses more than 10 dB and low insertion losses less than 0.53 dB. Moreover, the wide-band success with low-cost and miniaturized size of this proposed phase shifter will be of convenience for the combinations of antenna array systems and other microwave systems.

ACKNOWLEDGMENT

This work was supported in part by National Basic Research Program of China (973 Program) (No. 2014CB339900), and National Natural Science Foundations of China (No. 61422103 and No. 61327806). In addition, the corresponding Chinese patent (No. 201410426042.1) has been pending.

REFERENCES

- [1] B. Schiffman, "A new class of broadband microwave 90-degree phase shifters," *IRE Trans. Microw. Theory Tech.*, vol. MTT-6, no. 4, pp. 232-237, Apr. 1958.
- [2] J. L. R. Quirarte and J. P. Starski, "Novel Schiffman phase shifters," *IEEE Trans. Microw. Theory Tech.*, vol. 41, no. 1, pp. 9-14, Jan. 1993.
- [3] S. Y. Zheng, W. S. Chan, and K. F. Man, "Broadband phase shifter using loaded transmission line," *IEEE Microw. Wireless Compon. Lett.*, vol. 20, no. 9, pp. 498-500, Sep. 2010.
- [4] S. H. Yeung, T. K. Sarkar, M. Salazar-Palma, and A. Garcia-Lamperez, "A multisection phase correcting network for broadband quadrature power splitter design," *IEEE Microw. Wireless Compon. Lett.*, vol. 23, no. 9, pp. 468-470, Sep.

2013.

- [5] S. H. Yeung, Z. Mei, T. K. Sarkar, and M. Salazar-Palma, "Design and testing of a single-layer microstrip ultrawideband 90 differential phase shifter," *IEEE Microw. Wireless Compon. Lett.*, vol. 23, no. 3, pp. 122-124, Mar. 2013.
- [6] L. Guo and A. Abbosh, "Phase shifters with wide range of phase and ultra-wideband performance using stub-loaded coupled structure," *IEEE Microw. Wireless Compon. Lett.*, vol. 24, no. 3, pp. 167-169, Mar. 2014.
- [7] P.-S. Huang and H.-C. Lu, "Broadband differential phase-shifter design using bridged T-type bandpass network," *IEEE Trans. Microw. Theory Tech.*, vol. 62, no. 7, pp. 1470-1479, July 2014.
- [8] J.-S. Hong and M. J. Lancaster, *Microstrip Filters for RF/Microwave Applications*, Wiley, Chapters 1 and 2, 2001.



Yongle Wu received the B.Eng. degree in Communication Engineering and the Ph. D degree in Electronic Engineering from Beijing University of Posts and Telecommunications (BUPT), Beijing, China, in 2006 and 2011, respectively.

During April to October in 2010, he was a Research Assistant at the City University of Hong Kong (CityU), Kowloon, Hong Kong. In 2011, he joined the BUPT. He is currently an Associate Professor with the School of Electronic Engineering, BUPT. His research interests include microwave components and wireless systems design.



Siyue Zhou received the B.Eng. degree in Telecommunications Engineering from Chongqing University of Posts and Telecommunications (CQUPT), China, in 2013, and is currently working toward the Ph.D. degree at Beijing University of Posts and Telecommunications (BUPT), Beijing, China.

Her research interests include microwave components and wireless systems design.



Xiaochuan Shen received the B.Eng. degree in Electronic Information Engineering from Shijiazhuang Tiedao University, China, in 2013, and is currently working toward the Ph.D. degree at Beijing University of Posts and Telecommunications (BUPT), Beijing, China.

His research interests include microwave components and circuits design.



Yuanan Liu received the B.E., M.Eng. and Ph.D. degrees in Electrical Engineering from University of Electronic Science and Technology of China, Chengdu, China, in 1984, 1989 and 1992, respectively.

In 1984, he joined the 26th Institute of Electronic Ministry of China to develop the Inertia Navigating System. In 1992,

he began his first post-doctor position in EMC Lab of Beijing University of Posts and Telecommunications (BUPT), Beijing, China. In 1995, he started his second post-doctor in Broadband Mobile Lab of Department of System and Computer Engineering, Carleton University, Ottawa, Canada. From July, 1997, as Professor, he is with Wireless Communication Center of College of Telecommunication Engineering, BUPT, Beijing, China, where he is involved in the development of next-generation cellular system, wireless LAN, Bluetooth application for data transmission, EMC design strategies for high speed digital system, and EMI and EMS measuring sites with low cost and high performance.

Mode Matching in Microstrip Antenna with both Electric and Magnetic Surface Current on Sidewall in Cavity Model

Fazel Rangriz Rostami, Gholamreza Moradi, and Reza Sarraf Shirazi

Department of Electrical Engineering
Amirkabir University of Technology, Tehran, Iran
fazel.rangriz@aut.ac.ir, ghmoradi@aut.ac.ir, sarraf@aut.ac.ir

Abstract — A model is developed to calculate the input impedance of a coaxially fed circular microstrip disc antenna in L band and C band. A mode matching approach with both electric and magnetic surface current is used, which makes it possible to improve the effects of modes. In addition, the method of images is used to remove the ground plane. Finally comparison is made with CST studio results, as it can be seen the theoretical calculations for input impedance are in good agreement with CST studio results except for minor shift in frequency.

Index Terms — Antennas, cavity model, input impedance, microstrip antennas, mode matching,

I. INTRODUCTION

Some papers have studied the subject of input impedance for microstrip antennas of various configurations [1], [2]. Several papers analyze coaxial feed microstrip antenna in conjunction with the cavity model of circular disk with different techniques, e.g., Green's function technique [3], Vector Hankel Transform with Galerkin's method [4], equivalent current ribbon mode [5], and multiport analysis [6]. An improved cavity model formulation to predict accurate input impedance of coax-fed circular microstrip antenna has been reported in [7]. Computation and optimization of input impedance of coax-fed microstrip antenna are discussed in [8].

The present paper uses cavity Green's-function technique along with mode matching technique for evaluating the input impedance of a probe-fed circular ring microstrip antenna. Figure 1 shows the antenna, which consists of a circular disk mounted on a grounded dielectric, the antenna has a radius equal to a , the fringing fields along the circumference of the antenna are taken into account by replacing the patch radius a by the effective radius a_e [9]. Antenna is driven by a coaxial line through the ground plane at radial distance r_0 from the center of the patch. The thickness and the dielectric constant of the substrate are denoted by h and ϵ ,

respectively. In order to have less frequency shift compared with CST studio results, effective dielectric constant can be used [9]. The permeability μ of the substrate is equal to that of the air, i.e., $\mu = \mu_0$. To determine the input impedance of the antenna, it is necessary to find the electric field solution beneath the circular patch [10]. In general this solution takes the form of a cylindrical mode expansion, with each mode being determined to within an arbitrary constant. To find all of these constants additional boundary conditions are required, which are obtained by considering the wall admittances. These wall admittances y_n fix the ratio between the z -directed electric field and the ϕ -directed magnetic field for each mode [10]. In this paper we use both electric and magnetic surface currents on the sidewall in cavity model in order to calculate the sidewall admittance. It is noticeable that, considering both currents do not appear to be available in the literature.

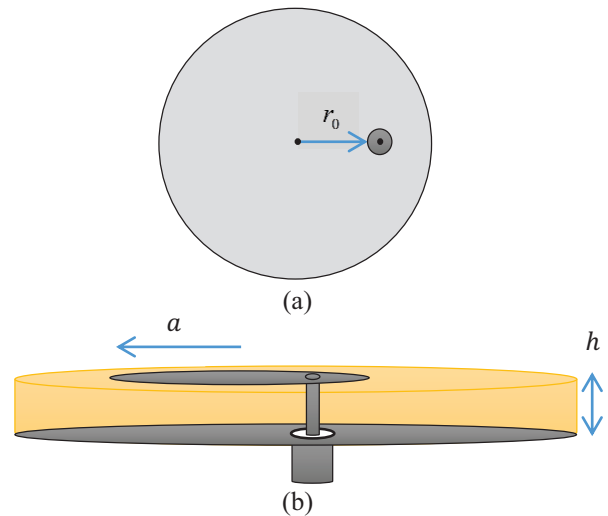


Fig. 1. Geometry of microstrip disc antenna: (a) top view of patch, and (b) 3D structure.

II. CALCULATION OF WALL ADMITTANCE

As shown in Fig. 2, region *I* is defined by $r < a$, and region *II* is defined by $r > a$, the method of images is used to remove the ground plane, so that the sidewall extends along the z - axis from $-h$ to $+h$.

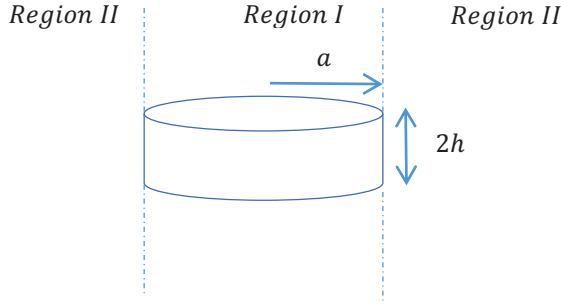


Fig. 2. Two regions of the problem.

In order to calculate wall admittance at the boundary between regions *I* and *II*, electric and magnetic fields with respect to the electric and magnetic vector potential in cylindrical coordinate are written as [12]:

$$E_\phi = \frac{\frac{\partial}{\partial r} F_z(r, \phi, z)}{\varepsilon_0} - \frac{\frac{\partial}{\partial z} \frac{\partial}{\partial \phi} A_z(r, \phi, z) i}{\omega r \varepsilon_0 \mu_0}, \quad (1)$$

$$E_z = -\omega A_z(r, \phi, z) i - \frac{\frac{\partial^2}{\partial z^2} A_z(r, \phi, z) i}{\omega \varepsilon_0 \mu_0}, \quad (2)$$

$$H_\phi = -\frac{\frac{\partial}{\partial r} A_z(r, \phi, z)}{\mu_0} - \frac{\frac{\partial}{\partial z} \frac{\partial}{\partial \phi} F_z(r, \phi, z) i}{\omega r \varepsilon_0 \mu_0}, \quad (3)$$

$$H_z = -\omega F_z(r, \phi, z) i - \frac{\frac{\partial^2}{\partial z^2} F_z(r, \phi, z) i}{\omega \varepsilon_0 \mu_0}, \quad (4)$$

where i is imaginary unit. Applying Fourier transform and Fourier series with respect to z and ϕ variables, respectively, result in Helmholtz equation for z component of vector potentials:

$$\left(r^2 \frac{\partial^2}{\partial r^2} + r \frac{\partial}{\partial r} + k_r^2 r^2 - n^2 \right) \begin{Bmatrix} \tilde{A}_z(r, \phi) \\ \tilde{F}_z(r, \phi) \end{Bmatrix} = 0, \quad (5)$$

in which $k_r = \sqrt{k_0^2 - k_z^2}$, and k_0 is the free space wave number, in every region and $-\infty < k_z < \infty$, solution of Helmholtz equation leads to the following equations:

$$\tilde{A}_z^I = h_n e^{i n \phi} J_n(k_r r), \quad (6)$$

$$\tilde{F}_z^I = q_n e^{i n \phi} J_n(k_r r), \quad (7)$$

$$\tilde{A}_z^{II} = f_n e^{i n \phi} H_n^{(2)}(k_r r), \quad (8)$$

$$\tilde{F}_z^{II} = g_n e^{i n \phi} H_n^{(2)}(k_r r), \quad (9)$$

where J_n and $H_n^{(2)}$ are Bessel function of the first kind and Hankel function of the second kind, respectively. h_n , q_n , f_n and g_n are constant values. By substituting (6)-(9) in (1)-(4), electric and magnetic field in every region can be obtained.

The boundary conditions on surface of the wall are given by:

$$\tilde{H}_{\phi, n}^{II}(a, \phi) - \tilde{H}_{\phi, n}^I(a, \phi) = \tilde{J}_{z, n}, \quad (10)$$

$$\tilde{E}_{z, n}^I(a, \phi) - \tilde{E}_{z, n}^{II}(a, \phi) = -\tilde{M}_{\phi, n}, \quad (11)$$

$$\tilde{H}_{z, n}^I(a, \phi) = \tilde{H}_{z, n}^{II}(a, \phi), \quad (12)$$

$$\tilde{E}_{\phi, n}^I(a, \phi) = \tilde{E}_{\phi, n}^{II}(a, \phi). \quad (13)$$

Magnetic and electric surface current on wall surface in main space and in Fourier space is as following:

$$\tilde{J}(\phi, z) = \hat{z} \sum_n J_n e^{i n \phi} \{U(h+z) - U(z-h)\}$$

$$\tilde{\vec{J}}(\phi, k_z) = \hat{z} \sum_n J_n e^{i n \phi} \frac{2 \sin(h k_z)}{k_z}, \quad (14)$$

$$\vec{M}(\phi, z) = \hat{\phi} \sum_n M_n e^{i n \phi} \{U(h+z) - U(z-h)\}$$

$$\vec{\vec{M}}(\phi, k_z) = \hat{\phi} \sum_n M_n e^{i n \phi} \frac{2 \sin(h k_z)}{k_z}, \quad (15)$$

in which $U(z)$ is the unit step function. By substituting (14) and (15) in (10) and (11), respectively, h_n , q_n , f_n and g_n are found with respect to J_n and M_n , then inverse Fourier transform are applied. Because of inverse transform, each equation has $\exp(i k_z z)$ term. In order to eliminate the z dependence of equations, averaging with respect to z variable is taken as following:

$$\frac{\int_{-h}^h e^{i k_z z} dz}{2h} = \frac{\sin(h k_z)}{h k_z}, \quad (16)$$

then, wall admittances y_n are defined as ratio between the z - directed electric field and the ϕ - directed magnetic field for each mode in main space [10]:

$$H_{\phi, n}^{II}(a, \phi) = -y_n E_{z, n}^{II}(a, \phi), \quad (17)$$

$$H_\phi(a, \phi) = \sum_n J_n e^{i n \phi}, \quad (18)$$

$$E_\phi(a, \phi) = \sum_n M_n e^{i n \phi}, \quad (19)$$

$$J_n = -y_n M_n. \quad (20)$$

After some mathematical simplification, the following equation for y_n can be obtained:

$$y_n^1 = \frac{\left(C^2 - 2AD + C\sqrt{B^2 - 4AD + C^2 + 2BC} + BC \right) + D}{2A}, \quad (21)$$

$$y_n^2 = -\frac{\left(2AD - C^2 + C\sqrt{B^2 - 4AD + C^2 + 2BC} - BC \right) - D}{2A}, \quad (22)$$

in which, A, B, C and D have integral form as following:

$$A = \frac{1}{\pi} \int_0^\infty \frac{\sin^2(hk_z) k_r^2 H_n^{(2)}(ak_r) J_n(ak_r)}{hk_z 2\omega k_z \varepsilon_0} dk_z, \quad (23)$$

$$B = -\frac{1}{\pi} \int_0^\infty \frac{\sin^2(hk_z)}{hk_z} \left(\frac{\omega n \varepsilon_0 J_n(ak_r) H_n^{(2)}(ak_r) i}{2\omega k_z \varepsilon_0} - \frac{\omega a k_r \varepsilon_0 J_{n+1}(ak_r) H_n^{(2)}(ak_r) i}{2\omega k_z \varepsilon_0} \right) dk_z, \quad (24)$$

$$C = -\frac{1}{\pi} \int_0^\infty \frac{\sin^2(hk_z) k_r H_n^{(2)}(ak_r) J_n(ak_r) i}{hk_z 2k_z} dk_z, \quad (25)$$

$$D = \frac{1}{\pi} \int_0^\infty \frac{\sin^2(hk_z)}{hk_z} \left(\frac{\omega \varepsilon_0 H_n^{(2)}(ak_r) J_{n+1}(ak_r)}{2k_z} - \frac{n a k_r \varepsilon_0 \mu_0 \omega H_n^{(2)}(ak_r) J_n(ak_r)}{2a^2 k_r^2 k_z \mu_0} - \frac{n^2 k_z H_n^{(2)}(ak_r) J_n(ak_r)}{2\omega a^2 k_r^2 \mu_0} \right) dk_z. \quad (26)$$

Since the integrand is an even function of k_z , the lower limit of integrals is changed to zero and the integral values are doubled. Because the equation with respect to y_n is a second-order polynomial, it has two answers, for each mode we choose one that gives positive real part.

III. INPUT IMPEDANCE

For calculation of input impedance, electric field in microstrip antenna is given by [11]:

$$E_z(r_0) = I_0 \sum_{n=-\infty}^{\infty} \frac{\omega \mu_0 J_n(kr_0) Y_n(kr_0) i}{4} - \frac{\omega \mu_0 J_n^2(kr_0) \zeta i}{4\xi}, \quad (27)$$

$$\zeta = a k Y_{n+1}(ak) i + \omega a y_n \mu_0 Y_n(ak) - n Y_n(ak) i,$$

$$\xi = a k J_{n+1}(ak) i + \omega a y_n \mu_0 J_n(ak) - n J_n(ak) i,$$

$$k = \sqrt{\varepsilon} k_0,$$

where J_n and Y_n are Bessel function of the first kind and second kind, respectively. The input impedance can be written as following with respect to Equation (27):

$$Z_{in} = -\frac{1}{I_0} \int_0^h E_z(r_0) dz. \quad (28)$$

IV. RESULTS

Figure 3 and Fig. 4 show the comparison between theoretical and CST studio input impedance for two values of substrate permittivity. In order to examine modes behavior in this paper we consider PEC patch and PEC ground plane in conjunction with lossless dielectric.

For each calculation we consider 10 modes, the modes having order of greater than 10 were found to have insignificant effect on the calculated input impedance. It is seen that the mode matching results are close to that obtained by the CST studio simulation except for negligible shift in frequency. Figure 5 shows the effect of source position on input impedance. As it can be seen by increasing the radius of feed position the input impedance increases and the results are close to CST studio results.

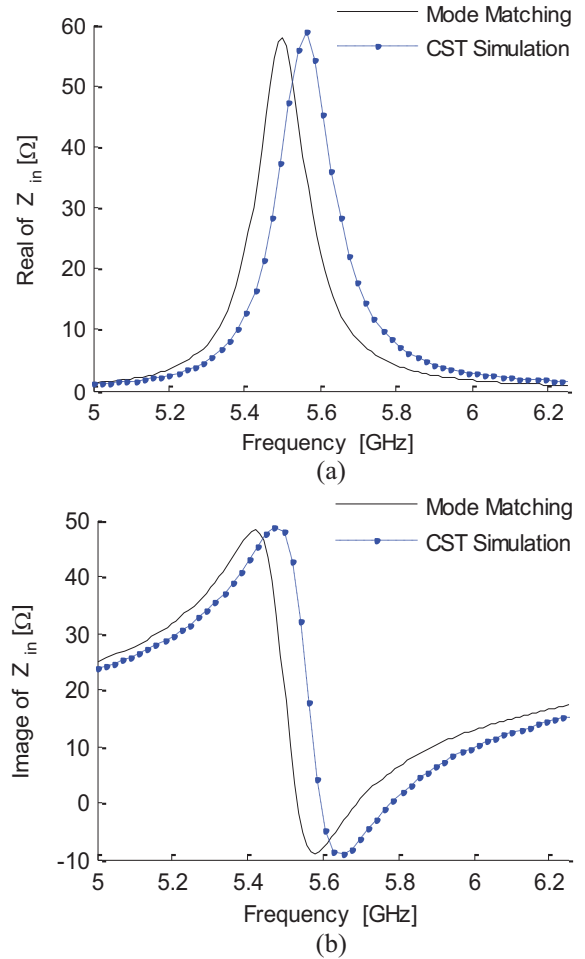


Fig. 3. Comparison between CST studio result and mode matching method. $a = 10mm, h = 1mm, \varepsilon_r = 2.2, r_0 = 2.725mm$, (a) real part and (b) imaginary part, respectively.

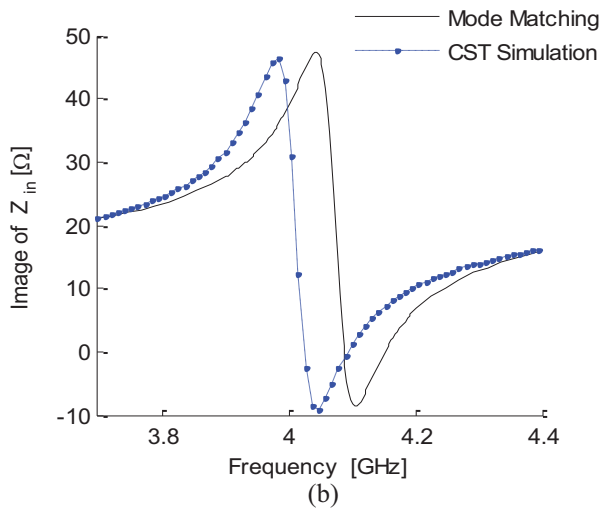
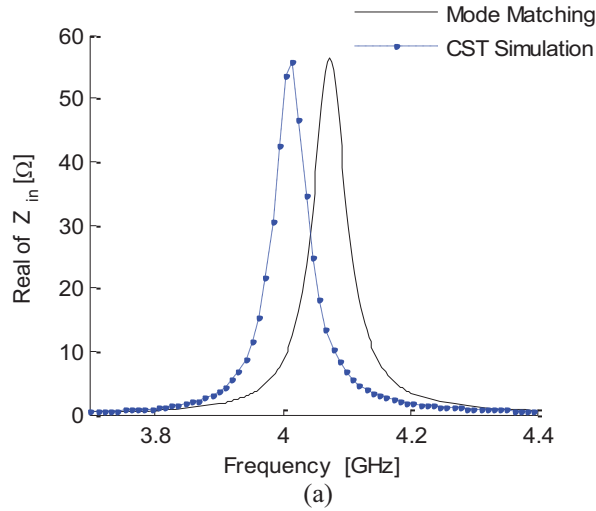


Fig. 4. Comparison between CST studio result and mode matching method. $a = 10\text{mm}, h = 1\text{mm}, \epsilon_r = 4.4, r_0 = 2.1\text{mm}$, (a) real part and (b) imaginary part, respectively.

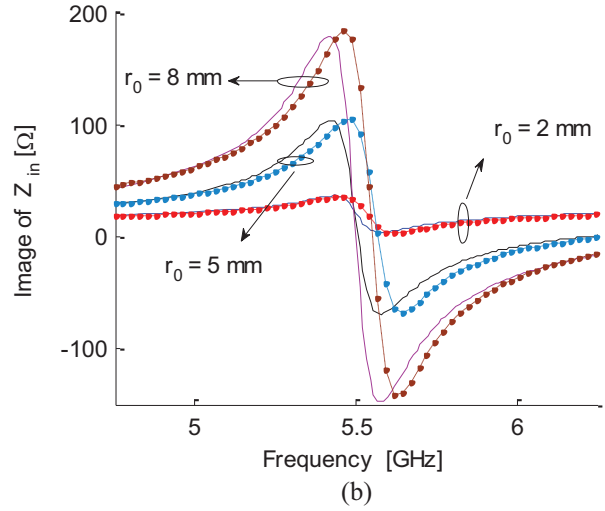
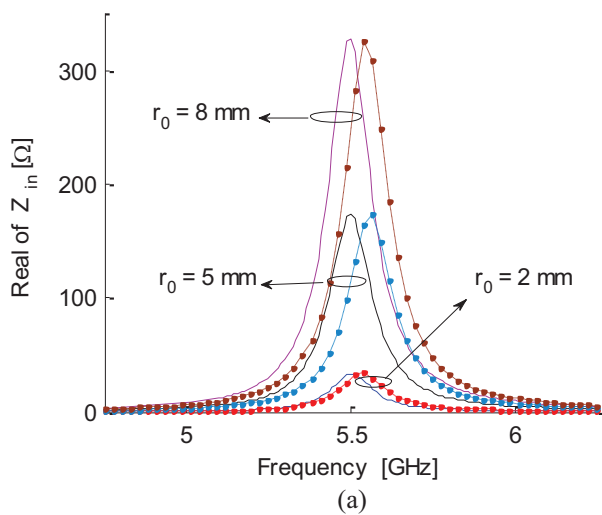


Fig. 5. Effects of source position on input impedance. $a = 10\text{mm}, h = 1\text{mm}, \epsilon_r = 2.2$, (a) real part and (b) imaginary part, respectively. Dashed lines: mode matching, dotted lines: CST studio simulation.

IV. CONCLUSION

In this paper, mode matching technique was used to calculate the input impedance of antenna for analysis of microstrip antenna with both electric and magnetic surface current on sidewall in cavity model. The results are in good agreement with simulation results except for about 2% shift in frequency. It is believed that these shifts in frequency in comparison with simulation results are because of fringing field at the edge of the patch and these can be compensated with defining better approximation for effective radius of patch. We believe that the concept that is used in this paper can be extended to other cylindrical shape structure like cylindrical slot.

REFERENCES

- [1] T. Samaras, A. Kouloglou, and J. N. Sahalos, "A note on the impedance variation with feed position of a rectangular microstrip-patch antenna," *IEEE Antennas and Propagation Magazine*, vol. 46, no. 2, pp. 90-92, 2004.
- [2] T. Günel, "Modified calculation for input impedance of probe-fed and inset-fed rectangular microstrip antennas," *Microwave and Optical Technology Letters*, vol. 57, no. 7, pp. 1650-1652, 2015.
- [3] Y. Sazanmi and A. Ishimaru, "A theoretical study of the input impedance of a circular microstrip disk antenna," *IEEE Transactions on Antennas and Propagation*, vol. 29, no. 1, pp. 77-83, 1981.
- [4] J. Kong, "Analysis of a circular microstrip disk antenna with a thick dielectric substrate," *Antennas and Propagation, IEEE Transactions on*, vol. 29, no. 1, pp. 68-76, 1981.

- [5] K.-F. Lee, K. Y. Ho, and J. S. Dahele, "Circular-disk microstrip antenna with an air gap," *Antennas and Propagation, IEEE Transactions on*, vol. 32, no. 8, pp. 880-884, 1984.
- [6] W. F. Richards, Y. T. Lo, and D. D. Harrison, "An improved theory for microstrip antennas and applications," *Antennas and Propagation, IEEE Transactions on*, vol. 29, no. 1, pp. 38-46, 1981.
- [7] J. Y. Siddiqui and D. Guha, "Improved formulas for the input impedance of probe-fed circular microstrip antenna," In *Antennas and Propagation Society International Symposium, 2003, IEEE*, vol. 3, pp. 152-155, 2003.
- [8] C. S. Gürel, E. Aydın, and E. Yazgan, "Computation and optimization of resonant frequency and input impedance of a coax-fed circular patch microstrip antenna," *Microwave and Optical Technology Letters*, vol. 49, no. 9, pp. 2263-2267, 2007.
- [9] G. Kumar and K. P. Ray, *Broadband Microstrip Antennas*, Artech House, 2002.
- [10] M. J. Mehler, T. S. M. Maclean, and A. K. Abbas, "Input impedance of a circular microstrip disc antenna using mode matching," *Electronics Letters*, vol. 22, no. 7, pp. 362-363, 1986.
- [11] G. Bahl and P. Ramesh, *Microstrip Antenna Design Handbook*, Artech House, 2001.
- [12] C. Balanis, *Advanced Engineering Electromagnetics*, John Wiley & Sons, 2012.

Design of Lowpass Filter and Lowpass-Highpass Diplexer with LTCC Technology

Chunxia Zhou^{1*}, Yongxin Guo², and Wen Wu¹

¹ Ministerial Key Laboratory of JGMT
Nanjing University of Science and Technology, Nanjing, 210094, China
zhouchx1010@gmail.com*, wuwen@njust.edu.cn

² Department of Electrical and Computer Engineering
National University of Singapore, Singapore 117583, Singapore
yongxin.guo@nus.edu.sg

Abstract— A compact lowpass filter (LPF) and a lowpass-highpass diplexer (LPD) with both sharp roll-off and wide stopband is presented in this paper. The proposed LPF is realized by cascading modified hairpin unit consisting of one U-shape stripline and one pair of offset-coupled striplines with multilayer low-temperature co-fired ceramic (LTCC) technology. The LPD is realized by shunting a lowpass filter and a highpass filter at a common junction to achieve all-reject in one port. Good agreement can be achieved by the simulated and measured results.

Index Terms — Coupled lines, Low-Temperature Co-fired Ceramic (LTCC), Lowpass filter (LPF), Lowpass-Highpass Diplexer (LPD).

I. INTRODUCTION

Compact, low cost, and highly integrated passive and active components are highly demanded by wireless-device manufacturers. The low temperature cofired ceramic (LTCC) technology, as one of the most promising methods, has been extensively utilized in recent years. LTCC offers layout flexibility and three-dimensional (3D) integration capability to produce embedded passive components, for example, filters [1, 2] and antennas [3], phase shift [4] and coupler [5]. The lowpass filter (LPF) is one of key passive components that are widely used in wireless systems to filter out unwanted signals. There are several conventional methods to design LPFs such as using shunt stubs, high-low impedance transmission lines, or cascading multiple resonators [6, 7]. However, it is quite hard to achieve LPFs with sharp attenuation skirt and compact size simultaneously. To overcome this difficulty, modified hairpin resonators have been widely adopted due to its compactness and flexibility. Various types of miniaturized and performance-improved LPFs have been studied based on hairpin resonators [8-14].

Elliptic-function LPFs with a wide stopband are presented in [8] by cascading microstrip stepped-impedance hairpin resonators. In [9], stopband-extended LPFs were realized by centrally tap-connecting the microstrip coupled-line hairpin resonator. In [10], a LPF with wide stopband was designed by cascading microstrip coupled-line hairpin resonator, semi-circle defected ground structures and semi-circle stepped-impedance shunt stubs. Stepped-impedance hairpin resonators with an interdigital structure [11, 12], shunt open-stubs [13], and radial stubs [14] were used for designing LPFs with sharp and expanded stopband.

In this paper, a compact LTCC LPF with sharp roll-off and wide stop-band is presented by cascading modified hairpin units. The unit consists of one U-shape stripline and one pair of offset-coupled striplines with multilayer LTCC technology. Measured results indicate that the designed filter has an ultra-wide stopband rejection better than 10 dB up to 20 GHz and a sharp roll-off of 81 dB/GHz. Furthermore, a lowpass-highpass diplexer (LHD) is presented to achieve all-reject in one port. It is realized by shunting a lowpass filter and a highpass filter at a common junction.

II. LOWPASS FILTER DESIGN

Figure 1 (a) shows the circuit schematic of the lowpass filter. It is realized by four sections of modified hairpin units. Each unit consists of one transmission line with electric length of θ_{Li} and impedance of Z_{Li} , and one pair of coupled lines with electric length of θ_{Ci} and even- and odd-mode impedances of Z_{ei} and Z_{oi} ($i=1, 2, 3, 4$). Figure 1 (b) gives the corresponding equivalent circuit, which is the prototype of elliptic-function LPF. The elliptic-function LPF is designed with cutoff frequency of $f=4.5$ GHz, passband ripple of 0.03 and attenuation in the stopband of -60 dB. With the element-value tables and frequency and element transformations [15], L-C

values of the 9-order elliptic-function LPF can be calculated as follows: $L_1=2.611$ (nH), $L_2=1.812$ (nH), $L_3=1.499$ (nH), $L_4=1.878$ (nH), $C_{g1}=0.097$ (PF), $C_{g2}=0.584$ (PF), $C_{g3}=0.803$ (PF), $C_{g4}=0.385$ (PF), $C_{p1}=0.686$ (PF), $C_{p2}=0.415$ (PF), $C_{p3}=0.399$ (PF) and $C_{p4}=0.497$ (PF). Then, the relationship between the parameters in Fig. 1 (a) and those in Fig. 1 (b) can be obtained [8]:

$$L_i = Z_i \sin(\theta_{L_i}) / \omega \quad (\text{H}), \quad (1)$$

$$C_{g_i} = (Z_{ei} - Z_{oi}) / (2\omega Z_{ei} Z_{oi} \cot(\theta_{C_i})) \quad (\text{F}), \quad (2)$$

$$C_{p_i} = 1 / (\omega Z_{ei} \cot(\theta_{C_i})) \quad (\text{F}), \quad (3)$$

($i = 1, 2, 3, 4$).

By comparing Equations (2) and (3), we can get:

$$Z_{ei} / Z_{oi} = (2C_{g_i} + C_{p_i}) / C_{p_i}. \quad (4)$$

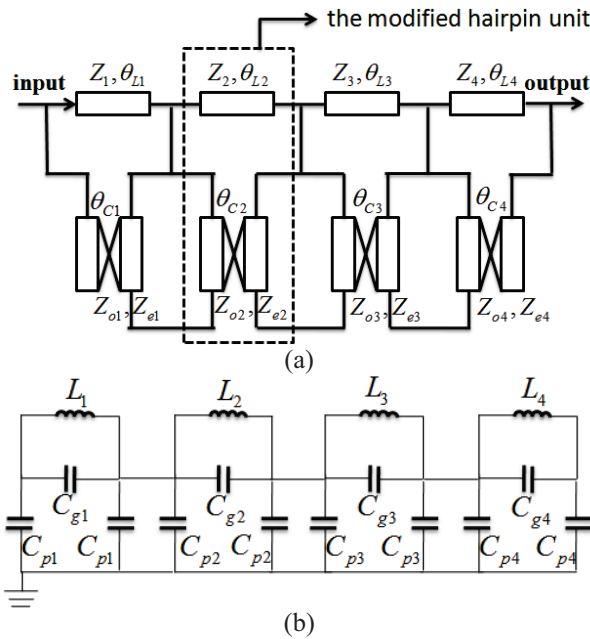


Fig. 1. Diagram of proposed LPF. (a) Circuit schematic and (b) corresponding equivalent circuit.

III. LOWPASS-HIGHPASS DIPLEXER DESIGN

Figure 2 shows the circuit schematic of the proposed LHD. It is realized by shunting a lowpass filter and a highpass filter at a common junction. It consists of five striplines with electric length of θ_i and impedance of Z_i ($i=1,2,3,4,7$), and four coupled lines with electric length of θ_i and even- and odd-mode impedance of Z_{ei} and Z_{oi} ($i=5,6,8,9$). To minimize reflections at the input port 1, the complex input admittances $Y_{in,LP}$ and $Y_{in,HP}$ of the two filters should satisfy at all frequencies the equation:

$$Y_{in} = Y_{in,LP} + Y_{in,HP} = Y_0. \quad (5)$$

This condition can be split into the following two conditions:

$$\text{Re}(Y_{in,LP}) + \text{Re}(Y_{in,HP}) = Y_0. \quad (6)$$

$$\text{Im}(Y_{in,LP}) + \text{Im}(Y_{in,HP}) = 0$$

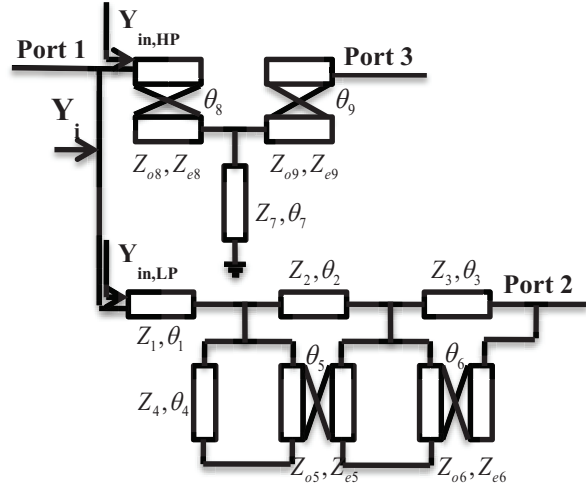


Fig. 2. Circuit schematic of the proposed LHD.

IV. FILTER AND DIPLEXER IMPLEMENTATION IN LTCC TECHNOLOGY

The filter and diplexer are designed in a 10-layer LTCC substrate, with the relative permittivity of 5.9, loss tangent of $\tan\delta=0.0015$, and thickness of each substrate layer of 96 μm . There are 11 metal layers from top to bottom. The 3D configuration of the proposed LPF is illustrated in Fig. 3. The configuration is build up according to the basic circuit shown in Fig. 1 (a). The sections of four transmission lines are realized by U-shape striplines in metal layer 5, layer 6 and layer 8, with width of 0.2 mm. According to Equation (1), we can get $\theta_{L1}=90^\circ$, $\theta_{L2}=49.4^\circ$, $\theta_{L3}=38.9^\circ$ and $\theta_{L4}=51.9^\circ$. The sections of four pairs of coupled lines are realized by offset-coupled striplines with width of 0.53 mm. Then adjusting the relatively positions of the offset-coupled striplines to satisfying Equation (4), we can get each Z_{ei} , Z_{oi} , and θ_{C_i} ($i=1,2,3,4$). With trial-and-error operations, the first pair of coupled lines is determined in layers 2 and 8, the second in layers 7 and 8, the third in layers in 6 and 7 and the forth in layers 4 and 6. Furthermore, $Z_{e1}=28.2 \Omega$, $Z_{o1}=22.1 \Omega$, $\theta_{C1}=25.8^\circ$, $Z_{e2}=50.6 \Omega$, $Z_{o2}=13.2 \Omega$, $\theta_{C2}=27.6^\circ$, $Z_{e3}=55 \Omega$, $Z_{o3}=10.9 \Omega$, $\theta_{C3}=28.7^\circ$, $Z_{e4}=48 \Omega$, $Z_{o4}=18.1 \Omega$, $\theta_{C4}=29.6^\circ$. After optimization using Ansoft HFSS, we can get that the lengths of the four striplines corresponding to θ_{L1} , θ_{L2} , θ_{L3} and θ_{L4} are 5.45 mm, 4.36 mm, 3.13 mm and 5.2 mm respectively. The lengths of the coupled striplines corresponding to θ_{C1} , θ_{C2} , θ_{C3} and θ_{C4} are 1.8 mm, 2 mm, 2.2 mm and 2.24 mm respectively. The designed parameters of the LPF are summarized in Table 1. The S-parameters in both the simulated and the measured results are shown in Fig. 4. The photo of the filter prototype is shown in Fig. 5. Its overall size is only

4.54×3.37×0.96 mm³. For comparison, Table 2 summarizes the performances of some published lowpass filters. As can be seen from the table, our proposed filter has the properties of sharp roll-off, ultra-wide stopband, and compact size simultaneously.

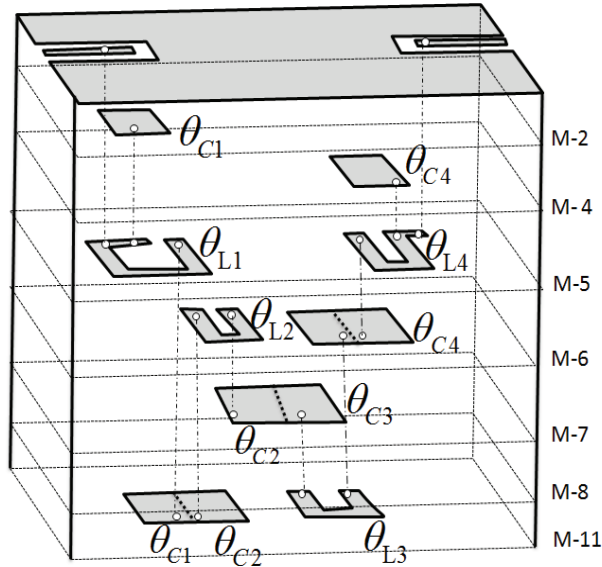


Fig. 3. 3D configuration of the proposed LPF.

Table 1: The designed parameters of the LPF

i	1	2	3	4
θ_{Li}	90°	49.4°	38.9°	51.9°
θ_{Ci}	25.8°	27.6°	28.7°	29.6°
Z_{ei} (Ω)	28.2	50.6	55	48
Z_{oi} (Ω)	22.1	13.2	10.9	18.1
L_{Li} (mm)	5.45	4.36	3.13	5.2
L_{Ci} (mm)	1.8	2	2.2	2.24

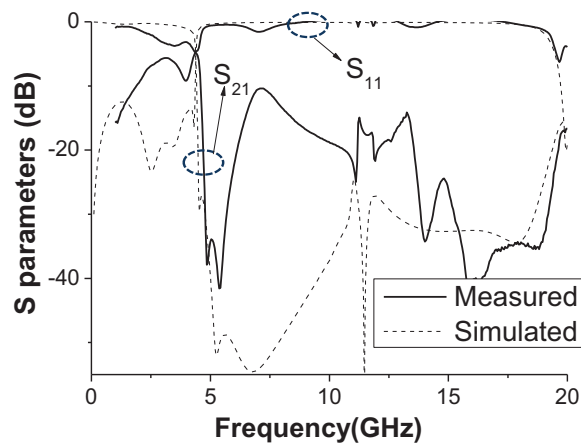


Fig. 4. Simulated and measured results of the LPF.

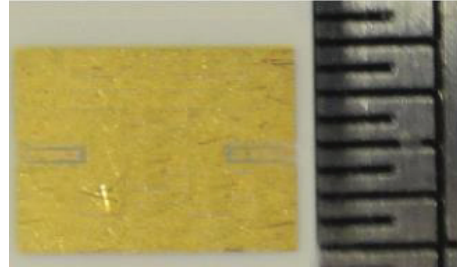


Fig. 5. Photo of the lowpass filter prototype.

Table 2: Performance comparisons among published filters and the proposed one

Ref.	Roll Off (dB/GHz)	Stopband Up to (GHz)	Circuit Size ($\lambda_g * \lambda_g$)
[8]	37	4.8	0.09*0.35
[9]	45	15	0.23*0.27
[10]	74	6	0.11*0.10
[11]	95	9	0.10*0.21
[12]	28	12	0.08*0.08
[13]	43.2	12	0.39*0.83
This work	81	20	0.14*0.11

The 3D configuration of the proposed LHD is illustrated in Fig. 6. The configuration is built up according to the basic circuit shown in Fig. 2. The sections of five transmission lines are realized by microstrip line in the top metal (θ_1) with width of 0.2 mm, U-shape striplines in metal layer 6 (θ_2) and layer 4 (θ_3) with width of 0.2 mm, stripline in layer 4 (θ_4) with width of 0.6 mm and L-shape stripline in metal layer 6 (θ_5) with width of 0.2 mm. The sections of four pairs of coupled lines are realized by offset-coupled striplines in layers 4 and 7 (θ_5) with width of 0.6 mm, the second in layers 2 and 7 (θ_6) with width of 0.6 mm, the third in layers in 5 and 6 (θ_8) with width of 0.2 mm and the fourth in layers 4 and 6 (θ_9) with width of 0.6 mm. To satisfying Equation (5), the design parameters are determined as follows: $\theta_1=43^\circ$, $\theta_2=47^\circ$, $\theta_3=46^\circ$, $\theta_4=29^\circ$, $\theta_5=37^\circ$, $\theta_6=20^\circ$, $\theta_7=47^\circ$, $\theta_8=25^\circ$ and $\theta_9=10^\circ$.

After optimization using Ansoft HFSS, we can get that the lengths of one microstrip line and four striplines corresponding to θ_1 , θ_2 , θ_3 , θ_4 and θ_7 are 3.3 mm, 3.6 mm, 3.5 mm, 2.2 mm and 1.6 mm respectively. The lengths of the coupled striplines corresponding to θ_5 , θ_6 , θ_8 and θ_9 are 2.7 mm, 1.5 mm, 1.9 mm and 0.5 mm respectively. The designed parameters of the LHD are summarized in Table 3. Both the simulated and the measured results are shown in Fig. 7. The photo of the diplexer prototype is shown in Fig. 8. Its overall size is only 5.8×5.3×0.96 mm³. For comparison, Table 4 summarizes the performances of some published diplexers.

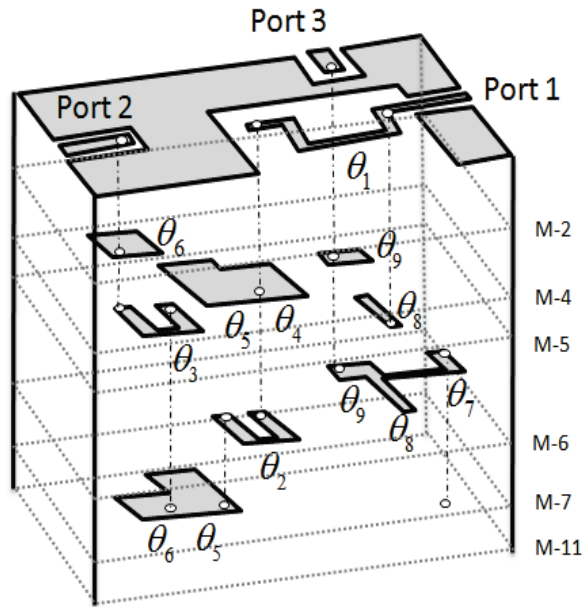


Fig. 6. 3D configuration of the proposed LHD.

Table 3: The designed parameters of the LHD

i	1	2	3	4	5	6	7	8	9
θ_i	43°	47°	46°	29°	37°	20°	47°	25°	10°
L_i (mm)	3.3	3.6	3.5	2.2	2.7	1.5	1.6	1.9	0.5

Table 4: Performance of diplexers

Ref.	Type	f_c (GHz)	Size ($\lambda_g * \lambda_g$)
[15]	Lowpass-Bandpass	1.5	0.80*0.41
[16]	Lowpass-Highpass	0.92	0.43*0.20
This work	Lowpass-Highpass	4.5	0.18*0.16

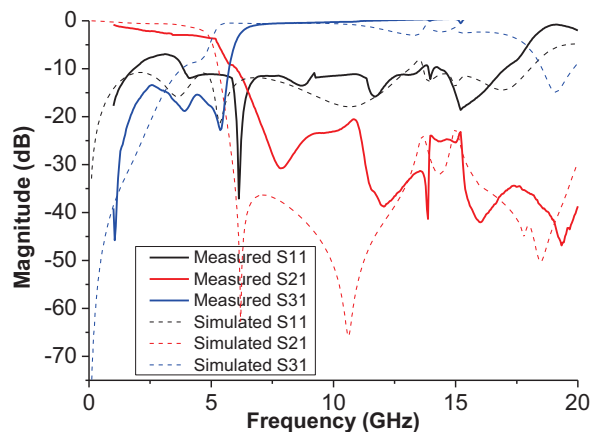


Fig.7. Simulated and measured results of the LHD.

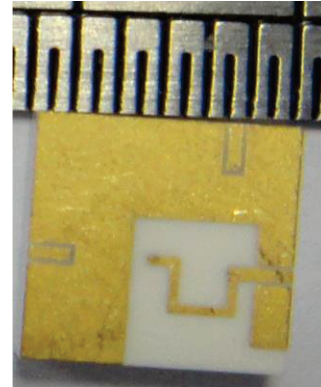


Fig. 8. Photo of the lowpass diplexer prototype.

V. CONCLUSION

A compact LPF and LHD with sharp roll-off skirt and wide stopband are implemented in multilayer LTCC. The LPF is realized by cascading modified hairpin unit consisting of one U-shape stripline and one pair of offset-coupled striplines. The designed filter has an ultra-wide stopband rejection better than 10 dB up to 20 GHz and a sharp roll off of 81 dB/GHz. Furthermore, the size of the filter is only $4.54 \times 3.37 \text{ mm}^2$. The LPD is realized by shunting a lowpass filter and a highpass filter at a common junction to achieve all-reject in one port. The size of the diplexer is $4.54 \times 3.37 \text{ mm}^2$. The measured results are in good agreements with the simulation predictions.

ACKNOWLEDGEMENT

This work was supported by the National Natural Science Foundation Committee of China (61401202).

REFERENCES

- [1] L. K. Yeung and K. L. Wu, "A compact second-order LTCC bandpass filter with two finite transmission zeros," *IEEE Trans. Microwave Theory & Tech.*, vol. 51, no. 2, pp. 337-341, Feb. 2003.
- [2] T. M. Shen, C. F. Chen, T. Y. Huang, et al., "Design of vertically stacked waveguide filters in LTCC," *IEEE Trans. Microwave Theory & Tech.*, vol. 55, no. 8, pp. 1771-1779, Aug. 2007.
- [3] R. L. Li, G. DeJean, M. Maeng, et al., "Design of compact stacked-patch antennas in LTCC multilayer packaging modules for wireless applications," *IEEE Trans. Compon., Packag., Manuf. Technol.*, vol. 27, no. 4, pp. 581-589, Mar. 2013.
- [4] A. Nafe and A. Shamim, "An integrable SIW phase shifter in a partially magnetized ferrite LTCC package," *IEEE Trans. Microwave Theory & Tech.*, vol. 63, no. 7, pp. 2264-2274, Jul. 2015.

- [5] C. H. Tseng, "Compact LTCC rat-race couplers using multilayered phase-delay and phase-advance T-equivalent sections," *IEEE Trans. Compon., Packag., Manuf. Technol.*, vol. 33, no. 2, pp. 543-551, May 2010.
- [6] I. S. Kim and S. W. Yun, "Compact LPF using asymmetrical microstrip step discontinuity for harmonic suppression," *Electron. Lett.*, vol. 41, no. 16, pp. 41-42, Aug. 2005.
- [7] J. L. Li, S. W. Qu, and Q. Xue, "Compact microstrip lowpass filter with sharp roll-off and wide stopband," *Electron. Lett.*, vol. 45, no. 2, pp. 110-111, Jan. 2009.
- [8] L. H. Hsieh and K. Chang, "Compact elliptic-function low-pass filters using microstrip stepped-impedance hairpin resonators," *IEEE Trans. Microw. Theory Tech.*, vol. 51, no. 1, pp. 193-198, Jan. 2003.
- [9] S. Luo, L. Zhu, and S. Sun, "Stopband-expanded low-pass filters using microstrip coupled-line hairpin units," *IEEE Microw. Wireless Compon. Lett.*, vol. 18, no. 8, pp. 506-508, Aug. 2008.
- [10] F. Wei, L. Chen, X. W. Shi, Q. L. Huang, and X. H. Wang, "Compact lowpass filter with wide stopband using coupled-line hairpin unit," *Electron. Lett.*, vol. 46 no. 1, pp. 88-90, Jan. 2010.
- [11] L. Li, Z. F. Li, and J. F. Mao, "Compact lowpass filters with sharp and expanded stopband using stepped impedance hairpin units," *IEEE Microw. Wireless Compon. Lett.*, vol. 20, no. 6, pp. 310-312, Jun. 2010.
- [12] V. K. Velidi and S. Sanyal, "Sharp roll-off lowpass filter with wide stopband using stub-loaded coupled-line hairpin unit," *IEEE Microw. Wireless Compon. Lett.*, vol. 21, no. 6, pp. 301-303, Jun. 2011.
- [13] X. B. Wei, P. Wang, M. Q. Liu, and Y. Shi, "Compact wide-stopband lowpass filter using stepped impedance hairpin resonator with radial stubs," *Electron. Lett.*, vol. 47, no. 15, pp. 862-863, Jul. 2011.
- [14] M. Kufai and Z. Raida, "Lowpass filter with reduced fractal defected ground structure," *Electron. Lett.*, vol. 49, no. 3, pp. 199-200, Jan. 2013
- [15] P. H. Deng and J. T. Tsai, "Design of microstrip lowpass-bandpass diplexer," *IEEE Microw. Wireless Compon. Lett.*, vol. 23, no. 7, pp. 332-334, Jul. 2013.
- [16] M. Jung and B. W. Min, "Microstrip lowpass-highpass diplexer for a quadplexer application," *Microw. Opt. Technol. Lett.*, vol. 56, no. 9, pp. 332-334, Jul. 2014.
- [17] J. S. Hong and M. J. Lancaster, *Microstrip Filters for RF/Microwave Applications*, New York: Wiley, 2001.



Chun-Xia Zhou (M'14) was born in Jiangsu Province, China, in 1985. She received the B.S. and Ph.D. degree in Electronic Engineering from Nankai University, Tianjin, China, in 2007 and 2012, respectively.

From September 2010 to February 2012, she was a joint Ph.D. student with the Department of Electrical and Computer Engineering, National University of Singapore (NUS), Singapore. From December 2012 to July 2012, she was a Research Fellow with Terahertz Science and Technology Research Center of China Academy of Engineering Physics, Chengdu, China. She is currently a Lecturer with the School of Electronic Engineering and Optoelectronic Technology, Nanjing University of Science and Technology, Nanjing, China. Her research interests include the design and optimization of microwave and millimeter-wave circuits, and microwave and millimeter-wave integrated circuits in CMOS technology.



Yong-Xin Guo (S'00-A'02-M'03-SM'05) received the Ph.D. degree from the City University of Hong Kong, Hong Kong, in 2001.

He is currently an Associate Professor with the Department of Electrical and Computer Engineering (ECE), National University of Singapore (NUS), Singapore, and Director of the Center for Microwave and Radio Frequency of the Department of ECE, NUS. Concurrently, he is a Senior Investigator with the National University of Singapore Research Institute (NUSRI), Suzhou, China, and Director of the Center of Advanced Microelectronic Devices, NUSRI. From September 2001 to January 2009, he was with the Institute for Infocomm Research, Singapore, as a Research Scientist. He has authored or co-authored 132 international journal papers and 150 international conference papers. His publications have been cited by others more than 1040 times (source: Scopus). He holds one Chinese Patent, one U.S. patent and four provisional U.S. patents. His current research interests include microstrip antennas for wireless communications, implantable/wearable antennas and body channel modeling for medical applications, wireless power and RF energy harvesting, microwave circuits, and monolithic microwave integrated circuit (MMIC) modeling and design.

Guo was the General Chair of the IEEE Microwave Theory and Techniques Society (MTT-S) International Microwave Workshop Series 2013 on "RF and Wireless Technologies for Biomedical and Healthcare Applications" (IMWS-Bio 2013), Singapore. He is an Associate Editor

for IEEE Antennas and Wireless Propagation Letters (AWPL). He was a recipient of the Young Investigator Award 2009, National University of Singapore and the 2013 “Raj Mittra” Travel Grant Senior Researcher Award.



Wen Wu (SM'10) received the Ph.D. degree in Electromagnetic Field and Microwave Technology from Southeast University, Nanjing, China, in 1997.

He is currently a Professor with the School of Electronic Engineering and Optoelectronic Technology and an Associate Director with the Ministerial Key

Laboratory of JGMT, Nanjing University of Science and Technology, Nanjing, China. He has authored and co-authored over 120 journal and conference papers. He has submitted five patent applications. His current research interests include microwave and millimeter-wave (mm-wave) theories and technologies, microwave and mm-wave detection, and multimode compound detection.

Wu was a six-time recipient of the Ministerial and Provincial-Level Science and Technology Award.

Ferrite-Loaded Substrate Integrated Waveguide Frequency-Agile Bandpass Filter

Qiu Dong Huang and Yu Jian Cheng*

EHF Key Laboratory of Fundamental Science, School of Electronic Engineering
University of Electronic Science and Technology of China, Chengdu 611731, P. R. China
chengyujian@uestc.edu.cn*

Abstract — In this paper, a ferrite-loaded substrate integrated waveguide (SIW) frequency tunable bandpass filter is presented. Two ferrite slabs are loaded at sidewalls of an SIW. When a DC magnetic bias is applied to the ferrite slabs, the equivalent width of the ferrite-loaded SIW is changed, which contributes to the tuning ability. As an example, a ferrite-loaded SIW frequency-agile bandpass filter is designed and fabricated according to this principle. Its center frequency can be adjusted from 12.35 GHz to 13.2 GHz. Within this frequency range, the insertion loss is changed from 2.3 dB to 3.9 dB and the return loss is better than 10 dB.

Index Terms — Bandpass filter, ferrite-loaded, frequency-agile, Substrate Integrated Waveguide (SIW).

I. INTRODUCTION

Reconfigurable microwave devices have received much attention because of growing demands for dynamic spectrum management in smart and miniaturized wireless systems. Ferrite materials are widely used in magnetic control devices. This is because operating characteristics of ferrite materials can be controlled by applied DC magnetic bias. Combined with the currently popular substrate integrated waveguide (SIW) technology [1-5], many ferrite-loaded SIW components are presented in recent years, such as tunable filters [6-7], reconfigurable antennas [8-9], phase shifters [10], tunable cavity resonators [11], isolators [12-13], switches [14-15], etc.

Microwave frequency tunable bandpass filters are important components in future systems. In [4], an electrically and magnetically tunable SIW bandpass filter is proposed. However, it is complicated to apply the voltage control and the magnetic control simultaneously. In [16]-[18], lumped elements, such as PIN diodes and varactors, are utilized to construct SIW reconfigurable filters. Limited by the operating frequency and power handling capacity of lump elements, it is difficult to develop this kind of reconfigurable filter in high frequency band.

In [19], a new concept of frequency tunable bandpass filter is proposed based on the ferrite-loaded SIW and shortly discussed. Detailed design process and experimental result are presented in this paper. This type of filter can work in high frequency with simple configuration. By applying DC magnetic bias to the ferrite slabs, the equivalent width of the SIW is changed. Thus, the operating frequency of this bandpass filter can be reconfigured by the DC magnetic bias.

II. FILTER IMPLEMENTATION

In this section, we firstly investigate the electrical property of the ferrite-loaded SIW, and then obtain the equivalent width of the ferrite-loaded SIW when the DC magnetic bias is perpendicular to the direction of propagation. After that, a frequency-agile inductive post bandpass filter is designed based on the ferrite-loaded SIW.

In our design, the used dielectric substrate is the Taconic TLY-5 with a thickness of 1.52 mm. Its permittivity and loss tangent are 2.2 and 0.0009, respectively. The used ferrite material is YIG-1850. Its saturation magnetization value is 1850 Gs, relative dielectric constant is 14.5, and 3 dB line width is 20 Oe, respectively.

A. Ferrite-loaded SIW

Figure 1 illustrates the configuration of the SIW loaded with ferrite slabs. Two rectangular ferrite slabs are loaded along the conducting sidewall. W_f and L_f are the width and length of the ferrite slabs, respectively. The thickness of the ferrite slabs is the same as the substrate. Applied DC magnetic bias, dH , is perpendicular to the loaded ferrite slabs. According to [14],

$$\frac{1 + \cos[2\pi f_c(W_2 - 2W_f)\sqrt{\mu_s \varepsilon_s}]}{1 - \cos[2\pi f_c(W_2 - 2W_f)\sqrt{\mu_s \varepsilon_s}]} = \left(\frac{|\mu_f| \varepsilon_s}{\mu_s \varepsilon_f} \right) \tanh^2 \left[2\pi f_c W_f \sqrt{|\mu_f \varepsilon_f|} \right] \quad (1)$$

In (1), W_2 is depicted in Fig. 1, f_c is the cutoff frequency of the TE₁₀ mode in the ferrite-loaded SIW, ϵ_s is the dielectric constant of the substrate, μ_s is the magnetic permeability of the substrate, ϵ_f is the dielectric constant of the ferrite, and μ_f is the effective permeability [20] of the ferrite, which can be written as:

$$\mu_f = \frac{\mu^2 - \kappa^2}{\mu}. \quad (2)$$

In (2), μ and κ are the permeability tensor elements of the ferrite material, which are related to the external bias, the saturation magnetization value and the operating frequency.

As shown in Fig. 2, the cutoff frequency calculated by (2) of the ferrite-loaded SIW varies with the DC magnetic bias. When the DC magnetic bias ranges from 0 to 0.16 T, the cutoff frequency varies from 9.51 GHz to 10.53 GHz.

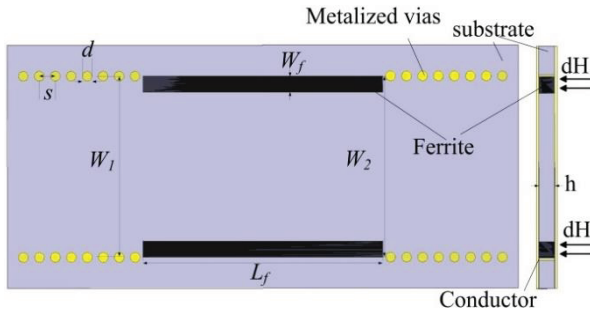


Fig. 1. Configuration of the ferrite-loaded SIW.

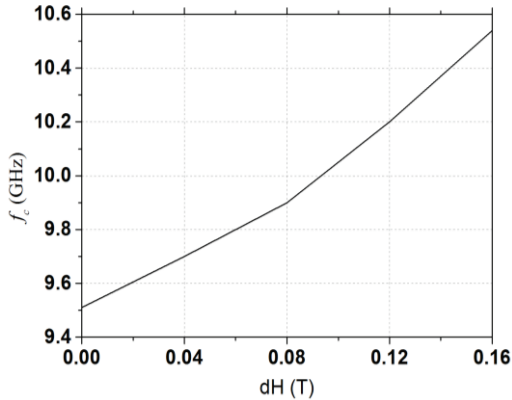


Fig. 2. Cutoff frequency of the ferrite-loaded SIW versus different internal bias dH .

Then, the equivalent width of the ferrite-loaded SIW, a_{eff} , can be calculated by:

$$a_{eff} = \frac{1}{2f_c \sqrt{\mu_s \epsilon_s}}. \quad (3)$$

As shown in Fig. 3, a_{eff} varies from 10.62 mm to

9.6 mm when the DC magnetic bias ranges from 0 to 0.16 T.

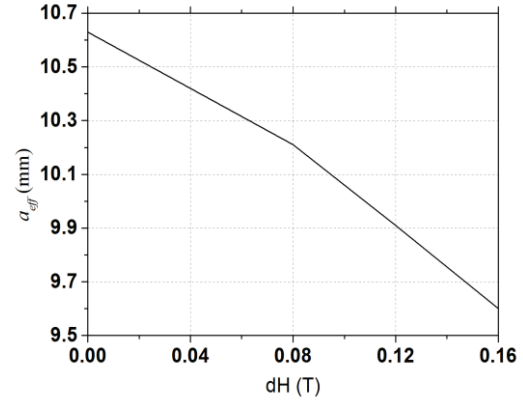


Fig. 3. Equivalent width of the ferrite-loaded SIW versus different internal bias dH .

B. Filter design

The configuration of the proposed ferrite-loaded SIW bandpass filter is shown in Fig. 4. Metalized posts are drilled on the centerline of the ferrite-loaded SIW. A maximally flat tunable bandpass filter is designed with a starting operating frequency centered at 12.65 GHz. Within the starting operating frequency band, the bandpass filter requires a bandwidth of 330 MHz and a minimum attenuation of 30 dB at 12.15 GHz. The tunable frequency range is 0.9 GHz. The design procedure of this kind of filter is listed as follows.

First, the minimum order, n , of the filter can be chosen according to the desired out-of-band rejection at the starting frequency without the DC magnetic bias. Then, the element values, i.e., g_0 to g_{n+1} , of the lowpass filter prototype can be calculated based on the method as described in [21]. Here, $n=3$, $g_0=1$, $g_1=1$, $g_2=2$, $g_3=1$ and $g_4=1$. After that, the lowpass filter prototype can be converted to the bandpass filter prototype through the K conversion as follows:

$$\frac{K_{01}}{Z_0} = \sqrt{\frac{\pi}{2}} \frac{B_\lambda}{g_0 g_1}, \quad (4)$$

$$\frac{K_{i,i+1}}{Z_0} = \frac{\pi B_\lambda}{2} \sqrt{\frac{1}{g_i g_{i+1}}}, \quad (5)$$

$$\frac{K_{n,n+1}}{Z_0} = \sqrt{\frac{\pi}{2}} \frac{B_\lambda}{g_n g_{n+1}}. \quad (6)$$

In (4)~(6),

$$B_\lambda = \frac{\lambda_{g1} - \lambda_{g2}}{\lambda_{g0}}. \quad (7)$$

In (7), λ_{g1} , λ_{g2} and λ_{g0} are the guide wavelength at the edge and the center frequencies of the starting operating frequency band.

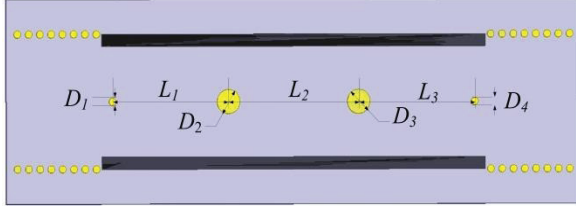


Fig. 4. Configuration of the proposed three-order frequency-agile filter.

Now, a bandpass filter can be realized based on the ferrite-loaded SIW structure. As shown in Fig. 5, an inductive post within a waveguide can be equivalent to the T-type network consisting of inductances and capacitances. When the metallized post is placed at the center point [22], there is

$$\frac{X_{ai} - X_{bi}}{Z_0} = \frac{a_{eff}}{2Z_0} \times \left[S_0 - \left(\frac{\pi D_i}{2\lambda} \right)^2 - \frac{5}{8} \left(\frac{\pi D_i}{2\lambda} \right)^4 - 2 \left(\frac{\pi D_i}{2\lambda} \right)^4 \left(S_2 - 2S_0 \frac{\lambda^2}{\lambda_g^2} \right)^2 \right], \quad (8)$$

$$\frac{X_{bi}}{Z_0} = \frac{a_{eff}}{\lambda_g} \times \frac{\left(\pi D_i / a_{eff} \right)^2}{\left(1 + \frac{1}{2} \left(\frac{\pi D_i}{\lambda} \right)^2 \right) \times \left(S_2 + \frac{3}{4} \right)}. \quad (9)$$

In (8) and (9),

$$S_0 = \ln \left(\frac{4a_{eff}}{\pi D_i} \right) - 2 + 2 \sum_{n=3,5,\dots}^{\infty} \left[\frac{1}{\sqrt{n^2 - \left(\frac{2a_{eff}}{\lambda} \right)^2}} - \frac{1}{n} \right], \quad (10)$$

$$S_2 = \ln \left(\frac{4a_{eff}}{\pi D_i} \right) - \frac{5}{2} - \frac{11}{3} \left(\frac{\lambda}{2a_{eff}} \right)^2 - \left(\frac{\lambda}{a_{eff}} \right)^2 \sum_{n=3,5,\dots}^{\infty} \left[\sqrt{n^2 - \left(\frac{2a_{eff}}{\lambda} \right)^2} - n + \frac{2}{n} \left(\frac{a_{eff}}{\lambda} \right)^2 \right]. \quad (11)$$

Besides, a_{eff} can be calculated by (3). Combined with (8)~(9), the equivalent parameters of posts in the ferrite-loaded SIW structure can be calculated with $dH=0$.

Here, the impedance inverter can be calculated by use of these equations:

$$\frac{K_{i,i+1}}{Z_0} = \tan \left(\frac{\Phi_i}{2} - \arctan \frac{X_{bi}}{Z_0} \right), \quad (12)$$

$$\Phi_i = -\arctan \left(2 \frac{X_{ai} - X_{bi}}{Z_0} \right) + \arctan \frac{X_{bi}}{Z_0}. \quad (13)$$

Taking the result calculated from (4)~(7) into (12)

and (13), the required X_{ai} and X_{bi} can be calculated. Thus, the dimensions of the ferrite-loaded bandpass filter can be determined.

Then, the distance between adjacent center vias is determined by the following equation:

$$L_i = \frac{\lambda_g}{2} \left[1 + \frac{1}{2\pi} (\Phi_i + \Phi_{i+1}) \right]. \quad (14)$$

After the tunable filter is designed at $dH=0$, the tuning range can be determined as follows. When a nonzero DC magnetic bias is applied to the ferrite slabs, the center frequency of the bandpass filter can be calculated by:

$$f_0 = f_c L_i \frac{1}{\sqrt{L_i^2 - \left[1 + \frac{1}{2\pi} (\Phi_i + \Phi_{i+1}) \right]^2}}. \quad (15)$$

In (15), D_i and L_i are kept constant, f_c is related with dH . As shown in Fig. 6, the computed result agrees well with the simulated one.

Now, the performance of the filter can be improved based on the full-wave optimization implemented by HFSS. The dimension of the ferrite slab is firstly optimized. For the structure as shown in Fig. 1, a bigger W_f leads to a better tuning ability but a worse return loss. Then, other parameters of the ferrite-loaded SIW bandpass filter are optimized slightly based on the calculated parameters. The final parameters are: $W_1=W_2=11.2$ mm, $d=0.6$ mm, $s=1$ mm, $W_f=1$ mm, $L_f=34$ mm, $L_1=L_3=10.4$ mm, $L_2=11.6$ mm, $D_1=D_4=0.6$ mm and $D_2=D_3=2$ mm.

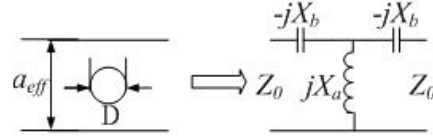


Fig. 5. Metalized post in a waveguide and its equivalent circuit.

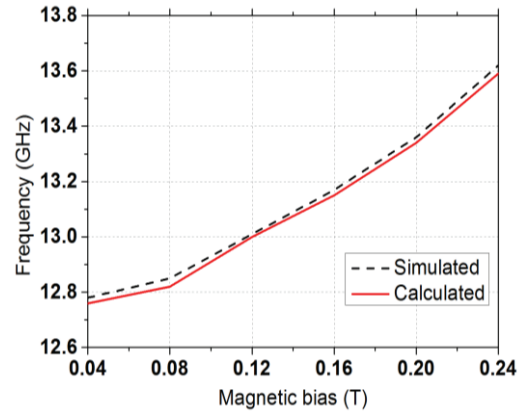


Fig. 6. Operating frequency of the bandpass filter versus DC magnetic bias.

III. EXPERIMENT RESULTS AND DISCUSSION

As shown in Fig. 7, a ferrite-loaded SIW frequency-agile bandpass filter is fabricated. A transition from the coaxial cable to the SIW [23] is employed in this design convenient for the test.

HFSS from Ansys is used in this work. Simulated results of the designed filter are shown in Fig. 8. When the internal magnetic bias is increased from 0 T to 0.24 T, the operating frequency of the filter can be adjusted from 12.65 GHz to 13.6 GHz. The return loss is better than 15 dB within the range. The insertion loss is changed from 1.9 dB to 3.8 dB. At the same time, the 3 dB bandwidth is decreased from 2.6% to 1.85%.

The measured results are shown in Fig. 9. Because of boundary conditions at the surface of the ferrite sample [20], the value of the actually applied external bias, dH' is bigger than the internal bias dH . When the external magnetic bias is varied from 0 T to 0.34 T, the center frequency of the ferrite-loaded SIW bandpass filter can be tuned from 12.35 GHz to 13.2 GHz. Besides, the 3 dB bandwidth is decreased from 4.8% to 3.2%. The insertion loss is changed from 2.3 dB to 3.9 dB. Over the whole working frequency, a better than 10 dB return loss is achieved.

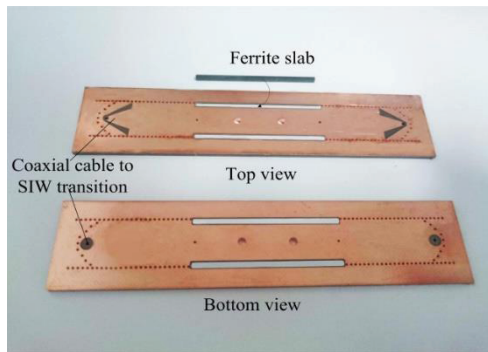


Fig. 7. Photograph of the fabricated ferrite-loaded SIW frequency-agile bandpass filter.

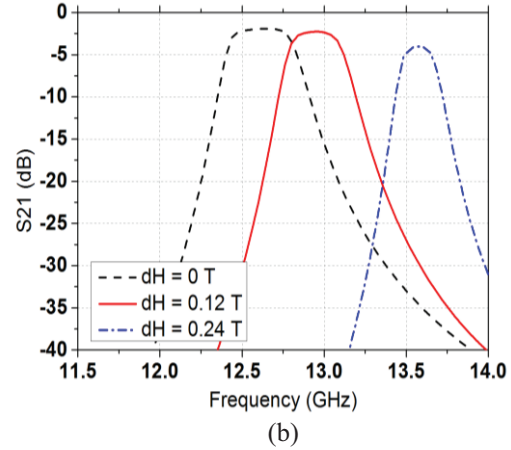
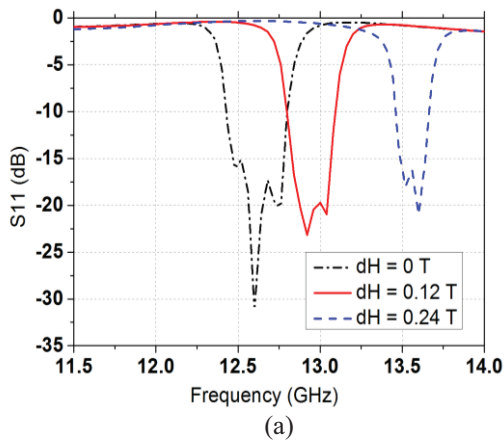


Fig. 8. Simulated S-parameter of the designed filter with different internal magnetic bias, dH . (a) Return loss and (b) insertion loss.

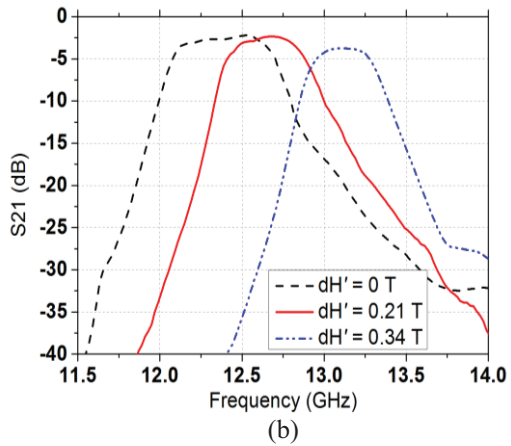
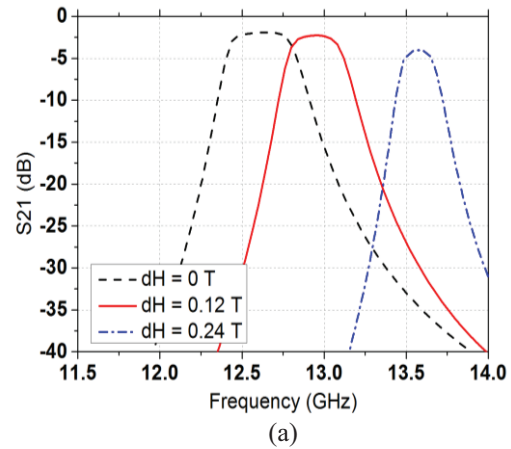


Fig. 9. Measured S-parameter with different total applied external magnetic bias, dH' . (a) Return loss and (b) insertion loss.

Because of machining errors, there exists a frequency shift of about 0.3 GHz compared with Fig. 8. The reason

that causes the frequency offset is analyzed as follows. There exist two grooves in the substrate through normal PCB process. This fabrication is not so accurate. The tolerance of the groove in the substrate is firstly discussed. As shown in Fig. 10, when W_2 varies 0.1 mm, the center frequency will change about 0.1 GHz. Besides, as shown in Fig. 11, when the width of the ferrite slab increases 0.05 mm, the center frequency of the filter will move about 0.05 GHz. That means machining errors of the groove and the ferrite slab make main contributions to the frequency shift. Furthermore, the roughness of the groove also has an impact on the performance of the filter.

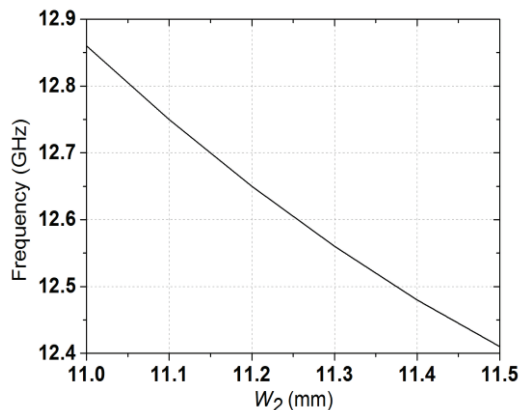


Fig. 10. Tolerance of W_2 .

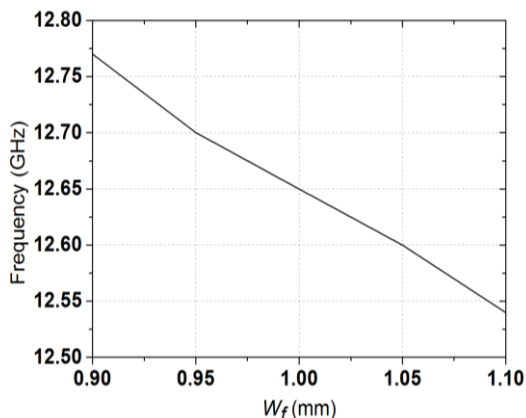


Fig. 11. Tolerance of the width of the ferrite slabs W_f .

IV. CONCLUSION

A new tunable ferrite-loaded SIW frequency-agile bandpass filter is designed and fabricated in this paper. It achieves the tuning ability by applying DC magnetic bias to the ferrite slabs, which are loaded along the partly metallized sidewall of the SIW. The fabricated ferrite-loaded bandpass filter can be tuned from 12.35 GHz to 13.2 GHz with a return loss of less than 10 dB when the external magnetic bias varies from 0 T to 0.34 T. The

measured results agree well with the simulated ones.

ACKNOWLEDGMENT

This work is supported in part by Science Foundation for Distinguished Young Scholars of Sichuan Province under 2015JQ0005, in part by Fundamental Research Funds for the Central Universities under grant ZYGX2014Z008, in part by Program for New Century Excellent Talents in University under grant NCET-13-0089, in part by the Foundation for the Author of National Excellent Doctoral Dissertation of PR China under grant number 201338, and in part by the National Program for Support of Top-Notch Young Professionals.

REFERENCES

- [1] J. Wu, Y. J. Cheng, and Y. Fan, "A Ka-band circular polarization planar array antenna with wideband characteristic and high efficiency," *IEEE Trans. Antennas Propag.*, vol. 64, no. 2, pp. 535-542, Feb. 2016.
- [2] Y. J. Cheng and X. L. Liu, "W-band characterizations of printed circuit board based on substrate integrated waveguide multi-resonator method," *IEEE Trans. Microw. Theory Techn.*, vol. 64, no. 2, pp. 599-606, Feb. 2016.
- [3] A. Doghri, T. Djerfai, A. Ghiotto, and K. Wu, "Substrate integrated waveguide directional couplers for compact three-dimensional integrated circuits," *IEEE Trans. Microw. Theory Techn.*, vol. 63, no. 1, pp. 209-221, Jan. 2015.
- [4] L. Wang, Y. J. Cheng, D. Ma, and C. X. Weng, "Wideband and dual-band high-gain substrate integrated antenna array for E-band multi-gigahertz capacity wireless communication systems," *IEEE Trans. Antennas Propag.*, vol. 62, no. 9, pp. 4602-4611, Sep. 2014.
- [5] Y. J. Cheng, Y. X. Guo, and Z. Q. Liu, "W-Band large-scale high-gain planar integrated antenna array," *IEEE Trans. Antennas Propag.*, vol. 62, no. 6, pp. 3370-3373, June 2014.
- [6] S. Adhikari, A. Ghiotto, and K. Wu, "Simultaneous electric and magnetic two-dimensionally tuned parameter-agile SIW devices," *IEEE Trans. Microw. Theory Techn.*, vol. 61, no. 1, pp. 423-435, Jan. 2013.
- [7] S. Adhikari, S. Hemour, A. Ghiotto, and K. Wu, "Magnetically tunable ferrite-loaded half-mode substrate integrated waveguide," *IEEE Microw. Wireless Compon. Lett.*, vol. 25, no. 3, pp. 172-174, Mar. 2015.
- [8] L. R. Tan, R. X. Wu, C. Y. Wang, and Y. Poo, "Ferrite-loaded SIW bowtie slot antenna with broadband frequency tunability," *IEEE Antennas and Wireless Propag. Lett.*, vol. 13, no. 3 pp. 325-328, Feb. 2014.
- [9] L. R. Tan, R. X. Wu, and Y. Poo, "Magnetically reconfigurable SIW antenna with tunable frequencies

- and polarizations," *IEEE Trans. Antennas Propag.*, vol. 13, pp. 2772-2776, June 2015.
- [10] A. Nafe and A. Shamin, "An integrable SIW phase shifter in a partially magnetized ferrite LTCC package," *IEEE Trans. Microw. Theory Tech.*, vol. 63, no. 7, pp. 2264-2274, July 2015.
- [11] S. Adhikari, Y. J. Ban, and K. Wu, "Magnetically tunable ferrite loaded substrate integrated waveguide cavity resonator," *IEEE Micro. Wireless Comp. Lett.*, vol. 21, no. 3, pp. 139-141, Mar. 2011.
- [12] Y. J. Cheng, Q. D. Huang, Y. R. Wang, and J. L. W. Li, "Narrowband substrate integrated waveguide isolators," *IEEE Microw. Wireless Compon. Lett.*, vol. 24, no. 10, pp. 698-700, Oct. 2014.
- [13] F. Fesharaki, C. Akyel, and K. Wu, "Broadband substrate integrated waveguide edge-guided mode isolator," *Electron. Lett.*, vol. 49, no. 4, pp. 269-271, Feb. 2013.
- [14] A. Ghiotto, S. Adhikari, and K. Wu, "Ferrite-loaded substrate integrated waveguide switch," *IEEE Microw. Wireless Compon. Lett.*, vol. 22, no. 3, pp. 120-122, Mar. 2012.
- [15] Q. D. Huang, Y. J. Cheng, and J. L. W. Li, "Surface-loaded ferrite substrate integrated waveguide switch," *IEEE Microw. Wireless Compon. Lett.*, vol. 25, no. 3, pp. 232-234, Apr. 2015.
- [16] H. Joshi, H. H. Sigmarsson, S. Moon, D. Peroulis, and W. J. Chappell, "High-Q fully reconfigurable tunable bandpass filters," *IEEE Trans. Microw. Theory Tech.*, vol. 57, no. 12, pp. 3525-3533, Dec. 2009.
- [17] M. Armendariz, V. Sekar, and K. Entesari, "Tunable SIW bandpass filters with PIN diodes," *IEEE Microwave Conference (EuMC)*, pp. 830-833, 2010.
- [18] S. Sirci, J. D. Martinez, M. Taroncher, and V. E. Boria, "Varactor-loaded continuously tunable SIW resonator for reconfigurable filter design," *IEEE 41st European Microwave Conference (EuMC)*, pp. 436-439, 2011.
- [19] Q. D. Huang and Y. J. Cheng, "Ferrite-loaded substrate integrated waveguide frequency-agile bandpass filter," in *IEEE MTT-S International Microwave Workshop Series on Advanced Materials and Processes for RF and THz Applications*, Suzhou, China, July 2015.
- [20] D. M. Pozar, *Microwave Engineering*, 4th ed., New York: Wiley, 2011.
- [21] R. G. L. Matthaei, L. Young, and E. M. T. Jones, *Microwaves Filters, Impedance-Matching Networks and coupling Structures*, New York, McGraw-Hill, 1964.
- [22] N. Marcuvitz, *Waveguide Handbook*, New York, 1986.
- [23] S. Mukherjee, P. chongder, K. V. Srivastava, and A. Biswas, "Design of a broadband coaxial to

substrate integrated waveguide (SIW) transition," in *Proc. Asia-Pacific Microw. Conf.*, Seoul, Korea, pp. 896-898, 2013.



Qiu Dong Huang received the B.S. degree from Chongqing University of Posts and Telecommunication, Chongqing, China, in 2009, and is currently working toward the M.S. degree at the University of Electronic Science and Technology of China. His recent research interests include substrate integrated waveguide (SIW) ferrite devices and X-band communication system.



Yu Jian Cheng was born in Sichuan Province, China, in April 1983. He received the B.S. degree from University of Electronic Science and Technology of China, in 2005 and the Ph.D. degree without going through the conventional Master's degree at Southeast University, Nanjing, China, in 2010. Since 2010, he has been with the School of Electric Engineering, University of Electronic Science and Technology of China, and is currently a Professor. From 2012 to 2013, he was a Research Staff in the Department of Electrical and Computer Engineering, National University of Singapore. His current research interests include microwave and millimeter-wave antennas, arrays and circuits, as well as microwave high-power techniques. He has authored or co-authored more than 90 papers in journals and conferences.

Cheng was the recipient of the National Program for Support of Top-Notch Young Professionals, the award of One Hundred Person Project of UESTC in 2014, New Century Excellent Talents in University in 2013, National Excellent Doctorate Dissertation of China in 2012, and the award of Jiangsu Province Excellent Doctorate Dissertation in 2011. He is the Senior Member of the IEEE and the Chinese Institute of Electronics. Now, Cheng has served on review boards of various technical journals.

Simulating CW Light Propagation Through Macroscopic Scattering Media Via Optical Phase Conjugation

Yi-An Huang, Cheng-Hao Tsai, and Snow H. Tseng*

Graduate Institute of Photonics and Optoelectronics
National Taiwan University, Taipei, 10617 Taiwan
r98941072@ntu.edu.tw, r98941072@ntu.edu.tw, stseng@ntu.edu.tw*

Abstract — The pseudospectral time-domain (PSTD) technique is advantageous for modeling macroscopic light scattering problems but falls short to model a light source of realistic dimensions. We report a novel simulation technique that enables modeling a finite-width, continuous-wave (CW) light source within PSTD simulations that was infeasible before. By exploiting the mathematical characteristics of Maxwell's equations, the instability problem of the PSTD algorithm can be overcome. We demonstrate the reported simulation enables modeling the CW optical phase conjugation (OPC) phenomenon of light propagation through a scattering medium. Specific simulation findings show that monochromatic phase-conjugated light can be focused through scattering medium. On a wider scope, the reported method enables implementing a finite-width, CW, plane-wave light source in a PSTD simulation for general optics and electromagnetic problems.

Index Terms — CW, Maxwell's equations, multiple scattering, optical phase conjugation, PSTD, simulation.

I. INTRODUCTION

Biomedical optical techniques are generally limited to surface applications due to the limited penetration depth of optical wavelengths. If optical wavelengths can penetrate deeper through biological tissue structures, the applicability of biomedical optics can be extended beyond the surface. In 2007, Lerosey et al. reported experimentally demonstrating delivering electromagnetic wave beyond the diffraction limit by means of random metallic scatterers [1]. Recently, much research effort to enhance the penetration depth of visible light through turbid media has been reported [2-4]. Utilization of the optical phase conjugation (OPC) phenomenon has been reported to enhance light penetration through turbid media (e.g., biological tissue) by canceling out the incoherent light scattering effect that causes opacity [5]. The OPC phenomenon causes multiply scattered light to propagate in reversed directions, retrace its previous scattering trajectory, and essentially penetrate through

turbid media. Initial experimental effort was done by utilizing a nonlinear crystal [5]; later, a digital optical phase conjugation technique using an optical wavefront sensor and spatial light modulator was reported that significantly enhances the performance, speed, and flexibility of light penetration [6]. Due to the extreme complexity involved for light propagation through macroscopic random media, such phenomena are difficult to analyze. An accurate simulation technique based upon the Maxwell's equations that can account for the wave characteristics of light is desired.

Based upon numerical solutions of Maxwell's equations, the pseudospectral time-domain (PSTD) technique is computationally economic and can model macroscopic light scattering problems [7] that the finite-difference time-domain (FDTD) technique falls short. However, due to the Fourier transforms involved, the conventional PSTD algorithm is incompatible with field discontinuities therefore cannot model a light source of realistic dimensions; typically in a PSTD simulation the light source is modeled by a plane wave with infinite extent. In this manuscript, we report a novel simulation technique that enables modeling a CW plane wave light source of arbitrary width within a PSTD simulation for the first time. The CW OPC simulation consists of two parts: the modeling of *forward propagation* and the modeling of *backward propagation*. In Section III (*forward propagation*): the implementation of a finite-width, CW light source is explained in detail. The key to successfully implementing a finite-width, plane-wave illumination is discussed. In Section IV (*backward propagation*): simulating the reversed propagation of CW OPC phenomenon is described. Together, the *forward propagation* and *backward propagation* enable robust modeling of the CW OPC phenomenon of light penetration through large-scale turbid media (e.g., biological tissues structures).

II. PSEUDOSPECTRAL TIME-DOMAIN ALGORITHM

To model the OPC phenomenon, the PSTD

algorithm [7] is employed to obtain numerical solutions of Maxwell's equations. The PSTD algorithm is advantageous for large-scale electromagnetic wave propagation problem. In the PSTD algorithm, temporal derivatives of Maxwell's equations are calculated using a 2nd-order central difference scheme, whereas the spatial derivatives are evaluated by forward and inverse Fourier transforms:

$$\left\{ \frac{\partial E}{\partial x} \right\} = -F^{-1} \{ jk_x \cdot F \{ E \} \}, \quad (1)$$

E is the electric vector field, k_x is the wave number, and F represents the Fourier transform. Since computer calculations are based on discrete numbers, discretization of the continuous electromagnetic fields is necessary. According to the Nyquist sampling theorem, the spatial derivatives calculated in Eq. (1) is of spectral accuracy (meaning as accurate as it can get with the given information), allowing the PSTD technique, with a coarse grid of two spatial samples per wavelength, to achieve similar accuracy as the finite-difference time-domain (FDTD) technique (FDTD requires 20 spatial samples per wavelength.) The coarse spatial grid points enables simulating the large-scale optical phenomena with economic computational memory; for example, to simulate a 3-D light scattering problem with the same computational memory, the PSTD technique can model up to approximately 1000-time larger light scattering problem than the FDTD technique. Finally, the anisotropic perfectly matched layer (APML) absorbing boundary condition [8] is implemented to absorb all outgoing waves. If all outgoing waves never re-interact with the medium, the optical simulation can be considered as being practically isolated in vacuum.

III. FORWARD PROPAGATION

Biomedical optics typically involve a macroscopic scattering medium illuminated by a finite-width, CW light source; thus, a simulation technique capable of modeling a finite-extent illumination in a large-scale light scattering problem is needed. The FDTD simulation of light propagation through small-scale turbid media has been reported [9]; however, the employed hard source [10] generates artificial scattering that causes inevitable error to the simulation. The PSTD algorithm is computationally memory-efficient and can model larger problems; simulation of the pulse OPC phenomenon using the PSTD algorithm has been reported [11]. However, previous reported simulation technique falls short to model the CW OPC phenomenon that is more realistic for most optical techniques. Furthermore, due to the Fourier transforms involved, the widely used total-field/scattered-field (TF/SF) formulation [10] for FDTD simulations is not compatible with the PSTD algorithm; also, the PSTD algorithm

cannot handle a point light source [12]. As a result, a CW light source of realistic size that is stable in a large-scale PSTD light scattering simulation was not feasible, seriously hindering the applicability of the PSTD technique to model practical problems. A finite-width, CW light source compatible with the PSTD algorithm is required.

By exploiting the mathematical characteristics of Maxwell's equations, we report a novel method to implement an arbitrary CW light source that is stable in the PSTD simulation. A flow chart of the PSTD algorithm is shown in Fig. 2. The characteristics of Maxwell's equations are such that the electromagnetic fields depend on the changes of local electromagnetic fields rather than remote electromagnetic fields. Therefore, the numerical artifacts caused by field discontinuities are most pronounced in its vicinity; the effect of field discontinuities far away is limited as it decreases inversely with distance squared. A locally continuous electromagnetic field suffices for the PSTD algorithm to update the local electromagnetic field. To model a CW light source within the simulation space, the electromagnetic field of a finite-width, sinusoidal CW plane-wave is added into the *source region* at each time-step:

$$E_i = e^{-\frac{(y-y_0)^2}{\sigma_y^2}} \cos[k(x-x_0) - \omega t], \quad (2)$$

(x_0, y_0) is the center of the light source, whereas width and thickness denote the x -dimension and y -dimension of the *source region*, respectively (as shown in Fig. 1). To prevent artificial scattering from the *source region*, the inserted optical field is added into space as a "soft source" [13]. A Gaussian profile (Eq. (2)) is employed in the y -direction to smooth out field discontinuities of the finite-width plane wave.

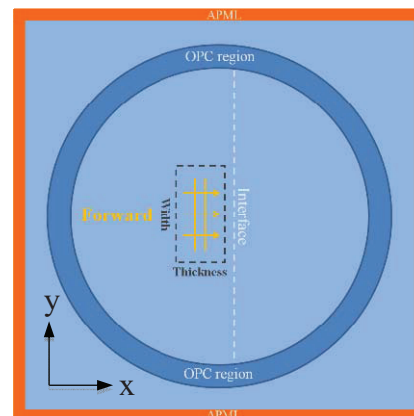


Fig. 1. Schematics of simulating a finite-width, CW plane wave light source in a PSTD simulation. A CW plane wave superimposed into the simulation space in the source region (the dashed rectangular region).

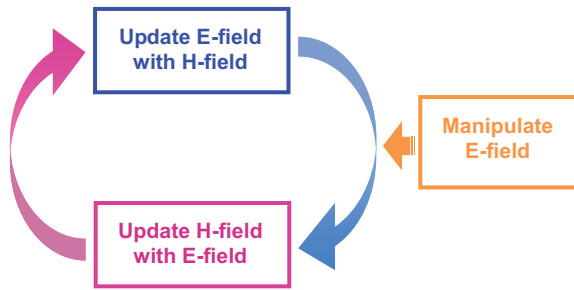


Fig. 2. Flow chart of PSTD algorithm of modeling CWOPC phenomenon. The E -field and H -field are updated consequently from each other. As the E - and H -fields are updated based upon Maxwell’s equations, manipulation of the fields is performed to generate the desired light source.

Instead of a point light source in the PSTD simulation, the incident light is introduced into the simulation space as a piecewise continuous segment of electromagnetic fields (e.g., 5- μm -by-10- μm patch of smooth electromagnetic field), as shown in Fig. 3 (a). The piecewise continuous segment of field ensures stability of the PSTD algorithm, thus, the electromagnetic fields inside or outside the source region is stable and can be updated correctly with light propagating in the forward direction (Fig. 3 (b)). Initially, as the incident field is initially added into the simulation space, transient numerical artifacts of high-frequency oscillation emerge due to the abrupt discontinuity of the electromagnetic fields. Without the constant amplitude of an infinite plane wave in x - and y -directions, edges of the finite-width plane wave deteriorates (Figs. 3 (c) and 3 (d)). With support from the finite-width CW plane wave continuously added into the source region, the incident plane wave continues to propagate in the forward direction while maintaining its width w (Fig. 3 (e)). As the emitted light reaches steady state, instability at the edges disappears leaving only a finite-width, CW plane wave propagating steadily in the forward direction within the PSTD simulation (Fig. 4).

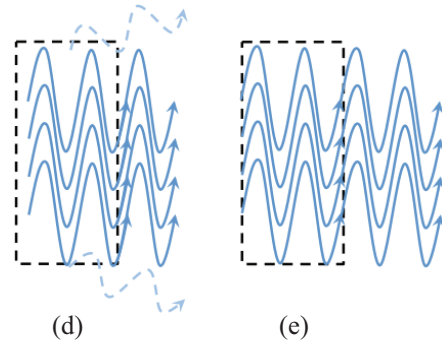
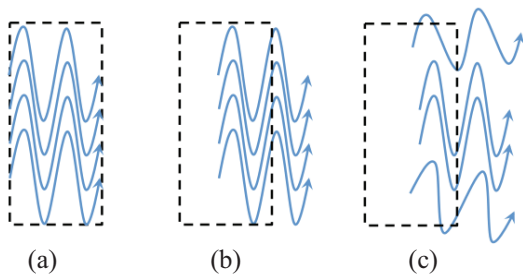


Fig. 3. Schematics of implementing a finite-width CW plane wave light source in the PSTD simulation. (a) A plane wave with a cross-sectional width w is added into the *source region* (dashed box). (b) As time evolve, light propagates in the forward direction. (c) Without the neighboring field of an infinite plane wave, edges of the finite-width plane wave deteriorate. (d) Incident field is added into the *source region* in the next time-step. Supported by the incident finite-width plane wave continuously added into the *source region*, the field continues to propagate in the forward direction steadily.

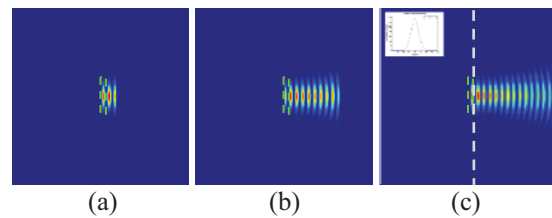


Fig. 4. (Media 1) A stable light source emitting a CW, finite-width, plane wave in a PSTD simulation. (a) Sinusoidal electromagnetic field added into space at the *source region* (the green dashed rectangular region). (b) Later inserted electromagnetic field propagates and connects with the previously inserted electromagnetic field. (c) Once the steady state is reached, the sequentially inserted electromagnetic fields together form a CW, finite-width propagating plane wave. The CW cross-sectional amplitude profile of the light beam is shown in the inset-figure (as measured along the white dashed line in Fig. 1).

Width of the *source region* determines the cross-sectional extent of the emerging CW light, whereas the amplitude of the CW light is proportional to the thickness of the *source region*. For instance, the amplitude E_{z0} of the sinusoidal plane wave $E_{zi} = A \cdot \sin(kx - \omega t)$ emitted from the *source region*

as is given by:

$$E_{z_0} = \frac{m \cdot \Delta x}{c \cdot \Delta t} E_{z_1}, \quad (3)$$

where m is the number of grid layers of the *source region*, Δx and Δt are the spatial and temporal grid spacing, respectively, and c is the speed of light. Incident light as a patch of continuous field of the *source region* is added into the simulation; this minimizes the numerical artifacts to maintain numerical stability. The field added into the simulation is proportional to the area of the *source region*, therefore, amplitude of the incident light is proportional to the *thickness* ($m \cdot \Delta x$) of the *source region*. Light generated from this CW light source propagates in the direction of the Poynting vector. For a typical OPC simulation of light propagation through turbid medium, the turbid medium is illuminated by the incident CW light, where light scatters into various directions. Once the steady state is reached, the outward propagating CW light is recorded in the *OPC region* (as shown in Fig. 1), which is later used in modeling *backward propagation* of phase-conjugated light, as discussed in Section IV.

Simulation artifacts caused by discontinuity of the electromagnetic field must be minimized to maintain numerical stability. The *source region* is smooth and continuous both in the x - and y -directions with minute discontinuities at the edges. For a finite-width plane wave, the discontinuity at the edges of the *source region* causes numerical artifacts. It is critical that the source region be wide and smooth enough in both x - and y -directions; if the *source region* is too narrow, numerical artifacts emerge due to the Gibbs' phenomenon. By increasing the piecewise continuity of the field in the *source region* and its neighborhood, the numerical artifacts are reduced. Or, smoothening the inserted electromagnetic field with a Gaussian profile can also significantly reduce the high-frequency numerical artifacts. If the overall electromagnetic field only consists of a small fraction of the electromagnetic field that is discontinuous, the simulation artifacts are localized and decay as the CW steady state is reached. Convergence analyses show that error decreases rapidly as the *source region* becomes thicker than a few grid points.

The proposed light source implementation enables creating a CW, plane-wave light source of arbitrary width. The amplitude of light emitted from the proposed light source in vacuum is shown in Fig. 5 (a). The amplitude profiles of a CW plane wave is measured adjacent to the *source region*. Due to diffraction of light, the amplitude profile is not constant but varies in space; for a plane wave with a larger cross-section, the profile becomes constant with undulation at the edge of the plane wave. The amplitude of light emitted from the proposed light source

embedded in a scattering medium is shown in Fig. 5 (b); the scattering medium consists of 800 6- μm -diameter, dielectric ($n = 1.2$) cylinders clustered in a region of 180- μm -radius. Light reflected and refracted from the scattering medium interferes with light emitted from the CW light source; the superposition of all these light components result in a complex amplitude profiles of Fig. 5 (b). As demonstrated in Fig. 5, a CW light source with realistic dimensions can be implemented without instabilizing the PSTD simulation; the proposed simulation technique enables PSTD modeling a CW, finite-width, plane-wave light source embedded inside a macroscopic scattering medium.

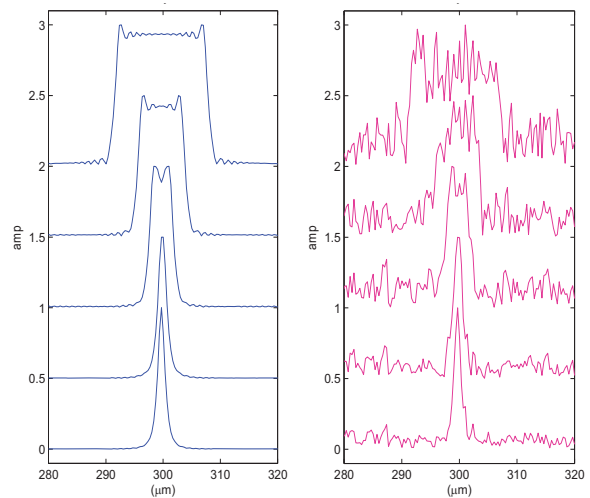


Fig. 5. (a) Implementation of a CW light source of various widths (w) in vacuum. (b) Implementation of a CW light source of various widths (w) embedded in a scattering medium (from bottom to top) $w = 1, 2, 4, 8,$ and $16 \mu\text{m}$, respectively. The scattering medium consists of 800 6- μm -diameter, dielectric ($n = 1.2$) cylinders clustered in a region of 180- μm -radius. The amplitude profile (measured along the white dashed line of Fig. 1) is more complex due to interference of light reflected and refracted from the scattering medium.

IV. BACKWARD PROPAGATION

In modeling the *backward propagation*, the OPC reversed propagation of light is generated with the CW amplitude and phase previously recorded in the *forward propagation*. Similar to the *forward propagation*, the phase-conjugated electromagnetic field is added into the *OPC region* (Fig. 6) as a soft source [13]. Having the OPC region implemented as a soft source eliminates the artificial reflection from the *OPC region*. After the simulation reaches steady state, the temporal variation of the electromagnetic field becomes periodic: the electromagnetic field at everywhere oscillates with the same frequency throughout the entire simulation space.

In the *forward propagation*, the electromagnetic field in the *OPC region* is recorded and the CW amplitude and phase are calculated via Fourier transform. In the *backward propagation*, the phase-conjugated CW steady-state sinusoidal electromagnetic field is added into the *OPC region* to generate the reversed propagation of phase-conjugated light. The added field emerging at the *OPC region* essentially serves as the “light source” in the *backward propagation*. Simulation artifacts occur as the initially added electromagnetic fields caused by the abrupt variations at the boundary of the *OPC region*. The discontinuities at the edges excite high-frequency numerical artifacts; as the CW electromagnetic field is continuously added into the *OPC region*, numerical artifacts gradually decay, leaving only the steady-state, phase-conjugated light propagating in reversed directions.

In Fig. 7, a simulation of phase-conjugated, CW light propagation is depicted. The scattering medium consists of 1600 6- μm -diameter, dielectric ($n = 1.2$) cylinders clustered in a region of 180- μm -radius. Initially, phase-conjugated light ($\lambda = 8 \mu\text{m}$) is added into space at the ring-shaped *OPC region* (Fig. 6). The phase-conjugated light is continuously added into the ring-shaped *OPC region* and merges with the neighboring field to form a smooth, CW phase-conjugated light propagating through the scattering medium as shown in Figs. 7 (b,c). The CW, monochromatic, phase-conjugated light of wavelength λ back-propagates through the scattering medium and reconstructs the original emitted light profile (Fig. 8).

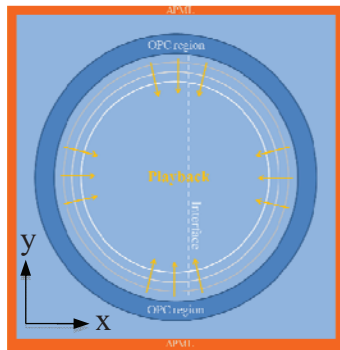


Fig. 6. CW light recorded in the *forward propagation* is phase-conjugated and added into the *OPC region* (the blue shaded region) as a soft source.

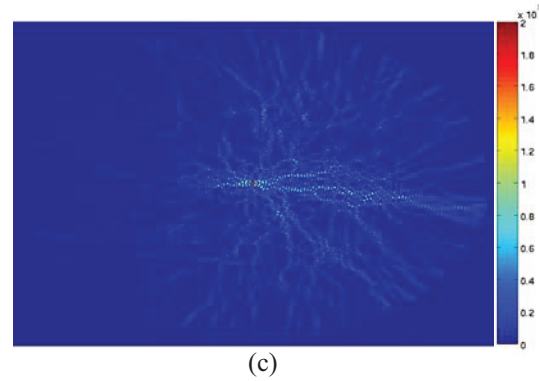
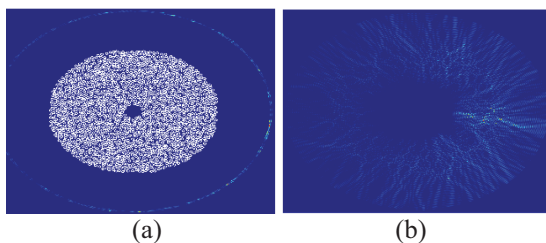


Fig. 7. (Media 2) Modeling the *backward propagation* of phase-conjugated light through scattering medium. (a) Phase-conjugated light ($\lambda = 8 \mu\text{m}$) is added into space at the ring-shaped *OPC region* and converges upon a scattering medium consisting of 1600 6- μm -diameter, dielectric ($n = 1.2$) cylinders clustered in a region of 180- μm -radius. (b) Phase-conjugated light is continuously added into space at the ring-shaped *OPC region*, and merges with the previously added field. (c) The electromagnetic field merges to form a smooth, CW phase-conjugated light propagating through the scattering medium towards its center as the simulation reaches steady state.

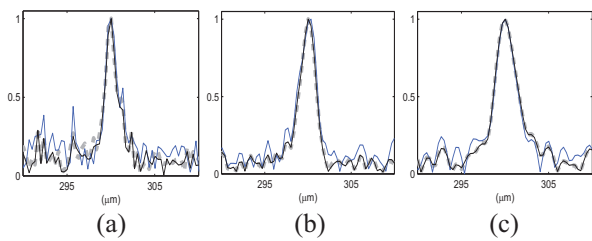


Fig. 8. Simulating phase-conjugated light back-propagating through a scattering medium to a narrow peak. The scattering medium consists of 1600 randomly positioned, 6- μm -diameter dielectric ($n = 1.2$) cylinders. A 4- μm -wide plane-wave light source (wavelength λ) is embedded at the center of the scattering medium. From top to bottom: (a) $\lambda = 1 \mu\text{m}$, (b) $\lambda = 2 \mu\text{m}$, (c) $\lambda = 3 \mu\text{m}$, respectively. In each subplot, the forward propagation light profile (gray dashed line) is compared to the back-propagated light (blue line) and the back-propagated light with a soft sink to eliminate the outgoing light component (black solid line).

The field discontinuity is minimized by continuously adding field at the *OPC region* which maintains numerical stability of the PSTD simulation. The CW phase-conjugated light is added into space in the *OPC region* at every time-step. For the same reason as the CW light source described in Section II, a wide and smooth enough of electromagnetic field at the *OPC*

region is required to avoid numerical artifacts. A convergence analysis is shown in Fig. 9. Various factors affect the convergence, mainly related to the geometry such as refractive index distribution, size of the scattering medium, optical wavelength of incident light, complexity of the scattering medium, etc. Generally larger scattering medium or more complex geometry would require longer run-time to converge. For the reported simulations, an *OPC region* with a thickness of ~ 10 layers is sufficient to minimize numerical artifacts.

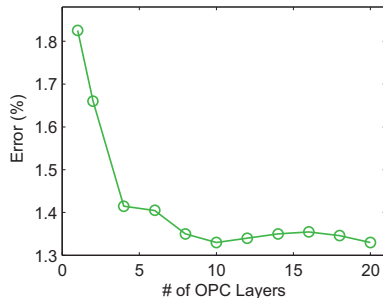


Fig. 9. Convergence analysis for the numbers of layers of the *OPC region*. The errors are evaluated by calculating the normalized, root-mean-square error between the forward outgoing and playback incoming cross-sectional profiles of the E-field. As the layers of the *OPC region* is increased, the error rapidly decreases. A 10-layer *OPC region* is sufficient to insure numerical stability.

V. DISCUSIONS

PSTD algorithm is vulnerable to discontinuities; by adding piecewise continuous electromagnetic fields, instabilities of the PSTD algorithm can be avoided. A finite-width, CW light source of arbitrary width *inside* a PSTD simulation can be modeled with the proposed simulation technique. The number of layers of the *OPC region* has to be large enough to ensure piecewise continuity. The performance of the proposed method can be evaluated by comparing the outgoing wave and the incoming wave in the *forward propagation* and *backward propagation*, respectively. If the proposed method works properly, the outgoing field would match the incoming field as in time reversal. To quantitatively evaluate the performance, the error is evaluated by calculating the normalized root-mean-square error of the E-field of the incoming and outgoing wave along an arbitrary cut:

$$Error_{RMS} = \sqrt{\frac{\sum_{i=1}^n [E_{Playback}(i) - E_{Forward}(i)]^2}{n}}, \quad (4)$$

where $E_{Forward}$ and $E_{Playback}$ are the E-field amplitude recorded along the selected cut (as shown in Figs. 1 and 6, respectively). Based upon the uniqueness theorem, the electromagnetic field along an arbitrary cut matches only if the forward propagation and backward propagation are both modeled accurately. In Fig. 9, we demonstrate that as the number of layers of the OPC region increases beyond a threshold, the error is minimized. A minimal number of layers of the source region and OPC region are required to maintain numerical stability. In order to generate an undistorted backward propagating field, the OPC region has to match the wavefront morphology. This requirement can be met when the light is scattered into all directions by a random medium, and the OPC region is far enough whereas outgoing light mostly impinges the OPC region normally. The amplitude of the simulation has to be properly scaled (Eq. 3) to satisfy energy conservation where the number of layers is proportional to the amount of light “added” in to the simulation space.

The forward and backward propagation of light through a scattering medium is simulated using the proposed simulation technique. A finite-width, CW, plane-wave light source is embedded inside a scattering medium; the scattering medium consists of 1600 randomly-positioned, 6- μm -diameter dielectric ($n = 1.2$) cylinders within a round region with an overall diameter of 360 μm . Various widths of the CW light source are modeled. Due to interference of scattered light caused by the scattering medium, a complex amplitude profile is recorded. The simulation technique reported in this manuscript makes it possible, for the first time, to accurately simulate the CW OPC phenomenon of a light propagation through macroscopic turbid media (e.g., biological tissues) using the PSTD algorithm [14]. As shown in Fig. 10, the OPC backward propagation of a 4- μm -wide, CW light source illuminating a 1000- μm -by-1000- μm turbid medium consisting of 670 biological cells is simulated using 12 Intel CPUs that took ~ 48 hours. Recently, a two-dimensional (2-D) FDTD simulation analysis of phase-conjugated light propagation through scattering medium has been reported [9]. Due to the limitations of the FDTD technique, a smaller geometry of 60- μm -by-100- μm was modeled. Another simulation analysis has been reported by Carminati et al. [2] where a scattering medium (cylindrical region of radius $R = 1.91 \mu\text{m}$) is modeled by a cluster of *idealized point dipoles*. Instead of treating each scatterer as an idealized point dipole, we model the scattering medium via a grid-based PSTD simulation. To date, the reported simulation technique is the only method that can model such large-scale CW OPC phenomenon based upon numerical solutions of Maxwell’s equations.

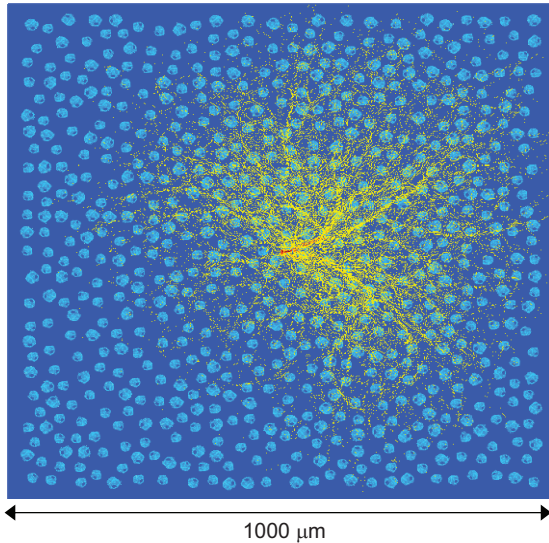


Fig. 10. CW OPC simulation of light propagating through a biological turbid medium. Light illuminating a 1000- μm -by-1000- μm tissue consisting of 670 randomly positioned biological cells is simulated. The diameter of each biological cell is approximately 20-30 μm . The illumination electromagnetic wavelength $\lambda = 4 \mu\text{m}$ with a cross-sectional width of 10 μm .

ACKNOWLEDGMENT

This research is supported by the Taiwan National Science Council Grant NSC 99-2112-M-002-016-MY3, NSC 102-2112-M-002-020 and NSC 102-2628-M-002-006-MY3. The authors thank Changhuei Yang and Meng Cui for insightful discussions.

REFERENCES

- [1] G. Lerosey, J. De Rosny, A. Tourin, and M. Fink, "Focusing beyond the diffraction limit with far-field time reversal," *Science*, vol. 315, pp. 1120-1122, 2007.
- [2] R. Pierrat, C. Vandenbem, M. Fink, and R. Carminati, "Subwavelength focusing inside an open disordered medium by time reversal at a single point antenna," *Physical Review A*, vol. 87, 041801(R), 2013.
- [3] J.-H. Park, C. Park, H. Yu, J. Park, S. Han, J. Shin, S. H. Ko, K. T. Nam, Y.-H. Cho, and Y. Park, "Subwavelength light focusing using random nanoparticles," *Nat Photonics*, vol. 7, pp. 455-459, 2013.
- [4] I. M. Vellekoop, A. Legendijk, and A. P. Mosk, "Exploiting disorder for perfect focusing," *Nature Photonics*, vol. 4, pp. 320-322, 2010.
- [5] Z. Yaqoob, D. Psaltis, M. S. Feld, and C. Yang, "Optical phase conjugation for turbidity suppression in biological samples," *Nature Photonics*, vol. 2, pp. 110-115, 2008.
- [6] M. Cui and C. Yang, "Implementation of a digital optical phase conjugation system and its application to study the robustness of turbidity suppression by phase conjugation," *Optics Express*, vol. 18, pp. 3444-3455, 2010.
- [7] Q. H. Liu, "Large-scale simulations of electromagnetic and acoustic measurements using the pseudospectral time-domain (PSTD) algorithm," *IEEE Transactions on Geoscience and Remote Sensing*, vol. 37, pp. 917-926, 1999.
- [8] S. D. Gedney, "An anisotropic perfectly matched layer-absorbing medium for the truncation of FDTD lattices," *IEEE Transactions on Antennas and Propagation*, vol. 44, pp. 1630-1639, 1996.
- [9] J. L. Hollmann, R. Horstmeyer, C. Yang, and C. A. DiMarzio, "Analysis and modeling of an ultrasound-modulated guide star to increase the depth of focusing in a turbid medium," *Journal of Biomedical Optics*, vol. 18, 2013.
- [10] A. Taflove and S. C. Hagness, *Computational Electrodynamics: The Finite-Difference Time-Domain Method*, Artech House, Boston, 2005.
- [11] S. H. Tseng, "PSTD simulation of optical phase conjugation of light propagating long optical paths," *Optics Express*, vol. 17, pp. 5490-5495, 2009.
- [12] T. W. Lee and S. C. Hagness, "A compact wave source condition for the pseudospectral time-domain method," *IEEE Wireless Propag. Lett.*, vol. 3, pp. 253-256, 2004.
- [13] A. Taflove and S. C. Hagness, *Computational Electrodynamics: The Finite-Difference Time-Domain Method*, Artech House, 2000.
- [14] S. H. Tseng, W. Ting, and S. Wang, "2-D PSTD Simulation of the time-reversed ultrasound-encoded deep-tissue imaging technique," *Biomedical Optics Express*, vol. 5, pp. 882-894, 2014.

Analysis of Highly Sensitive Photonic Crystal Biosensor for Glucose Monitoring

M. S. Mohamed¹, Mohamed Farhat O. Hameed^{2,3}, Nihal F. F. Areed^{2,4},
M. M. El-Okr⁵, and S. S. A. Obayya²

¹ Basic Science Department, Faculty of Engineering
Misr University for Science and Technology (MUST), El-Motameyz Uptown, 6th of October City, Giza, Egypt

² Centre for Photonics and Smart Materials, Zewail City of Science and Technology
Sheikh Zayed District, 6th of October City, Giza, Egypt
sobayya@zewailcity.edu.eg

³ Mathematics and Engineering Physics Department, Faculty of Engineering
Mansoura University, Mansoura 35516, Egypt

⁴ Department of Electronics and Communications Engineering, Faculty of Engineering
Mansoura University, Mansoura 35516, Egypt

⁵ Physics Department, Faculty of Science
Al-Azhar University, Nasr City, Cairo, Egypt

Abstract — In this study, a novel compact and fully integrated 2D photonic crystal (PhC) biosensor with high sensitivity has been proposed for Glucose monitoring. The simulation results are obtained using 2D finite element time domain method (FETDM). To evaluate the performance of the suggested design, the transmission spectrum through the reported structure has been calculated. The effect of the structure geometrical parameters of the biosensor is studied to maximize the biosensor sensitivity. The suggested biosensor offers high sensitivity of 422 nm/RIU with high linearity. Additionally, the suggested biosensor has a simple design and is easy for fabrication. The enhancement of the sensitivity of the PhC biosensor is very important to amplify the detection of the small variation in analyte's physical properties. Therefore, the achieved sensitivity enhancement can improve the applications of Glucose monitoring.

Index Terms — Biosensor, finite element time domain method, photonic crystal, sensitivity, transmission.

I. INTRODUCTION

Biosensors are devices used for detecting and analyzing samples with different characteristics [1,2]. The work in the biosensors depends on the response to the change in the physical properties of the analyzed samples. There are a lot of types of biosensors such as physicochemical, piezoelectric, optical, and electro-

chemical biosensors. The sensing in the biosensors represents the detecting power against the change in the physical properties of the analyzed samples. The biosensors have a wide range of applications such as food analysis, DNA classifications, microbial biosensors, and Glucose monitoring [3]. Therefore, biosensors have attracted the interest of many researchers all over the world. Recently, the photonic crystal (PhC) biosensor has gained enormous interest due to its simplicity and high sensitivity [4-8]. The 2D PhCs have many related applications such as waveguides, logic gates [9], filters [10], polarization converters [11], PhC router and PhC image encryptors [12,13]. Additionally, the 2D PhC can confine the optical state in very small dimensions. Making a defect through the periodicity of the structure of a 2D PhC shows allowed modes in the photonic bandgap region [14]. The transmission of the electromagnetic wave through the defected area is affected by the change of refractive indices of the composed material. For these reasons, the 2D PhC is exploited for biosensing applications. The sensitivity of the 2D PhC biosensor can be calculated by measuring the shift in resonance wavelength at which maximum transmission through PhC structure occurs. The more displacement of peaks with a satisfied quality factor, the higher sensitivity that can be obtained [4,5]. In this regard, Hsiao and Lee [4] have reported a computational study of PhC nano-ring resonator for biochemical sensing with a maximum sensitivity of 6 nm/RIU. Additionally, Pal et

al. [15] have achieved a sensitivity of 64.5 nm/RIU using hetero-structure slab PhC by detecting the resonance wavelength for analytes of air, water, and isopropanol. Further, Olyae et al. [5] have investigated four-channel label-free PhC biosensor using nanocavity resonators which offer a sensitivity of 65.7 nm/RIU. Moreover, Dorfner et al. [16] have enhanced the sensitivity to 103 ± 1 nm/RIU using different concentrations of bovine serum albumin (BSA) solution. Further, Kim et al. [17] reported a sensitivity of 135 nm/RIU by using matched liquids at different five refractive indices from 1.296 to 1.372 with a step of 0.019. Further, Najafgholinezhad and Olyae [6] have presented PhC biosensor with the temperature dependent investigation of microcavity resonator with a sensitivity of 141.67 nm/RIU. Dündar et al. [18] have also studied different concentrations of sugar-water solutions which resulted in a sensitivity of 280 nm/RIU. In addition, Kita et al. [19] have used liquids of refractive indices from 1.00 to 1.37, and they have demonstrated a sensitivity of 350 nm/RIU. In this paper, a novel design of 2D PhC biosensor with high sensitivity is proposed and analyzed. The effect of the structure geometrical parameters of the reported design on the biosensor sensitivity is investigated to maximize the biosensor sensitivity. In this regard, the effect of the radius of the central microcavity in the midway of the defected 2D PhC is studied thoroughly. Additionally, the impact of the surrounding holes around the central microcavity that are filled with the glucose solution is reported. The simulation results are obtained by using finite element time domain method (FETDM) [20-22]. The suggested biosensor offers high sensitivity of 422 nm/RIU which is greater than that reported in [4-6, 15-19]. Further, the proposed biosensor has an easy and accurate label-free performance due to the detection of the target molecules in their natural form. The molecular interaction due to the change in the glucose concentration results in an analyte refractive index variation. Consequently, resonance wavelength shift will occur and hence the biosensor sensitivity can be obtained. In this study, the sensitivity is defined as the resonance wavelength shift $\Delta\lambda$ per analyte refractive index change Δn [5]. The detection of the resonance wavelength shift gives information about the corresponding glucose concentration change and the corresponding molecular interactions. Moreover, the suggested label-free PhC biosensors can effectively measure the effective refractive index variation near the active sensing surface.

II. PHOTONIC BANDGAP STRUCTURE

The considered PhC platform consists of GaN dielectric slab drilled with air holes. The air holes of radius $r = 0.345a$ are forming hexagonal lattice as shown in Fig. 1 (a) with a lattice constant $a = 500$ nm. The dielectric constant of the GaN dielectric slab is equal to 4.94 at wavelength $\lambda = 1400$ nm.

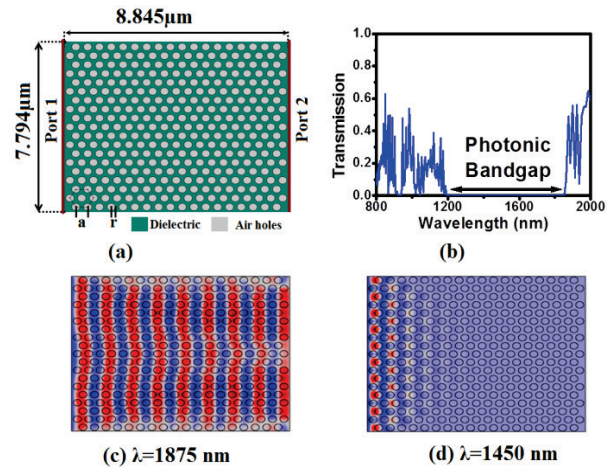


Fig. 1. (a) Cross-section of 2D PhC, (b) transmission spectrum curve through the 2D PhC, (c) field distribution at $\lambda = 1875$ nm, and (d) field distribution at $\lambda = 1450$ nm.

The GaN has a wide range of applications in different optical fields such as light emitting diodes (LEDs) and solar cells [23, 24]. It has very high crystalline quality due to its low-temperature depositing [25]. Further, the GaN is insoluble in water [26]. Additionally, the GaN can be operated in different applications under high temperature like optoelectronics (charge screening, light flow control) [27,28]. The GaN is also a good candidate for photonic crystal applications [29] due to the high index contrast between its dielectric permittivity of 4.94 and that of the air. Therefore, a good confinement can be obtained through the defected channel with the analyte filled central cavity and hence high sensitivity can be obtained. The transmission value T is calculated from the formula $T = |E_{out}/E_{in}|^2$, where E_{in} is the incident input field by port 1 and E_{out} is the received output field by port 2. Figure 1 (b) represents the transmission spectra through the 2D PhC. It evident from this figure that there is a photonic bandgap from $\lambda = 1200$ nm to 1850 nm. Figures 1 (c) and 1 (d) present the field distributions at wavelengths of 1875 nm and 1450 nm, respectively. The field distribution diagrams are in consistency with the transmission shown in Fig. 2 (b). At $\lambda = 1875$ nm, the light is propagating through the PhC structure while it is forbidden at a wavelength of 1450 nm. The photonic bandgap range is necessary for selecting the allowed modes for the suggested 2D PhC biosensor. The effects of the structure geometrical parameters on the sensitivity of the proposed designs have been studied using the FETDM with perfectly matched layer boundary conditions [21, 22]. In this study, the size of the finite elements variates from 0.00285 to 0.637 μm . The element growth rate that determines how fast the elements should grow from small to large over the studied domain is equal to 1.3. Additionally, the curvature factor that limits how large the element size

can be along the curved boundaries of the suggested structure is fixed at 0.3.

III. DESIGN CONSIDERATION AND NUMERICAL RESULTS

As shown in Fig. 2 (a), the 2D PhC biosensor is formed by removing the central horizontal row of air holes from the basic composition of the studied 2D PhC. Further, a microcavity of radius R is added in the midway of the central channel defect. The central cavity is filled with analyte sample of glucose solution with refractive index [30]:

$$n = 0.00011889C + 1.33230545, \quad (1)$$

where C is the glucose concentration in (g/L). The effect of the microcavity radius R on the sensitivity is studied to maximize the biosensor sensitivity. In this study, Gaussian pulse of width $0.4 \mu\text{m}$ with a central carrier wavelength of $1.4 \mu\text{m}$ has been adopted to feed the proposed structure from port 1. The change in the concentration of the glucose affects the transmission of the traveling electromagnetic wave as shown in Fig. 2.

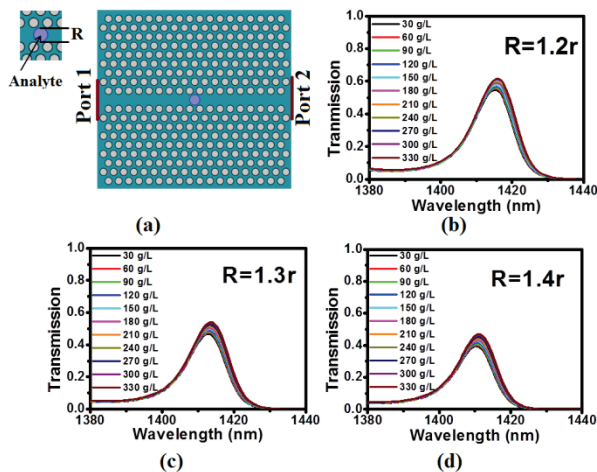


Fig. 2. (a) The cross-section of the 2D PhC biosensor with the central microcavity filled with the analyte (glucose solution). The transmission spectra through the proposed 2D PhC biosensor with microcavity of radii: (b) $R=1.2r$, (c) $R=1.3r$, and (d) $R=1.4r$.

Figures 2 (b), 2 (c), and 2 (d) show the transmission spectra that are obtained at different radii of the microcavity, $1.2r$, $1.3r$, and $1.4r$ at different glucose concentrations. It is revealed from these figures that the displacement of the peaks due to changes in the analyte refractive index is weak. Therefore, very small sensitivity can be obtained for the suggested design. Figure 3 shows the variation of the resonance wavelength with the glucose concentration at different R values. It is evident from this figure that the resonance wavelength is slightly affected by the change in the glucose concentrations.

Therefore, the sensitivity of the proposed sensor will be very small. In this study, the sensitivity is defined as the resonance wavelength shift per the change in the analyte refractive index ($\Delta\lambda/\Delta n$) [5]. The Δn change is calculated according to the change in the glucose concentration as may be noted from Equation (1). In order to enhance the transmission and the sensitivity of the 2D PhC biosensor, the radius of the central microcavity is increased and some of the surrounding air holes are removed.

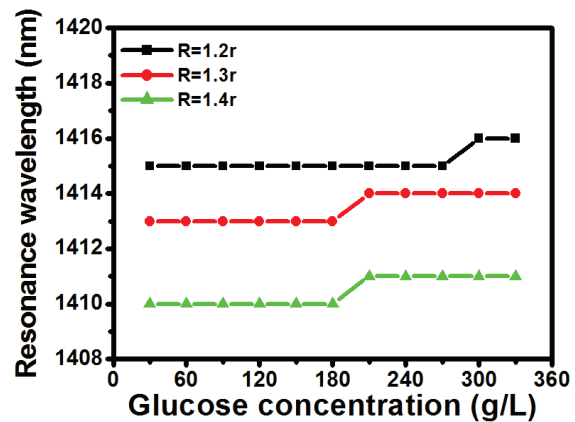


Fig. 3. The shift in the resonance wavelength as a function of the glucose concentration at different R values $1.2r$, $1.3r$, and $1.4r$.

The new design of the 2D PhC biosensor is shown in Fig. 4 (a). Figure 4 (b) and 4 (c) show the field distribution at $R=3.4r$ and $1.4r$ at the corresponding resonance wavelengths 1403 nm and 1411 nm , respectively at concentration $c=330 \text{ g/L}$. It is revealed from these figures that the transmission through the PhC design is enhanced by increasing the central cavity radius R from $1.2r$ to $3.4r$. Figures 5 (a), 5 (b), and 5 (c) show the transmission through the suggested sensor at different glucose concentrations and at different microcavity radii R . It is evident from these figures that the sensitivity and transmission increase by using the improved design. At $R = 3r$, $3.2r$ and $3.4r$, the sensitivity is equal to 35 nm/RIU , 201.4 nm/RIU , and 186.5 nm/RIU , respectively. All of these results are also confirmed in Fig. 5 (d), where the resonant wavelengths are plotted against the glucose concentration change. Due to the index contrast between the refractive indices of the GaN and the glucose solution, reflection and refraction occur to the introduced electromagnetic beam in the proposed structure. The measured transmission depends on the refraction when the electromagnetic wave transfers from the GaN to the glucose solution [31]. As the microcavity radius increases, the amount of filled glucose solution and its effect on the transmission of the traveling electromagnetic wave through the defected region will be increased. Consequently, the shift in the resonance

wavelength due to the glucose refractive index change can be detected with high sensitivity.

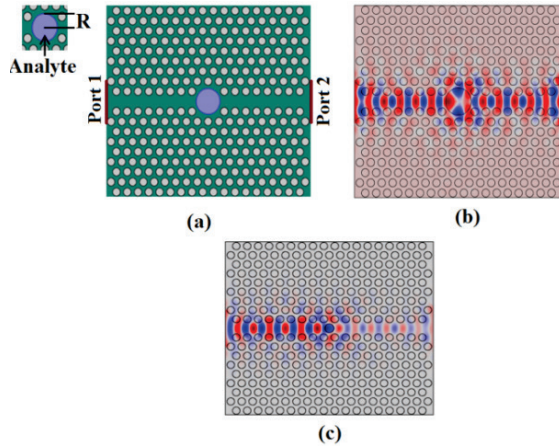


Fig. 4. (a) Cross-section of the 2D PhC biosensor with the large central microcavity filled with the analyte (glucose solution). Field distribution through the suggested design with glucose concentration $c=330$ g/L at: (b) $R=3.4r$ ($\lambda=1403$ nm) and (c) $R=1.4r$ ($\lambda=1411$ nm).

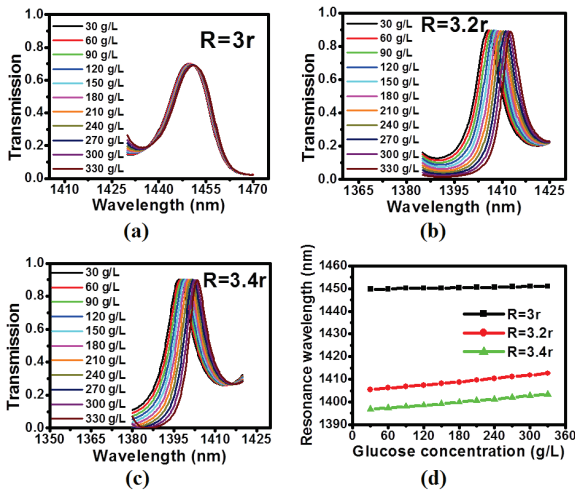


Fig. 5. The transmission spectra through the proposed biosensor at different glucose concentrations at: (a) $R=3r$, (b) $R=3.2r$, (c) $R=3.4r$, and (d) shift in the resonance wavelength as a function of the glucose concentration at different microcavity radii.

In order to further increase the sensitivity and transmission of the proposed sensor, the surrounding holes around the central microcavity are filled with the glucose solution as shown in Fig. 6 (a). Additionally, it is important from the practical point of view to keep the minimum separation between the edges of the central microcavity and the surrounding holes filled by glucose solution at 15 nm. This separation value is the suitable

limit in the practical consideration. Then, the radius of the central microcavity R is tested with values of $3r$, $3.1r$, and $3.2r$ as shown in Figs. 6 (b), 6 (c), and 6 (d). It is observed from these figures that the shift in the resonance wavelength becomes greater than that in the previous tests. It is also noted that the sensitivity increases with increasing the radius of the central microcavity in this structure. The shift in the resonance wavelengths as a function of the glucose concentration is represented in Fig. 7. It is evident from this figure that the resonance wavelength changes linearly with the glucose concentration change. The biosensor sensitivities are equal to 280 nm/RIU, 301.3 nm/RIU and 330.3 nm/RIU corresponding to $R=3r$, $3.1r$, and $3.2r$, respectively.

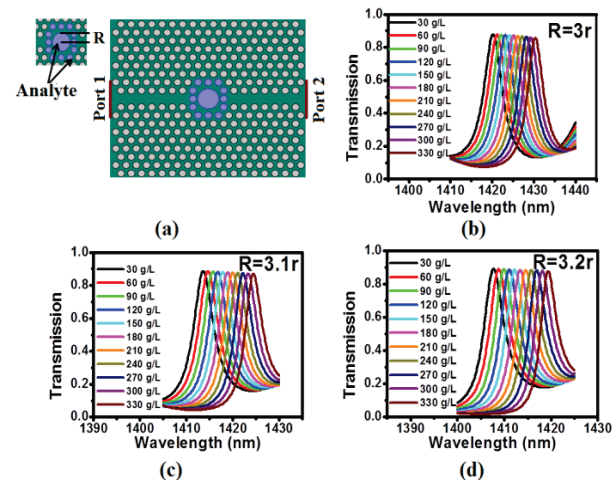


Fig. 6. (a) Cross-section of the modified 2D PhC biosensor with large central microcavity surrounded by 12 holes filled with the analyte (glucose solution). The transmission spectra at different glucose concentrations at: (b) $R=3r$, (c) $R=3.1r$, and (d) $R=3.2r$.

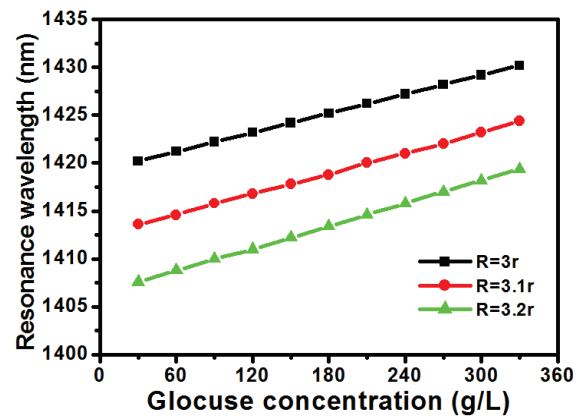


Fig. 7. The shift in the resonance wavelength as a function of the glucose concentration for the suggested 2D PhC biosensor at different R values.

In order to enhance the sensitivity of the suggested 2D PhC biosensor, the ellipticity of the central microcavity surrounded by holes filled with glucose solution is studied. In this investigation, the effect of the major diameter is changed from 2.2a to 2.6a with a step of 0.1a. However, the minor diameter is fixed at 2.2a because of practical consideration to keep the minimum separation between the edges of surrounding holes filled with glucose solution and the central microcavity at 15 nm. It is evident from Fig. 8 that the sensitivity is affected by changing the major diameter of the elliptical microcavity. The proposed 2D PhC biosensor offers high sensitivity of 422 nm/RIU at the major radius 2.6a which is greater than that reported in [16-19].

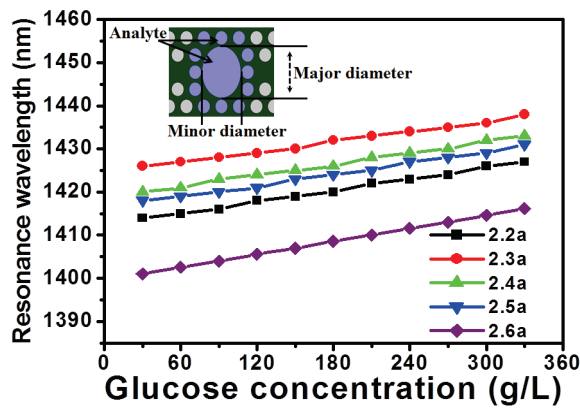


Fig. 8. Shift in the resonance wavelength as a function of glucose concentration at different values of the major diameter of the elliptical microcavity.

The quality factor of the suggested biosensor is also evaluated using the resonance wavelength λ_0 and the full width at the half maximum of the output transmission $\Delta\lambda_{FWHM}$ as given by $(\lambda_0/\Delta\lambda_{FWHM})$. The numerical results reveal that the suggested PhC biosensor has an average quality factor of 549.2. The crosstalk (CT) of the proposed 2D PhC biosensor is calculated as [13]:

$$CT = 20 \log (T_{\text{desired}} / T_{\text{undesired}}), \quad (2)$$

where T_{desired} is the desired transmission at certain resonance wavelength and $T_{\text{undesired}}$ is the undesired transmission at the same resonance wavelength. The proposed 2D PhC offers an average CT of 20 dB which shows the effectiveness of the proposed biosensor.

IV. EXPERIMENTAL APPROACH

In this study, the GaN dielectric slab is used as a background material for the suggested PhC biosensor. There are different techniques that are used to grow the GaN dielectric slab [32-35]. The nitride-based layers can be grown on silicon substrates by selective wet etching. The selective wet etching process starts with the growth of multilayer structure by metal organic vapor epitaxy on Si (111) substrate. Then, the drilled air holes of the

photonic crystal structure are formed by inductively coupled plasma etching process [32-34]. The GaN dielectric slab can also be produced by selective thermal decomposition (STD) technique. In this regard, the GaN is selectively decomposed at a temperature of $\sim 1000^\circ\text{C}$ under NH_3/H_2 ambient conditions and the drilled air holes are formed by using electron beam lithography method (EBLM). Arita et al. (2012) have used the STD and high crystalline nitride dielectric slab with the highly smoothed surface has been obtained [35]. Additionally, Baroni et al. (2010) have demonstrated tunable cavities with different sizes filled with liquid crystals (LCs). They have used free standing Si using a membrane to ease the infiltration of LC into the holes in the photonic structure. A glue can also be used to block the unfilled air holes. Therefore, it is believed that the suggested design with the selectively filled central cavity and surrounding air holes can be achieved successfully [36]. Further, the elliptical microcavity hole could be established practically as reported by Quiñónez et al. [37] and Vogelaar et al. [38].

V. CONCLUSION

A novel, compact and highly sensitive biosensor based on PhC platform has been proposed and analyzed in this paper. The 2D PhC biosensor comprises a hexagonal lattice of cylindrical holes that are perforated in a dielectric material. A gradation in the change of the 2D PhC biosensor structure tends to enhance the sensitivity. It is found that the 2D PhC biosensor with elliptical microcavity surrounded by holes filled with analyte exhibits the highest sensitivity of 422 nm/RIU. The numerical results also reveal that the wavelength shift is linearly proportional to the glucose concentration. Further, the proposed design has an amplified sensitivity with high detection of small variation in the glucose concentration. The enhancement of the 2D PhC biosensor will give high quality promising applications for glucose monitoring.

REFERENCES

- [1] A. P. F. Turner, I. Karube, and G. S. Wilson, *Biosensors Fundamentals, and Applications*. Oxford University Press, 1987.
- [2] F. G. Bănică, *Chemical Sensors, and Biosensors: Fundamentals and Applications*. John Wiley & Sons, 2012.
- [3] A. Cavalcanti, B. Shirinzadeh, M. Zhang, and L. C. Retly, "Nanorobot hardware architecture for medical defense," *Sensors*, vol. 8, no. 5, pp. 2932-2958, May 2008.
- [4] F. Hsiao and C. Lee, "Computational study of photonic crystals nano-ring resonator for biochemical sensing," *IEEE. Sens. J.*, vol. 10, no. 7, pp. 1185-1191, July 2010.
- [5] S. Olyae, S. Najafgholinezhad, and H. A. Banaei,

- “Four-channel label-free photonic crystal biosensor using nanocavity resonators,” *Photonic Sensors*, vol. 3, no. 3, pp. 231-236, September 2013.
- [6] S. Najafgholinezhad and S. Olyaei, “A photonic crystal biosensor with temperature dependency investigation of micro-cavity resonator,” *Optik*, vol. 125, pp. 6562-6565, November 2014.
- [7] S. I. Azzam, Mohamed F. O. Hameed, R. E. A. Shehata, A. M. Heikal, and S. S. A. Obayya, “Multichannel photonic crystal fiber surface plasmon resonance based sensor,” *Journal of Optical Quantum Electronics*, vol. 48, no. 142, pp. 1-11, February 2016.
- [8] M. F. O. Hameed, M. El-Azab, A. M. Heikal, S. M. El-Hefnawy, and S. S. A. Obayya, “Highly sensitive plasmonic photonic crystal temperature sensor filled with liquid crystal,” *IEEE Photonics Technology Letter*, vol. 28, no. 1, pp. 59-62, October 2015.
- [9] R. M. Younis, N. F. F. Areed, and S. S. A. Obayya, “Fully integrated AND and OR optical logic gates,” *IEEE Photonics Technology Letters*, vol. 26, no. 19, pp. 1900-1903, October 2014.
- [10] M. F. O. Hameed, A. M. Heikal, B. M. Younis, M. Abdelrazzak, and S. S. A. Obayya, “Ultra-high tunable liquid crystal-plasmonic photonic crystal fiber polarization filter,” *Journal of Optics Express*, vol. 23, no. 6, pp. 7007-7020, March 2015.
- [11] M. F. O. Hameed, M. Abdelrazzak, and S. S. A. Obayya, “Novel design of ultra-compact triangular lattice silica photonic crystal polarization converter,” *IEEE J. Lightwave Technology*, vol. 31, no. 1, pp. 81-86, January 2013.
- [12] N. F. F. Areed and S. S. A. Obayya, “Novel design of symmetric photonic bandgap based image encryption system,” *Prog. Electromagn. Res. C*, vol. 30, pp. 225-239, June 2012.
- [13] N. F. F. Areed and S. S. A. Obayya, “Novel all-optical liquid photonic crystal router,” *IEEE Photonic Tech. L.*, vol. 25, no. 13, pp. 1254-1256, May 2013.
- [14] J. D. Joannopoulos, S. G. Johnson, J. N. Winn, and R. D. Meade, *Photonic Crystals Molding the Flow of Light*. Princeton University Press, 2007.
- [15] S. Pal, E. Guillermain, R. Sriram, B. L. Miller, and P. M. Fauchet, “Silicon photonic crystal nanocavity-coupled waveguides for error-corrected optical biosensing,” *Biosens. Bioelectron.*, vol. 26, pp. 4024-4031, June 2011.
- [16] D. Dorfner, T. Zabel, T. Hürlimann, N. Hauka, L. Frandsen, U. Rant, G. Abstreiter, and J. Finley, “Photonic crystal nanostructures for optical biosensing applications,” *Biosens. Bioelectron.*, vol. 24, pp. 3688-3692, May 2009.
- [17] S. Kim, J. Lee, H. Jeon, and H. J. Kim, “Fiber-coupled surface-emitting photonic crystal band edge laser for biochemical sensor applications,” *Appl. Phys. Lett.*, vol. 94, 133503, April 2009.
- [18] M. A. Dündar, E. C. I. Ryckebosch, R. Nötzel, F. Karouta, L. J. Van Ijzendoorn, and R. W. Van der Heijden, “Sensitivities of InGaAsP photonic crystal membrane nanocavities to hole refractive index,” *Opt. Express*, vol. 18, no. 5, pp. 4049-4056, March 2010.
- [19] S. Kita, K. Nozaki, and T. Baba, “Refractive index sensing utilizing a CW photonic crystal nanolaser and its array configuration,” *Opt. Express*, vol. 16, no. 11, pp. 8174-8180, May 2008.
- [20] H. Butt, Q. Dai, and T. D. Wilkinson, “Photonic crystals & metamaterial filters based on 2D arrays of silicon nanopillars,” *Prog. Electromagn. Res.*, vol. 113, pp. 181-183, February 2011.
- [21] P. Seshu, *Text Book of Finite Element Analysis*. PHI, 2012.
- [22] S. Obayya, *Computational Photonics*. John Wiley & Sons, 2011.
- [23] H. Amano, M. Kito, K. Hiramatsu, and I. Akasaki, “P-Type conduction in Mg-doped GaN treated with low-energy electron beam irradiation (LEEBI),” *Japanese Journal of Applied Physics*, vol. 28, L2112, December 1989.
- [24] Y. Arakawa, “Progress in GaN-based quantum dots for optoelectronics applications,” *IEEE Journal of Selected Topics in Quantum Electronics*, vol. 8, no. 4, pp. 823-832, August 2002.
- [25] H. Amano, N. Sawaki, I. Akasaki, and Y. Toyoda, “Metalorganic vapor phase epitaxial growth of a high quality GaN film using an AlN buffer layer,” *Applied Physics Letters*, vol. 48, no. 5, pp. 353, 1986.
- [26] C. M. Foster, R. Collazo, Z. Sitar, and A. Ivanisevic, “Aqueous stability of Ga- and N-polar gallium nitride,” *Langmuir*, vol. 29, pp. 216-220, 2013.
- [27] A. Di Carlo, “Tuning optical properties of GaN-based nanostructures by charge screening,” *Physica Status Solidi*, (a), 183, pp. 81-85, January 2001.
- [28] S. J. Pearton, C. R. Abernathy, M. E. Overberg, G. T. Thaler, A. H. Onstine, B. P. Gila, F. Ren, B. Lou, and J. Kim, “New applications advisable for gallium nitride,” *Materials Today*, vol. 5, no. 6, pp. 24-31, June 2002.
- [29] X. X. Fu, B. Zhang, X. Kang, J. Deng, C. Xiong, T. Dai, X. Jiang, T. Yu, Z. Chen, and G. Zhang, “GaN-based light-emitting diodes with photonic crystals structures fabricated by porous anodic alumina template,” *Opt. Exp.*, 19(s5), pp. 1104-1108, 2011.

- [30] Y. L. Yeh, "Real-time measurement of glucose concentration and average refractive index using a laser interferometer," *Opt. Lasers Eng.*, vol. 46, pp. 666-670, September 2008.
- [31] H. Sato, H. Iba, T. Naganuma, and Y. Kagawa, "Effects of the difference between the refractive indices of constituent materials on the light transmittance of glass-particle-dispersed epoxy-matrix optical composites," *Philosophical Magazine B*, vol. 82, no. 13, pp. 1369-1386, 2002.
- [32] D. Néel, S. Sergent, M. Mexis, D. Sam-Giao, T. Guillet, C. Brimont, T. Bretagnon, F. Semond, B. Gayral, S. David, X. Checoury, and P. Boucaud, "AlN photonic crystal nanocavities realized by epitaxial conformal growth on nanopatterned silicon substrate," *Appl. Phys. Lett.*, vol. 98, 261106, June 2011.
- [33] N. V. Triviño, G. Rossbach, U. Dharanipathy, J. Levrat, J. A. Castiglia, J. F. Carlin, K. A. Atlasov, R. Butté, R. Houdré, and N. Grandjean, "High-quality factor two dimensional GaN photonic crystal cavity membranes grown on silicon substrate," *Appl. Phys. Lett.*, vol. 100, 071103, February 2012.
- [34] T. T. Wu, S. Y. Lo, H. M. Huang, C. T. Tsao, T. C. Lu, and S. C. Wang, "High-quality factor nonpolar GaN photonic crystal nanocavities," *Appl. Phys. Lett.*, vol. 102, 191116, May 2013.
- [35] M. Arita, S. Kako, S. Iwamoto, and Y. Arakawa, "Fabrication of AlGaIn two-dimensional photonic crystal nanocavities by selective thermal decomposition of GaN," *Appl. Phys. Express*, vol. 5, 126502, December 2012.
- [36] P. Baroni, Q. Tan, V. Paeder, and M. Roussey, "Switchable photonic crystal cavity by liquid crystal infiltration," *J. Eur. Opt. Soc.*, vol. 5, 10057, November 2010.
- [37] F. Quiñónez, J. W. Menezes, L. Cescato, V. F. Rodriguez-Esquerre, H. Hernandez-Figueroa, and R. D. Mansano, "Band gap of hexagonal 2D photonic crystals with elliptical holes recorded by interference lithography," 14(11), pp. 4873-4879, May 2006.
- [38] L. Vogelaar, W. Nijdam, H. A. G. M. van Wolferen, R. M. de Ridder, F. B. Segerink, E. Flück, L. Kuipers, and N. F. van Hulst, "Large area photonic crystal slabs for visible light with waveguiding defect structures: fabrication with focused ion beam assisted laser interference lithography," *Adv. Mater.*, vol. 13, no. 20, October 2001.

Ultra-Wideband Polarization Conversion Metasurface Based on Topology Optimal Design and Geometry Tailor

Sai Sui¹, Jibao Yu¹, Hua Ma¹, Jieqiu Zhang¹, Jiafu Wang¹, Zhuo Xu², and Shaobo Qu¹

¹ College of Science, Air Force Engineering University
Xi'an, Shaanxi 710051, China
suisai_mail@foxmail.com

² Electronic Materials Research Laboratory
Key Laboratory of the Ministry of Education Xi'an Jiaotong University, Xi'an, Shaanxi 710049, China

Abstract — We presented a topology optimization method based on genetic algorithm (GA) combined geometry tailor scheme (GTS) to realize ultra-wideband polarization conversion metasurfaces (UPCM) in microwave range. The present method takes the connectivity condition of the elements into consideration, thereby resulting in good optimization efficiency. As examples, a UPCM is designed by topology optimization, which is composed of the dielectric substrate sandwiched with patched metallic patterns and continuous metal background. Three plasmon resonances are generated by electric and magnetic resonances, which lead to bandwidth expansion of cross-polarization reflection. The simulated results show that the maximum conversion efficiency is nearly 100% at the three plasmon resonance frequencies and the 3 dB bandwidth range from 5.66 to 24.68 GHz can be achieved for both normally incident x- and y-polarized waves.

Index Terms — Genetic Algorithm (GA), geometry tailor, Metamaterials (MMs), metasurface, topology design.

I. INTRODUCTION

Metamaterials (MMs) [1] are artificial media with pitches smaller than the wavelength, which have numerous intriguing artificial electromagnetic responses not attainable with naturally occurring materials. In recent years, many researches worldwide focus on metasurfaces [2], planar metamaterials, which are two-dimension MMs consist of cells repeated periodically throughout a medium. Many MMs have been applied to manipulate electromagnetic characteristics including transmissions and polarizations in sub-wavelength scale, such as polarization manipulation through anisotropic and chiral MMs from microwave terahertz to optical frequency regimes [3], [4].

Recently, the manipulation of polarization is essential for communication, sensing, and other applications. However, narrow working bandwidth is

still one of the main problems. In general, the bandwidth can be broadened by multilayer structures. For example, a highly efficient broadband polarization transformation slab has been achieved by stacking twisted complementary circular symmetric split-ring resonators. However, this may be very complicated for irregular shapes and therefore restrict the MMs to regular shape. It is also difficult to find the optimal structures for the MMs using the intuition and empiricism testing. To break through the limitation of bandwidth performances, topology design method was adopted due to the complex nature of the problem, which is based on some kind of intelligent algorithms, such as genetic algorithm (GA).

In this paper, we propose an ultra-wideband polarization conversion metasurfaces (UPCM) design method based on the GA [5] with a geometry tailor scheme (GTS), which is a new type of operator for tailoring pattern shapes. Therefore, the GA with GTS not only can improve the metamaterial topology optimization simulation-efficiency, but also can improve the optimal result searching ability and convergence speed. Firstly, we develop the topology design method with GTS, which operates on matrix of evolution algorithm, as an algorithm operator. The GTS can remove the isolated points in the elements not by natural selection and evolution, but by forcing to wipe them. Secondly, as an example, an UPCM is designed and optimized, then, a comparison between conventional topology method who use natural selection and evolution and topology method with GTS is employed, which demonstrates the topology method with GTS can obtained faster convergence speed of optimization than the conventional topology method. Finally, the effectiveness of the present design method is confirmed by an instance. Both the simulated and optimization results show that the bandwidth is very wide for both x- and y-polarized waves under normal incidence, attaining a 3 dB bandwidth range from 5.66 to 24.68 GHz.

Furthermore, the efficiency is close to 100% at the three plasmon resonance frequencies, respectively.

II. TOPOLOGY DESIGN METHOD WITH GTS

A. Encoding approach of topology optimization

According to the analysis of GA, the evolutionary structural optimization is just an evolution process under a certain optimization strategy, with which the schema is related to the defining length of the chromosome and thus decides the code number.

Figure 1 shows a single-layer metasurface with a dielectric substrate under consideration and the unit cell of its periodic structure extended infinitely. The unit cell is divided into $N \times N$ lattice (10×10 lattice is handled in this paper) to represent the metasurface with an arbitrary element shape in terms of 1s and 0s in the GA. The 1 and 0 correspond to the perfect conductor patch (pixels in Fig. 1) and the free space (blank pixels), respectively. In the present method, the unit-cell geometry tries to work for extensive polarizations bandwidth. So, in the GA, the region is encoded into a 100-bit binary string. The GA starts with a random population and then generates the metasurface element shapes through selection, crossover, mutation and one more operator proposed in this paper. Also the GA keeps the best individual after each generation (elitism strategy). The size of the unit cell must be determined by both p and h , which are encoded by a 18 bit binary string.

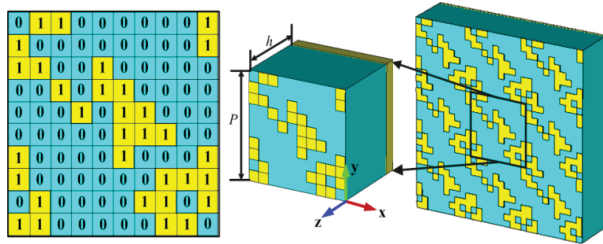


Fig. 1. The configuration and encoding approach of topology design.

B. GTS design

Not only typical GA operators but also a new-type of operator is needed for the optimization design of the MMs element shape taking into account the connectivity condition of the elements. The relation of the basic functions for the analysis with 1s and 0s in the GA is shown in Fig. 1. Most of the metasurface element shapes generated by the GA include the point contact of the isolated lattice points inside the unit cell. If the conductors of an optimized metasurface element have such points, it means that they do not touch each other analytically, which don't contribute to metasurface performance. Therefore, the isolated lattice points should

be wiped when fabricating these elements, which can improve the optimization speed and simulation speed. We propose here a GTS, which is a new method for geometry tailor.

Figure 2 shows the flowchart of the optimization-design method based on the GA incorporated with the GTS. This scheme removes the critical points not by natural selective and evolution of GA, but by forcing to eliminate them. The eliminate engine, geometry tailor, works as a sieve, which can search and eliminate the isolated point of geometry matrix. It should be noted here that the GTS can improve optimization simulation efficient by ignoring those isolated pixels which is not contacts physically.

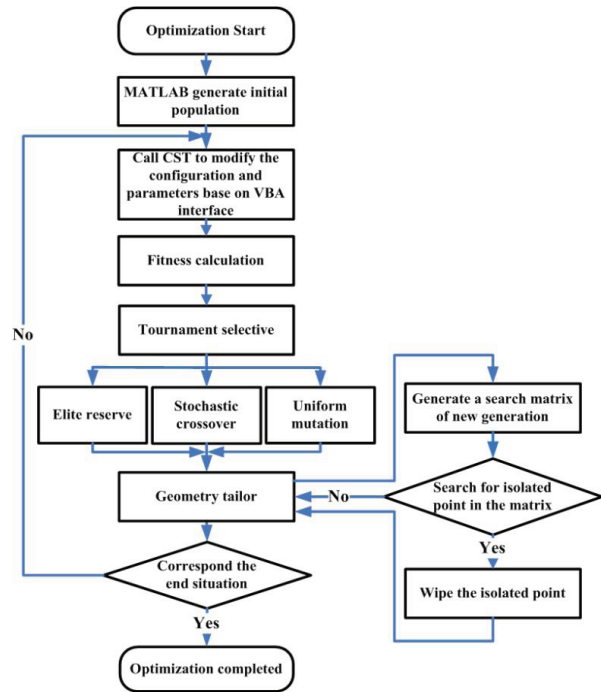


Fig. 2. The flowchart of optimization design with GTS.

C. Fitness function

The numerical simulation is carried out to analyze the reflection behavior of the polarizer with a commercial program, CST MICROWAVE STUDIO 2011 (CST). In the process of simulation, the periodic boundary conditions are used in the x and y directions, and broadband Gaussian-modulated pulse sources with x -polarized and/or y -polarized electric fields are used as the excitation source in the simulation for the linear polarization.

Figure 3 illustrates the comparison between conventional GA and GA with GTS. The fitness function is created according to the goal of expanding polarization bandwidth, which considered the maximal polarization bandwidth and minimal thickness, the more bandwidth the smaller fitness value. In GA, 100 populations are

employed in a generation and the selection scheme is tournament selection with two best individuals reproduced, realizing the uniform genetic and mutation process. The crossover probability is set as 0.8, the mutation rate set as 0.01, and the stop condition is related to the fitness goals or is set as truncation limited by the maximum generation number of 30. As shown clearly in Fig. 3, the algorithm convergence speed and stability of UPCM with GTS is much better than conventional ones.

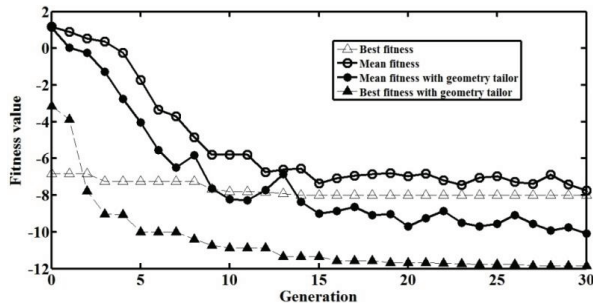


Fig. 3. The best fitness and average fitness comparison.

III. SIMULATION RESULT

In order to verify the ultra-wideband property of such metasurface, full-wave simulations are performed with CST. Figure 4 shows the simulated cross- and co-polarization reflection and polarization-conversion ratio versus frequency. As shown in Fig. 4, strong cross-polarization reflection occurs under both y-polarized and x-polarized normal incidences. Furthermore, the cross-polarization reflection band is very wide. The 3 dB bandwidth is from 5.44 GHz to 24.68 GHz for both y-polarized and x-polarized incident waves. As mentioned above, the ultra-wideband property is resulted from the three plasmon resonance frequencies at 7.23 GHz, 11.88 GHz, and 23.16 GHz, where the polarization conversion efficiency is nearly 100%, as shown in Fig. 5, a 1:4.3 3 dB bandwidth can be achieved for both normally incident x- and y-polarized waves.

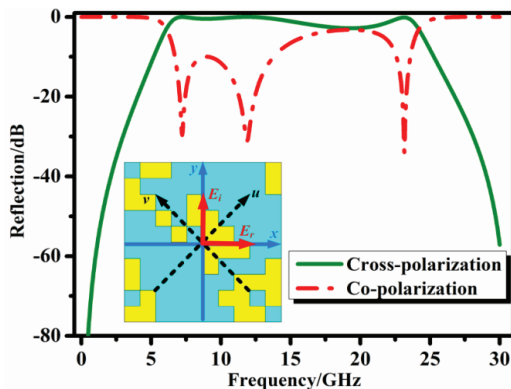


Fig. 4. The cross-polarization and co-polarization reflection.

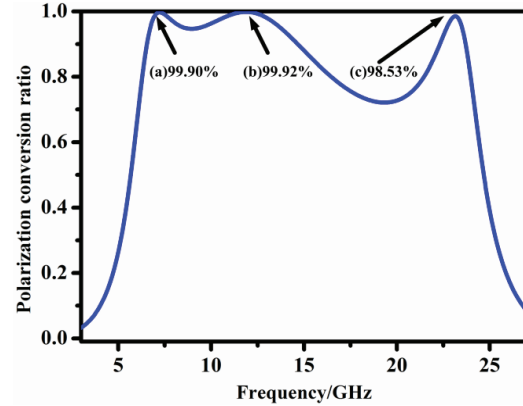


Fig. 5. The polarization conversion ratio.

IV. EXPERIMENT RESULT

To confirm the proposed polarization conversion metasurface, a 320×320 mm² sample of the proposed metasurface is fabricated and measured. The experiment system is demonstrated in Fig. 6, in which the sample is illuminated by two vertical horns antenna, so the cross-polarization ratio can be measured. The sample is fabricated by PCB technology. Figure 7 shows the measured results, which are measured by several horn antennas of different working band, ranging from 1 to 30 GHz. Through the comparison of the available results, we can conclude that the measurements are well corresponding with the simulation result.

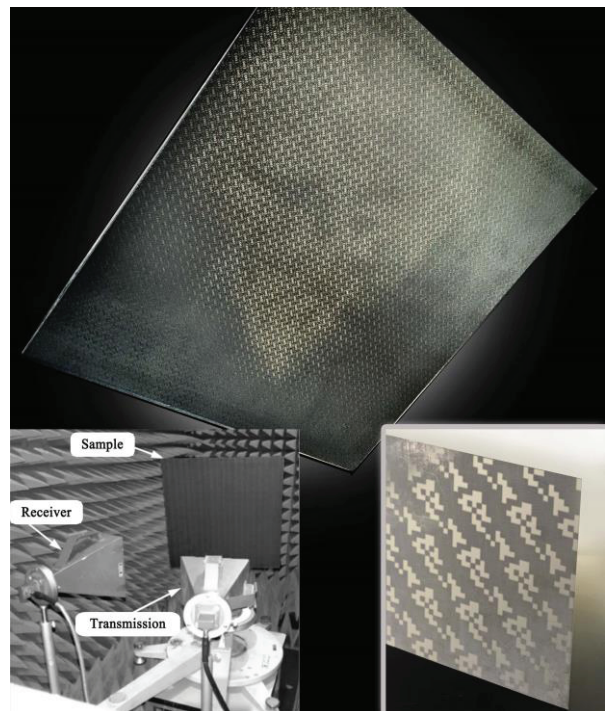


Fig. 6. The fabricated sample of design metasurface and its measurement system.

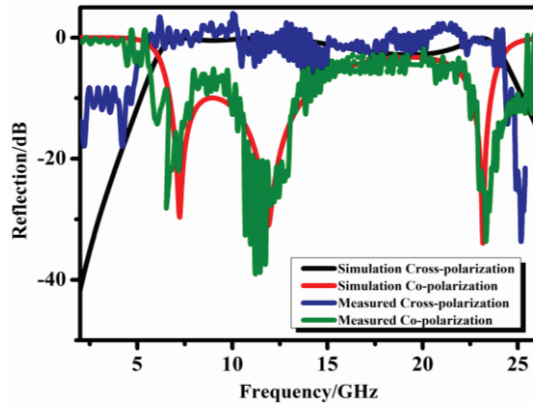


Fig. 7. The measured cross-polarization and co-polarization reflection.

V. CONCLUSION

In conclusion, by means of simulation, we demonstrate that UPCM can be realized using reflective metasurfaces at microwave frequencies by topology design. Due to multiple electric and magnetic resonances, cross-polarization reflection bandwidth can be expanded significantly. An improved topology with GTS has been proposed to achieve better design of UPCM. As an explicit example, we designed and verified a UPCM with a 1:4.3 3 dB bandwidth. Furthermore, the maximum conversion efficiency is up to 100% at the three plasmon resonance frequencies. Because of the easy design, such polarization conversion metasurfaces are of great application values in the polarization controlled devices and other MMs.

ACKNOWLEDGEMENT

This work is supported by the National Natural Science Foundation of China (Project No. 61331005, 11204378, 11274389), the Foundation for the Author of National Excellent Doctoral Dissertation of PR China (FANEDD) (Grant No. 201242), and the China Postdoctoral Science Foundation (Grant Nos. 2013M532131, 2013M532221). We acknowledge Pang Yongqiang of Air Force Engineering University for his valuable discussion to the manuscript and stimulating.

REFERENCES

- [1] J. B. Pendry, A. J. Holden, W. J. Stewart, and I. Youngs, "Extremely low frequency plasmons in metallic mesostructures," *Phys. Rev. Lett.*, vol. 76, no. 25, pp. 4773-6, June 1996.
- [2] C. L. Holloway, E. F. Kuester, J. A. Gordon, et al., "An overview of the theory and applications of metasurfaces: The two-dimensional equivalents of metamaterials," *IEEE Antenn. Propag. M.*, vol. 54, no. 2, pp. 10-35, April 2012.
- [3] S. Wu, Z. Zhang, Y. Zhang, K. Zhang, L. Zhou, X. Zhang, and Y. Zhu, "Enhanced rotation of the polarization of a light beam transmitted through a silver film with an array of perforated S-shaped holes," *Phys. Rev. Lett.*, vol. 110, no. 20, pp. 207401-5, May 2013.
- [4] Y. Zhao and A. Alù, "Manipulating light polarization with ultrathin plasmonic metasurfaces," *Phys. Rev. B*, vol. 84, no. 20, pp. 205428-6, November 2011.
- [5] K. A. Diest, *Numerical Methods for Metamaterial Design*, Springer, 2013.



Sai Sui received his master degrees from the Air Force Engineering University of China. His research interests include metamaterial of electromagnetic wave design and optimization design.

A Circuit Human Body Model for an Indirect Lightning Strike Analyzed by means of an FDTD Method

V. A. Alrim, S. A. Amanatiadis, A. X. Lalas, and C. S. Antonopoulos

Department of Electrical and Computer Engineering
Aristotle University of Thessaloniki, Thessaloniki, GR-54124, Greece
chanto@auth.gr

Abstract — In the present paper, a simplified lumped element human body, stroked by a lightning touch voltage, is designed and analyzed using the finite-difference time-domain (FDTD) method. The extracted results are compared with an electronic circuit simulator validating our numerical method. Moreover, other touch voltage scenarios are investigated, measuring and comparing the current that flows through different body parts. Additionally, the induced current to a human body, being in the vicinity of a lightning stroked object, is accurately calculated through the FDTD algorithm. The inability of the circuit modeler to simulate non-contact configurations proves the necessity of our numerical algorithm, while the possibility of the electric discharge effect is introduced.

Index Terms — Circuit model, FDTD, high voltage, human body, lightning.

I. INTRODUCTION

Lightning is a natural phenomenon that may have a serious impact on human beings, because of its impressive appearance and mainly its severe threats imposed on life and structures [1-3]. Several mechanisms have been so far reported to explain its interaction with humans, like the direct strike that occurs when the lightning channel terminates on the body, exposing it at the full lightning current [4-6]. However, only a small percentage of the incidents are due to this case; consequently the more realistic touch voltage and side flash cases are examined in this work. The first one occurs if the person holds a lightning stroked object, while the latter when the human stands close to it and a discharge path is created between the object and the human.

The proposed method uses a simplified human model, realized with lumped elements [7]. The current flow through the human body is extracted by means of a home-made FDTD algorithm [8], while it is compared with an electronic circuit simulator for the simple case of a telephone-mediated strike. The results are almost identical proving the FDTD efficiency even under the

condition of low frequencies. Likewise, utilizing our numerical algorithm, the current flow through various parts of the human body is measured for diverse cases of touch voltage strikes. Several scenarios have been studied such as the contact of the head and hand with a grounded or ungrounded stroked object, e.g., the aforementioned telephone device. Furthermore, a popular arrangement that involves the contact of the human hand with a grounded or an ungrounded stroked object is also thoroughly examined. For the above cases, the current which flows through different human body parts is measured via the FDTD method.

Moreover, the implemented algorithm is employed at problems of more complicated geometries and conditions, without making additional approximations, unlike its electronic simulation counterpart. Finally, a non-contact scenario is investigated revealing a further impact of a lightning strike. In particular, the induced current because of a side flash is computed, at several body parts, whereas the possibility of an electric discharge should not be ignored, due to its devastating effect on humans.

II. THEORETICAL ASPECTS

The circuit model of the human body related to a lightning strike, approximating the body parts via lumped elements, as in Fig. 1, has been proposed in [6], [7]. It consists of commonly accepted lines including an internal resistance split of approximately 1 k Ω between arms, torso, and legs as internal components. The skin resistivity parts are significantly larger than their internal counterparts, exhibiting a parallel resistance and capacitance of 10 k Ω and 0.25 μ F, respectively, except for head's capacitance, which is increased.

Our test scenario involves a grounded telephone that mediates the lightning current to the human body, since the lightning may strike the telephone wire directly and as a result, its power passes in the telephone set. In normal operation the person holds the telephone with one hand (point 2 in Fig. 1 (b)), and presses the handset to the ear (point 1), creating a capacitive coupling of approximately 88 μ F, in the case of the lightning strike.

This touch voltage application has a return path via the feet (point 3) or any other body part that touches an earthed structure. Another scenario examines a corresponding application, where the telephone device is not grounded or the floor insulation is adequately efficient, and the circuit only involves points 1 and 2. On the third one, the input voltage is connected directly at point 2, simulating the contact of the human with any ungrounded stroked object, while on the latter case the object is assumed grounded, so the return path is completed via the feet (point 3).

The second application does not involve the coupling capacitance, since the human is now not touching the stroked device or alternatively the stroked wire, but is standing in its vicinity at distance d , as illustrated in Fig. 1 (a).

The main extracted result from the numerical algorithm is the current that flows through several body parts for the examined situations. It is measured via the current density that flows through a circular loop, as

$$I = \iint \vec{J} \cdot d\vec{S}. \quad (1)$$

The strike is modelled as a double exponential function defined by its two time parameters t_1 , t_2 and its peak value A . Although, in the literature the lightning is implemented as a current source, in our work a voltage source is selected, because the strike is mediated via the telephone or an alternative device. The double exponential voltage has the form [9] of:

$$v(t) = A(e^{-t/t_1} - e^{-t/t_2}). \quad (2)$$

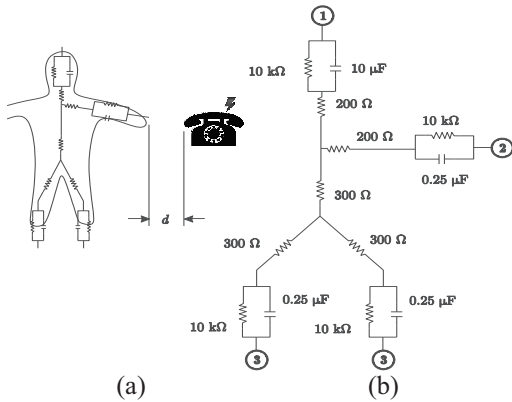


Fig. 1. (a) The telephone mediated lightning strike scenario, and (b) the circuit model of a human body.

III. FDTD ALGORITHM

The indirect lightning strike analysis on a circuit human body model is performed via an FDTD algorithm that includes lumped elements. The conventional FDTD update equations for the electric \vec{E} and the magnetic \vec{H} field are derived starting from the Maxwell equations:

$$\nabla \times \vec{E} = -\mu \frac{\partial \vec{H}}{\partial t}, \quad (2a)$$

$$\nabla \times \vec{H} = \varepsilon \frac{\partial \vec{E}}{\partial t} + \vec{J}, \quad (2b)$$

where ε and μ are the dielectric permittivity and the magnetic permeability of the medium respectively, while $\vec{J} = \sigma \vec{E}$ is conduction current, for conductivity σ .

Utilizing 1st order finite differences to approximate the original equations and the conventional Yee lattice [9] for the electric and the magnetic field components, their update equations are extracted straightforwardly as [8]:

$$E_x|_{i,j,k}^{n+1} = \frac{2\varepsilon - \sigma\Delta t}{2\varepsilon + \sigma\Delta t} E_x|_{i,j,k}^n + \frac{2\Delta t}{2\varepsilon + \sigma\Delta t} \frac{1}{\Delta h} \left(H_z|_{i,j+1/2,k}^{n+1/2} - H_z|_{i,j-1/2,k}^{n+1/2} - H_y|_{i,j,k+1/2}^{n+1/2} + H_y|_{i,j,k-1/2}^{n+1/2} \right), \quad (3)$$

for the E_x electric field component, while similar update equations are derived for the rest components. The lumped elements are imported in the equations as conduction currents \vec{J} located at the desired electric field component locations, Fig. 2. Thus, assuming a lumped element positioned at an E_x component, the final update equation for this specific location is evaluated as:

$$E_x|_{i,j,k}^{n+1} = E_x|_{i,j,k}^{n+1} - I_x^{n+1} \left(E_x|_{i,j,k}^{n+1}, E_x|_{i,j,k}^n, \dots, E_x|_{i,j,k}^1 \right), \quad (4)$$

where the function $I_x^{n+1}(\dots)$ depends on the relation that connects the current and the voltage, namely

$$I_x^{n+1} = \frac{2\Delta t}{2\varepsilon + \sigma\Delta t} \frac{E_x|_{i,j,k}^{n+1} + E_x|_{i,j,k}^n}{2R}, \quad (5a)$$

$$I_x^{n+1} = \frac{C}{2\varepsilon + \sigma\Delta t} \left(E_x|_{i,j,k}^{n+1} - E_x|_{i,j,k}^{n-1} \right), \quad (5b)$$

for a resistor R and a capacitor C , respectively [10].

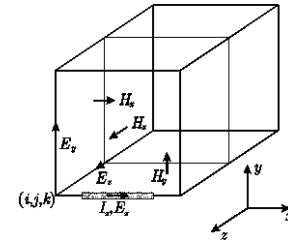


Fig. 2. The utilized Yee lattice.

IV. TOUCH VOLTAGE ANALYSIS

A. Numerical verification

Firstly, the initial touch voltage case is explored where the head and the arm are connected to the input voltage via 88 pF capacitances. The human body is realized as parallel lumped elements in the FDTD algorithm connected through lossless wires, while the dimension from head to feet is about 1.8 m to realistically model the average human height. The feet and input voltage touch the ground, modeled as a perfect electric conductor (PEC) boundary condition. The remaining boundaries are terminated with a 4-cell

perfect matched layer (PML) to approximate the free space. Although, other terminating techniques can be utilized, such as MUR-I for dielectric materials [11, 12], PML is advantageous for domains involving lumped elements in free-space. The domain is divided in $60 \times 52 \times 37$ cubic cells of 8 cm edge dimensions, while the time-step is set to $\Delta t = 177.4$ ps, a setup that is maintained throughout our analysis. The minimum wavelength of the analysis is extracted through a Fourier transformation of the input signal and the resulting wavelengths per unit cell are approximately 200. This value is expected due to the problem's relatively low frequencies, typically about 20 MHz for a double exponentially modeled lightning. On the other hand, the PSPICE electronic circuit simulator is utilized to compare the extracted FDTD results. The electronic simulator is selected for comparison due to its advantageous performance for closed loop lumped element scenarios. The input voltage is calculated via (2) setting $A = 9.5$ kV, $t_1 = 66.7$ μ s and $t_2 = 0.54$ μ s, leading to the typical double exponential waveform of Fig. 3, where the rise time is 0.25 μ s and the pulse time is 50 μ s [13].

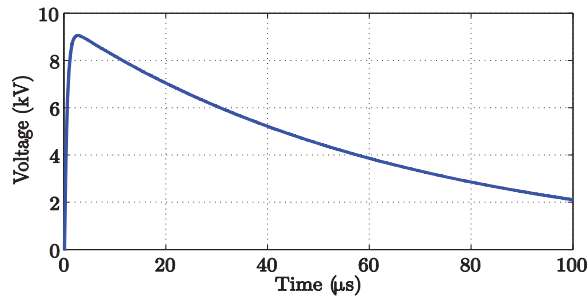


Fig. 3. Input voltage of the stroked telephone.

The comparison of the current flow in the human's arm between the two individual numerical methods, sketched in Fig. 4. As observed, the implemented FDTD method is effectively accurate at low frequency problems which use lumped element networks, revealing that a touch voltage strike is lethal for a human since the current outreaches 1 A.

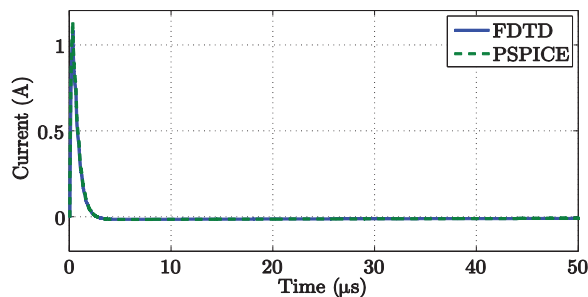


Fig. 4. Comparison of the current flow at the human hand in the touch voltage scenario between the implemented FDTD algorithm and the PSPICE simulator.

B. Touch voltage scenarios

After verifying the accuracy of the numerical algorithm, several different setups are examined to extend the applicability of the FDTD method. Initially, the previous setup is retained and the current flow through several different body parts is extracted via (1) and depicted in Fig. 5. One can easily discern that the current which flows through the torso is double the value of other body parts. This outcome is straightforward since the current from the head and arm is added, flows through torso, and then it is divided at the legs.

The next scenario involves the same telephone mediated strike except that the device is now ungrounded. The location of the source is assumed between the head and the hand and the current that flows through them, represented in Fig. 6, is significantly bigger than the one through the legs and torso since there is no return path via the ground. Although, this current is not larger than 25 mA, it should not be ignored and this is a major advantage of the FDTD algorithm compared to the electronic simulator. The latter is not capable of calculating the current outside closed loops, which is necessary on several complicated situations.

Additionally, the situation where the human simply touches a grounded lightning stroked object is investigated and the outcomes are sketched in Fig. 7. The human head is not included in the closed loop circuit, because of the return path through the feet, and the fact that its current is negligible. However, the current that flows across the hand and the torso exceeds 1 A and is obviously lethal for the human, while at feet the current is divided by half.

As a last touch voltage case, we study the impact of an ungrounded lightning stroked object when the human comes in contact with it. The results are corresponding to our previous scenario except that the current is now about 15 times decreased due to the ungrounded object, depicted in Fig. 8. The current flows again from the hand through the torso and it is divided at feet, with a maximum value of approximately 85 mA, which is adequate to disturb the human. As already mentioned, the FDTD algorithm is capable of calculating this considerable current, unlike the electronic simulator counterpart.

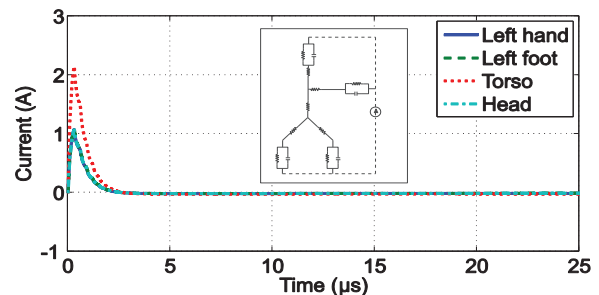


Fig. 5. Current flow through several body parts in the case of a grounded telephone mediated strike.

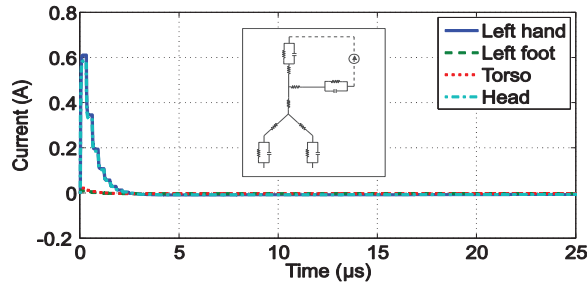


Fig. 6. Current flow through several body parts for ungrounded telephone mediated strike.

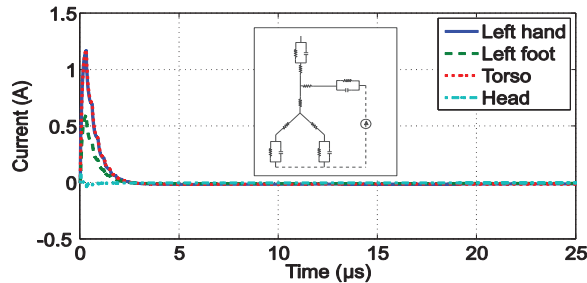


Fig. 7. Current flow through several body parts of a human touching a lightning stroked grounded device.

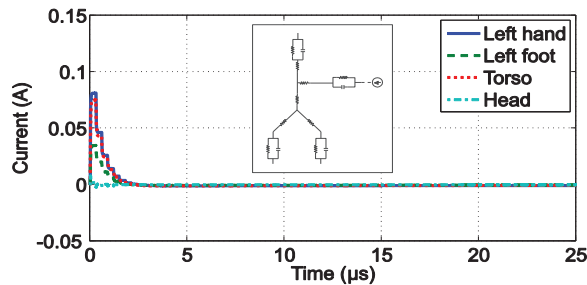


Fig. 8. Current flow through several body parts of a human touching a lightning stroked ungrounded device.

V. SIDE FLASH INVESTIGATION AND DISCHARGE POSSIBILITY

In the previous section, our numerical algorithm calculated the current that flows through body parts that are outside closed loops, revealing a first advantage compared to the electronic circuit simulator. Although, the simulation time of the latter is significantly reduced compared to the FDTD method, it is not capable of solving more complicated implementations, unless some approximations are applied, which can easily lead to degraded results. In this section, the side flash scenario is examined, where the lightning stroked object is not in direct contact with the human and the induced current to several body parts is extracted through (1), and depicted in Figs. 9 to 12. In this case, it is obvious that the current at each body part is increased drastically as the human approaches the stroked device, but is not lethal because of the effect's short duration and the current's low

values. Specifically, the current through the arm is slightly exceeding 100 mA, even at distance $d = 10$ cm. Furthermore, at torso it is fairly increased for any distance, but it remains at low levels, while at legs it is divided by half with respect to the touch voltage scenarios. Finally, the current through the head remains at negligible levels, less than 10 mA.

It is critical to mention that the electric field between the arm and the device receives extremely high values, increasing the possibility of a hazardous electric discharge. Therefore and owing to its significance, the disruptive effect technique is briefly introduced in the present work [14]. In this manner, we are able to estimate the possibility of an electric discharge versus the temporal variation of the potential between two points $V(t)$, calculated through the electric field data of the numerical algorithm. According to this approach, the time integral DE of the difference between the evaluated potential $V(t)$ and a predefined voltage V_0 is:

$$DE = \int_{t_{on}}^{t_{off}} (V(t) - V_0)^k dt, \quad (6)$$

where k is another predefined parameter. If the integral in (3) exceeds a specific DE threshold, a hazardous electrostatic discharge is very likely to occur. The values of V_0 , k , and DE are acquired through measurements, rather than analytically, and their accuracy depends on the problem under study [15, 16]. However, the relevant literature lacks data for the examined distances, and further measurements are necessary to estimate accurately the electric discharge possibility, which is outside the scope of the present work.

The distribution of the electric field at $t = 4 \mu s$, is illustrated in Fig. 13 (a) for the lightning stroked object at distance $d = 20$ cm. Here, the extremely high value of the potential difference between the hand and the source is revealed, confirming the increased possibility of an electric discharge. Moreover, in Fig. 13 (b), where the electric field distribution of a touch voltage scenario is depicted, one can observe the concentration of the field at the capacitors. At both cases, the zero electric field corresponds to the location of the conductors, as expected from the theory.

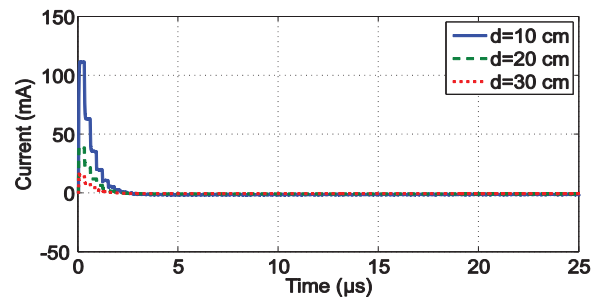


Fig. 9. Current flow through human's hand for induced by a stroked object at distance d .

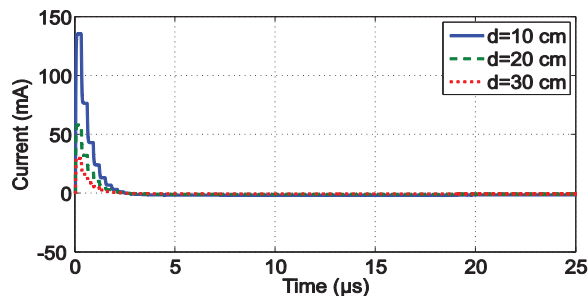


Fig. 10. Current flow through human's torso for induced by a stroked object at distance d .

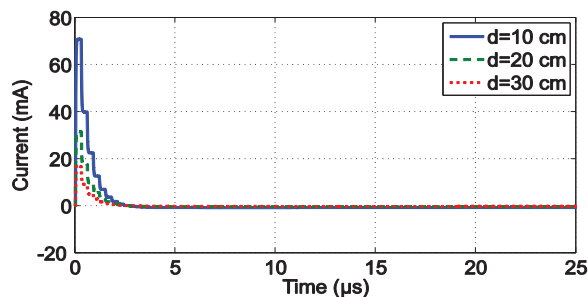


Fig. 11. Current flow through human's leg for induced by a stroked object at distance d .

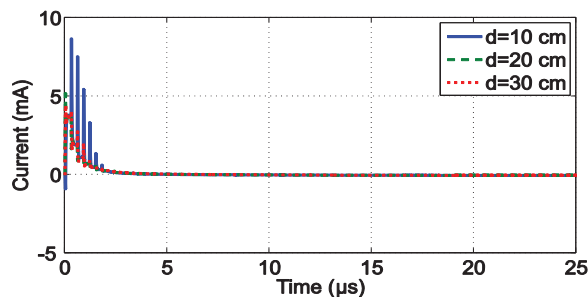


Fig. 12. Current flow through human's head for induced by a stroked object at distance d .

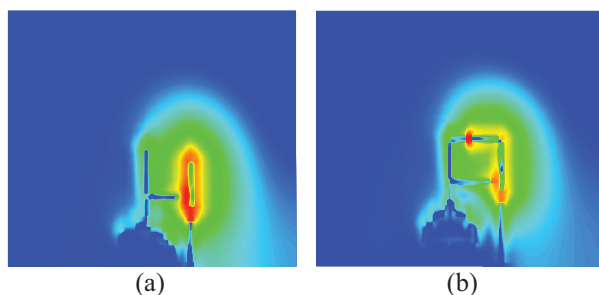


Fig. 13. Distribution of electric field at: (a) side flash and (b) touch voltage scenarios.

VI. CONCLUSION

The circuit model of the human body, stroked by touch voltage of a lightning, has been modeled in the

present paper. The results, extracted by the FDTD algorithm and the electronic circuit simulator, have been compared successfully, while the current flow through several body parts of various scenarios has been investigated. In the non-contact case of a side flash, the FDTD method has proven that applies effectively unlike the electronic circuit solver that is unable to solve it without inaccurate approximations. Moreover, a brief introduction to the disruptive effect technique has been involved in order to estimate the possibility of a hazardous electric discharge effect. Overall, the FDTD algorithm is more effective to solve complicated problems, even at low frequencies.

ACKNOWLEDGMENT

This research has been co-financed by the EU (European Social Fund - ESF) and Greek national funds through the Operational Program "Education and Lifelong Learning" of the National Strategic Reference Framework (NSRF) – Research Funding Program: ARISTEIA. Investing in knowledge society through the European Social Fund.

REFERENCES

- [1] M. Szczerbiński, "Lightning hazards and risks to humans: Some case studies," *J. Electrostat.*, vol. 59, no. 1, pp. 15-23, 2003.
- [2] C. Gomes and M. Ab Kadir, "A theoretical approach to estimate the annual lightning hazards on human beings," *Atmos. Res.*, vol. 101, no. 3, pp. 719-725, 2011.
- [3] I. Pop, V. Topa, C. Munteanu, A. Racasan, and E. Merdan, "Human exposure to power frequency electric field inside very high voltage substations," *IEE Environ. Eng. Manag. J.*, vol. 10, no. 4, pp. 499-504, 2011.
- [4] M. O. Goni, E. Kaneko, and A. Ametani, "Simulation of lightning return stroke currents and its effect to nearby overhead conductor," *ACES J.*, vol. 24, no. 5, pp. 302-307, 2009.
- [5] S. Cristina and A. Orlandi, "Calculation of the induced effects due to a lightning stroke," *IEE Proc. B Electr. Power App.*, vol. 139, no. 4, pp. 374-380, 1992.
- [6] V. Cooray, *The Lightning Flash*, IET Power Engineering Series, vol. 34, London, 2003.
- [7] A. D. Dias, M. Tello, D. S. Gazzana, and G. C. Potier, "Revisiting lightning body model," in *Proc. X international Symposium on Lightning Protection*, Curitiba, Brazil, 2009.
- [8] A. Taflove and S. C. Hagness, *Computational Electrodynamics: The Finite-Difference Time-Domain Method*, Artech House, Norwood, 1995.
- [9] Kane S. Yee, "Numerical solution of initial boundary value problems involving Maxwell's equations in isotropic media," *IEEE Trans.*

- Antennas Propag.*, vol. 14, no. 3, pp. 302-307, 1966.
- [10] W. Sui, D. A. Christensen, and C. H. Durney, "Extending the two-dimensional FDTD method to hybrid electromagnetic systems with active and passive lumped elements," *IEEE Transactions on Microwave Theory and Techniques*, vol. 40, no. 4, pp. 724-730, 1992.
- [11] B. Mukherjee and D. K. Vishwakarma, "Application of finite difference time domain to calculate the transmission coefficient of an electromagnetic wave impinging perpendicularly on a dielectric interface with modified MUR-I ABC," *Defence Science Journal*, vol. 62, no. 4, pp. 228-235, 2012.
- [12] B. Mukherjee, "Numerical solution in FDTD for absorbing boundary condition over dielectric surfaces," *Journal of Advance Research in Scientific Computing*, vol. 4, pp. 13-23, 2012.
- [13] W. Jia and Z. Xiaoqing, "Double-expression of lightning current waveforms," in *Proc. Conference on Environ-mental Electromagnetics (CEEM)*, Dalian, P. R. China, 2006.
- [14] A. Jones, "Evaluation of the integration method for analysis of non-standard surge voltages," *AIEE Trans. Power App. Syst.*, vol. 73, pp. 980-990, 1954.
- [15] R. Caldwell and M. Darveniza, "Experimental and analytical studies of the effect of non-standard waveshapes on the impulse strength of external insulation," *IEEE Trans. Power App. Syst.*, vol. PAS-92, no. 4, pp. 281-284, 1973.
- [16] Z. Datsios, P. Mikropoulos, and T. Tsovilis, "Estimation of the minimum shielding failure flashover current for first and subsequent lightning strokes to overhead transmission lines," *Electr. Pow. Syst. Res.*, vol. 113, pp. 141-150, 2014.

Numerical Analysis of Thermal Gradient & Magnetic Field using Ferrofluid Cooling

Harry Garg¹, Sahib Singh², Vipender Singh Negi¹, Ashish Singh Kharola¹,
and Arun K. Lall²

¹Optical Devices & Systems
CSIR-CSIO, Chandigarh, 160030, India
harry.garg@gmail.com, vipender@live.com, ashish_kharola1988@yahoo.com

²Mechanical Engineering
PEC University of Technology, Chandigarh, 160012, India
s.sahib68@gmail.com, lallkarun@gmail.com

Abstract — Ferrofluid is a colloidal suspension of single domain magnetic particles of diameter approximately 10 nm, coated with a molecular layer of a dispersant and suspended in a liquid carrier. Ferrofluids may form the basis for next generation noiseless, vibration free passive cooling technique. The pumping ability of ferrofluid depends on temperature gradient and magnetic field orientation. The proposed work covers numerical analysis of heat transfer, magnetism and flow characteristics of ferrofluids. Thermal conductivity and viscosity of ferrofluid governs the heat transfer and flow characteristics. The variation of flow with the direction of magnetic field has been investigated in this paper.

Index Terms — Coupled system, ferrofluid, magnetic field, passive cooling, pyromagnetic coefficient.

I. INTRODUCTION

Ferrofluid is a temperature sensitive magnetic fluid which means that its magnetization is function of temperature. A section of Ferrofluid exposed to heat source and external magnetic field directed in a specific orientation results in non-uniform magnetic body force, such a heat transfer is called thermo-magnetic convection [1] and this resultant flow of ferrofluid can be controlled by varying ferrofluid properties, magnetic field strength and temperature distribution. Thermo-magnetic convection can be useful in situations where convective heat transfer alone is inadequate in dissipating heat effectively. Cooling using ferrofluid is a passive cooling technique and it utilizes waste heat from the system to induce the flow in the presence of a magnetic field. The synergistic effect of magnetization, temperature and gradient produces a noiseless and vibration free cooling.

The stability of the magnetic colloid depends on the thermal contribution and on the balance between attractive (Vander Waals and dipole-dipole) and repulsive (Steric and electrostatic) interactions. In order to avoid agglomeration, the magnetic particles are coated with a shell of an appropriate material called surfactant.

A prototype of a miniature automatic cooling device using ferrofluid has previously been described by Love et al. [2] & Li et al. [3]. Streck and Jopek [4] simulated ferrofluid flow in a channel between two parallel plates

Aminfar et al. [5] have investigated numerically the hydrothermal characteristics of a water based ferrofluid in vertical rectangular duct. The magnetic field is produced by a current carrying wire which is placed along the length of the duct.

The flow state in a magnetic fluid [6] heat transport device is investigated numerically. Model geometry of the device is considered when the device is placed vertically. From the results of the calculation a qualitative explanation is made for the flow state of experimental device when the magnetic field is affected.

Wrobel et al. [7] studied thermo-magnetic convective flow of paramagnetic fluid in an annular enclosure with a round rod core and a cylindrical outer wall numerically and experimentally. Their results shows that magnetizing force affects the heat transfer rate and a strong magnetic field can control the magnetic convection of paramagnetic fluid.

Kikura et al. [8] carried experimental investigations in a cubical enclosure and concentric horizontal annuli under the influence of a varying magnetic field. The permanent magnet was placed at different sides of the enclosure and the effect of magnetic field gradient on the ferrofluid heat transfer was studied.

Lajvardi et al. [9] report an experimental work on

the convective heat transfer of ferrofluid flowing through a heated copper tube in the laminar regime in the presence of magnetic field.

Demuren & Grotjans [10] discussed simplification of flow by considering density variations in the body force term, which is a source and sink momentum in the direction of gravity. The density difference is related to the coefficient of thermal expansion and the temperature difference. This approach works very well for small density differences and has enabled simplified solution of many buoyant flow problems.

Lopez et al. [11] developed a new consistent Boussinesq type approximation. The density variations were considered in the advection term of the Navier-Stokes equations. The new approximation allows accurate treatment of situations with differential rotation or when strong vortices appear in the interior of the domain.

Although many theoretical and experimental investigations have been carried for ferrofluid flow behaviour but the investigations on how ferrofluid flow depends on the thermal conductivity and orientation of magnetic field are sparse. Besides this, the investigations were carried on novel technique to enhance the heat dissipation capacity using ferrofluid.

II. MECHANISM OF FLOW

Ferrofluid being paramagnetic obeys Curie's Law and therefore its behaviour is directly related to temperature and magnetization. The change of magnetization of ferrofluid with temperature is defined by term called pyromagnetic coefficient. Magnetization of ferrofluid decreases with increase in temperature. The temperature, at which the magnetization of the fluid is negligible, is called Curie temperature.

Figure 1 shows the flow mechanism of ferrofluid, magnetic fluid in hot region near heat source being at a higher temperature loses its magnetic properties. An external magnet is placed in the vicinity creates a magnetic field. The relatively cold ferrofluid behind experiences a greater magnetic attraction force and due to this greater attraction, cold ferrofluid pushes hot ferrofluid on the other end, thus resulting in fluid flow. This body force on fluid section near heat source is directly related to the external magnetic field, magnetic susceptibility, temperature gradient and pyromagnetic coefficient. Combining the two effects, i.e., heat and orientation of magnetic field with suitable geometry and thermo magnetic properties of ferrofluid results in flow and heat dissipation from the system.

Thus, important requirement for fluid pumping is temperature gradient and magnetization variation with temperature. Also, the flow can be controlled by varying external magnetic field and temperature gradient within the fluid. A series of experiments were conducted to study the effect of external magnetic field and

temperature distribution. The results showed that fluid flow can be controlled by changing the position of the magnet.

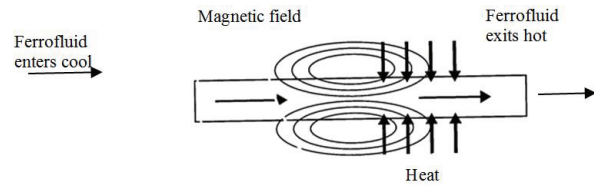


Fig. 1. Mechanism of flow.

Nomenclature

Symbol	Physical Quantity
ρ	Density (kgm^{-3})
T	Temperature (K)
u	Velocity (ms^{-1})
k	Thermal conductivity ($\text{Wm}^{-1}\text{K}^{-1}$)
p	Pressure (N/m^2)
ν	Viscosity of the fluid (Pa.s)
M	Magnetization vector (Am^{-1})
B	Magnetic induction (Wbm^{-2})
H	Magnetic field (Am^{-1})
F	Kelvin body force (Nm^{-3})
μ	Permeability of medium (Hm^{-1})
μ_0	Permeability of air or vacuum $4\pi \times 10^{-7} (\text{Hm}^{-1})$
χ_m	Total magnetic susceptibility
χ_0	Differential magnetic susceptibility of the ferrofluid
α	Thermal expansion coefficient of the fluid (K^{-1})
T_0	Reference temperature (K)

III. GOVERNING EQUATIONS

The equations governing the ferrofluid flow under the effect of applied magnetic field are magnetostatic equation, mass conservation equation, momentum equation and the energy equation in the frame of Boussinesque approximation. The nomenclature is shown above.

A. Magnetostatic equations

Ferrofluids are non-conducting, so Maxwell's equations are for non-conducting medium and no currents are simplified to:

$$\nabla \times \mathbf{H} = 0, \quad (1)$$

$$\nabla \cdot \mathbf{B} = 0. \quad (2)$$

Magnetic flux density \mathbf{B} is given as:

$$\mathbf{B} = \mu \mathbf{H} = \mu_r \mu_0 \mathbf{H}, \quad (3)$$

$$\mathbf{B} = \mu_0 (1 + \chi_m) \mathbf{H}, \quad (4)$$

where, $\mu_r = (1 + \chi_m)$ is the relative permeability. The relationship between the magnetization vector \mathbf{M} and magnetic field vector \mathbf{H} can be written in the form:

$$\mathbf{M} = \chi_m \mathbf{H}, \quad (5)$$

where, χ_m is the magnetic susceptibility of material is a dimensionless proportionality constant that indicates the degree of magnetization \mathbf{M} of a material in response to an applied magnetic field \mathbf{H} . The magnetic induction \mathbf{B} , the magnetization vector \mathbf{M} and the magnetic field vector \mathbf{H} are related by the following relation:

$$\mathbf{B} = \mu_0(\mathbf{H} + \mathbf{M}). \quad (6)$$

B. Equations governing fluid flow

The mass conservation equation is given as:

$$\frac{\partial \rho}{\partial t} + \nabla \cdot (\rho \mathbf{u}) = 0. \quad (7)$$

Ferrofluid are incompressible, i.e., density is constant, and the continuity equation reduces to:

$$\rho \nabla \cdot \mathbf{u} = 0. \quad (8)$$

The momentum equation is given by the following equation:

$$\rho \frac{\partial \mathbf{u}}{\partial t} + \rho(\mathbf{u} \cdot \nabla) \mathbf{u} = \nabla \cdot [-p\mathbf{I} + (\mu(\nabla \mathbf{u} + (\nabla \mathbf{u})^T) - \frac{2}{3}\mu(\nabla \cdot \mathbf{u})\mathbf{I})] + \mathbf{F}. \quad (9)$$

Since, ferrofluid is incompressible fluid, therefore density is constant and the momentum equation reduce to:

$$\rho \frac{\partial \mathbf{u}}{\partial t} + \rho(\mathbf{u} \cdot \nabla) \mathbf{u} = \nabla \cdot (-p\mathbf{I} + \mu(\nabla \mathbf{u} + (\nabla \mathbf{u})^T) + \mathbf{F}. \quad (10)$$

The momentum equation results from the application of Newton's second law of motion to the fluid element. The first term on the right of the Equation (10) represents net pressure force; the second term represents net effect of viscous normal and shear stress. The last term provides the body force on fluid per unit volume. In case of ferrofluids, the body force term in the momentum equation represents the Kelvin body force per unit volume and is given by the following equation:

$$\mathbf{F} = (\mathbf{M} \cdot \nabla) \mathbf{B}. \quad (11)$$

Thus, the momentum equation for ferrofluids reduces to:

$$\rho \frac{\partial \mathbf{u}}{\partial t} + \rho(\mathbf{u} \cdot \nabla) \mathbf{u} = \nabla \cdot (-p\mathbf{I} + \mu(\nabla \mathbf{u} + (\nabla \mathbf{u})^T) + (\mathbf{M} \cdot \nabla) \mathbf{B}). \quad (12)$$

Using value of \mathbf{M} and \mathbf{B} from (5) and (6) the body force can be written as:

$$\mathbf{F} = \mu_0(\chi_m \mathbf{H} \cdot \nabla)(1 + \chi_m) \mathbf{H}, \quad (13)$$

where χ_m is treated solely as being dependent on the temperature and is given as:

$$\chi_m = \frac{\chi_0}{1 + \alpha(T - T_0)}. \quad (14)$$

The energy equation for ferrofluids is the energy equation for an incompressible fluid and follows the modified Fourier's law as:

$$\rho c_p \left(\frac{\partial T}{\partial t} + \mathbf{u} \cdot \nabla T \right) = k \nabla^2 T + \mu \Phi - \mu_0 T \frac{\partial \mathbf{M}}{\partial T} \cdot (\nabla \cdot \mathbf{H}), \quad (15)$$

where, $\mu \Phi$ is the viscous dissipation is defined as:

$$\Phi = \left(2 \left(\left(\frac{\partial u_x}{\partial x} \right)^2 + \left(\frac{\partial u_y}{\partial y} \right)^2 + \left(\frac{\partial u_z}{\partial z} \right)^2 \right) + \left(\frac{\partial u_y}{\partial x} + \frac{\partial u_x}{\partial y} \right)^2 + \left(\frac{\partial u_y}{\partial z} + \frac{\partial u_z}{\partial y} \right)^2 + \left(\frac{\partial u_x}{\partial z} + \frac{\partial u_z}{\partial x} \right)^2 - \frac{2}{3} (\nabla \cdot \mathbf{u})^2 \right). \quad (16)$$

The last term in the energy Eq. (15) represents the thermal power per unit volume due to the magnetocaloric effect.

IV. DESCRIPTION OF MODEL

Figure 2 shows the basic arrangement of the experiment. The model consists of a channel, a permanent magnet and a heat source. Here, length of channel is 100 mm and width is 5 mm. The length of magnet is 25 mm and the width is 10 mm. Strength of magnet is 1 Tesla. The initial temperature of the fluid is 293.15 K. The surrounding medium is air at an initial temperature of 293.15 K. Heat is applied by considering heat source and magnet is placed near it. Fresh fluid enters the section near the magnet from the reserved storage on the left as and magnetic fluid pumping effect re-circulates it to storage to bring down temperature of fluid for next cycle of operation and thus the flow sustains in a continuous loop.

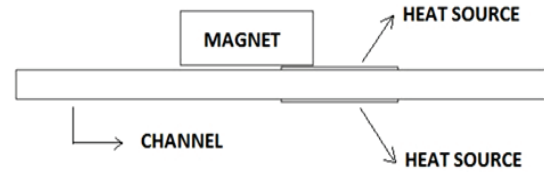


Fig. 2. 2D model of cooling system.

The various meshing parameters used in the simulation are shown in Table 1.

Table 1: Meshing parameters

Mesh Parameter	Value
Minimum element quality	0.1577
Average element quality	0.9292
Triangular elements	2776
Quadrilateral elements	268
Edge elements	325
Vertex elements	20

V. RESULTS

This model is solved using COMSOL Multiphysics by applying heat transfer, fluid flow and magnetic based physics on ferrofluids. Modifications were made in the momentum equation by adding Kelvin body force. Simulations studies are then carried to get the velocity distribution, temperature distribution and magnetization variation. The reference properties of ferrofluid used in simulation are shown in Table 2.

Table 2: Properties of Ferrofluid used in simulation

Property	Value
Density (kg/m^3)	1050.0
Viscosity (Pa-s)	0.0030
Susceptibility	0.3860
Thermal conductivity ($\text{Wm}^{-1}\text{K}^{-1}$)	0.1500
Specific heat ($\text{Jkg}^{-1}\text{K}^{-1}$)	1715.0
Thermal expansion coefficient (K^{-1})	0.0009
Curie temperature (K)	345.00 ± 5

Figure 3 shows the velocity plot. The maximum velocity close to edge of magnet is 8.01 mm/s . From the velocity plot, it is observed that the velocity is high near the poles of the magnet. Streamlines are also shown in the velocity plot indicating the path followed by fluid particles. Two humps in the streamlines near the poles of the magnet indicate a stronger magnetic force at the poles.

Figure 4 shows the temperature of ferrofluid. The maximum temperature is 326 K and is near the heat source. Magnetic field lines and magnetic flux density distribution is shown in Fig. 5.

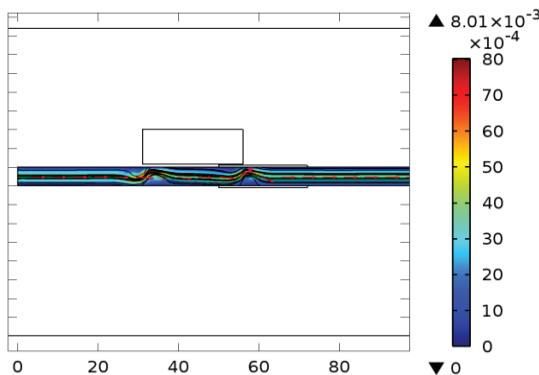


Fig. 3. Velocity profile of ferrofluid.

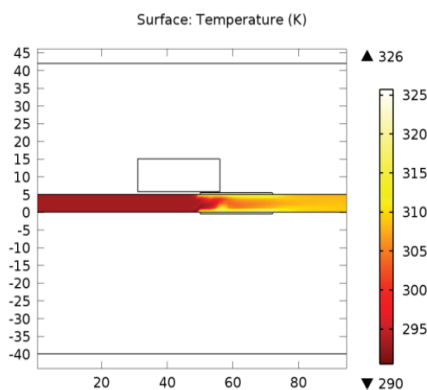


Fig. 4. Temperature of ferrofluid.

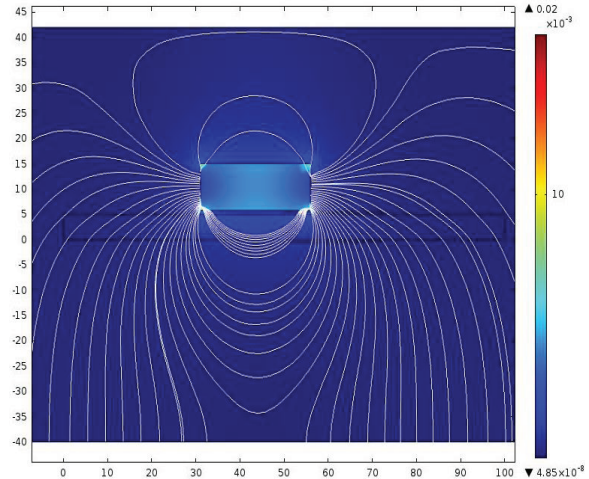


Fig. 5. Magnetic field lines.

Velocity variation along the length of the channel is shown in Fig. 6. The two peaks in the velocity profile represent the position of the poles of the magnet. It is also observed that the velocity magnitude near the two poles is different.

The smaller velocity at the right pole is because fluid in this region being at a higher temperature loses magnetization and hence experiences a lower magnetic force.

The variation of the magnetization along the length of the channel is shown in Fig. 7. Two peaks represent the region near the poles. The value of magnetization of the fluid near the right pole is less because of high temperature of the fluid in this region. The value of average velocity, resultant body force and power of fluid is given in Table 3.

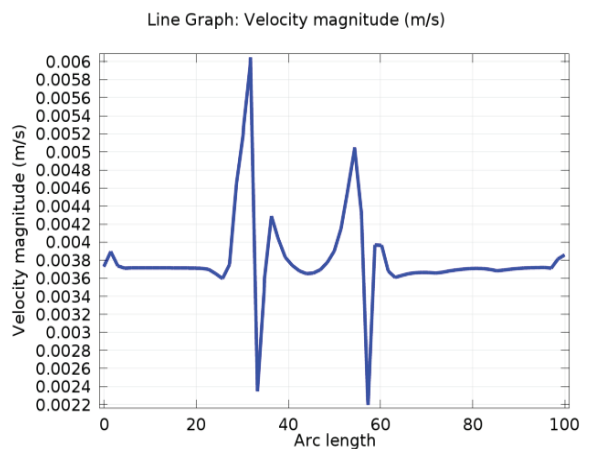


Fig. 6. Graph showing variation of velocity along length of channel.

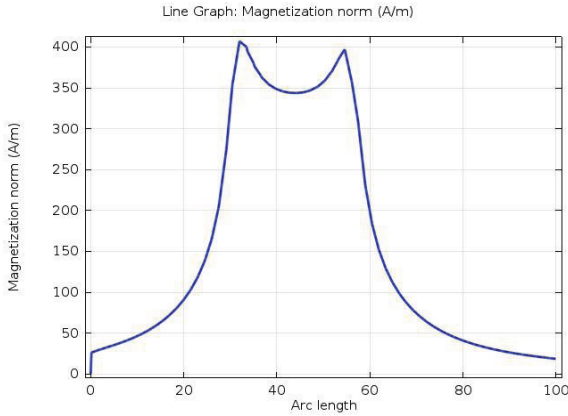


Fig. 7. Variation of magnetization of fluid along the length of channel.

Table 3: Value of output parameters

Property	Value
Average velocity	2.490 mm/s
Resultant body force	8.380 N/m ³
Power of fluid	0.34 μW

A. Effect of variation in thermal conductivity of fluid

With increase in thermal conductivity of the fluid, two associated effects were observed. First effect is that with increased heat transfer rate in the ferrofluid decreases temperature gradient within the fluid, with decrease in temperature gradient the body force of ferrofluid decreases. Second effect is, by increasing the thermal conductivity, the heat carried away by the fluid from the heat source increases and this tends to increase the temperature gradient across the hot and cold junction of ferrofluid. Thus, by increasing the conductivity the temperature gradient increases across the two ends due to greater heat being carried and starts decreasing when it is conducted within the fluid.

Figure 8 shows the velocity variation with conductivity. The graphs show that at a particular value of conductivity, the velocity is maximized.

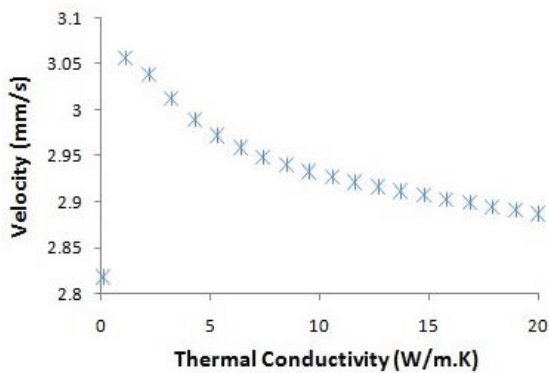


Fig. 8. Velocity variation with thermal conductivity.

B. Effect of changing the orientation of magnetic field

In numerical analysis, the effect of changing the orientation of the field is studied. Figure 9 shows magnet placed in the horizontal direction. The arrows in the diagram show distribution of the magnetic field.

Figure 10 shows the velocity distribution in the channel under the magnetic field. There is a disturbance in the flow and two curves are formed at the exit and entry of the fluid.

Figure 11 shows temperature of ferrofluid in horizontal orientation with a maximum temperature of 333 K near heat source. As can be seen from Fig.12, the velocity has decreased for vertical position.

Figure 13 shows the temperature of ferrofluid with a maximum temperature of 346 K. Table 4 compares the values of different parameters for both positions of the magnet.



Fig. 9. Direction of magnetic flux density for magnet in horizontal and vertical position.

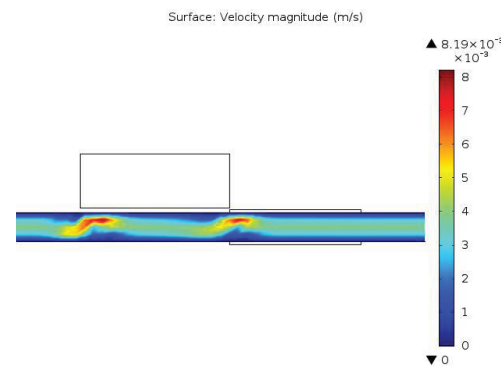


Fig. 10. Velocity of ferrofluid in horizontal position.

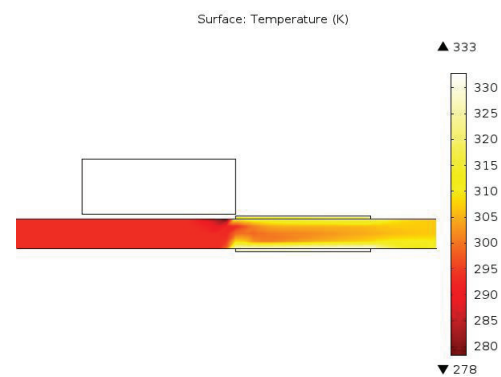


Fig. 11. Temperature of ferrofluid in horizontal position.

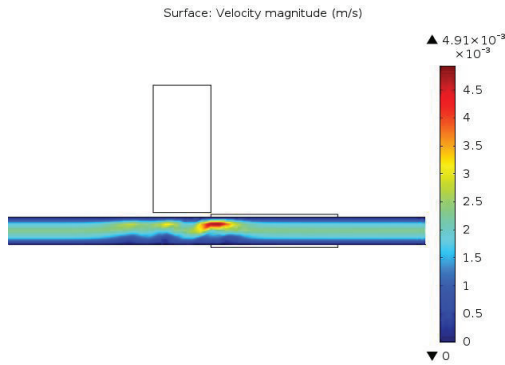


Fig. 12. Velocity of ferrofluid in vertical position.

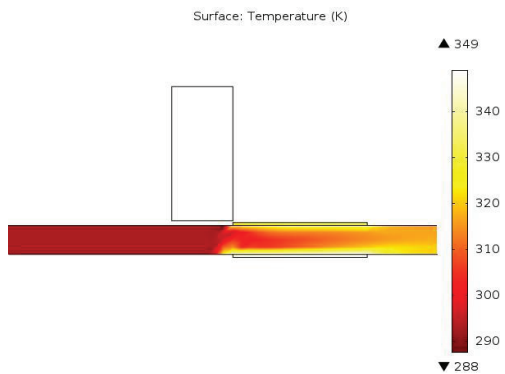


Fig. 13. Temperature of ferrofluid in vertical position.

Table 4: Comparison in different position of magnet

Physical Quantity	Magnet in Horizontal Position	Magnet in Vertical Position
Average velocity at outlet (mm/s)	2.567	1.680
Average temperature at outlet (K)	308.1	315.8
Body force (N/m ³)	8.805	4.544
Power of fluid (μW)	0.062	0.014

VI. CONCLUSION

This paper reports numerical studies on ferrofluid flow phenomena in presence of magnetic field to obtain flow, velocity distribution, temperature distribution and magnetization. Important conclusions drawn from simulation studies are:

1. Thermal conductivity of fluid influences the velocity and temperature distribution of ferrofluid. With increase in conductivity of fluid, the velocity of fluid may decrease depending on the amount of decrease in temperature gradient in the fluid.
2. The velocity of the fluid is locally high close to magnetic field and heating area.
3. Orientation of the magnetic field influences the ferrofluid flow. The velocity of ferrofluid is

relatively high when the magnetic field lines are parallel to the flow direction. Since maximum number of magnetic field lines are parallel to the flow direction (interacting magnetic flux) when magnet is placed in a horizontal direction.

4. The thermal gradient has direct effect on the flow of ferrofluid under influence of magnetic field.
5. It was found that flow rate increases with increase in magnetic field and increase in temperature gradient along the flow direction.

ACKNOWLEDGMENT

The authors are thankful to the Department of Science & Technology, India vide their grant number DST/TSG/FF/2011/187.

REFERENCES

- [1] R. E. Rosenweig, "Ferrohydrodynamics," *Cambridge University Press*, London, 1985.
- [2] L. J. Love, J. F. Jansen, T. E. Mcknight, Y. Roh, and T. J. Phelps, "Ferrofluid induced flow for microfluidic applications," *IEEE Trans. Mechatronics*, vol. 10, pp. 68-76, 2005.
- [3] Q. Li, W. Liang, H. Sun, and J. F. Jansen, "Investigation on operational characteristics of a miniature automatic cooling device," *International Journal of Heat and Mass Transfer*, vol. 51, pp. 5033-5039, 2008.
- [4] T. Streck and H. Jopek, "Computer simulation of heat transfer through ferrofluid," *Journal of Solid State Physics*, vol. 244 pp. 1027-103, 2006.
- [5] H. Aminfar, M. Mohammadpourfard, and S. Ahangar Zonouzi, "Numerical study of the ferrofluid flow and heat transfer through a rectangular duct in the presence of a non-uniform transverse magnetic field," *Journal of Magnetism and Magnetic materials*, vol. 327, pp. 31-42, 2013.
- [6] H. Yamaguchi, I. Kobori, Y. Uehata, and K. Shimada, "Natural convection of magnetic fluid in a rectangular box," *Journal of Magnetism and Magnetic materials*, vol. 201, pp. 264-267, 1999.
- [7] W. Wrobel, E. Fornalik-Wajs, and J. S. Szmyd, "Experimental and numerical analysis of thermo-magnetic convection in a vertical annular enclosure," *International Journal of Heat and Fluid Flow*, vol. 31, pp. 1019-1031, 2010.
- [8] H. Kikura, T. Sawada, and T. Tanahashi, "Convection of a magnetic fluid in a cubic enclosure," *Journal of Magnetism and Magnetic materials*, vol. 122, pp. 315-318, 1993.
- [9] M. Lajvardi, J. Moghimi-Rad, I. Hadi, A. Gavili, T. Dallali-Isfahani, F. Zabihi, and J. Sabbaghzadeh, "Experimental investigation for enhanced ferrofluid heat transfer under magnetic field effect," *Journal of Magnetism and Magnetic Materials*, vol. 322, pp. 3508-3513, 2010.

- [10] A. Demuren and H. Grotjans, "Buoyancy-driven flows, beyond the Boussinesq approximation," *Numerical Heat Transfer, Part B: Fundamentals*, vol. 56, pp. 1-22, 2009, DOI: 10.1080/10407790902970080.
- [11] J. M. Lopez, F. Marques, and M. Avila, "The Boussinesq approximation in rapidly rotating flows," *J. Fluid Mech.*, vol. 737, pp. 56-77, 2013.



Harry Garg is working as Senior Scientist in CSIR-CSIO Chandigarh, India. He received doctoral degree from PEC University of Technology, Chandigarh. His research interest includes design and development of opto-mechanical systems, micro scale heat transfer using nano-coolants and ferrofluid, CFD design and development for Aerodynamics.



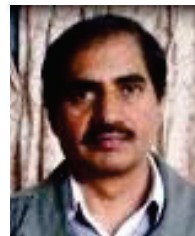
Sahib Singh received B.Tech. degree in Mechanical Technology, Ferozepur, and Masters in Mechanical Engineering from PEC University of Technology Chandigarh. His research interests includes engineering materials, ferrofluids and liquid cooling.



Vipender Singh Negi is working as Research Fellow in CSIR-CSIO Chandigarh, India. He has completed his bachelor degree in Mechanical Engineering from Panjab University. He is working for FEA of glass grinding and polishing; other areas of his interests are CFD, heat transfer, ferro-hydrodynamics and mechatronics.



Ashish Singh Kharola is working as Project Assistant in CSIR-CSIO Chandigarh, India. He has completed his degree in Mechanical Engineering from Kurukshetra University. He is working on ferrofluid analysis. He has also been certified in Computer Aided Tool Engineering, from Central Institute of Tool Design, Hyderabad. Other areas of his interests are heat transfer, automobile engineering, and CAE.



Arun K. Lall is working as a Professor in the Mechanical Engineering Department in PEC University of Technology, Chandigarh. He received his Doctoral degree from IIT, Kanpur. His research interests includes FEM/FEA, enhanced heat transfer, tribology and CFD analysis.

